

Ultra-High Frequency Magnetic Resonance Imaging

By

Arthur W. Magill, MSc

Thesis submitted to the University of Nottingham
for the degree of Doctor of Philosophy,
September 2006

Contents

Abstract	viii
Acknowledgements	x
List of Symbols	xi
1 Introduction	1
1.1 Scope of this Thesis	2
2 Principles of MRI	5
2.1 Introduction	5
2.2 Nuclear Magnetic Resonance	6
2.2.1 Nuclear Magnetisation	6
2.2.2 Larmor Precession	10
2.2.3 Relaxation	12
2.2.4 Free Induction Decay	14
2.3 Magnetic Resonance Imaging	15
2.3.1 Contrast	15

2.3.2	Signal Localisation	16
2.3.3	Slice Selection	17
2.3.4	Frequency Encoding	19
2.3.5	Phase Encoding	23
2.3.6	Spin Echoes and Gradient Echos	24
2.3.7	k -Space	26
2.3.8	Spinwarp Imaging	27
2.3.9	Echo Planar Imaging	28
2.3.10	Burst Imaging	30
2.3.11	Extended Phase Graph	31
2.3.12	Parallel Imaging and SENSE	36
2.4	Instrumentation	40
2.4.1	Main Magnet	40
2.4.2	Shim Coils	43
2.4.3	Gradient Coils	43
2.4.4	Waveform Controller	44
2.4.5	RF System	44
3	RF Probe Design	47
3.1	Introduction	47
3.2	Transmission, Reception and Reciprocity	48
3.3	Resonance	50
3.4	Probe Losses	52

3.5	Specific Absorption Rate (SAR)	53
3.6	Signal-to-Noise Ratio (SNR)	54
3.7	The Preamplifier	58
3.8	Impedance Matching	59
3.9	Transmit/Receive Switching	62
3.10	Probe Design	64
3.10.1	Volume Probes	64
3.10.2	Quadrature	68
3.10.3	Surface Coils and Active Detuning	70
3.10.4	Array Probes	71
3.11	High Field Effects	76
3.11.1	Wavelength	76
3.11.2	Material Properties	76
3.11.3	RF Penetration	77
3.11.4	Dielectric Resonance and Interference	79
3.11.5	Coupling	82
3.11.6	Heating	82
4	EM Modelling Theory	84
4.1	Introduction	84
4.2	Finite Element Method (FEM)	85
4.3	Finite Difference Time Domain (FDTD)	86
4.4	Method of Moments (MoM)	87

4.5	The Transmission Line Matrix Method (TLM)	88
4.5.1	The Scattering Matrix	90
4.5.2	Heterogeneous Modelling and Stubs	93
4.5.3	Mesh Parameters	94
4.5.4	Voxel Size, Timestep and Stability	99
4.5.5	Extracting the Fields	99
4.5.5.1	Rotating B_1 Field	100
4.5.5.2	Electric Field and SAR	101
4.5.6	Excitation	101
4.5.7	Boundary Conditions	102
4.5.8	Frequency Response and Convergence	103
4.5.9	Alternative Mesh Geometries	104
4.5.10	Implementation Details	105
4.6	Simulation Models	106
4.6.1	Probe Models	107
4.6.2	Human Models	107
4.6.3	Tissue Properties	108
5	RF Probe Modelling	110
5.1	Introduction	110
5.2	The Birdcage Probe	111
5.2.1	Instantaneous and Rotating Fields	112
5.2.2	Field Homogeneity vs. Frequency	113

5.2.3	Phase Variation vs. Frequency	116
5.2.4	Sample Conductivity	116
5.2.5	Signal-to-Noise Ratio (SNR)	120
5.2.6	Specific Absorption Rate (SAR)	126
5.3	The Microstrip	129
5.3.1	Microstrip Theory	129
5.3.2	The Microstrip as a Probe Element	133
5.3.3	Time and Frequency Response	134
5.3.4	Microstrip Fields	138
5.3.5	Strip Geometry	142
5.3.6	Adding an RF Shield	156
5.4	A Microstrip Array Probe	159
5.4.1	Single Strip Response	159
5.4.2	Transmission	164
5.4.3	Reception	164
5.5	Discussion	167
6	Simulated Imaging	169
6.1	Introduction	169
6.2	Transmit and Receive Field Dependency	170
6.3	Bloch Simulation	170
6.3.1	Relaxation	172
6.3.2	Instantaneous Nutation	172

6.3.3	Modelling RF Transmit Field Inhomogeneity	174
6.3.4	Signal Reception and B_1^- Inhomogeneity	175
6.3.5	Echos and Intravoxel Dephasing	175
6.3.6	Implementation Details	176
6.4	Imaging Sequences	178
6.4.1	The Simulation Phantom	178
6.4.2	Quantifying Image Error	179
6.4.3	Simulated Two Dimensional Imaging	179
6.5	Imaging with the Microstrip Probe	180
6.5.1	Reception	183
6.5.2	Transmission	187
6.6	Sequential Transmit Imaging	193
6.6.1	Testing the New Sequence	197
6.6.2	SENSE Reconstruction	204
6.6.3	Limitations of the New Sequence	212
6.7	Discussion	212
7	Hardware Implementation	215
7.1	Introduction	215
7.2	The Probe	216
7.3	The Multiplexer	218
7.3.1	RF Switching	219
7.3.2	Control Logic	220

7.3.3	Performance	223
7.4	Imaging at 3T	224
7.5	Discussion	225
8	Discussion	228
8.1	Summary	228
8.2	Future Work	229
8.3	Conclusions	232
	References	233

Abstract

This thesis addresses the problem of radiofrequency probe design for Ultra High Frequency Magnetic Resonance Imaging (7T).

The signal-to-noise ratio available in Magnetic Resonance Imaging (MRI) is determined by the static magnetic field strength, causing a continued drive toward higher fields to enable faster image acquisition at finer spatial resolution. The resonant frequency increases linearly with static field strength. At 7T the proton resonant frequency is 300MHz, with a wavelength of approximately 13cm in tissue. As this is smaller than the dimensions of the human head, the phase of the radiofrequency (RF) signal varies considerably across the sample, producing field cancellation due to interference.

A full wave electromagnetic simulator, using the Transmission Line Matrix (TLM) method, was developed to investigate RF probes at high frequency. A Birdcage probe operating at 64, 128 and 300MHz (corresponding to 1.5, 3 and 7T) was simulated, loaded with an anatomically detailed human head model. A half-wave microstrip was investigated for use as a high frequency probe element. Magnetic and electric fields produced by a single microstrip were simulated, and the strip dimensions varied to investigate the effect on field penetration into the head and Specific Absorption Rate (SAR). A transmit-receive array probe using four microstrip elements was then developed.

Bloch simulations were run, using TLM generated magnetic fields, to investigate imaging at short wavelength. Parallel receive probes are demonstrated to offer considerable advantage over volume probes, as signals from receive elements can be combined without interference. There is no transmit equivalent to parallel reception; simultaneous excitation of independent probe elements causes interference in exactly the same manner as a volume probe. A new imaging sequence was developed using a Burst-like encoding to allow sequential excitation of probe elements, without interference, which can be recalled in a single readout. An improvement in image homogeneity was demonstrated, and SENSE acceleration of the new imaging sequence is shown.

The sequence was implemented at 3T using a purpose built four element microstrip probe. An RF multiplexer was also built to enable transmit element switching during the imaging sequence. It was demonstrated that images due to different RF excitations, acquired in a single EPI readout, can be separated.

”We often fail to realize how little we know about a thing until we attempt to simulate it on a computer”

D. E. Knuth (1968), The Art of Computer Programming,
Vol 1 - Fundamental Algorithms, Addison-Wesley.

Acknowledgements

Studying for a PhD is always an adventure. Mine was no exception and many people have helped me along the way. I would like to thank the following in particular:

Marcello Alecci, who first inspired me to study RF probe design, and Irene Tracey for telling me to stop talking about studying for a PhD, and to get on and do it.

Paul Glover, my supervisor, who has an instinct for electromagnetic design that I can only hope to match one day. Alexa Jones, my partner-in-crime and cable monkey for most of my PhD (who found a face in every image I've ever acquired). Ben Wilton for helping to explain Burst and coding the sequential transmit imaging scheme described in chapter 6.

My many office mates for useful, entertaining and occasionally MR related conversation: Benito, Silvia, Wietske, Mike, Clemente, Rosa, Bhavna, Alex, Matt, Nic, Gianlo, Luca, Terry. Also to Lesley, for a cheery 'Good morning' at whatever time I stumbled in to the MR centre.

Computational electromagnetics is a power hungry business. My simulations would probably still be running without machine time generously donated by Dave Flitney (FMRIB, Oxford) with four DEC Alphas, Steve Greedy (GGIEMR, Nottingham) with four DEC Alphas and less users, and Andrew Peters (SPMMRC, Nottingham), the proud owner of a 10 node dual Operton cluster, which he allowed me to help 'burn in'.

I didn't spend the whole of the past four years in the lab. My housemates have provided a welcome distraction: Fee, Ally, Rick (and Jo), Judith, Eleri, Kelly and Nicki. I'd especially like to thank Nicki, my girlfriend, for putting up with all those late nights I've spent at the lab, and reminding me that I have a real life away from the computers.

Finally I want to thank Mum and Dad, for supporting me through my many years of study and, more importantly, for teaching me to be curious about the world around me.

Thank you all.

List of Symbols

γ	Gyromagnetic ratio
ε	Permittivity
ε_0	Permittivity of free space
ε_r	Relative permittivity
η	Filling factor
λ	Wavelength
μ	Permeability
μ_0	Permeability of free space
μ_r	Relative permeability
ξ	Electromotive Force (EMF)
ρ	Density
σ	Conductivity (electrical)
ϕ	Phase
ψ	Signal to noise ratio (SNR)
Ψ	Receiver noise matrix
ω	Angular frequency ($= 2\pi f$)
ω_0	Resonant Larmor frequency at field strength B_0
B_0	Static magnetic field
B_1	RF magnetic field
B_1^+	Positive rotating RF field
B_1^-	Negative rotating RF field
C	Capacitance
E	Electric field
f	Frequency
G	Magnetic field gradient
I	Current
L	Inductance
M	Sample magnetisation
P	Power
Q	Quality factor
R	Resistance
T_1	Longitudinal relaxation time constant
T_2	Transverse relaxation time constant
T_2^*	Effective transverse relaxation time constant
V	Voltage
X	Reactance
Z	Impedance ($= R + iX$)

Chapter 1

Introduction

Nuclear Magnetic Resonance (NMR) was first observed by Purcell [1] and Bloch [2] in 1946, work for which they shared the Nobel prize in 1952. NMR developed into a powerful tool for the analysis of chemical structures, that is today a standard part of the chemists' toolkit. In 1973 Lauterbur [3] and Mansfield [4] developed techniques to use NMR to generate images of a sample, for which they received the Nobel prize in 2003. Magnetic Resonance Imaging (MRI) has since become a standard clinical method. The development of function imaging [5, 6] has also made MRI an invaluable tool in psychology and physiology, allowing researchers to investigate not only the structure, but also the functioning of the human brain.

When Bloch *et al.* [7] first demonstrated 'nuclear induction', they used a 0.18T static magnetic field produced by a lecture-demonstration magnet over a 2cm³ volume. The resulting radiofrequency (RF) signal was detected using a small coil of wire wrapped around the sample container. Since that experiment, the instrumentation used in NMR and MRI has grown considerably in both complexity and cost. In particular, for human and animal experiments, a highly homogeneous magnetic field must be generated over a volume large enough to contain the body part being examined.

It has long been recognised that it is desirable to work at the highest possible magnetic field strength, to improve the signal-to-noise ratio (SNR) available

in NMR and MRI experiments. Field strengths used in both research and clinical machines have continued to increase over the past 30 years.

Increasing the static field strength increases the frequency at which excited nuclei resonate. High frequency RF effects have traditionally limited the rise in static field strength. Initially it was not thought possible to image at resonant frequencies greater than 10–30MHz, due to the reduced RF penetration depth. This limit has clearly been exceeded, with clinical systems now routinely operating at 1.5T (64MHz).

The MRI community has recently seen another shift to higher field systems, with 7T (300MHz) human imaging systems now installed at several sites around the world and a 9.4T (400MHz) human system now in use. Above 128MHz there is a qualitative change in the RF design problem, as the proton resonant wavelength is shorter than the dimensions of the human body, making it more difficult to produce a uniform RF field over the sample volume.

1.1 Scope of this Thesis

In this thesis, high frequency ($>128\text{MHz}$) RF probe design is investigated. Radiofrequency magnetic fields generated by probes at short wavelength (relative to the sample size) are investigated through full wave electromagnetic simulation, using the Transmission Line Matrix (TLM) method. At short wavelength the phase of the RF field varies significantly over the sample volume. It is demonstrated that field inhomogeneity is largely caused by interference between fields generated by spatially separate parts of the RF probe (rungs on a Birdcage, for example). It is shown that parallel receive arrays offer a considerable improvement in image homogeneity, as signals received by different probe elements can be combined without phase information, preventing the signal cancellation seen with volume probes. There is no direct transmit equivalent to parallel reception. Fields produced by separate probe elements transmitting simultaneously interfere in exactly the same manner as fields produced by different parts of a volume probe. A

method is developed to rapidly excite probe elements in sequence, rather than simultaneously, avoiding interference between the transmit fields.

Chapter two introduces the fundamental principles of nuclear magnetic resonance and magnetic resonance imaging. An overview of a typical magnetic resonance imaging system is also given.

Chapter three discusses the principles of radiofrequency probe design for MRI. The operation of an RF probe is described, and important probe parameters are defined. A brief historical overview of widely used probe designs is then given. Changes in the RF design problem, as the operating frequency is increased, are then discussed.

Chapter four discusses full wave electromagnetic modelling. An overview of the Finite Element Method (FEM), the Finite Difference Time Domain (FDTD) method and the Method of Moments (MoM) is given. The Transmission Line Matrix (TLM) method is then described in detail, and its implementation discussed. All electromagnetic modelling work presented in this thesis was done using TLM. This chapter finishes with a brief review of the development of human models for electromagnetic simulation, and a description of the model used in this work.

Chapter five demonstrates TLM modelling of RF probes. A simple approximation to a Birdcage probe is used to investigate changes in the radiofrequency magnetic (B_1) field as the operating frequency is increased. The microstrip is then introduced as an RF probe element, and the effects of changing the strip geometry investigated. A four-element microstrip array probe is then developed, and the magnetic and electric fields it produces are investigated.

Chapter six investigates imaging using highly inhomogeneous transmit and receive B_1 fields. A Bloch simulator is developed and validated using three different imaging sequences (Spinwarp, Echo Planar and Burst). Realistic TLM simulated B_1 fields are then used in the Bloch simulator to investigate the effects of inhomogeneity in the transmit and receive B_1 fields. A new imaging sequence is then proposed, using a Burst-like transmit sequence to separately encode excitation from different probe elements, allowing mag-

netisation from all probe elements to be combined without interference, producing a more uniform excitation. Acceleration of the new imaging sequence using SENSE is then demonstrated.

Chapter 7 describes the implementation of the microstrip array probe developed in chapter five, and the sequential excitation method introduced in chapter six. Installation of the 7T scanner was incomplete when this work was carried out, so the probe was built to resonate at 128MHz for use in the Nottingham 3T machine. An RF multiplexer was also built to replace the standard TR switch, allowing the excitation element to be switched during the imaging sequence. First images acquired using the new sequence are presented, demonstrating the separation of different image profiles produced by excitation with different transmit elements.

Chapter 8 discusses the finding of this work, and presents some areas for further development.

Chapter 2

Principles of Magnetic Resonance Imaging

2.1 Introduction

This chapter introduces the theoretical foundations of Nuclear Magnetic Resonance (NMR) and Magnetic Resonance Imaging (MRI).

The origins of nuclear magnetisation are briefly discussed and the behaviour of a sample under an applied magnetic field investigated. NMR is fundamentally a quantum process; there is no classical argument for quantised angular momentum. However, once the postulate of quantised spin is accepted, Newtonian physics can be used to explain most MR phenomena. Larmor precession and the Free Induction Decay (FID) are described here using classical mechanics.

The fundamentals of image formation are then described. Signal localisation is introduced, making image formation possible. Three different imaging sequences are then examined (Spinwarp, EPI and Burst). A brief overview of parallel imaging methods is given, focussing particularly on the SENSE method.

Finally, a description of a complete MRI system is given, explaining the function of the main hardware components.

2.2 Nuclear Magnetic Resonance

The nuclear magnetic resonance effect arises from the interaction between the intrinsic angular momentum of nuclei and an external magnetic field.

Intrinsic angular momentum, more commonly known as spin, is a fundamental property of matter, like mass or charge. Electrons, protons and neutrons all possess spin, which may be positive or negative (corresponding to two rotational directions) and is quantised.

The magnitude of spin angular momentum is [8]

$$|\mathbf{p}| = \hbar\sqrt{I(I+1)} \quad (2.1)$$

where \hbar is Planck's constant divided by 2π and I is the spin quantum number, which may have integer or half integer values. Spin within a nucleus is additive. Positive and negative spins cancel, so nuclei containing multiple particles may possess zero net spin. Only nuclei containing an odd number of protons or neutrons have non-zero net spin.

2.2.1 Nuclear Magnetisation

Moving charges generate a magnetic field, and the nucleus is no exception. Associated with nuclear spin \mathbf{p} is a nuclear magnetic moment

$$\boldsymbol{\mu} = \gamma\mathbf{p} \quad (2.2)$$

where γ is a nucleus dependent constant called the gyromagnetic ratio. The behaviour of this magnetic moment under an applied magnetic field is the basis for the nuclear magnetic resonance phenomenon. Table 2.1 lists the gyromagnetic ratios of some nuclei used in biomedical magnetic resonance.

Nucleus	Spin	Relative Sensitivity	Gyromagnetic Ratio γ /MHzT ⁻¹
¹ H	$\frac{1}{2}$	1.000	42.58
¹³ C	$\frac{1}{2}$	0.016	10.71
¹⁹ F	$\frac{1}{2}$	0.830	40.05
³¹ P	$\frac{1}{2}$	0.066	17.25
²³ Na	$\frac{3}{2}$	0.093	11.27

Table 2.1: Properties of some NMR active nuclei. Relative sensitivity is the ratio $(\gamma/\gamma_{\text{proton}})^3$ [9].

In the absence of an external magnetic field, the orientation of sample spins is random. When a magnetic field \mathbf{B}_0 is applied to the system, sample spins align parallel and antiparallel to the applied field. By convention, the static field in MRI is applied along the z -axis

$$\mathbf{B}_0 = B_0 \hat{\mathbf{z}} \quad (2.3)$$

The component of the magnetic moment parallel to the applied field is then

$$\mu_z = \gamma \hbar m_I \quad (2.4)$$

where the quantum number m_I can have values

$$m_I = -I, -I + 1, \dots, I \quad (2.5)$$

For a spin- $\frac{1}{2}$ system $m_I = \pm \frac{1}{2}$ giving two possible states for μ_z

$$\mu_{z,n} = \begin{cases} +\frac{1}{2}\gamma\hbar & \boldsymbol{\mu}_n \text{ aligned with } \mathbf{B}_0 \\ -\frac{1}{2}\gamma\hbar & \boldsymbol{\mu}_n \text{ aligned against } \mathbf{B}_0 \end{cases} \quad (2.6)$$

The magnitude of the nuclear magnetic moment $|\boldsymbol{\mu}| > \mu_z$, so the moment must also have a transverse component

$$|\mu_{xy}| = \sqrt{|\boldsymbol{\mu}|^2 - \mu_z^2} = \frac{\gamma\hbar}{\sqrt{2}} \quad (2.7)$$

implying that the nuclear magnetic moment cannot align exactly to the applied magnetic field. It is not possible to know more than one component

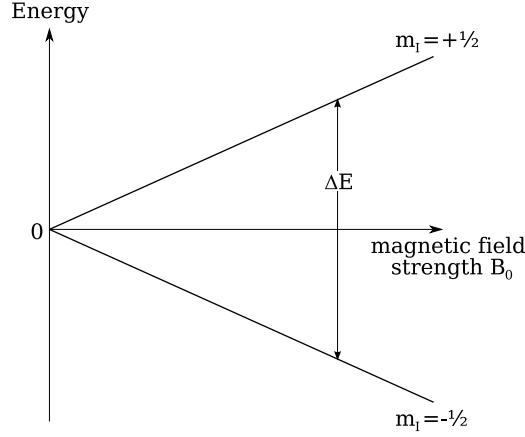


Figure 2.1: The energy difference between spin states increases with the applied field strength B_0 .

of the nuclear magnetic moment simultaneously, so while the magnitude of the transverse component can be calculated, its phase remains unknown.

Spins aligned with the field are in a lower energy state than spins aligned against it (fig. 2.1). The energy difference between the two states can be shown to be [10]

$$\Delta E = \gamma \hbar B_0 \quad (2.8)$$

The energy difference leads to an imbalance in spin state population. Using the Boltzmann relationship

$$\frac{N_{\uparrow}}{N_{\downarrow}} = \exp\left(\frac{\Delta E}{k_B T_s}\right) \quad (2.9)$$

where N_{\downarrow} and N_{\uparrow} are the number of spins aligned with and against the applied field, T_s is the temperature of the spin system and k_B is Boltzmann's constant. As the energy difference between the two spin states is small ($\Delta E \ll k_B T_s$), eqn. 2.9 can be approximated as

$$\frac{N_{\uparrow}}{N_{\downarrow}} \approx 1 + \frac{\Delta E}{k_B T_s}. \quad (2.10)$$

The population difference is then

$$N_{\uparrow} - N_{\downarrow} \approx N_s \frac{\gamma \hbar B_0}{2 k_B T_s} \quad (2.11)$$

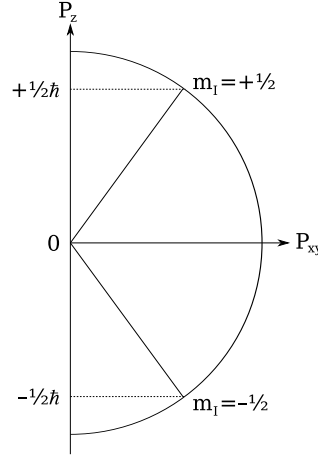


Figure 2.2: Angular momentum.

where N_s is the total number of spins in the sample. The bulk magnetisation of the sample is given by the sum of the magnetic moments of all the nuclei it contains. The phase of the transverse magnetisation is random and sums to zero, leaving the bulk magnetisation as

$$\mathbf{M} = \sum_{n=1}^{N_s} \mu_{z,n} \hat{z} \quad (2.12)$$

which, on substituting eqns. 2.6 and 2.11 gives

$$M_0 = \frac{\gamma^2 \hbar^2 B_0 N_s}{4k_B T_s} \quad (2.13)$$

aligned with the applied field. The magnetisation of the sample depends on its temperature and the strength of the applied magnetic field. Live samples such as human volunteers have a well defined temperature that cannot be changed, so sample magnetisation can only be increased by increasing the strength of the applied magnetic field. This point is discussed further in chapter 3 in the context of the achievable signal-to-noise ratio.

Magnetic resonance is often described as a low sensitivity technique. At room temperature, applying a field of 1T produces a difference in proton population of approximately three nuclei per million. Detecting such a small change is clearly a challenge!

2.2.2 Larmor Precession

Thus far, the spin system has been described in its equilibrium state. To investigate a sample, it must be disturbed from its resting state. The return to equilibrium then gives information about the sample composition. The sample is perturbed by applying a resonant oscillating magnetic field across it, perpendicular to the static field.

The resonant frequency of the system is determined by the energy gap between spins in the up and down states (eqn. 2.8) which, combined with Planck's law

$$E = \hbar\omega \quad (2.14)$$

give the resonant Larmor frequency

$$\omega_L = \gamma B_0 \quad (2.15)$$

For protons in a static field in the range 0.1–10T, $\omega/2\pi$ is between 4.3–430MHz, which is in the HF to UHF radiofrequency band.

The effect of an RF pulse on the sample can only be fully described using a quantum mechanical description of the system. However, a classical model describing the behaviour of the bulk sample magnetisation \mathbf{M} is surprisingly effective, providing an accurate description of most NMR imaging methods. The advantage of the classical model is that it is more familiar and intuitive than the quantum description.

Classically, a magnetic moment placed in an external magnetic field experiences a torque

$$\mathbf{L} = \mathbf{M} \times \mathbf{B} \quad (2.16)$$

causing it to rotate. The torque is related to the change in angular momentum

$$\frac{d\mathbf{P}}{dt} = \mathbf{L} \quad (2.17)$$

If all sample spins are coherent $\mathbf{M} = \sum \boldsymbol{\mu}$. Substituting eqn. 2.2 into eqn. 2.17, and combining with eqn. 2.16 gives

$$\frac{d\mathbf{M}}{dt} = \gamma \mathbf{M} \times \mathbf{B} \quad (2.18)$$

which is the Bloch equation [2]. It states that the sample magnetisation \mathbf{M} precesses about the applied magnetic field \mathbf{B} . In the absence of an RF field, the sample magnetisation precesses about \mathbf{B}_0 at the Larmor frequency ω_L .

Now consider what happens if a second magnetic field is applied to the sample, rotating about \mathbf{B}_0 at the Larmor frequency. Sample magnetisation now precesses about the combined field

$$\mathbf{B} = \mathbf{B}_0 + \mathbf{B}_1 \quad (2.19)$$

The process is easier to visualise if we transform to a new frame of reference, rotating about \mathbf{B}_0 at the Larmor frequency. In the rotating frame, precession about the static \mathbf{B}_0 field appears stationary, making the effective static field \mathbf{B}'_0 zero.

In the transverse plane, the applied B_1 field is

$$\mathbf{B}_1(t) = 2B_1^e(t) \cos(\omega_{\text{rf}}t) \hat{\mathbf{x}} \quad (2.20)$$

where $B_1^e(t)$ is the RF pulse envelope. This field, which oscillates in only one direction, may be decomposed into two counter-rotating components

$$\mathbf{B}_1(t) = \mathbf{B}_1^+(t) + \mathbf{B}_1^-(t) \quad (2.21)$$

where

$$\mathbf{B}_1^+(t) = B_1^e(t) \{ \cos(\omega_{\text{rf}}t) \hat{\mathbf{x}} + \sin(\omega_{\text{rf}}t) \hat{\mathbf{y}} \} \quad (2.22)$$

and

$$\mathbf{B}_1^-(t) = B_1^e(t) \{ \cos(\omega_{\text{rf}}t) \hat{\mathbf{x}} - \sin(\omega_{\text{rf}}t) \hat{\mathbf{y}} \} \quad (2.23)$$

Using the complex phasor notation, the transverse magnetisation is

$$B_1 = B_{1x} + iB_{1y} \quad (2.24)$$

and eqns. 2.22 and 2.23 may be written as

$$B_1^+(t) = B_1^e(t) e^{i\omega_{\text{rf}}t} \quad (2.25)$$

and

$$B_1^-(t) = B_1^e(t) e^{-i\omega_{\text{rf}}t} \quad (2.26)$$

In the rotating frame of reference, the B_1^+ component appears stationary. The B_1^- component rotates in the negative sense about the z -axis at a rate of $2\omega_{\text{rf}}$, which is far enough away from resonance that its effect is negligible.

The effective magnetic field, seen by the sample in the rotating frame of reference, is then

$$\mathbf{B}_{\text{eff}} = B_1^e \hat{\mathbf{x}} \quad (2.27)$$

The sample magnetisation precesses about the x -axis and into the transverse plane. The rotation produced, often called the flip or nutation, is

$$\alpha = \int_0^\tau \gamma B_1(t) dt \quad (2.28)$$

where τ is the duration of the RF pulse. For a rectangular pulse envelope this reduces to

$$\alpha = \gamma B_1 \tau \quad (2.29)$$

Therefore applying an RF pulse at the resonant frequency tips the sample magnetisation away from the equilibrium position and into the transverse plane. The angle α by which the magnetisation vector is tipped depends upon the amplitude of the applied B_1 field and the duration for which it is applied.

2.2.3 Relaxation

Having shown how to excite the sample we now turn our attention to the mechanism by which it returns to equilibrium, a process known as relaxation. There are in fact two relaxation processes: spin-lattice relaxation and spin-spin relaxation.

Spin-lattice relaxation is the process by which spins revert back into alignment with the static magnetic field, releasing energy to the molecular lattice as they do so. The rate of recovery of longitudinal magnetisation M_z is characterised by the time constant T_1

$$\frac{dM_z}{dt} = -\frac{M_z - M_0}{T_1} \quad (2.30)$$

where M_0 is the longitudinal sample magnetisation at equilibrium.

The second process is spin-spin relaxation, which causes the bulk transverse sample magnetisation to decay without affecting longitudinal magnetisation. It is caused by the exchange of energy between spins, leading to spin dephasing and a reduction in the detectable NMR signal. Spin-spin relaxation is also an exponential decay, characterised by the time constant T_2

$$\frac{dM_{xy}}{dt} = -\frac{M_{xy}}{T_2} \quad (2.31)$$

where M_{xy} represents the sample magnetisation in the transverse plane. Note that although energy is exchanged within the spin system, T_2 relaxation does not represent a loss of energy from the system. Spin-spin relaxation times are generally shorter than spin-lattice relaxations. At 7T, typical tissue T_1 values are of the order of 1–1.5s, while T_2 values are approximately 30ms.

Experimentally, the NMR signal decays faster than T_2 predicts. Inhomogeneity in the B_0 field causes slight shifts in the local resonant frequency, leading to additional spin dephasing. This accelerated decay rate is called T_2^* and given by

$$\frac{1}{T_2^*} = \frac{1}{T_2} + \frac{1}{T_2'} \quad (2.32)$$

where T_2' accounts for imperfections in the B_0 field.

Including T_1 and T_2 effects in the Bloch equation (eqn. 2.18) gives [2]

$$\frac{d\mathbf{M}}{dt} = \gamma\mathbf{M} \times \mathbf{B} - \frac{M_x\hat{\mathbf{x}} + M_y\hat{\mathbf{y}}}{T_2} - \frac{(M_z - M_z^0)\hat{\mathbf{z}}}{T_1} \quad (2.33)$$

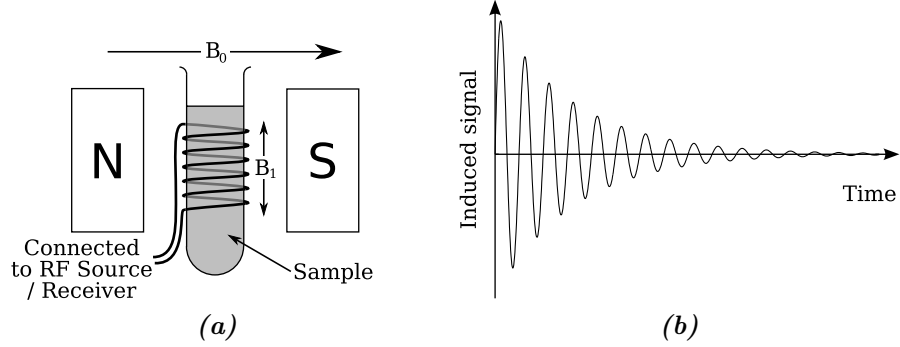


Figure 2.3: Free Induction Decay (FID): (a) basic experimental setup and (b) the acquired signal.

which describes the evolution of sample magnetisation over time. With knowledge of the applied magnetic fields, the Bloch equation can be used to model the NMR signal detected from a sample due to a given imaging sequence. This method is used in chapter 6 to investigate a novel imaging sequence.

2.2.4 Free Induction Decay

The most basic NMR experiment is the generation of a Free Induction Decay (FID) signal. A sample is placed in a uniform static magnetic field B_0 , surrounded by an RF coil used to generate an oscillating B_1 field (fig. 2.3a). Sample magnetisation initially aligns to the static magnetic field. A radio-frequency pulse is then applied to the RF coil, oscillating at the Larmor frequency, causing the spins to tip into the transverse plane. The RF source is then switched off, and the signal induced in the coil by the sample magnetisation via Faraday induction is recorded. The result is the exponentially decaying signal at the resonant frequency (fig. 2.3b). The rate of decay depends upon B_0 homogeneity and T_2 of the sample material. This is the FID signal, which forms the basis for all NMR experiments.

2.3 Magnetic Resonance Imaging

Introducing spatial encoding into the NMR response from a sample allows images of the sample to be constructed. NMR imaging was first developed in the early 1970's. In 1973, Lauterbur proposed using a field gradient to localise the NMR signal [3]. A field gradient was applied in a series of different directions, each creating a projection through the sample. The projections were then combined to form an image using backprojection, a method borrowed from X-ray tomography [11].

In the same year, selective excitation was proposed by Mansfield's group in Nottingham [12]. A variety of methods for selectively exciting a slice through a sample were described, including slice selection in the exact form it is used today.

The first Fourier imaging method was published by Ernst's group in Zürich in 1975 [13], using non-selective excitation, 2D phase encoding and frequency encoded readout. However, they noted that using a computer with 12kB of RAM, it was impractical to collect and process full volume data, and demonstrated the method only in 2D.

In 1977 Mansfield introduced a technique for fast imaging which he called Echo Planar Imaging (EPI) [14]. This is remarkable, as most 'basic' imaging sequences had yet to be invented (the Aberdeen group published Spinwarp imaging in 1980 [15]), and EPI is still the fastest known imaging sequence, making the current profusion of fMRI studies possible.

2.3.1 Contrast

To be useful as a biomedical tool, MRI must be capable of differentiating between different tissue types. There are three sources of contrast in MRI: spin density, T_1 relaxation and T_2 relaxation. For proton imaging, spin density corresponds to water content levels, which are similar in all soft tissue. However, T_1 values show much greater variation making T_1 -weighted imaging sequences useful for anatomical scans. Many diseases can

be characterised by a change in tissue T_2 value, making T_2 -weighted imaging a valuable tool for detecting and monitoring the spread of disease within the body [10].

All three contrast mechanisms are present in any imaging sequence, but usually only one mechanism is emphasised. By adjusting the timing of a sequence the relative sensitivity to T_1 , T_2 or spin density can be adjusted.

2.3.2 Signal Localisation

To create an image of a sample, a process for localising the NMR signal is required. This is done by superimposing a small, spatially varying magnetic field onto B_0 , to make the resonant frequency a function of position. Consider a magnetic field \mathbf{B}_{grad} , aligned to the z -axis but whose magnitude varies linearly in the x direction

$$\mathbf{B}_{grad} = x G_x \hat{\mathbf{z}} \quad (2.34)$$

where G_x is a constant. Applying the gradient field to the sample causes the Larmor frequency vary linearly as a function of position along the x -axis

$$\omega(x) = \gamma(B_0 + x G_x) \quad (2.35)$$

The gradient field may vary along any of the three axes, and is fully represented by the tensor

$$\mathbf{G} = \begin{bmatrix} \hat{\mathbf{x}}\hat{\mathbf{x}}\frac{\partial B_x}{\partial x} & \hat{\mathbf{x}}\hat{\mathbf{y}}\frac{\partial B_x}{\partial y} & \hat{\mathbf{x}}\hat{\mathbf{z}}\frac{\partial B_x}{\partial z} \\ \hat{\mathbf{y}}\hat{\mathbf{x}}\frac{\partial B_y}{\partial x} & \hat{\mathbf{y}}\hat{\mathbf{y}}\frac{\partial B_y}{\partial y} & \hat{\mathbf{y}}\hat{\mathbf{z}}\frac{\partial B_y}{\partial z} \\ \hat{\mathbf{z}}\hat{\mathbf{x}}\frac{\partial B_z}{\partial x} & \hat{\mathbf{z}}\hat{\mathbf{y}}\frac{\partial B_z}{\partial y} & \hat{\mathbf{z}}\hat{\mathbf{z}}\frac{\partial B_z}{\partial z} \end{bmatrix} \quad (2.36)$$

As the static field \mathbf{B}_0 is aligned to the z -axis, the x and y components of \mathbf{B}_{grad} do not significantly effect the resonant frequency of the system and may be neglected, allowing the tensor to be reduced to a vector containing

only the B_z terms

$$\mathbf{G} = \frac{\partial B_z}{\partial x} \hat{\mathbf{x}} + \frac{\partial B_z}{\partial y} \hat{\mathbf{y}} + \frac{\partial B_z}{\partial z} \hat{\mathbf{z}} \quad (2.37)$$

An MRI system typically has three independent orthogonal gradient coils, each designed to produce a field gradient G_x , G_y and G_z varying linearly along its respective axis, producing a total gradient field

$$\mathbf{G} = G_x \hat{\mathbf{x}} + G_y \hat{\mathbf{y}} + G_z \hat{\mathbf{z}} \quad (2.38)$$

The magnetic field at point \mathbf{r} is then

$$\mathbf{B}(\mathbf{r}) = (B_0 + \mathbf{G} \cdot \mathbf{r}) \hat{\mathbf{z}} \quad (2.39)$$

The following sections introduce three methods for signal localisation using the gradient field. Selective excitation is introduced via slice selection. Localisation of the resulting NMR signal is then described using frequency and phase encoding. These methods may be combined to generate three dimensional images of a sample.

2.3.3 Slice Selection

Slice selection is a technique used to excite a slab of spins in a sample and forms the first stage of most imaging sequences. Applying a linear field gradient across the sample makes the spin resonant frequency a function of distance along the gradient axis. If the slice select gradient is applied along the z -axis,

$$\omega(z) = \gamma(B_0 + zG_{sl}). \quad (2.40)$$

If an RF pulse is now applied to the sample, only those spins resonant at or close to the frequency of the RF pulse will be affected (such that $\Delta B_0 < B_1$ [16]), so that only a slice of the sample is excited (fig. 2.4). The position of the excited slice along G_{sl} can be changed by changing the frequency of the RF pulse. The thickness of the slice is determined by the gradient amplitude.

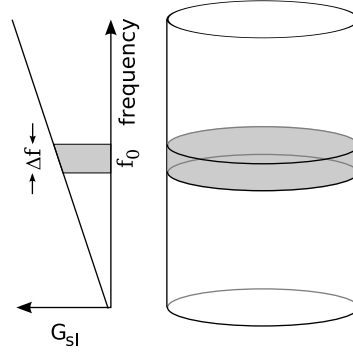


Figure 2.4: When an RF pulse is applied in the presence of a linear field gradient, a slab of magnetisation perpendicular to the gradient is excited.

For a more mathematical treatment, we start by considering the Bloch equations (eqn. 2.18) in the presence of the linear field gradient G_{sl} . Neglecting the effects of relaxation, the evolution of sample magnetisation is given by

$$\frac{dM_x}{dt} = \gamma M_y G_{sl} z \quad (2.41a)$$

$$\frac{dM_y}{dt} = \gamma M_z B_1(t) - \gamma M_x G_{sl} z \quad (2.41b)$$

$$\frac{dM_z}{dt} = \gamma M_y B_1(t) \quad (2.41c)$$

It is convenient at this point to move to a new frame-of-reference which rotates at the angular frequency $\gamma G_{sl} z$ about the z -axis, making the rotational frequency a function of distance along the slice axis. In the new rotating frame $x' y' z'$, eqn. 2.41 becomes

$$\frac{dM_{x'}}{dt} = \gamma M_{z'} B_1(t) \sin(\gamma G_{sl} z'(t + T)) \quad (2.42a)$$

$$\frac{dM_{y'}}{dt} = \gamma M_{z'} B_1(t) \cos(\gamma G_{sl} z'(t + T)) \quad (2.42b)$$

$$\frac{dM_{z'}}{dt} = \gamma (M_{x'} B_{y'} - M_{y'} B_{x'}) \quad (2.42c)$$

where t is time and the pulse extends from $-T$ to $+T$. Three assumptions are now used to simplify the problem: the spin system response is linear, variations in $M_{z'}$ are small ($dM_{z'}/dt \approx 0$), and $M_{z'} \approx M_0$. These assumptions are valid for small flip angles. Although not strictly valid, the model is also found to work well for larger flip angles. Eqns. 2.42a and 2.42b can

be combined using the complex notation $M_{+'} = M_{x'} + iM_{y'}$, to give the rotating signal $M_{+'}$

$$\frac{dM_{+'}}{dt} = i\gamma M_0 B_1(t) e^{i\gamma G_{sl} z' (t+T)} \quad (2.43)$$

which is then integrated and transformed back into the original rotating frame-of-reference

$$M_+(z) = i\gamma M_0 e^{-i\gamma G_{sl} z T} \int_{-T}^{+T} B_1(t) e^{i\gamma G_{sl} z t} dt \quad (2.44)$$

Eqn. 2.44 is the Fourier transform of $B_1(t)$, where $\omega = \gamma G_z z$. That is, the profile of the excited slice is the Fourier transform of the RF pulse envelope. If an infinitely long RF pulse could be applied to the sample, an infinitely thin slice would be excited (fig. 2.5a). In practice the RF pulse has a finite duration, giving it a finite bandwidth and causing the excited region to have some thickness. If a rectangular pulse envelope is used (fig. 2.5b), a slice with a sinc profile is excited. A slice with a rectangular profile is more useful, which can be achieved by giving the RF pulse a sinc envelope (fig. 2.5c).

The term $e^{-i\gamma G_{sl} z T}$ in 2.44 represents a continuous phase shift across the depth of the slice. The phase shift can be corrected by applying a reversed slice gradient for half the duration of the original slice select gradient period, as shown in fig. 2.6 [17].

The principle of slice selection can be extended to excite an arbitrary region of the sample by using a carefully designed RF pulse envelope [18, 19]. The principle is further extended by Transmit SENSE [20], in which multiple RF transmit channels are used to give additional degrees of freedom in pulse envelope design.

2.3.4 Frequency Encoding

Frequency encoding uses the same principle as slice selection, but the field gradient is applied during image readout rather than excitation and so only influences the precession frequency of spins that have already been excited. Applying a linear field gradient G_{fr} across the sample makes the precession

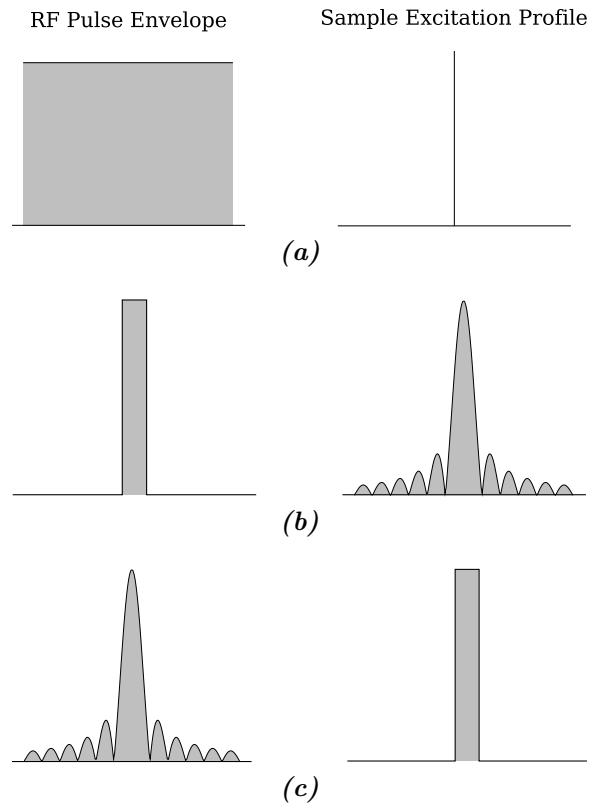


Figure 2.5: Slice excitation profile: (a) an infinitely long RF pulse excites an infinitely thin sample slice, (b) a rectangular pulse envelope excites a sinc profile, and (c) a sinc pulse profile excites a rectangular cross section.

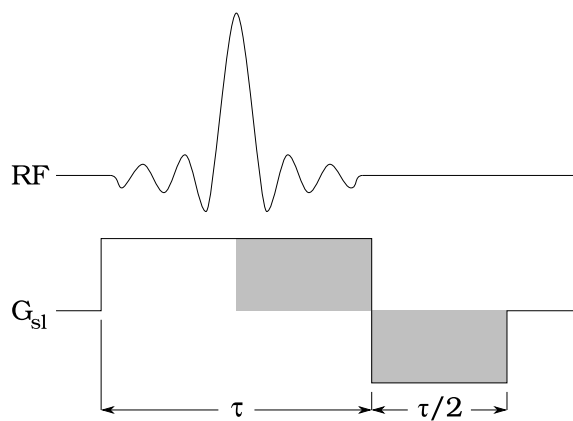


Figure 2.6: Slice selective excitation followed by a negative gradient lobe to refocus spins across the depth of the slice.

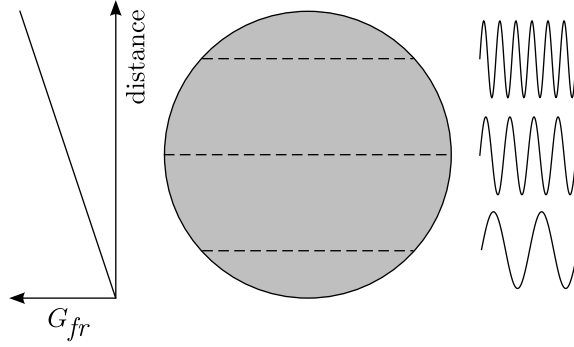


Figure 2.7: Applying a linear field gradient across the sample makes the precession frequency position dependent.

frequency a function of position along the gradient axis (fig. 2.7):

$$\begin{aligned}\omega(x) &= -\gamma(B_0 + G_{fr}x) \\ &= \omega_0 + \gamma G_{fr}x\end{aligned}\tag{2.45}$$

The observed signal is then

$$s(t) = \int_{sample} \rho(x) e^{-i(\omega_0 + \gamma G_{fr}x)t} dx\tag{2.46}$$

where $\rho(x)$ is the projection of the spin density function along the x -axis

$$\rho(x) = \int \int \rho(\mathbf{r}) dy dz\tag{2.47}$$

The signal is then demodulated to remove the RF carrier frequency ω_0 , leaving the envelope

$$s(t) = \int_{sample} \rho(x) e^{-i(\gamma G_{fr}t)x} dx\tag{2.48}$$

which is the Fourier transform of $\rho(x)$. Fourier transforming the acquired signal produces a projection of the sample magnetisation along the gradient axis (fig. 2.8). If the frequency encoding gradient is orthogonal to the slice select gradient, the two techniques can be combined to image the spin density of a column through the sample (fig. 2.9).

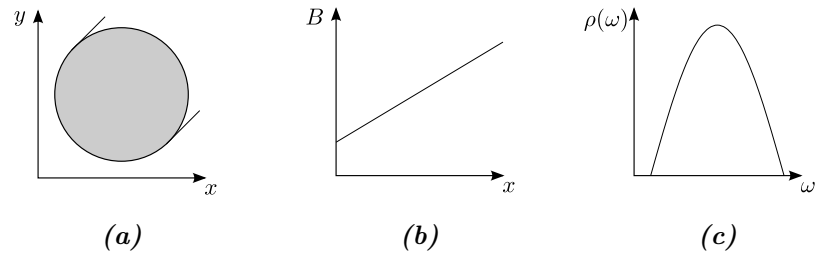


Figure 2.8: Signal localisation in one dimension: (a) a cylindrical sample, (b) the applied gradient field, and (c) the resulting signal spectrum.

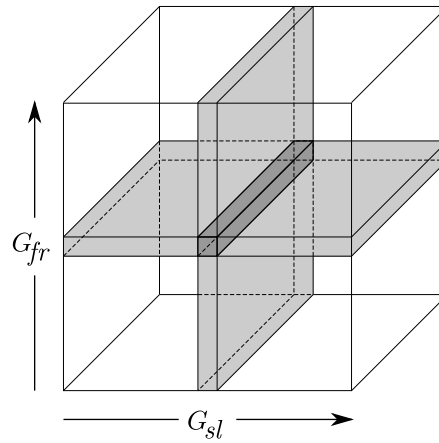


Figure 2.9: Combining slice selection and frequency encoding localises the signal to a column through the sample.

2.3.5 Phase Encoding

Frequency encoding acquires a series of time points during a single echo (eqn. 2.48 and fig. 2.10a). The same result may be achieved by exciting the sample a number of times and applying a constant gradient for a different duration T_{ph} each time before sampling a single data point (fig. 2.10b) [13]. If the y gradient is used, the acquired signal is

$$s(T_{ph}) = \int_{sample} \rho(y) e^{-i\gamma G_{ph} T_{ph} y} dy \quad (2.49)$$

Repeating the experiment at many different values of T_{ph} samples the complete signal. The Fourier transform of the acquired signal is then the projection of signal intensity along the gradient axis as before.

While requiring more acquisitions than frequency encoding (one per sample point), phase encoding can be separately applied to all three orthogonal axes, localising the signal to a point and making 3D imaging possible. Phase encoding can also be used in combination with slice selection and frequency encoding, forming the basis for most common imaging sequences.

Varying T_{ph} allows the complete echo signal to be acquired. However, it also means that the time between the excitation pulse and the sampled point varies. During this time the echo signal undergoes T_1 and T_2^* decay.

Returning to eqn. 2.49 it can be seen that the location of the sampled point is determined by the product $G_{ph} T_{ph}$. However, as the gradient is switched off by the time the signal is sampled, it is the sum effect rather than the exact waveform that is important. Eqn. 2.49 can be written more generally as

$$s(T_{ph}) = \int_{sample} \rho(y) e^{-i\phi(T_{ph})} dy \quad (2.50)$$

where

$$\phi(T_{ph}) = \gamma \int_0^{T_{ph}} G_{ph} d\tau \quad (2.51)$$

For a constant gradient amplitude $\phi(T_{ph})$ reduces to $G_{ph} T_{ph}$. By varying the amplitude of the gradient, rather than the duration, exactly the same

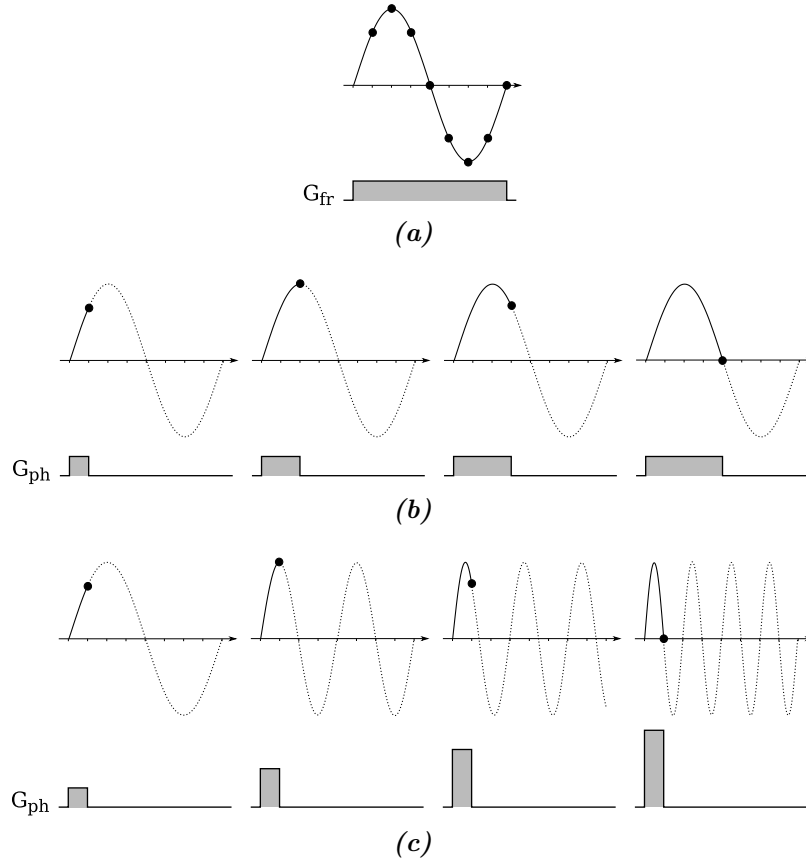


Figure 2.10: Frequency and phase encoding: (a) frequency encoding samples a single echo at many points; (b) phase encoding achieves the same result by exciting the sample many times and acquiring one point from each echo; (c) the time between excitation and acquisition is made constant by varying the gradient amplitude.

sampling of the echo is achieved but each point has undergone the same degree of T_1 and T_2^* relaxation (fig. 2.10c) [15].

2.3.6 Spin Echoes and Gradient Echos

In imaging, it is not generally the FID signal that is sampled, but an echo. The FID signal decays due to T_2^* effects dephasing the transverse magnetisation. An echo is formed when the transverse magnetisation is refocused.

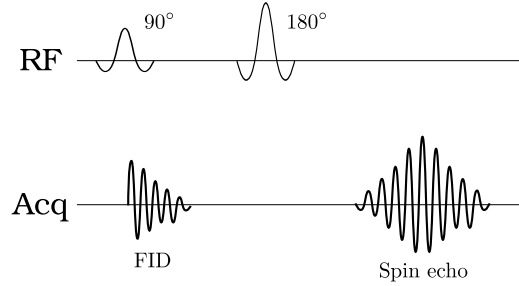


Figure 2.11: A spin echo sequence.

There are two commonly used echo formation methods, spin echoes and gradient echoes.

Consider the two-pulse sequence shown in fig. 2.11. The 90_x° pulse flips the sample magnetisation into the transverse plane. The nuclear spins are initially coherent, but will steadily dephase due to T_2^* effects as described in section 2.2.3, causing the detectable signal to decay. Applying a 180_y° pulse will then flip the spins like a pancake, reversing the sign of the phase shift. A spin that had been precessing fast (slow), and built up a positive (negative) phase shift, will now show a negative (positive) phase shift. However, the local effects that caused it to precess fast (slow) have not changed, and the spin will tend to catch up (slow down) back to zero shift. At time τ following the 180° pulse, the spins will refocus and produce an echo.

A gradient echo is formed by applying a linear field gradient across a sample. The gradient causes spins to precess at different rates at different positions across the sample, causing the bulk magnetisation to dephase. Reversing the field gradient will then reverse the dephasing effect. If the gradient is applied for a time τ before reversal, the echo will form at time τ after the reversal.

A spin echo refocuses T_2' effects due to susceptibility or field inhomogeneity and can be used to give true T_2 contrast, while a gradient echo cannot separate dephasing caused by T_2 effects for dephasing caused by B_0 field inhomogeneity, and gives T_2^* contrast.

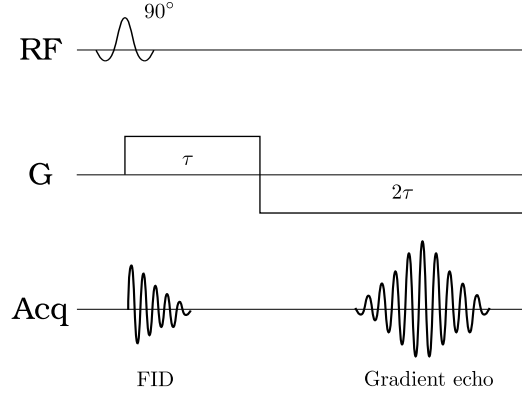


Figure 2.12: A gradient echo sequence.

2.3.7 k -Space

By analogy to the reciprocal lattice used in crystallography [21], it is helpful to introduce a reciprocal imaging space [4], called k -space in MRI. It can be considered as the Fourier space in which images are acquired, before being Fourier transformed into normal image space.

Following an RF pulse, image readout is determined by the gradient waveforms. The acquisition can be visualised by considering the readout trajectory through k -space, defined as

$$\mathbf{k}(t) = \gamma \int_0^t \mathbf{G}(t') dt' \quad (2.52)$$

where $\mathbf{G} = [G_x \ G_y \ G_z]^T$ is the vector gradient field and t is time following the RF pulse. The signal timecourse is then

$$s(t) = \int_{\text{sample}} \rho(\mathbf{r}) e^{-i\mathbf{k}(t) \cdot \mathbf{r}} d\mathbf{r} \quad (2.53)$$

The trajectory of $\mathbf{k}(t)$ shows the mapping from the one dimensional time-course signal to the two or three dimension sampling of the image in k -space [22]. During frequency encoding data points are recorded at regular intervals as k -space is swept, while during phase encoding the location in k -space is altered without sampling the signal, resulting in instantaneous jumps in the trajectory [10].

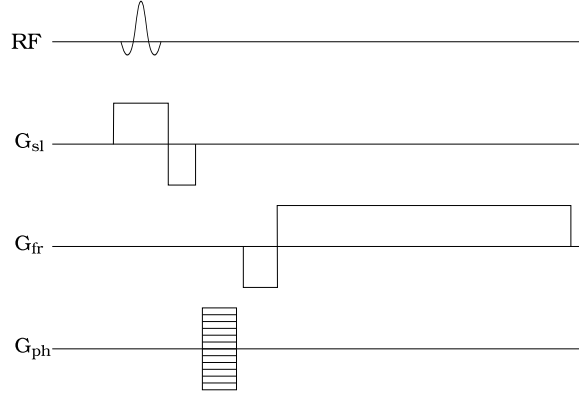


Figure 2.13: *Spinwarp imaging sequence.*

To fully sample an image, all four quadrants of k -space must be covered by the readout trajectory. Low spatial frequencies (large image structure) appear close to the origin, while higher spatial frequencies (edges and fine details) appear further out. An echo signal may be recalled at any point by directing the readout trajectory back towards the centre of k -space, until the spins irreversibly defocus through T_2 relaxation.

2.3.8 Spinwarp Imaging

Spinwarp imaging is the classic Fourier imaging sequence, introduced by the Aberdeen group [15] as a development of Fourier Zeugmatography [13]. The imaging sequence is shown in fig. 2.13. It consists of a slice selective 90° pulse, followed by a phase encoding gradient lobe and frequency encoded readout. Data is collected during the positive G_{fr} section. The negative lobe at the beginning of G_{fr} allows the full width of k -space to be acquired; without it, only the positive half could be collected [9]. This sequence represents a single horizontal line in k -space. It is repeated a number of times to acquire regularly spaced lines in k -space, each line offset by a different distance along k_y by a phase encoding lobe of a different amplitude (fig. 2.14). The acquired data is then Fourier transformed in 2D to produce the final image.

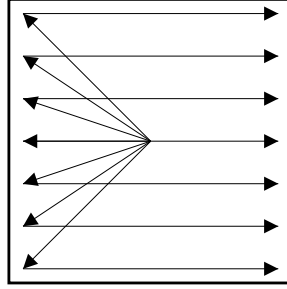


Figure 2.14: Spinwarp trajectory in k -space. Each horizontal line represents a separate acquisition.

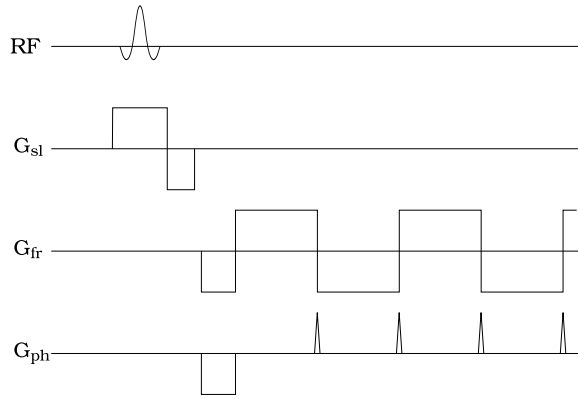


Figure 2.15: Echo planar imaging sequence.

2.3.9 Echo Planar Imaging

Echo Planar Imaging (EPI) is a much faster imaging technique, first introduced by the Nottingham group [14]. Whereas spinwarp imaging covers k -space using a series of acquisitions, EPI reads out the whole image in a single shot. The imaging sequence is shown in fig. 2.15, with the k -space trajectory in fig. 2.16. The principle is to zig-zag across k -space fast enough that the whole image can be read out before T_2^* relaxation smears out the image. The frequency encoding gradient G_{fr} is rapidly switched between maximum positive and maximum negative amplitude, sweeping across k -space in alternate directions. Between switching, a small ‘blip’ is applied to the phase encoding gradient, offsetting each sweep in k -space.

A peculiarity of Echo Planar Imaging is that alternate lines of k -space are traversed in opposite directions. Imperfections in gradient coils and their

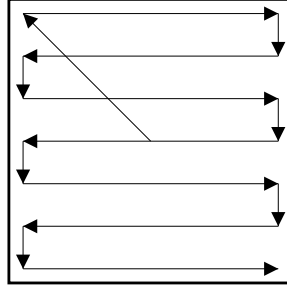


Figure 2.16: Echo planar k -space trajectory, covering the entire image in a single acquisition.

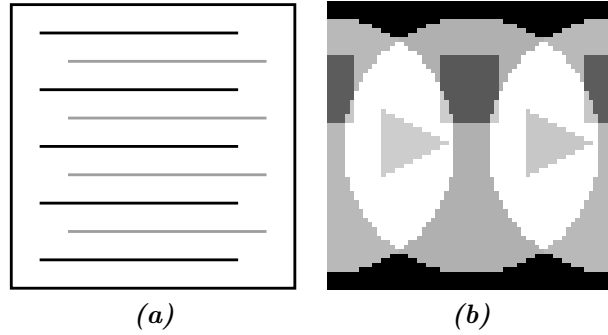


Figure 2.17: A small offset between alternate lines in k -space (a) causes the Nyquist ghosting artifact shown in (b).

drivers mean that there is usually a slight offset between lines collected in the positive and negative direction (fig. 2.17a), leading to a Nyquist ghosting artifact in the reconstructed image (fig. 2.17b). There are several methods for correcting the offset [23], all of which consist of applying an alternating phase shift to alternate lines in k -space.

The echo planar imaging sequence places a high demand on the frequency encoding or switched gradient. Initially, scanners had to have the gradient system upgraded to become ‘EPI capable’. Modern clinical systems are now able to run EPI sequences as standard.

EPI is important because it allows MRI scans to run fast enough to acquire dynamic information from living subjects. It has found particular use in functional MRI studies, used to investigate brain activity [5, 6]. A typical whole volume head scan can be performed in about 3 seconds on a 3T system using EPI.

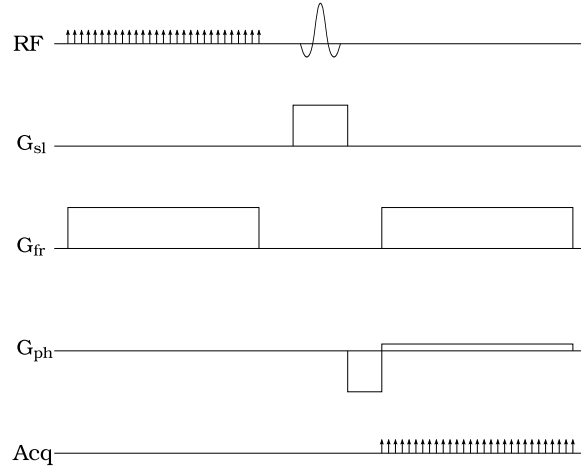


Figure 2.18: Burst imaging sequence.

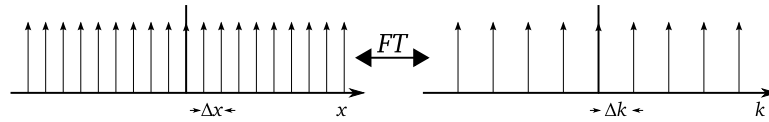


Figure 2.19: The Fourier transform of a series of pulses is a series of pulses.

2.3.10 Burst Imaging

A different approach to fast imaging is the Burst sequence [24], also known as DUFIS [25] or OUFIS [26]. Burst uses a train of regularly spaced, low flip-angle RF pulses, applied to the sample under a constant gradient G_{fr} (fig. 2.18). In section 2.3.3 it was shown that the excitation profile produced by an RF pulse applied under a constant gradient is approximately the Fourier transform of the pulse envelope. The Fourier transform of a series of pulses is, of course, a series of pulses (fig. 2.19). Using this principle the Burst sequence simultaneously excites a series of planes through the sample, in exactly the same way that a simple slice-selective pulse excites a single slab. If the constant gradient is then reversed, the excited planes through the sample will refocus, producing a train of gradient echoes. In this manner Burst provides a spatial encoding in one dimension.

The basic Burst sequence is not slice selective, in the traditional sense. Slice selection may be introduced by following the Burst excitation train with a

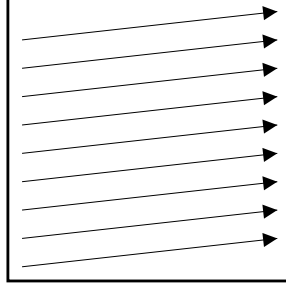


Figure 2.20: Burst trajectory in k -space.

slice selective inversion pulse [24]. Re-applying the readout gradient then generates a train of spin echoes, produced by the intersection of the Burst excited planes and the inversion plane. If the slice plane is perpendicular to the excitation planes, magnetisation is read out from columns or strips through the sample.

To complete the spatial localisation, phase encoding may be introduced during either excitation or readout by applying a constant or blipped gradient G_{ph} in the third orthogonal direction. If a constant gradient is used, the acquired lines in k -space are tilted by $\theta = \arctan(1/m)$, where m is the number of points in the read direction [27] (fig. 2.20). The angle is, however, small enough (0.9° for 64 points) that the effect is not noticeable in practice [25]. The advantage is that no gradient switching is required, making the acquisition virtually silent and placing minimal demand on the gradient system.

The main disadvantage of Burst is the low SNR it achieves. Burst excitation pulses are extremely selective. The series of RF pulses excite only thin planes through the sample, leaving much of the sample magnetisation unused. To overcome this problem, phase or frequency modulated excitation pulses have been used [26].

2.3.11 Extended Phase Graph

The description of Burst in the previous section is intuitive, but hides some of the subtlety of the Burst sequence. In this section the Extended Phase

Graph (EPG) [24] is described, and then used to give a more detailed explanation of the echoes generated by a Burst pulse train.

It may be shown that a sequence of n_p RF pulses can generate up to 3^{n_p-1} echoes [28]. A Burst sequence using 64 subpulses can potentially generate 10^{30} echoes! However, because the subpulses are regularly spaced many signal pathways coincide, reducing the number of echoes to $(3n_p-2)$. Even this produces 190 echoes from 64 subpulses. Keeping track of the interactions between so many echoes is a difficult task. Hennig developed the Extended Phase Graph representation for precisely this purpose [28, 29].

Consider an RF pulse of flip angle α , applied along the y -axis. The magnetisation \mathbf{M}' immediately following the pulse is

$$M'_x = M_x \cos \alpha - M_z \sin \alpha \quad (2.54a)$$

$$M'_y = M_y \quad (2.54b)$$

$$M'_z = M_x \sin \alpha + M_z \cos \alpha \quad (2.54c)$$

Using the complex notation $M_{xy} = M_x + iM_y$ this may be rewritten as

$$M'_{xy} = M_{xy} \cos^2 \frac{\alpha}{2} - M_{xy}^* \sin^2 \frac{\alpha}{2} - M_z \sin \alpha \quad (2.55a)$$

$$M'_z = M_z \cos \alpha + \frac{1}{2}(M_{xy} + M_{xy}^*) \sin \alpha \quad (2.55b)$$

Eqns. 2.55a and 2.55b show the two basic sources of echo formation. First consider eqn. 2.55a. Applying a pulse of arbitrary flip angle separates the transverse magnetisation into two components, one proportional to the pre-pulse magnetisation M_{xy} and the other proportional to its complex conjugate M_{xy}^* (neglecting the M_z component for the moment). By noting that the effect of a 180° pulse on the transverse magnetisation is

$$M_{xy} \xrightarrow{180^\circ_y} -M_{xy}^* \quad (2.56)$$

the fraction of transverse magnetisation $\sin^2(\frac{\alpha}{2})$ experiences a 180° -like pulse, introducing a phase reversal which leads to refocusing and the formation of a spin echo. The remaining fraction of transverse magnetisation $\cos^2(\frac{\alpha}{2})$ is unaffected by the RF pulse.

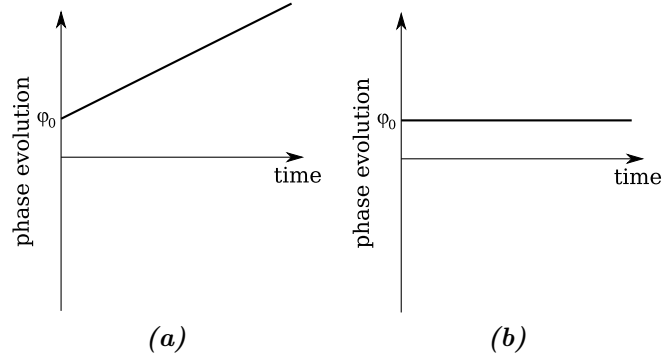


Figure 2.21: Phase evolution during free precession of (a) transverse magnetisation and (b) longitudinal magnetisation.

Eqn 2.55b describes the second echo formation mechanism. The term $\frac{1}{2}(M_{xy} + M_{xy}^*) \sin \alpha$ represents transverse magnetisation shifted into M_z , where it is stored. A later RF pulse can then recover this magnetisation back into the M_{xy} plane where it will refocus, leading to a stimulated echo. This is the previously neglected M_z component in eqn. 2.55a.

The Extended Phase Graph is a graphical representation of the above decomposition, showing the different echo formation paths produced by multiple RF pulses. First consider the free precession of transverse magnetisation $M_{xy}e^{-i(\phi_0 + \omega t)}$. The phase evolution of the transverse magnetisation $\phi = \phi_0 + \omega t$ is shown in fig. 2.21a. Figure 2.21b show the phase evolution of the longitudinal magnetisation, which is constant if T_1 relaxation is neglected.

From eqn. 2.55a, an RF pulse α divides the transverse magnetisation into four components

$$M_{xy} \xrightarrow{\alpha} \begin{cases} M'_{xy} = M_{xy} \cos^2 \frac{\alpha}{2} \\ M'_{xy} = -M_{xy}^* \sin^2 \frac{\alpha}{2} \\ M'_z = \frac{1}{2} M_{xy} \sin \alpha \\ M'_z = \frac{1}{2} M_{xy}^* \sin \alpha \end{cases} \quad (2.57)$$

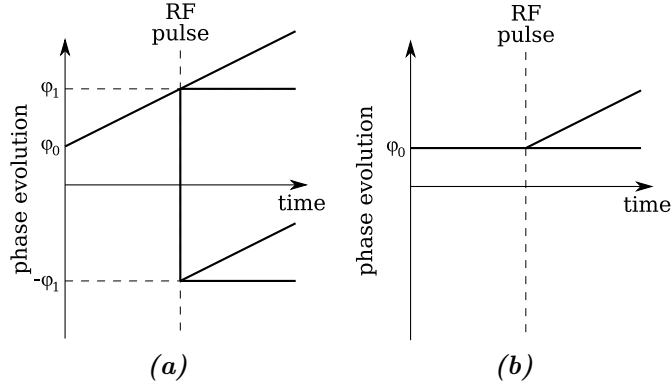


Figure 2.22: Branching rules shown on an extended phase graph for (a) transverse and (b) longitudinal magnetisation.

while from eqn. 2.55b the longitudinal magnetisation is split into two components

$$M_z \xrightarrow{\alpha} \begin{cases} M'_{xy} = -M_z \sin \alpha \\ M'_z = M_z \cos \alpha \end{cases} \quad (2.58)$$

These branching rules are the building blocks of the Extended Phase Graph, shown graphically in fig. 2.22.

To construct an extended phase graph, the phase evolution is initially assumed to start at zero. Applying a field gradient causes the sample magnetisation to precess, resulting in the phase evolution shown in fig. 2.21. For each RF pulse applied to the system, the branching rules are applied to each phase path on the extended phase graph, generating more phase coherence paths. When a phase coherence path crosses the horizontal axis during free precession all transverse magnetisation is in phase and an echo forms.

Fig. 2.23 shows an extended phase graph for the Burst sequence using $n_p = 6$ subpulses and a slice selective inversion pulse, producing three groups of echoes. A group of $n_p - 1$ higher-order echoes are produced before the inversion pulse. The same $n_p - 1$ higher order echoes are then refocused by the 180° pulse, followed by n_p primary echoes.

Primary echoes, produced by the interaction between individual subpulses and the inversion pulse, are used to generate the Burst image. Their amplitude is proportional to $\sin \theta$. Higher-order echoes result from interactions

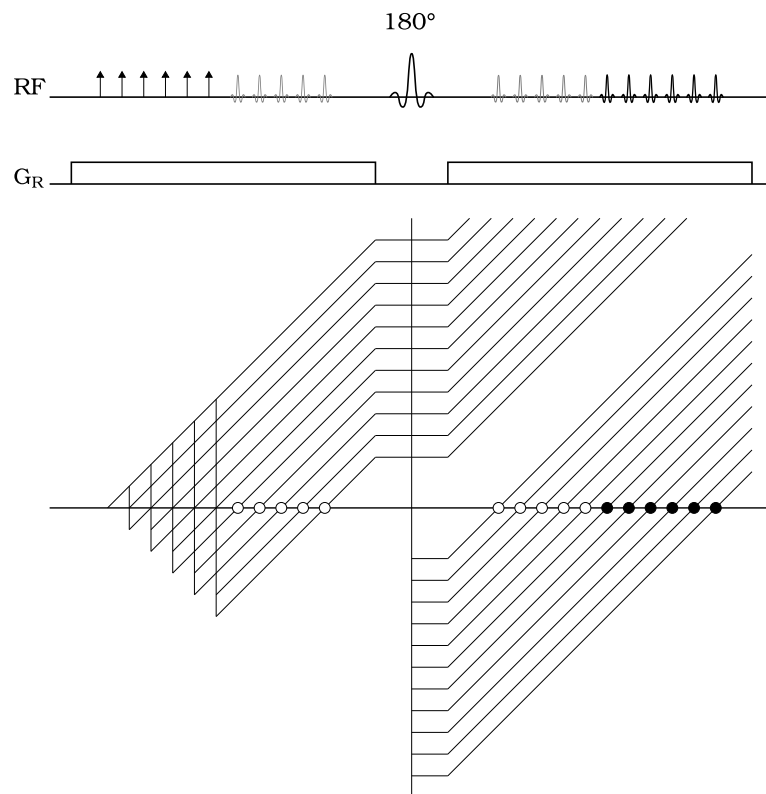


Figure 2.23: Extended phase graph for the spin echo Burst sequence using a slice selective 180° refocusing pulse. Primary echoes are marked \bullet , higher order echoes are marked \circ .

between two or more subpulses. Their amplitude is proportional to $\sin^k \theta$, where k is an odd integer ≥ 3 , are much smaller than the primary echoes. The primary echoes are actually a superposition of primary and higher-order echoes [26], but the relative amplitudes of the higher-order echoes are small enough that their presence can be neglected.

To speed up the Burst sequence, the 180° pulse can be placed closer to the Burst pulse train. The higher-order echoes will not then have time to focus, but the primary echoes are still produced in exactly the same manner.

2.3.12 Parallel Imaging and SENSE

Signal localisation methods introduced earlier in this chapter rely upon field gradients to encode position, and read out data sequentially using a single receive probe. In particular, phase encoding constrains the image acquisition rate, as each phase encoded point requires a separate echo acquisition.

An alternative encoding scheme is to use multiple receive probes to acquire data simultaneously, each probe providing a different component of spatial information. The simplest implementation of this approach is to use two receive probes, placed sufficiently far apart that they do not interact, simultaneously imaging two regions of the body [30]. A more challenging approach is to image a single region using multiple probes with overlapping fields-of-view.

Methods for combining images from multiple probe elements for uniform sensitivity or uniform noise were derived by Roemer *et al* [31]. They also show that, where no probe sensitivity information is available, the pixel-by-pixel root-sum-of-squares (RSS) method is optimal. If \mathbf{a} is a vector containing the pixel values detected by each probe element (the superscript T indicates the transpose)

$$\mathbf{a} = [a_1 \ a_2 \ \cdots \ a_{n_e}]^T \quad (2.59)$$

the pixel magnitude V in the reconstructed image is

$$v = \sqrt{\mathbf{a}^H \Psi^{-1} \mathbf{a}} \quad (2.60)$$

where the superscript H indicates the conjugate transpose and Ψ is the $n_e \times n_e$ receiver noise matrix, which is discussed in more detail in section 3.10.4. Assuming the probe elements are non-interacting, Ψ is the identity matrix.

Rather than increasing the SNR, parallel methods can also be used to accelerate image acquisition. There are two approaches: massively parallel and partially parallel methods. Massively parallel methods use array probes with approximately the same number of probe elements as data points to entirely replace phase encoding and acquiring a complete image from a single echo signal [32, 33]. Partially parallel methods use a smaller number of receive elements in combination with phase encoding, to reduce the number of required acquisitions [34]. Massively parallel methods have not yet seen wide use, but partially parallel methods have become a standard technique in regular clinical use.

Initial reconstruction methods, while showing promise in simulation, were not stable enough for clinical application [35]. The first clinically applicable method was SMASH (SiMultaneous Acquisition of Spatial Harmonics) [36]. SMASH uses a probe array with a series of elements in the phase encoding direction. The elements are designed such that channels can be combined to produce different spatial harmonics in sensitivity in the phase encoding direction. These spatial harmonics reproduce the same effect in the acquired data as phase encoding gradients. Hence several phase encoding steps may be reconstructed from a single, parallel, acquisition. A generalisation of SMASH has since been demonstrated, allowing arbitrary probe configurations designed to optimise SNR rather than produce spatial harmonics [37].

Shortly after SMASH, the SENSE (SENSitivity Encoding) method was introduced [38]. While SMASH performs the reconstruction in k -space, the SENSE reconstruction is done in image space. During a SENSE acquisition, k -space is undersampled in the phase encoded direction, causing Nyquist aliasing in image space (fig. 2.24). Data is simultaneously acquired by multiple probe elements, each with a different sensitivity profile. Using knowledge

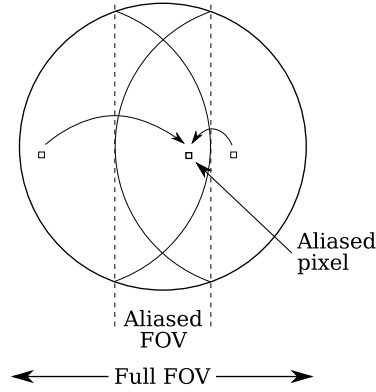


Figure 2.24: Undersampling the image in k -space causing Nyquist aliasing, folding the edges of the image into the centre, superimposing pixels.

of the sensitivity profiles, aliased images may be unfolded and combined to produce a single, fully sampled image. Undersampling each channel reduces the number of phase encoding steps, reducing the overall acquisition time.

The SENSE algorithm is applicable to an arbitrary k -space trajectory, and does not place restrictions on the probe configuration (although probe designs may be optimised for SENSE acquisition, as discussed in section 3.10.4). In the general case, SENSE reconstruction involves the inversion of a large matrix, requiring considerable computing resources. Cartesian reconstruction is described in this section, which considerably simplifies the reconstruction, as each aliased pixel is unfolded separately.

Data is acquired using an array probe with n_e elements. Data from each channel is Fourier transformed to produce an image in the normal manner. However, the phase encoded direction is undersampled such that n_p pixels are superimposed in each subimage. For each pixel ρ , a vector is constructed from the aliased data for each probe element

$$\mathbf{a} = [a_1 \ a_2 \ \cdots \ a_{n_e}]^T \quad (2.61)$$

Central to the reconstruction is the sensitivity matrix S . Complex element sensitivities at n_p superimposed pixels form an $n_e \times n_p$ sensitivity matrix

$$S_{\gamma,\rho} = s_{\gamma}(\mathbf{r}_{\rho}) \quad (2.62)$$

where γ is the element number, ρ is the superimposed pixel, \mathbf{r}_ρ is the location of pixel ρ and s_γ is the sensitivity of element γ .

Folded pixel values \mathbf{a} may be calculated from the separate pixel values \mathbf{v} using the sensitivity matrix S

$$\mathbf{a} = S\mathbf{v} \quad (2.63)$$

However, we wish to perform the reconstruction in the reverse direction, generating an unfolded image from folded subimages. This is done using the unfolding matrix U , which is the pseudo-inverse of S [39]

$$U = (S^H \Psi^{-1} S)^{-1} S^H \Psi^{-1} \quad (2.64)$$

where S^H indicates the complex conjugate transpose of S and Ψ is the $n_e \times n_e$ receiver noise matrix, which describes noise correlation between receive channels. The unfolded pixels values \mathbf{v} for the originally aliased locations are then

$$\mathbf{v} = U\mathbf{a} \quad (2.65)$$

SENSE reconstruction relies upon highly accurate sensitivity maps, which are acquired by taking a set of reference images. A full image is acquired using a volume probe (usually the same probe that is used for excitation) and a full image for each element of the receive array. Noise is removed from the reference images by polynomial fitting. The array images are then divided by the volume reference to give the sensitivity maps [38].

Undersampling an image inevitably reduces the SNR. The SNR of a SENSE reconstructed image is

$$\text{SNR}_\rho^{\text{SENSE}} = \frac{\text{SNR}_\rho^{\text{full}}}{g_\rho \sqrt{R}} \quad (2.66)$$

where $\text{SNR}_\rho^{\text{full}}$ is the signal to noise ratio of the full image and R is the reduction factor. The extra factor g_ρ is a geometry factor, which accounts for noise amplification in the reconstructed image due to poor conditioning of the sensitivity matrix S . This occurs where probe elements have similar

sensitivities to aliased pixels, making the pixels difficult to separate. It is defined as

$$g_\rho = \sqrt{(S^H \Psi^{-1} S)_{\rho, \rho}^{-1} (S^H \Psi^{-1} S)_{\rho, \rho}} \geq 1 \quad (2.67)$$

Increasing the reduction factor R increases the number of pixels superimposed in the folded images, which tends to increase the geometry factor. In practice the maximum usable reduction factor is limited by the g -factor before the ultimate limit, the number of receive elements n_e , is reached.

2.4 Instrumentation

This section gives a brief overview of an entire magnetic resonance imaging system. The most significant part of any MR system is the main magnet. Fig. 2.25 shows a photograph of the magnet of the 7T Philips Acheiva system at Nottingham. The bore of the magnet contains the shim and gradient coils (fig. 2.26). The RF probe is attached to the patient bed, and inserted into the magnet with the subject at the beginning of a scan.

A schematic diagram of the different components needed to drive the MR system is shown in fig. 2.27. The operation of these components is described in the following sections.

2.4.1 Main Magnet

The main component of an MRI system, in terms of size and cost, is the magnet which provides the static \mathbf{B}_0 field. A typical clinical system uses a 1.5T magnet. Standard research systems currently operate at 3T, with strong interest in higher field systems including the new Philips 7T machine at Nottingham. For comparison, the Earth's magnetic field is approximately $50\mu\text{T}$.



Figure 2.25: The Philips 7T Acheiva system at Nottingham, fitted with the standard Birdcage probe.

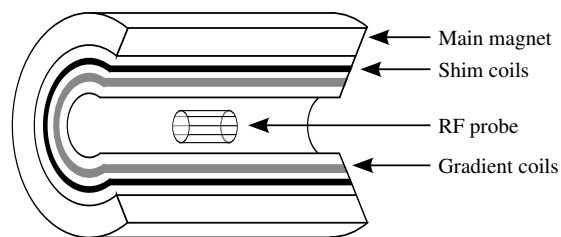


Figure 2.26: The main magnet, containing the shim coils, gradient coils and RF probe.

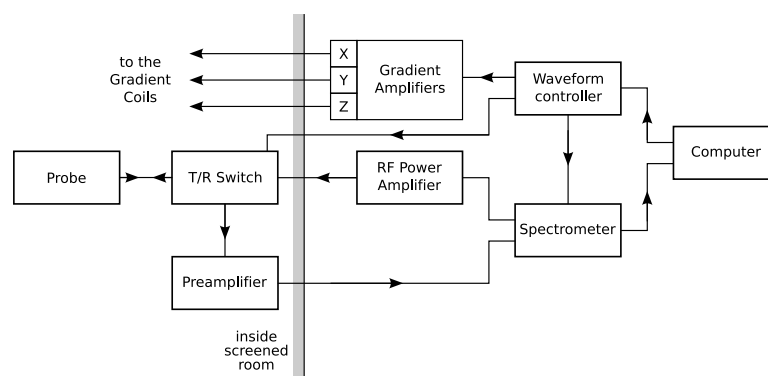


Figure 2.27: Schematic diagram of an MRI scanner.

An MRI system requires the main magnet to be highly spatially uniform and have good temporal stability. Field homogeneity is defined as [40]

$$\text{homogeneity} = \frac{B_0^{\max} - B_0^{\min}}{B_0^{\text{mean}}} \quad (2.68)$$

and typically measured in parts per million (ppm). A spatial uniformity better than 5ppm is required for imaging, with even higher uniformity needed for spectroscopy. Non-uniformity in \mathbf{B}_0 is the main source of error in the Larmor resonant frequency, leading to image artifacts and enhanced T_2^* decay. Temporal variations can also lead to image artifacts if the variation is on the same time scale as image acquisition. A more common problem is longer term drift, which causes problems when acquiring a series of images.

Early MR systems used resistive magnets, but to achieve the high field strengths used in modern systems requires a superconductive magnet. The magnet is wound from superconducting wire, eliminating Ohmic heat generation and allowing very high field strengths to be reached. The most common material for the wire is a niobium-titanium alloy, which becomes superconducting at temperatures below 10K. The wires are held in a superconducting state by immersion in liquid helium at 4K. The helium is contained in a dewar to limit heat absorption from the surroundings. However, some heat is absorbed causing the helium to boil off over time. A cold head is included to reliquify helium as it boils off, allowing the system to be left for several months between refills. The carefully controlled environment of a superconducting magnet allows for very high temporal field stability of the order of 0.1ppm/hour [41].

Another important property of a magnet is how far the fringe field (the field outside the scanner bore) stretches. A large fringe field will not affect the imaging capability of the scanner, but makes siting the magnet more difficult. For safety reasons, access must be restricted to areas exposed to more than 0.5mT (to prevent interference with pacemakers, for example). The 50mT contour is typically about 3m from the magnet in any direction. There is also a limit to the field at which the MR equipment itself will operate.

Most magnets include either a passive or active shield to reduce the size of the fringe field. A passive shield surrounds the magnet with a large quantity of iron to help contain the magnetic flux. Active shielding involves adding extra windings to the outside of the magnet, in which the current flows in the reverse direction to cancel out some of the magnetic flux outside the magnet bore [42]. Active shielding is widely used on clinical systems. The disadvantage of active shielding is that some of the flux inside the bore is also cancelled out. This can be overcome at low to medium field, but high field ($>3\text{T}$) research systems still use passive shielding. The Nottingham 7T system is surrounded by 200 tonnes of passive iron shielding.

2.4.2 Shim Coils

When a sample is placed into the static B_0 field, the field is distorted by susceptibility boundaries in the sample. For human or animal subjects the effect is particularly pronounced at air-tissue boundaries such as the sinuses. To restore B_0 field homogeneity, a set of shim coils are included in the magnet. These are resistive coils, usually at room temperature, capable of producing field corrections distributed as several orders of spherical harmonics.

After placing the sample in the scanner, the B_0 field is ‘shimmed’ by adjusting currents in the shim coils. Field homogeneity is measured by examining an FID signal in the absence of field gradients. An FID from a poorly shimmed field is shown in fig. 2.28*a*. Shim currents are then adjusted to produce a large amplitude exponentially decaying FID (fig. 2.28*b*), indicating a homogeneous B_0 field. The process is often now automated (e.g. [43]).

2.4.3 Gradient Coils

During an imaging sequence the static B_0 field is deliberately altered by the addition of linear field gradients used to localise the NMR signal (section 2.3.2). Early imaging experiments used shim coils used to generate field gradients [13], but it was quickly found that imaging speed was limited by

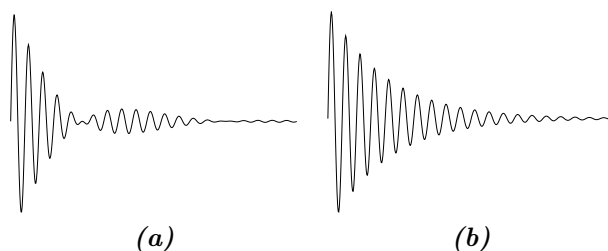


Figure 2.28: An FID is used to shim the B_0 field: (a) an uneven FID represents a poor shim, (b) a uniform exponential decay shows a good shim.

the time taken to switch the shim coils, and separate low inductance higher power gradient coils were added.

Gradient coils are large resistive coils, set inside the bore of the main magnet (fig. 2.26). An MRI system typically has three orthogonal gradient coils. Due to the high current carried by coils during an imaging sequence ($\sim 600\text{A}$), the coils are often water cooled to prevent over heating. Gradient coils typically produce a field gradient of 30mT/m , with the highest absolute field of approximately 6mT produced at the edge of the field of view.

2.4.4 Waveform Controller

The waveform controller oversees control of the MR system during an experiment. A pulse sequence is downloaded from the master computer at the start of a scan. The waveform controller then generates the required gradient waveforms, which are passed to the gradient amplifiers, sets the frequency generated by the RF synthesizer and produces the RF pulse envelope. It also gates the digitiser during reception.

2.4.5 RF System

The RF system is responsible for generating the oscillating B_1 field used to excite the sample, and for reading back the NMR signal it produces.

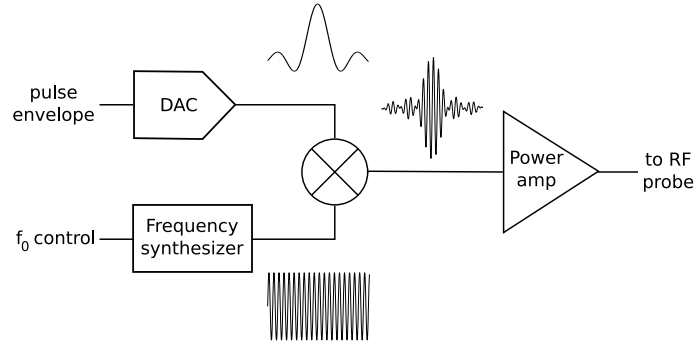


Figure 2.29: An RF transmit channel.

The RF signal is generated by the spectrometer. An adjustable frequency synthesizer produces the pure radio frequency signal ω_0 , which is then mixed with a pulse envelope (for example a sinc function) and passed to the RF power amplifier (fig. 2.29). The required peak RF power level is high; the Nottingham 7T system is equipped with a 4kW amplifier. However, a typical imaging sequence consists of a small number of short RF pulses, so the average transmitted power is much lower.

The RF probe then converts the electrical signal from the power amplifier into a homogeneous oscillating magnetic field inside the sample. The probe, in combination with the power amplifier, must be capable of generating a $15\text{--}20\mu\text{T}$ \mathbf{B}_1 field inside the sample [44]. Probe design is discussed in more detail in the next chapter.

Following excitation, the system switches to receive mode. The receive probe detects the weak rotating magnetic field generated by the sample due to the NMR effect and converts it back to an electrical signal via Faraday induction. The same probe may be used for both transmission and reception. However, because the transmit signal ($\sim\text{kV}$) is much larger than the receive signal ($\sim\mu\text{V}$), the preamplifier must be protected from the transmit system. A TR (Transmit/Receive) switch is used to isolate the preamplifier during RF transmission. TR switch design is discussed in chapter 7.

The first amplification stage is then provided by the preamplifier, having a typical gain of 20dB [45]. The preamplifier is placed physically close to the probe to reduce SNR loss in the connecting cable. The amplified

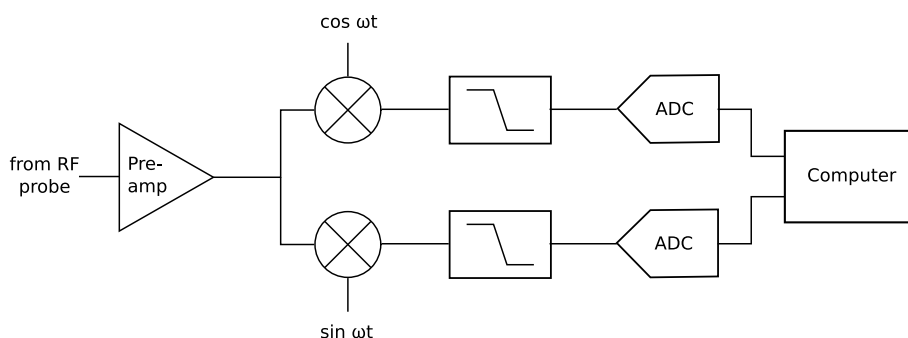


Figure 2.30: An RF receive channel.

signal is then fed back to the spectrometer outside the shielded room. The spectrometer splits the received signal and mixes it with a reference signal at 0° and 90° to generate real and imaginary channels at a lower intermediate frequency (fig. 2.30). Both channels are then low-pass filtered and digitised. The sampled data is then passed to the main computer for reconstruction.

Modern systems often sample the intermediate or radio frequency signal directly, and perform quadrature detection and low pass filtering digitally [44]. It is also now common for MR systems to have multiple independent receive channels for use in parallel imaging. Some research systems are also being fitted with multiple transmit channels [46, 47, 48].

Chapter 3

Radiofrequency Probe Design

3.1 Introduction

The radiofrequency probe is the interface between the sample and the MRI system. During transmission the probe generates a uniform magnetic field rotating at the Larmor frequency, perpendicular to the static B_0 field, to nutate sample magnetisation out of alignment with the static field and into the transverse plane. During reception the probe detects the magnetic field generated by precessing sample magnetisation as it relaxes back to the equilibrium state.

This chapter introduces the principles behind the operation of the RF probe. The role of the probe in transmission and reception is considered. Sources of loss from the probe are discussed, and the reciprocal problem of noise generated by the probe and sample is examined. The preamplifier is then introduced and the requirement for impedance matching is discussed.

A review of some common RF probe designs is then given. Volume probes are introduced and quadrature operation discussed. The surface coil is then discussed as a means to achieve higher SNR, at the cost of a smaller field-

of-view. Array probes are then discussed as a way to regain a larger field-of-view while maintaining the high SNR of the surface coil. The specific problem of coupling between probe elements is then investigated.

Specific issues in designing probes for high frequency operation, as the RF wavelength approaches the sample size, are then considered. Changes in tissue properties with increasing excitation frequency are investigated, and their influence upon the B_1 field inside the sample considered. Finally, changes in the SAR distribution inside the sample are discussed.

3.2 Transmission, Reception and Reciprocity

Ampère's law states that a current passing through a wire creates a magnetic field

$$\frac{1}{\mu_0} \oint_C \mathbf{B} \cdot d\boldsymbol{\ell} = \int_S \mathbf{J} \cdot d\mathbf{S} \quad (3.1)$$

This is the principle by which an RF transmit probe creates a magnetic field. The probe is designed to produce a current distribution \mathbf{J} to generate a uniform magnetic field over the volume of interest.

During reception, the rotating magnetic field generated by the sample induces an EMF ξ in the receive probe via Faraday induction

$$\xi = \oint_C \mathbf{E} \cdot d\boldsymbol{\ell} = -\frac{d}{dt} \int_S \mathbf{B} \cdot d\mathbf{S} \quad (3.2)$$

A receive probe is usually designed to have uniform sensitivity over the volume of interest.

There is a striking similarity between the transmit and the receive problem, which is embodied by the principle of reciprocity. It states that the sensitivity of a probe to a particular location is given by the field that would be generated at that location by a hypothetical unit current flowing in the probe [16, 49].

As discussed in section 2.2.2, spins are only influenced by a magnetic field rotating in the same sense as their precession. Consider a hypothetical probe

which generates a perfect linearly polarised magnetic field

$$\mathbf{B}_1 = B_1 \cos \omega t \hat{\mathbf{x}} \quad (3.3)$$

This field may be decomposed into two counter rotating components. Using the complex phasor notation

$$\hat{B}_1 = \frac{1}{2} (B_1 e^{i\omega t} + B_1 e^{-i\omega t}) \quad (3.4)$$

where $B_{1x} = \text{Re}[\hat{B}_1]$ and $B_{1y} = \text{Im}[\hat{B}_1]$. The $B_1 e^{i\omega t}$ component, rotating in the same sense as spin precession, causes a nutation, while the $B_1 e^{-i\omega t}$ component is wasted.

More generally, a probe will generate the elliptic magnetic field

$$\mathbf{B}_1 = \text{Re} \left[\left(\hat{B}_{1x} \hat{\mathbf{x}} + \hat{B}_{1y} \hat{\mathbf{y}} \right) e^{i\omega t} \right] \quad (3.5)$$

where \hat{B}_{1x} and \hat{B}_{1y} are complex phasors. The $\hat{\mathbf{z}}$ component of the \mathbf{B}_1 field is small in comparison to B_0 and may therefore be neglected.

Eqn. 3.5 may be separated into two counter rotating components

$$\hat{B}_1^+ = \frac{1}{2} \left(\hat{B}_{1x} + i\hat{B}_{1y} \right) e^{i\omega t} \quad (3.6)$$

$$\hat{B}_1^- = \frac{1}{2} \left(\hat{B}_{1x} - i\hat{B}_{1y} \right)^* e^{-i\omega t} \quad (3.7)$$

where \hat{B}_1^+ and \hat{B}_1^- are the magnetic fields rotating in the same and opposite direction to nuclear precession. The above expressions are in the stationary frame-of-reference. The term $e^{\pm i\omega t}$ is often dropped, when working in the respective rotating frames.

Because spins are only influenced by a magnetic field rotating in the same sense as their precession, only the \hat{B}_1^+ component of the probe field causes spin nutation. The principle of reciprocity is based in the stationary frame of reference. When using quadrature phase sensitive detection, the received signal is detected in the rotating frame-of-reference. A rather surprising effect of the rotating frame is that while spin nutation depends upon the field

component \hat{B}_1^+ rotating in the same sense as spin precession, the received signal depends upon the counter-rotating field \hat{B}_1^- [49]. At low frequency, where the signal phase does not vary significantly over the sample volume, the positive and negative rotating field components are virtually identical. At higher frequency, however, the \hat{B}_1^+ and \hat{B}_1^- fields differ significantly, and it has been clearly demonstrated that receive sensitivity does indeed depend on the negatively rotating field component [50].

3.3 Resonance

All RF probes are resonant structures, but the reason for resonance is subtle. The probe is an inductor, designed to create, or be sensitive to, a magnetic field. The energy stored in the magnetic field created by a current I passing through an inductor L is

$$U = \frac{1}{2}I^2L \quad (3.8)$$

where I is the peak current. This is the energy available to the probe from the NMR experiment. The probe is not a pure inductor, but also possess resistance R . It therefore dissipates energy via Ohmic heating

$$W = \frac{1}{2}I^2R \quad (3.9)$$

where I is again the peak current. The efficiency of a probe is measured by the ratio of stored to dissipated energy

$$Q = 2\pi \frac{\text{peak stored energy}}{\text{energy dissipated per cycle}} \quad (3.10)$$

where Q is a dimensionless quantity called the quality or Q -factor. Substituting eqns. 3.8 and 3.9 into eqn. 3.10 gives

$$Q = \frac{\omega U}{W} = \frac{\omega L}{R} \quad (3.11)$$

An inductor is not by itself resonant; the addition of capacitance to the probe makes a resonant circuit. The NMR signal induces an EMF ξ in the probe, which is the voltage measured directly across the probe terminals

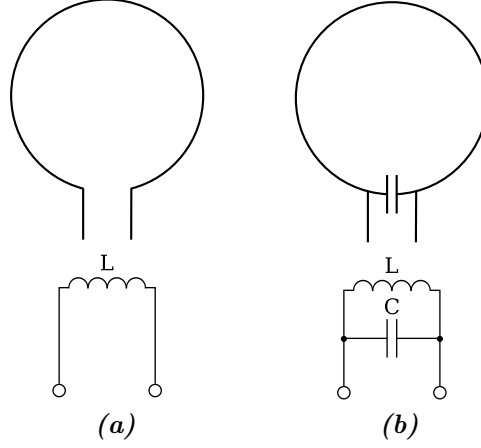


Figure 3.1: A simple RF probe and its equivalent circuit:
 (a) the probe in isolation is not resonant; (b) adding a capacitor forms a parallel resonant circuit.

(fig. 3.1a). Adding a capacitor across the probe creates a parallel resonant circuit (fig. 3.1b). At resonance, the voltage V across the capacitor is [51]

$$V = Q\xi \quad (3.12)$$

The sensitivity of the probe to the magnetic field has not changed. However, the detectable signal across the probe increases by a factor of Q . The resonant frequency of the circuit is

$$\omega_0 = \frac{1}{\sqrt{LC}} \quad (3.13)$$

where L is the inductance of the probe and C is the value of the capacitor, selected to resonate the circuit at the Larmor frequency.

Most practical probe designs use several capacitors distributed around the circuit. This is done to produce a more even current distribution in the probe, and hence produce a more uniform B_1 field. This also reduces the electric field produced by the probe, which is important for reducing the SAR.

The Q -factor can also be defined in terms of the width of the resonance peak

$$Q = \frac{f_0}{\Delta f} \quad (3.14)$$

where f_0 is the resonant frequency and Δf is the -3dB bandwidth. This provides a simple, practical method for measuring Q .

An RF probe typically has an unloaded Q of several hundred, which drops by a factor of five or more when the probe is loaded [52, 53]. The drop is important, indicating that the probe couples to the sample. If a probe does not couple well to the sample, it will not generate a strong excitation field inside it, and will not be sensitive to the NMR signal it generates [16]. Often both the unloaded and loaded Q are quoted for a probe.

3.4 Probe Losses

There are three sources of power loss at the RF probe: resistive loss in the probe itself, power absorbed by the sample and radiation [54].

An RF probe with resistance R_p will dissipate power $P = I^2 R_p$ through resistive heating. Most probes are constructed from copper foil and have a resistance of less than 0.5Ω . For large conducting samples, such as the human head, power dissipated in the probe is insignificant compared to power dissipated in the sample at frequencies greater than a few Megahertz [16].

Power dissipates in the sample via two mechanisms. Biological tissue is a lossy dielectric, so currents due to the radiofrequency electric field inside the sample dissipate power as heat. The electric field serves no useful purpose, and should therefore be minimised. The rotating magnetic field induces eddy currents inside the sample, which also dissipate power via ohmic heating. Unlike the electric field, the magnetic field is necessary for the probe to function and cannot be reduced.

Power dissipated in the sample can be modelled as an equivalent series resistance R_s in the probe circuit [55]. From the definition of the quality

factor (eqn. 3.11) it can be seen that increasing the circuit resistance reduces the Q . A reduction in Q is indeed seen as a sample is inserted into the probe, providing a simple method to measure the power dissipated in the sample. If the quality factors of the unloaded and loaded probe are Q_0 and Q_ℓ respectively, a “sample quality factor” Q_s can be calculated as [56]

$$\frac{1}{Q_s} = \frac{1}{Q_\ell} - \frac{1}{Q_0} \quad (3.15)$$

The power deposited in the sample is then

$$P_s = \frac{B_1^2 \omega L}{2Q_s} \quad (3.16)$$

The final loss mechanism is radiation. An MR probe is a near field device and should not radiate, but in practice this is hard to achieve as the operating wavelength approaches the probe dimensions. Energy lost due to radiation from a circuit can be modelled as an equivalent resistance, called the radiation resistance, defined as

$$R_r = \frac{\langle P_r \rangle}{I^2} \quad (3.17)$$

where $\langle P_r \rangle$ is the mean radiated power and I is the driving current. If the probe is approximated as a small loop antenna, the radiation resistance [57]

$$R_r = 31,200 \frac{A^2}{\lambda^4} \quad (3.18)$$

where A is the area of the loop (the probe cross section). Radiation from the probe increases as the wavelength reduces. For a probe with a 15cm radius, $R_r = 5\Omega$ at 128MHz, increasing to $R_r = 156\Omega$ at 300MHz. In practice these estimates are a little high, but it is still clear that radiation loss becomes significant as the operating frequency increases [58].

3.5 Specific Absorption Rate (SAR)

A significant proportion of power lost from the probe is absorbed by the sample, where it dissipates as heat. Clearly it is important to restrict the

temperature rise inside live samples such as human volunteers. The exact change in temperature depends upon many factors such as tissue type, location and perfusion. A useful approximation to temperature change is to monitor the Specific Absorption Rate (SAR), which is defined as

$$\text{SAR} = \frac{\text{total RF energy dissipated in sample}}{\text{exposure time} \times \text{sample weight}} \quad (3.19)$$

The power P dissipated in the sample is

$$P = \int_{\text{sample}} \frac{\sigma(\mathbf{r}) |\mathbf{E}(\mathbf{r})|^2}{2} d\mathbf{r} \quad (3.20)$$

where σ is the sample conductivity and \mathbf{E} is the electric field. The SAR is then calculated as

$$\text{SAR} = \frac{\tau}{2T_R} \int_{\text{sample}} \frac{\sigma(\mathbf{r}) |\mathbf{E}(\mathbf{r})|^2}{\rho(\mathbf{r})} d\mathbf{r} \quad (3.21)$$

where τ/T_R is the RF duty cycle and ρ is the sample density.

The International Electrotechnical Commission (IEC) produce regularly updated guidelines for SAR limits for MRI [59]. The current IEC normal operating mode limits are 4 W/kg over the whole body, 3.2 W/kg over the head and 10 W/kg over any 10g sample of tissue. All of these limits are averaged over a 6 minute period. There is also a peak limit of not more than 3 times the above values over any 10 second period.

3.6 Signal-to-Noise Ratio (SNR)

The limit of detection of any signal is determined by the signal-to-noise ratio (SNR). An MR scanner is typically sited inside an RF screened room to reduce external sources of noise. However, the NMR signal generated by the sample is small enough that thermal noise produced by the probe and sample limit signal detection.

The signal detected by the probe is the EMF induced in it by precessing sample magnetisation, which is

$$\xi = - \int_{\text{sample}} \frac{\partial}{\partial t} \mathbf{B}_1^- \cdot \mathbf{M} dV \quad (3.22)$$

where \mathbf{B}_1^- is the receptive field of the probe and \mathbf{M} is the sample magnetisation [60]. If \mathbf{B}_1^- is homogeneous over the sample volume

$$\xi = \omega_0 B_{1tr}^- M_0 V_s \cos \omega_0 t \quad (3.23)$$

where B_{1tr} is the transverse component of the RF field. The resonant frequency ω_0 is proportional to the static field strength

$$\omega_0 = -\gamma B_0 \quad (3.24)$$

Sample magnetisation M_0 is also proportional to the static field strength

$$M_0 \propto B_0 \quad (3.25)$$

and therefore the NMR signal amplitude increases as the square of the static magnetic field strength

$$\xi \propto B_0^2 \quad (3.26)$$

We now turn to the noise in the detected signal. In 1928 Johnson [61] observed and Nyquist [62] explained that any electrical conductor generates noise due to the thermal excitation of electric charges. For a conductor of resistance R , the RMS noise voltage generated is

$$N = \sqrt{4k_B T R \Delta f} \quad (3.27)$$

where T is the absolute temperature, Δf is the acquisition bandwidth and k_B is Boltzmann's constant.

There are two significant sources of resistance in the probe circuit: the probe itself and the sample. Fig. 3.2 shows an equivalent circuit for the NMR receive head, showing the induced signal ξ and the probe and sample

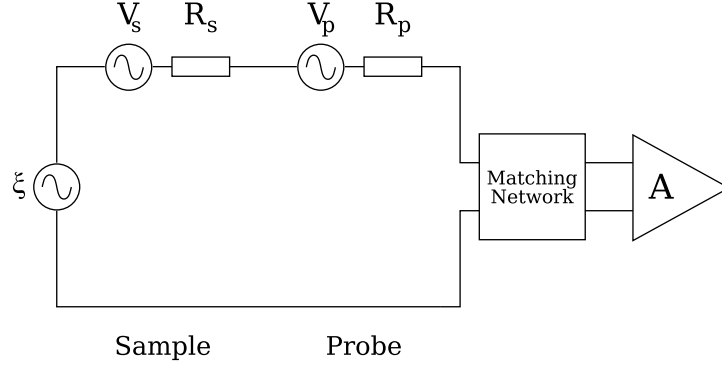


Figure 3.2: The probe detects the NMR signal ξ . At the same time, noise is introduced into the signal from the sample and the probe. Probe resistance R_p introduces N_p and the sample loading resistance R_s introduces N_s .

resistances R_p and R_s . Voltage sources N_p and N_s represent noise generated by resistances R_p and R_s .

The signal-to-noise ratio ψ of the detected signal is

$$\psi = \frac{\xi}{N_p + N_s} \quad (3.28)$$

where ξ is the EMF induced by the NMR signal and N_p and N_s are noise voltages generated by the probe and sample respectively.

Substituting eqn. 3.27 into eqn. 3.28 gives

$$\psi \propto \frac{\xi}{\sqrt{R_p + R_s}} \quad (3.29)$$

Clearly, SNR is maximised by minimising the probe and sample resistance.

Probe resistance is minimised by using good conductors (usually copper) and careful construction. At high frequency the skin effect reduces the conducting cross section of the probe, making $R_p \propto \sqrt{\omega_0}$ [60]. As ω_0 rises linearly with the static field strength

$$R_p \propto \sqrt{B_0} \quad (3.30)$$

The probe must magnetically couple to the sample in order to detect the NMR signal. Currents due to thermal fluctuation of charge carriers (ions and electrons) generate a magnetic field that is detected by the probe. This can be modelled as a series resistance R_s in the probe circuit. Unlike probe noise, sample noise cannot be controlled by the probe designer.

Noise generated inside the sample is unaffected by changes in field strength, but probe-sample coupling increases linearly with frequency, increasing the probe sensitivity to thermal noise in the sample. Using eqn. 3.27, the sample equivalent resistance increases as [63]

$$R_s \propto N_s^2 \propto B_0^2 \quad (3.31)$$

Substituting eqns. 3.26, 3.30 and 3.31 into eqn. 3.29 gives the SNR

$$\psi \propto \frac{B_0^2}{\sqrt{B_0^2 + \alpha\sqrt{B_0}}} \quad (3.32)$$

where α depends on the ratio of R_s to R_p . For small samples such as those used in microscopy, or at low frequency, probe noise dominates and SNR rises with field strength as [60]

$$\psi \propto B_0^{7/4} \quad (3.33)$$

At higher frequency or for larger samples, sample noise dominates and SNR rises with static field strength as [55]

$$\psi \propto B_0 \quad (3.34)$$

For the human head, sample noise is dominant above 8MHz [16]. It is interesting to note that SNR is defined by the sample, giving an intrinsic SNR [55] that cannot be improved upon through probe design. This is a fundamental limit in magnetic resonance; where sample noise dominates, SNR can only be improved by lowering the sample temperature or increasing the static field strength.

A final SNR consideration is the filling factor η , defined as [64]

$$\eta = \frac{\int_{\text{sample}} (B_1^-)^2 dV}{\int_{\text{all space}} (B_1^-)^2 dV}. \quad (3.35)$$

Signal is only generated inside the sample, but noise is generated over the whole volume over which the probe is sensitive. An ideal probe is therefore sensitive only to the volume of the sample ($\eta = 1$). Probes designed for human imaging, especially of the head, are a compromise between filling factor and patient comfort. A probe with a high filling factor gives high SNR but leaves little space around the patient, making the scanner feel more claustrophobic.

3.7 The Preamplifier

Having detected the signal from the sample with the maximum SNR, it is important to amplify the signal without further degrading it. This is done by the preamplifier. In practice the preamplifier does also introduce a certain amount of noise. This is indicated by the noise figure which is defined as [65]

$$F = 20 \log_{10} \left(\frac{\text{SNR}_{\text{in}}}{\text{SNR}_{\text{out}}} \right) \quad (3.36)$$

when using the voltage SNR. An ideal amplifier has a noise figure of 0; a high quality preamplifier might have a noise figure of 0.5dB, reducing the signal-to-noise ratio by 11%.

Because the signal induced in the probe is small the preamplifier should be placed physically close to the probe to minimise losses in the connecting cable. In clinical systems, the preamplifier is often integrated into the probe housing. The output from the preamplifier should be strong enough that noise introduced by further sections of the receive chain does not significantly change the SNR.

3.8 Impedance Matching

It was shown in section 3.3 that adding a capacitor across the probe terminals increases the signal voltage available for detection. In this section it is shown how to transfer that signal from the probe to the preamplifier to maintain maximum SNR.

Maximum power is transferred from the probe to the preamplifier when the preamplifier input impedance Z_{in} is matched to the probe impedance Z_{probe} [66]

$$Z_{in} = Z_{probe}^* \quad (3.37)$$

However, it is more important to transfer the signal with maximum SNR than maximum power. The preamplifier noise factor is also a function of Z_{in} , so the impedance that achieves maximum SNR is not the same as the impedance for maximum power transfer [67]. The probe impedance should be transformed to the maximum SNR point, rather than the amplifier input impedance. In the following discussion Z_{in} refers to the maximum SNR point.

As MRI uses a narrow bandwidth, the probe only needs to match the preamplifier in a narrow band around the Larmor frequency. The probe impedance is transformed using a resonant matching circuit [68]. Many different matching circuits are available, one of which is shown in figure 3.3.

The probe can be modelled as reactance X_p in series with resistance R_p (fig. 3.3a). Adding a reactance X_t (where X_t has the opposite sign to X_p) in parallel with the probe forms a resonant circuit (fig. 3.3b). The probe is usually inductive, making X_t capacitive. The resonant circuit has series equivalent resistance R_{eq} and reactance X_{eq} (fig. 3.3c), both of which vary with frequency as shown in fig. 3.4. On resonance the circuit has resistance $R_{eq} = Q\omega_0 L$, where L is the probe inductance, and zero reactance. At frequencies ω_a and ω_b either side of resonance the probe resistance is matched to the preamplifier resistance ($R_{eq} = R_{in}$), provided $R_{in} < Q\omega_0 L$. At ω_a and ω_b the circuit also has reactance $\pm X_{eq}$, which may be cancelled out by adding a series reactance $X_m = X_{in} \mp X_{eq}$ (fig. 3.3d), fully matching the probe impedance to the preamplifier.

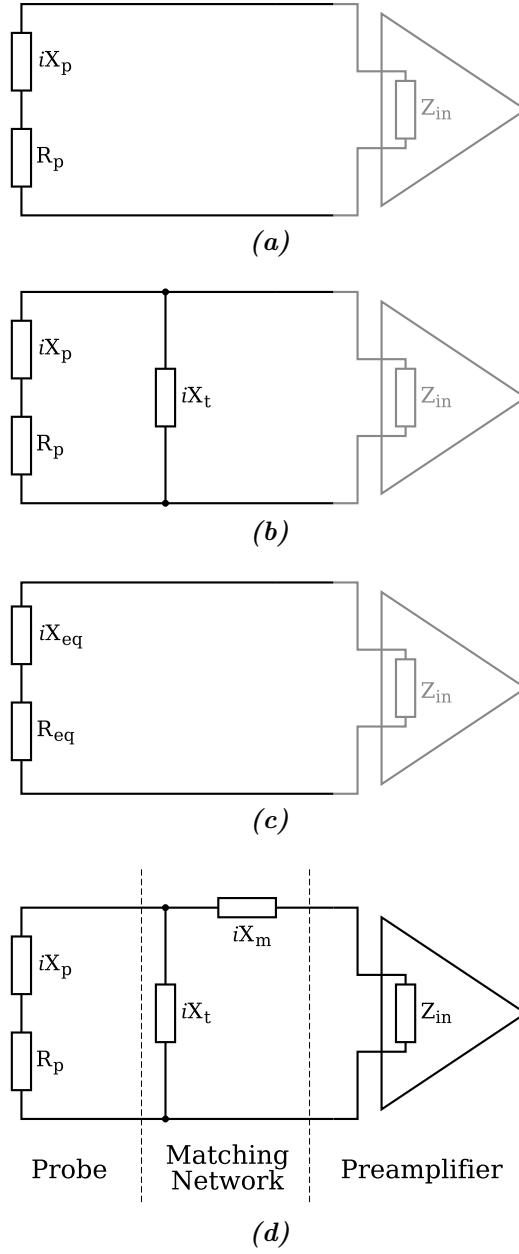


Figure 3.3: The probe is modelled as (a) reactance X_p in series with resistance R_p ; (b) Adding reactance X_t in parallel the probe transforms the impedance of the circuit, which can be considered as the equivalent circuit shown in (c). The value of X_t is selected to match the circuit resistance R_{eq} to the preamplifier resistance R_{in} . The circuit reactance can then be adjusted by (d) adding X_m , such that $X_{eq} + X_m = X_{in}$.

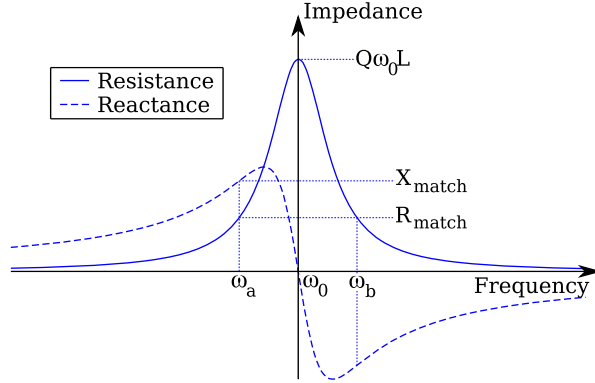


Figure 3.4: The parallel resonant circuit impedance vs. frequency. At resonance the circuit has the pure resistance $Q\omega_0 L$. Either side of resonance at frequencies ω_a and ω_b the circuit has the desired resistance R_{match} but also has the reactive component $\pm X_{match}$.

Note that the parallel resonant circuit in fig. 3.3b does not resonate at the Larmor frequency ω_L . It is only with the addition of the matching component X_m that the complete circuit resonates at ω_L , and then only if Z_{in} is purely resistive. As standard, most RF equipment is matched to 50Ω resistive with no reactive component.

It is also important to match the probe impedance to that of the power amplifier. If the probe and power amplifier are not matched, some transmit power will reflect back into the power amplifier at the mismatch. This is undesirable both because it makes the transmit chain less efficient, and because the reflected power must be dissipated. A circulator may be placed between the power amplifier and the probe to direct any reflected power away from the power amplifier and into a dummy load.

Using ideal components, the matching network is lossless as it contains no resistance. Real reactive components are never purely reactive, but also have a resistive component. Reactive component quality is measured using the Q factor (eqn. 3.10). Real inductors have a Q of less than 50 at 300MHz, whereas high quality capacitors have a Q of 1000 or more at the same frequency [69], making it attractive to construct the matching network from capacitive rather than inductive components. For this reason it is prefer-

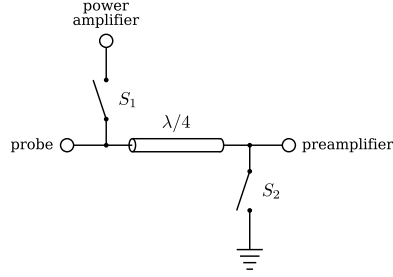


Figure 3.5: Schematic diagram of the TR switch.

able to match at ω_a rather than ω_b as this point has a positive reactance (inductive), which is cancelled by adding a series capacitor.

The matching circuit in fig. 3.3 is easily understood, but is not ideal as a practical circuit. It is unbalanced, making it more susceptible to interference. Using a balanced design the common mode rejection of the circuit is increased, making it much less sensitive to external interference sources [16].

3.9 Transmit/Receive Switching

To use a probe for both transmission and reception, it must be switched between the power amplifier (transmission) and the preamplifier (reception), which is done by the TR (Transmit/Receive) switch. The transmit signal is typically eight orders of magnitude more powerful than the receive signal; if the preamplifier is exposed to the transmit signal it will be permanently damaged.

Fig. 3.5 shows a schematic diagram of a basic TR switch, consisting of two PIN diode switches [70] and a quarter wave transformer. During transmission both switches are closed. Closing S_1 connects the probe to the RF power amplifier, while closing S_2 short circuits the preamplifier input to ground. The quarter wave transmission line section acts as an impedance transformer, converting the low impedance point at the preamplifier input to a high impedance at the opposite end, preventing the transmit signal from passing to the preamplifier.

During reception both switches are opened. Opening S_1 disconnects the power amplifier, while opening S_2 disconnects the preamplifier input from ground, allowing the received signal to pass directly to the preamplifier.

A series switch is used for S_1 to provide the greatest isolation in the off state. Using the shunt switch for S_2 in combination with the quarter wave line means that the only extra component introduced by the TR switch during reception is the quarter wave section, minimising signal loss.

The performance of a TR switch is characterised by its insertion loss and isolation [70]. Insertion loss I_L measures the signal degradation introduced by the switch in the receive state. It is defined as

$$\begin{aligned} I_L \text{ (dB)} &= 10 \log_{10} (P_{out} - P_{in}) \\ &= 20 \log_{10} \left(\frac{V_{in}}{V_{out}} \right) \end{aligned} \quad (3.38)$$

where P_{in} and P_{out} are the input and output signal power, and V_{in} and V_{out} are the input and output signal voltage. Note that the TR switch sits between the probe and the first amplification stage, making a low insertion loss critical. A good switch can achieve an insertion loss $I_L < 0.25\text{dB}$.

The attenuation provided by the switch in its open state is measured by its isolation, defined as

$$\begin{aligned} \text{isolation (dB)} &= 10 \log_{10} (P_{on} - P_{off}) \\ &= 20 \log_{10} \left(\frac{V_{on}}{V_{off}} \right) \end{aligned} \quad (3.39)$$

where P_{on} and P_{off} are the signal output power with the switch in the on and off states respectively. V_{on} and V_{off} are the corresponding output signal voltages. A good TR switch should provide an isolation greater than 40dB between the probe and preamplifier.

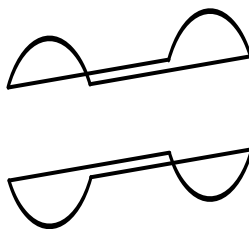


Figure 3.6: The saddle probe.

3.10 Probe Design

This section introduces some practical RF probe designs. The development of the volume probe is examined, and quadrature operation is introduced. The surface coil is then discussed, and its natural progression, the array probe. The issue of coupling between array probe elements is also discussed.

3.10.1 Volume Probes

In Bloch's original NMR experiments, the RF probe was a simple coil of wire, wrapped around the sample tube [7], progressing to rigid solenoids made from copper tubing in later experiments [16]. The introduction of superconducting magnets, where the static field is aligned with the magnet bore, made sample access difficult with a solenoid coil, the axis of which must be aligned perpendicular to the B_0 field. To improve sample access the saddle coil was introduced [71]. The saddle coil is effectively a pair of simple loop coils, wrapped onto the surface of a cylinder to make best use of the available space inside the magnet bore (fig. 3.6).

To produce a homogeneous rotating magnetic field in the transverse plane, the ideal current distribution on the surface of a cylinder is [40]

$$I(\theta) = I_0 \cos(\theta) \hat{z} \quad (3.40)$$

where θ is the azimuthal angle and \hat{z} is parallel to \mathbf{B}_0 . The saddle coil approximates this distribution with the four axial wire sections, plus two 'virtual' sections at $\theta = 90^\circ$ and 270° which always carry zero current.

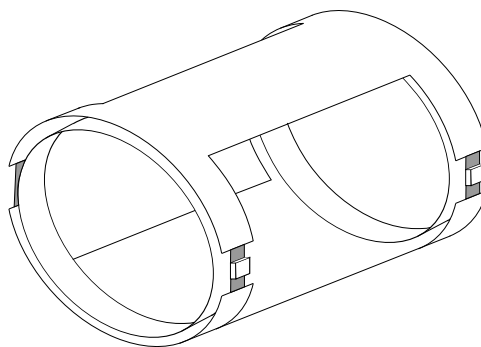


Figure 3.7: The Alderman-Grant probe.

The development of RF probes from this point has largely been finding better ways to approximate this current distribution using a small number of longitudinal conductors on a cylindrical surface.

Parasitic capacitance limits the operating frequency of both the solenoid and saddle probes. As the operating frequency increases, the required tuning capacitance becomes smaller than the parasitic capacitance, and the probe can no longer be tuned. In response to the introduction of superconducting magnets, and the higher field strengths made available, Schneider and Dullenkopf developed the slotted tube resonator [72]. The design is based around a stripline formed from two arched conductors in a coaxial cavity. The use of distributed capacitance and inductance allows the probe to operate over a greater frequency range.

Alderman and Grant [73] then took the principle of the slotted tube resonator, but returned to the use of lumped components to produce a much shorter probe (fig. 3.7). One of the primary motivations behind the design was to reduce the power dissipated in the sample, which is achieved by using a low inductance design (a lower voltage is developed across a low inductance) and by including guard rings to shield the sample from the electric field generated across the capacitors.

At radio frequencies, current only flows on the edges of a continuous conductor, so the Alderman-Grant probe offers a similar current path to the saddle coil. However, the probe has a lower inductance and so requires a

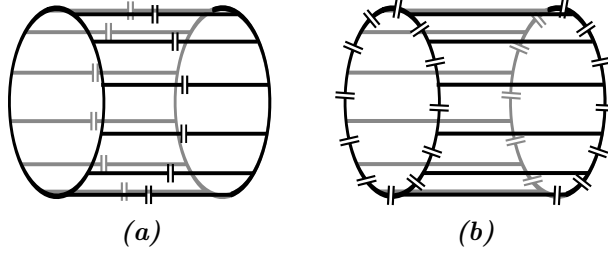


Figure 3.8: The (a) low pass and (b) high pass Birdcage probe.

higher capacitance to resonate at a given frequency and may be tuned to a higher frequency.

A better approximation to the current distribution of eqn. 3.40 is achieved by the Birdcage design introduced by Hayes *et al* [52], which allows probes with an arbitrary number of axial rungs (fig. 3.8). The only limitations are that the cylindrical surface must appear transparent to RF flux, and that inductive coupling increases between adjacent rungs as their proximity increases. Birdcage probes are typically constructed with 12–24 rungs. There are three variants on the Birdcage design: low pass with capacitors on the rungs (fig. 3.8a), high pass with capacitors on the end rings (fig. 3.8b) and bandpass with capacitors on both rungs and end rings (not shown).

The equivalent lumped element circuit for the low pass birdcage is shown in fig. 3.9, where $\frac{1}{2}L_1$ is the inductance of the end rings sections, L_2 is the inductance of the rungs and C are the capacitors. Opposite ends of the circuit are connected, forming a periodic ladder network. Each unit of the ladder network phase shifts the driving signal by $\Delta\phi$. To resonate, the total phase shift around the structure must be an integer multiple of 2π . By ignoring the inductance of the rungs L_2 and all mutual inductances, the resonant mode of the structure are found to be [52]

$$\omega = \frac{2}{\sqrt{L_1 C}} \sin\left(\frac{\pi M}{N}\right) \quad (3.41)$$

where M is the mode number. For $M = 1$, currents in the rungs are proportional to $\sin\theta$ where θ is the azimuthal angle, producing the required homogeneous B_1 field inside the cylinder.

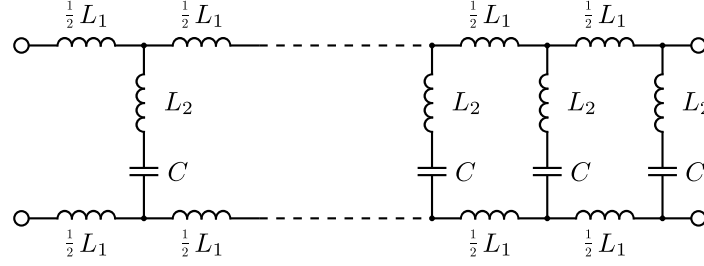


Figure 3.9: Equivalent circuit for the low pass birdcage probe.

The resonant frequency of the probe is increased by lowering the capacitors values. In the hundreds of megahertz range the required capacitance is lower than the parasitic capacitance of the probe, and the probe self-resonates below the required operating frequency.

RF probes are often surrounded by an RF screen. The screen prevents the probe from coupling to other circuits in the bore of the scanner, such as the gradient coils. In 1988 Röschmann filed a patent for the TEM probe design (fig. 3.10), returning to the use of transmission line elements and incorporating the screen into the probe design [74]. The probe, inspired by microwave cavity designs, is a re-entrant resonant cavity containing a series of resonant co-axial elements. When driven in the correct sequence, the co-axial elements drive the resonant modes of the cavity. The probe is driven at one or two points (for linear or quadrature mode, respectively) via capacitors connected to the out cylinders of the coaxial elements. Other elements inductively couple to the driven elements, completing the circuit. Like the Birdcage, the TEM probe supports several resonant modes (fig. 3.11). Again, the $M = 1$ mode produces a B_1 field suitable for imaging, making it important that the probe is tuned to the correct mode.

The TEM design was further developed by Vaughan *et al* [53], and demonstrated to perform well at high field strength [58, 75]. In the Birdcage probe, current flows between rungs via the end rings. The end-ring inductance limits the high frequency operation of the Birdcage. The TEM probe uses the RF screen to provide a low inductance current return path, giving the probe a very high self-resonance. A head sized probe can easily be tuned to several hundred megahertz. It also exhibits a high Q , in excess of 1000 when unloaded [53].

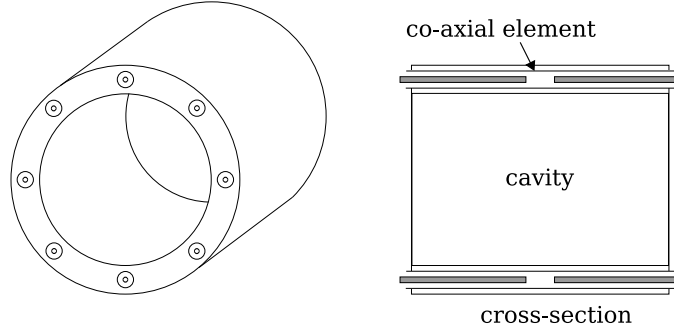


Figure 3.10: The TEM probe.

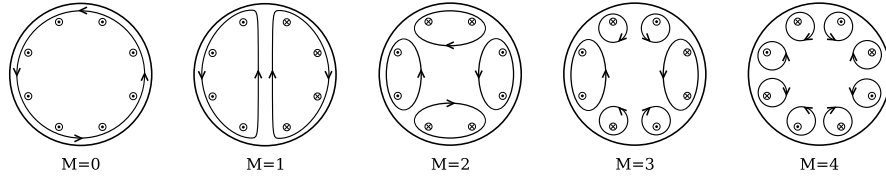


Figure 3.11: B_1 flux lines for the five resonant modes of an eight rung volume probe, where $M = 1$ is the normal imaging mode [53].

It has been claimed that the TEM probe is better suited to high frequency operation than the Birdcage probe [76], as it has a lower inductance (requiring larger tuning capacitance) and lower radiation loss. However, this is still the subject of debate, with other groups showing superior performance using Birdcage designs [77]. With careful optimisation, both Birdcage and TEM probes may be constructed at 300MHz [78].

3.10.2 Quadrature

Following a 90° RF pulse, nuclei in the sample precess anticlockwise about the static \mathbf{B}_0 field. The precession can be detected by a simple loop of wire (fig. 3.12), in which an EMF ξ_1 is generated by Faraday induction [60]

$$\xi_1 = -\frac{\partial}{\partial t} \{\mathbf{B}_1 \cdot \mathbf{M}\} \quad (3.42)$$

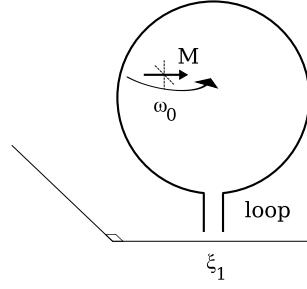


Figure 3.12: Linear detection using a single coil.

where \mathbf{B}_1 is the receptive field of the wire loop. The rotating sample magnetisation \mathbf{M} is detected as the sinusoidal signal

$$\xi_1 = \omega_0 B_1 M_0 \cos(\omega_0 t). \quad (3.43)$$

A single wire loop cannot distinguish between positive and negative rotating fields. The direction of rotation can be distinguished by adding a second wire loop (fig. 3.13). The EMF induced in the second loop is the same as that induced in the first, but phase shifted to account for the change in position around the sample. For the arrangement shown in fig. 3.13

$$\xi_2 = \omega_0 B_1 M_0 \sin(\omega_0 t) \quad (3.44)$$

Using complex phasor notation, the full rotating signal is then

$$\begin{aligned} \xi &= \xi_1 + i\xi_2 \\ &= \omega_0 B_1 M_0 e^{i\omega_0 t} \end{aligned} \quad (3.45)$$

Sample noise is a random signal with independent orthogonal components. When the two receive loops are orthogonal, noise detected by the loops is uncorrelated. Combining the two receive signals using eqn. 3.45 doubles the available signal, while increasing the RMS noise level by $\sqrt{2}$, giving an overall improvement of $\sqrt{2}$ in SNR [63].

There is also advantage in driving a probe in quadrature. When a probe is driven in linear mode (i.e. driven from a single point), the magnetic field produced is the sum of a positive and negative rotating field component.

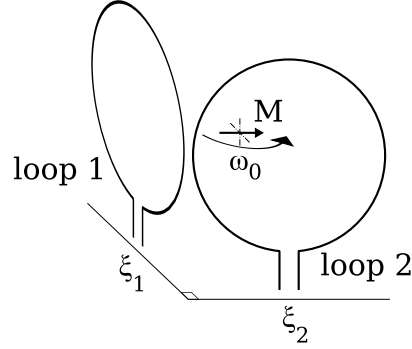


Figure 3.13: Quadrature detection using two orthogonal coils.

Only the positive rotating component contributes to sample excitation, while the negative rotating component has no effect upon the sample. However, energy dissipated in the sample due to the electric field is not directionally sensitive; both the positive and negative rotating components of the electric transmit field contribute to SAR. Driving the probe in quadrature mode generates only the positive rotating magnetic and electric fields, halving the transmit power with no reduction in induced sample magnetisation.

The quadrature principle has been described here using two independent coils, but is more commonly implemented using a volume probe with two feed points, separated in phase by 90° . Both Birdcage [52] and TEM [53] probes are commonly used in quadrature mode.

3.10.3 Surface Coils and Active Detuning

A surface coil is a flat probe which is placed directly on the surface of the sample [79]. At its simplest, it is a wire loop with several capacitors distributed around its circumference. Surface coils usually have a small field of view, which gives a high SNR because the coil only detects noise from a small volume.

The B_1 field produced by a surface coil is often quite inhomogeneous. The field intensity is high close to the probe, falling off rapidly further into the sample. A surface coil is commonly used as a receive probe in combination

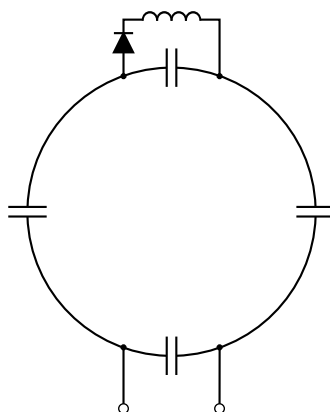


Figure 3.14: A trap used to actively detune a surface coil.

with a volume transmit probe. The volume probe gives good nutation homogeneity while the surface coil give good SNR over the volume of interest.

When a surface coil is placed inside a volume probe the two circuits strongly couple. During transmission the volume probe will induce a high current in the surface coil, risking burning the subject. During reception the volume probe loads the surface coil, coupling noise and reducing sensitivity. Coupling may be prevented by detuning one probe while the other is in use. This can be done using a trap circuit and a PIN diode switch (fig. 3.14). The trap is formed by an inductor connected in parallel with one of the probe capacitors, making a parallel resonant circuit which has a high impedance at resonance, preventing current flow in the probe. The PIN diode is used as a switch, opened and closed by a DC control signal (section 3.9). During transmission the surface coil is detuned, while during reception the volume probe is detuned.

3.10.4 Array Probes

The surface coil offers a high SNR over a small volume. If multiple surface coils can be used simultaneously and the signals combined to produce a single image, the SNR benefit can be retained while regaining a large field of view. This is the principle of the NMR phased array [31]. Like surface coils, array probes are usually used for reception in combination with a

volume transmit probe. The main difficulty in probe array design is to keep the individual array elements independent.

When two resonant elements are placed in close proximity, they interact. This is called coupling, and is determined by the mutual impedance between the elements and the relative currents they carry. Mutual impedance Z_{ij} is defined as

$$Z_{ij} = \frac{V_i}{I_j} \quad (3.46)$$

where V_i is the EMF induced in the i th element by current I_j flowing in the j th element [80]. Due to the principle of reciprocity, $Z_{ij} = Z_{ji}$. Like self impedance, mutual impedance is a complex quantity consisting of a resistive and a reactive part

$$Z_{ij} = R_{ij} + iX_{ij} \quad (3.47)$$

The reactive part is normally inductive for an MR probe. Inductive coupling causes peak splitting in resonant circuits, reducing sensitivity at the operating frequency (fig. 3.15a). Resistive coupling introduces noise correlation between channels of the array, reducing the independence of the channels and so reducing SNR [81].

Mutual inductance between loop elements may be reduced to zero by overlapping the loops (fig. 3.15b) [31]. This method is simple, and applicable to both transmit and receive arrays. However, only nearest neighbours may be decoupled in this way. Next nearest neighbour elements can also show significant coupling, especially at higher frequency.

The signal induced in a probe element by adjacent elements also depends upon the current those elements carry. Reducing the current reduces the coupled signal, without imposing constraints on the positioning of the elements. This can be achieved using low input impedance preamplifiers, and a suitable matching network (fig. 3.16). The network transforms the preamplifier input impedance to appear as an infinite series resistance in the probe circuit, while simultaneously transforming the probe impedance to noise match at the preamplifier input (usually 50Ω) [31, 67]. This method is widely used in parallel receive arrays but is not applicable to transmit el-

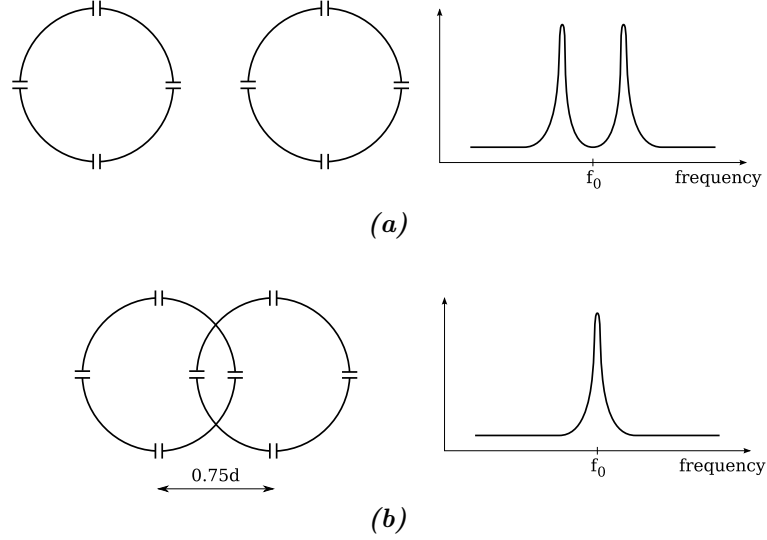


Figure 3.15: (a) Two loops, tuned to the same frequency, couple when placed in close proximity causing the resonance peak to split; (b) overlapping the loops by $0.75 \times$ diameter reduces the mutual inductance to zero and no splitting is seen [31].

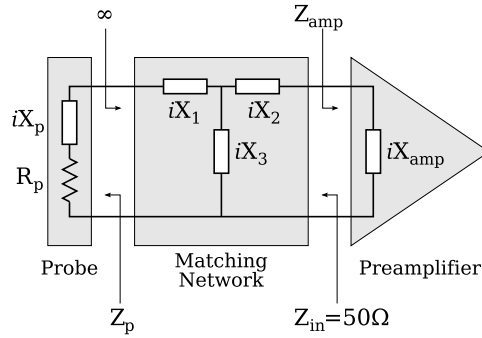


Figure 3.16: The matching network transforms the preamplifier input impedance Z_{amp} to ∞ , while transforming the probe impedance Z_p to Z_{in} [67]

elements, as reducing the current flowing in an element simply reduces the magnetic field it generates.

Mutual inductance between array elements may also be cancelled out by introducing capacitive coupling between elements [82, 83, 84, 85]. More generally, an n -element probe array may be decoupled using a suitable $2n$ -port passive network [86]. A potential problem with these networks is their dependence on the precise coupling between array elements, which in turn

depends upon the probe-sample coupling. It is not practical if the decoupling network needs adjusting for each individual patient. However, passive decoupling networks are attractive as they place no geometric constraints of the probe design, and may be used for both transmit and receive arrays.

Partially parallel acquisition methods such as SENSE and SMASH introduced a further parameter into array probe design, the geometry or g -factor. The g -factor describes the ability of a probe array to distinguish signal contribution from aliased locations [87]. It is defined as

$$g_\rho = \sqrt{(\mathbf{S}^H \mathbf{\Psi}^{-1} \mathbf{S})_{\rho, \rho}^{-1} (\mathbf{S}^H \mathbf{\Psi}^{-1} \mathbf{S})_{\rho, \rho}} \geq 1 \quad (3.48)$$

where \mathbf{S} is the sensitivity matrix and $\mathbf{\Psi}$ is the noise coupling matrix. If the probe elements have similar sensitivity profiles, there is little information available to unwrap the aliased data, leading to a high g factor and producing noise amplification. The noise in a SENSE reconstructed image is

$$N_{\text{SENSE}, \rho} = \sqrt{R} \cdot g_\rho \cdot N_{\text{full}, \rho} \quad (3.49)$$

where R is the undersampling or reduction factor. The noise in the fully sampled image is given by

$$N_{\text{full}, \rho} = \left(\sqrt{(\mathbf{S}^H \mathbf{\Psi}^{-1} \mathbf{S})_{\rho, \rho}} \right)^{-1} \quad (3.50)$$

Fig. 3.17 shows two possible stripline array probe designs. Assume phase encoding is in the horizontal direction. The first design (fig. 3.17a) is symmetric in the aliased direction, so the upper and lower probe elements provide very similar information about the central region of the sample, producing a high g -factor. The second design (fig. 3.17b) introduces asymmetry in the undersampled direction, increasing the information available to unwrap aliased voxels and reducing the g -factor.

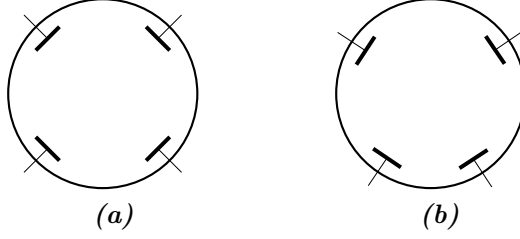


Figure 3.17: The g -factor depends upon probe symmetry. Symmetric probe designs (a) produce high g -factors. Introducing asymmetry in the aliased direction (b) produces a lower g -factor as the information available to unfold aliased data is increased.

The noise coupling matrix Ψ is an $n_e \times n_e$ matrix [88]

$$\Psi = \begin{pmatrix} 1 & \psi_{12} & \cdots & \psi_{1n_e} \\ \psi_{21} & 1 & & \psi_{2n_e} \\ \vdots & & \ddots & \vdots \\ \psi_{n_e1} & \psi_{n_e2} & \cdots & 1 \end{pmatrix} \quad (3.51)$$

where the noise coupling co-efficients ψ_{ij} are defined as

$$\psi_{ij} = \frac{R_{ij}}{\sqrt{R_{ii}R_{jj}}} \quad (3.52)$$

and R_{ij} is the real part of the mutual impedance between elements i and j .

Probes designed for partially parallel acquisition have to meet the dual requirements of strong decoupling between elements while maintaining a low g -factor, requirements that are often in direct opposition. For example, overlapping loop elements reduces coupling but increases the g -factor, as the overlapped elements have almost the same field of view. In such situations it is more important to maintain a low g -factor than reduce inductive coupling [87, 89].

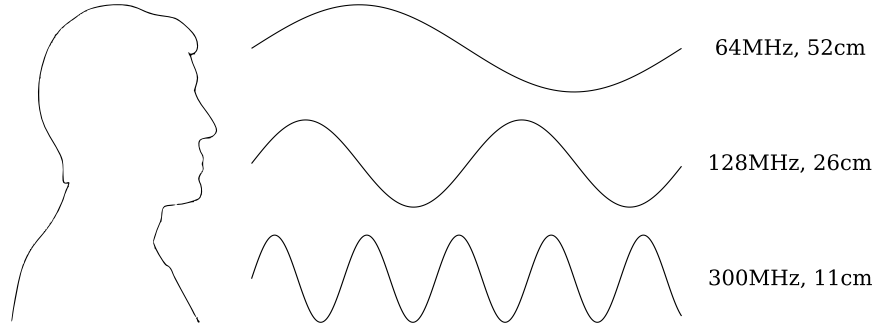


Figure 3.18: The resonant wavelength in tissue at 64, 128 and 300MHz in comparison to the size of the human head.

3.11 High Field Effects

3.11.1 Wavelength

As the static field strength increases, the resonant wavelength decreases. The wavelength inside the sample is further reduced by the high dielectric constant of tissue

$$\lambda_{\text{tissue}} = \frac{1}{\sqrt{\mu_r \epsilon_r}} \lambda_{\text{free space}} \quad (3.53)$$

where μ_r and ϵ_r are the relative permeability and permittivity of tissue. The permeability of soft tissue is approximately the same as that of free space, but the relative permittivity is in the range 60–80 at 300MHz, reducing the wavelength by a factor of approximately 8. Fig. 3.18 shows the resonant wavelength in tissue at 64, 128 and 300MHz in relation to the size of the human head. In this frequency range the transition is being made from the near field quasistatic regime, in which the signal has approximately the same phase throughout the head, to the far field in which the signal phase has to be taken into account.

3.11.2 Material Properties

As frequency increases the permittivity of tissue decreases (fig. 3.19), slightly counteracting the reduction in wavelength inside the sample. However, the effect is small. At the same time tissue conductivity increases, blurring

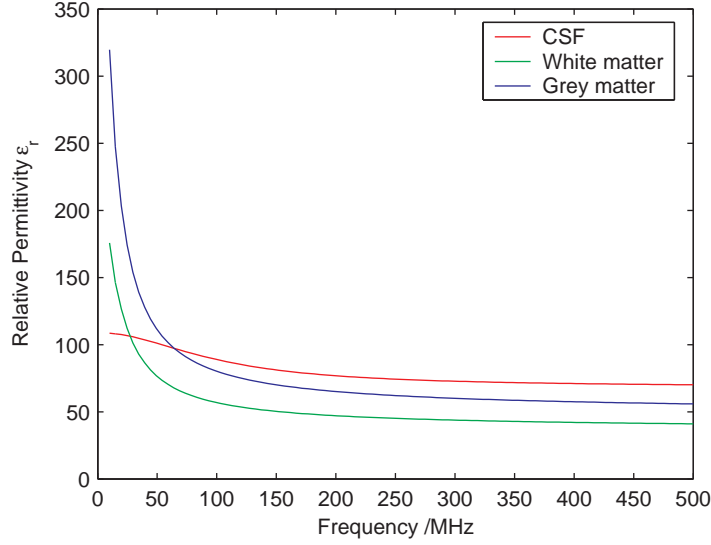


Figure 3.19: The relative permittivity ϵ_r of tissue reduces quickly with increasing frequency in the range 0–150MHz. Above 150MHz the relative permittivity slowly decreases.

any inhomogeneity in the B_1 field. The effect of sample conductivity is investigated in chapter 5. The change in tissue permittivity and conductivity with frequency is most pronounced below 100MHz.

The NMR parameters of the sample also change with static field strength (table 3.1). Longitudinal T_1 relaxation times increase with increasing static field strength, while the transverse T_2 relaxation times reduce. The effect of sample susceptibility on B_0 field homogeneity is also more pronounced at high field, further reducing T_2^* relaxation times. While UHF MRI potentially offers higher SNR, shorter T_2 and T_2^* relaxation times mean less time is available to collect the signal, while longer T_1 recovery times mean that more time is required between excitations for the sample magnetisation to return to equilibrium.

3.11.3 RF Penetration

One of the earliest concerns about increasing the resonant frequency was the reduction in RF penetration depth. Initial predictions suggested a limit

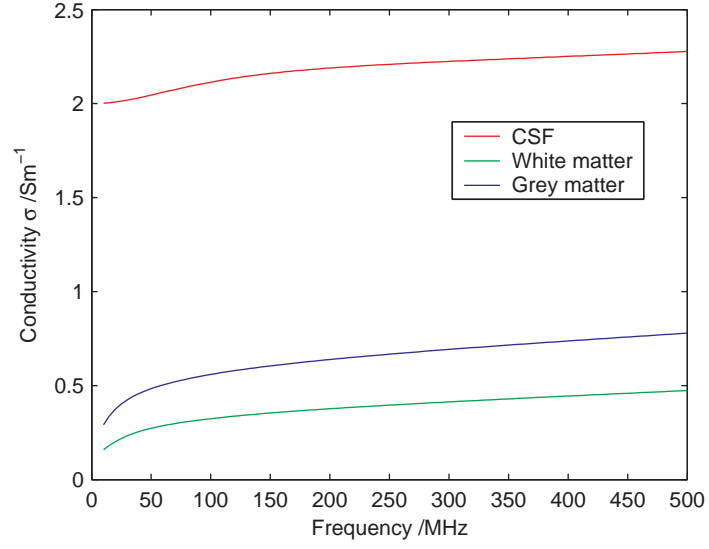


Figure 3.20: Tissue conductivity σ increases with increasing frequency.

Field Strength	Tissue	T_1 /ms	T_2^* /ms
3T	White matter	780	54.6
	Grey matter	1300	59.7
7T	White matter	1000	28.6
	Grey matter	1600	32.7

Table 3.1: Relaxation times for grey and white matter at 3 and 7T [90, 91].

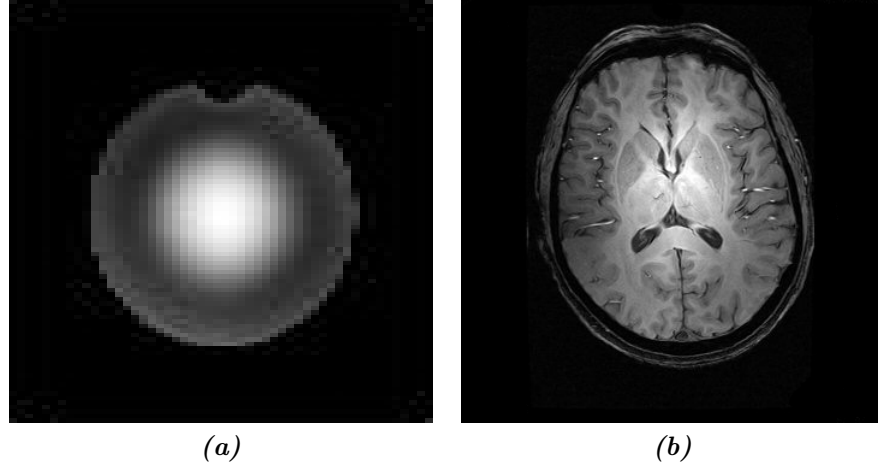


Figure 3.21: Interference patterns in (a) a saline phantom ($\sigma = 0.5\text{S/m}$) and (b) the human head.

in the 10–30MHz range [63, 92, 93]. The skin depth δ , the depth at which the current reduces by a factor of $1/e$, is defined as [94]

$$\delta = \sqrt{\frac{2}{\omega\sigma\mu}} \quad (3.54)$$

At 300MHz, for a tissue conductivity $\sigma = 0.5\text{S/m}$, the skin depth is 100 mm. However, the human body is not uniform but made up of isolated highly conductive regions separated by layers of less conductive connective tissue [56]. This reduces penetration effects, which in practice have not been a limiting factor at high field [95].

3.11.4 Dielectric Resonance and Interference

Central brightening is probably the most well known image artifact at high field. It is particularly strong in spherical phantoms, but is also visible in images of the head (fig. 3.21). Traditionally it has been ascribed to dielectric resonance [96, 97, 98], but it is now believed to be an interference or field focussing effect [50, 99, 100].

Dielectric resonance is caused by electromagnetic waves reflecting from the internal surfaces of the resonator and interfering with the source wave to

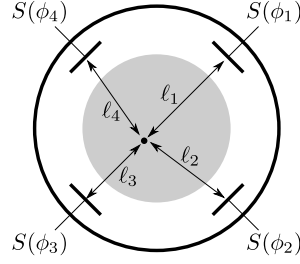


Figure 3.22: Different propagation delays from different probe elements causes interference in the B_1 field.

form a standing wave pattern. A resonator typically has several resonant modes, each at a different frequency with a different characteristic field pattern. The resonant frequency is determined by the geometry of the resonator, its electrical properties, and the electrical properties of its surroundings [50].

There are two major impediments to true dielectric resonance in the human body. The first is the conductivity of tissue, which rapidly damps internal reflected waves. The second is that the head is not a single, homogeneous region, but contains many boundaries between different tissues of widely varying permittivity and conductivity [56].

The real source of B_1 inhomogeneity at short wavelength is constructive and destructive interference. The excitation wavelength is of the same order as the sample size, so a significant phase shift is seen across the sample. At a particular location, the signal from different transmit elements (e.g. legs on a birdcage probe) will arrive with different phase (fig. 3.22). At some locations these signals will sum, leading to a bright spot. At other locations the excitation signals arrive out of phase and cancel out, causing dark regions. Similarly, during reception, the signal from a single location in the sample arrives at different probe elements with different phase. When the signals are summed (as they are implicitly by a volume probe) they again interfere. The symmetry of most probe designs leads to the bullseye pattern commonly observed in high field images.

Several methods for reducing the transmit and receive interference have been presented. During reception, parallel acquisition offers a significant advan-

tage, as the signal detected by each probe element is individually digitised without interference. The images are then combined by the acquisition computer either with phase information removed (magnitude images) or phase corrected, if accurate phase maps are available [100, 101].

During transmission there is no direct equivalent to parallel reception. Multiple probe elements emit an excitation signal into a single sample volume. Interference now occurs in the sample, rather than in the probe.

One approach to improving the transmit field homogeneity is RF shimming [58, 102]. The principle is to adjust the phase and amplitude of the excitation signal applied to each probe element individually. RF shimming does not prevent interference between transmit signals, but simply adjusts the individual transmit fields to minimise the variation in the net transmit field. For each scan session, appropriate attenuations and phase shifts, which depend upon the individual sample geometry, must be determined. Implementing RF shimming requires extra hardware to produce the driving signals, either in the form of independent transmit channels, or as power dividers, phase shifters and attenuators.

Extending the principle further, Transmit SENSE applies completely different excitation signals to each probe element simultaneously [20]. Transmit SENSE is an extension to the concept of designer pulses [18]. In principle, RF pulse envelopes can be designed to produce arbitrary excitation profiles. In practice, very complex excitation profiles require unrealistically long RF pulses, such that NMR relaxation times can no longer be ignored. Transmit SENSE uses multiple transmit channels to add extra degrees of freedom to pulse envelope design, allowing much shorter excitation pulses. Transmit SENSE offers the possibility of generating excitation profiles to counteract the effects of interference, producing a more uniform excitation. Note that the intention of Transmit SENSE is not to produce a uniform transmit field, but to produce a uniform sample nutation by the end of the excitation pulse.

Implementing transmit SENSE requires an large investment in extra hardware, as a complete transmit chain, including the power amplifier, must be provided for each probe element. However, transmit SENSE capable sys-

tems have been demonstrated at 3T [47, 48], and will certainly be built at higher field strength.

3.11.5 Coupling

As discussed in section 3.10.4, two circuits placed in close proximity magnetically couple. Faraday’s law gives the EMF ξ_1 induced in one circuit by current I_2 flowing in the other [94]:

$$\xi_1 = M_{12} \frac{dI_2}{dt} = i\omega M_{12} I_2, \quad (3.55)$$

where M_{12} is the mutual inductance between the circuits. The influence of one circuit on the other increases linearly with frequency. That is, the effect of coupling between probe elements, and between probe elements and the sample, increases linearly with the operating frequency. Coupling between elements in array probes becomes a more significant problem as the operating frequency increases.

It is important that a probe couples strongly to the sample, both for a transmit probe to induce a magnetic field inside the sample and for a receive probe to be sensitive to the NMR signal generated by the sample. However, increased probe-sample coupling also has some negative effects. As the sample couples more tightly to the probe, it has more effect upon the B_1 field generated by the probe, increasing the resonance shift seen as the probe is loaded and reducing B_1 field homogeneity [102].

3.11.6 Heating

Sample heating is a concern for probe design at any frequency, but at ultra high frequency the problem becomes more acute. There are three concerns as the static field strength is increased. Firstly, SAR increases as B_0^2 [92], so increasing the B_0 field strength from 3T to 7T increases the SAR by a factor of 5.4. Secondly, at short wavelength the inhomogeneous B_1 field generated by the RF probe leads to ‘hot spots’ in the SAR distribution, concentrating

the heating effect over a smaller volume. Finally, below 3T the highest SAR occurs at the sample surface where cooling is most efficient. In higher field systems the 'hot spots' tend to occur in the centre of the sample, where the natural cooling mechanisms of the human head function least well [99].

Chapter 4

Electromagnetic Modelling Theory

4.1 Introduction

Until recently, RF probes were designed using a combination of lumped element circuit analysis and quasistatic modelling [52, 103]. This works reliably at low field, where the wavelength at the operating frequency is much larger than the sample dimensions, but breaks down at shorter wavelength. The recent drive to build high field MR systems ($>3\text{T}$), combined with the increased availability of high power computing resources, has led to a growing interest in full wave electromagnetic modelling of RF probes. Full wave modelling allows the probe and sample to be investigated as a single system, which is important at higher frequency as sample-probe coupling becomes stronger.

Computation Electromagnetic Modelling (CEM) first started in the late 1960's with Yee's Finite Difference Time Domain (FDTD) algorithm [104] and Harrington's Method of Moments (MoM) [105]. The Finite Element Method (FEM) was initially used for structural analysis [106], but applied to electromagnetic problems in 1971 [107]. Johns introduced the Transmission Line Modelling (TLM) method in 1974 [108]. At this time comput-

ing resources were extremely limited so only the very simplest simulations could be attempted. By the mid 1980's computing power had reached the stage where more realistic models could be used, opening up the possibility of simulating electromagnetic interactions with the human body, such as exposure to radio waves (10kHz-10MHz) [109], modelling hyperthermia treatment (1GHz) [110], body currents induced by power lines (60Hz) [111] and SAR due to mobile phones (0.8-1.9GHz) [112, 113].

This chapter starts by reviewing the three electromagnetic modelling techniques most commonly used to simulate RF probes. The Transmission Line Modelling (TLM) method, used in this work, is then described in detail. Finally, human and probe simulation models are discussed.

4.2 Finite Element Method (FEM)

Several early projects applying CEM to RF probe design used the Finite Element Method (FEM) [114, 115, 116]. The Finite Element Method is based on the optimisation of a function with respect to a given variable. In electromagnetic modelling, the function is usually chosen to be the Lagrangian, and the corresponding variable can be the electric field \mathbf{E} , the scalar potential ϕ , or the vector potential \mathbf{A} [114]. The model space is discretised using a non-uniform tetrahedral mesh. The scalar and vector potential across each element are then approximated using an interpolation or 'shape' function, producing a set of linear equations, which are solved using any of a range of standard numerical methods [117].

FEM is the most computationally intensive of all the methods considered here, measured per cell. However, the tetrahedral mesh can be modified to match the model geometry, allowing uniform regions to be modelled with fewer large cells, while using small tetrahedra to model finer detail. This often reduces the total number of cells required to cover a model, when compared to FDTD.

4.3 Finite Difference Time Domain (FDTD)

Probably the most widely used full wave technique in MRI is Finite Difference Time Domain (FDTD) [118, 119, 120, 121, 122]. The method, first introduced by Yee in 1966 [104], is based on Maxwell's curl equations

$$\nabla \times \mathbf{E} = -\mu_0 \frac{\partial \mathbf{H}}{\partial t} \quad (4.1)$$

$$\nabla \times \mathbf{H} = \varepsilon \frac{\partial \mathbf{E}}{\partial t} + \sigma \mathbf{E} + \mathbf{J} \quad (4.2)$$

The problem space is first discretised into a regular mesh of 'Yee cells' (fig. 4.1). The electric field can then be calculated using the surrounding magnetic field components [94]

$$\begin{aligned} E_x^{n+1}(i + \tfrac{1}{2}, j, k) &= E_x^n(i + \tfrac{1}{2}, j, k) \\ &+ \frac{\Delta t}{\varepsilon} \left\{ \left[H_z^{n+\frac{1}{2}}(i + \tfrac{1}{2}, j + \tfrac{1}{2}, k) - H_z^{n+\frac{1}{2}}(i + \tfrac{1}{2}, j - \tfrac{1}{2}, k) \right] / \Delta y \right. \\ &\quad \left. + \left[H_y^{n+\frac{1}{2}}(i + \tfrac{1}{2}, j, k - \tfrac{1}{2}) - H_y^{n+\frac{1}{2}}(i + \tfrac{1}{2}, j, k + \tfrac{1}{2}) \right] / \Delta z \right\} \end{aligned} \quad (4.3)$$

and the magnetic field can be calculated from the surrounding electric field components

$$\begin{aligned} H_x^{n+\frac{1}{2}}(i, j + \tfrac{1}{2}, k + \tfrac{1}{2}) &= H_x^{n-\frac{1}{2}}(i, j + \tfrac{1}{2}, k + \tfrac{1}{2}) \\ &+ \frac{\Delta t}{\mu} \left\{ [E_y^n(i, j + \tfrac{1}{2}, k + 1) - E_y^n(i, j + \tfrac{1}{2}, k)] / \Delta z \right. \\ &\quad \left. + [E_z^n(i, j, k + \tfrac{1}{2}) - E_z^n(i, j + 1, k + \tfrac{1}{2})] / \Delta y \right\} \end{aligned} \quad (4.4)$$

with similar expressions for y - and z -field components. By applying suitable initial and boundary conditions, eqns. 4.3 and 4.4 can be alternately applied to simulate the propagation of an electromagnetic wave through the model. To maintain stability the time increment Δt must be kept smaller than the time taken for a wave to propagate from one node to the next [123].

The FDTD method is easy to implement [124] and able to model arbitrarily complex objects (to the precision of the chosen mesh). However, the regular

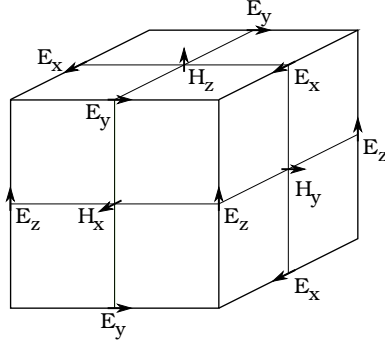


Figure 4.1: A Yee cell, illustrating the offset between electric and magnetic field modelled by FDTD.

mesh does not always fit well around a model, especially if the model contains fine features or discrete elements such as capacitors. Diagonal features such as thin angled plates can also be problematic, as these have to be fitted with a stair-step approximation. To improve model accuracy for either of these features a finer mesh has to be used, increasing the memory requirement and run time.

4.4 Method of Moments (MoM)

The Method of Moments (MoM), first introduced by Harrington in 1967 [105], is an integral method that calculates electromagnetic fields based on current flowing in a model. The electric field produced by a current can be written as

$$\mathbf{E}(\mathbf{r}) = -i\omega\mathbf{A}(\mathbf{r}) - \nabla\Phi(\mathbf{r}) \quad (4.5)$$

where

$$\mathbf{A}(\mathbf{r}) = \mu_0 \int_C \mathbf{I}(\mathbf{r}') G(\mathbf{r}, \mathbf{r}') d\mathbf{l}' \quad (4.6)$$

and

$$\Phi(\mathbf{r}) = \frac{i}{\omega\epsilon_0} \int_C \frac{dI(\mathbf{r}')}{d\mathbf{l}'} G(\mathbf{r}, \mathbf{r}') d\mathbf{l}' \quad (4.7)$$

where C denotes the current path and $G(\mathbf{r}, \mathbf{r}')$ is the free space Green's function [125]. The effects of permittivity and conductivity can be modelled by the addition of a 'volume equivalent current' that generates an extra electric field component [40]. The current path is then discretised into a number of

small segments and the current expanded as a set of basis functions. The solution to the discretised equations can then be written in terms of a matrix equation, the solution of which is found by inverting the matrix. As the matrix is usually large, the only practical way to perform the inversion is to use an iterative method, such as BCG-FFT [126].

As an integral method, MoM is well suited to modelling the fields generated by complex probe structures, using relatively few calculations. It is less well suited to modelling large, highly heterogeneous dielectric samples such as the human head. In view of this, a hybrid technique has been employed in which MoM is used to calculate the surface currents on the probe, and then using FDTD to calculate electromagnetic fields inside a model of the head [122, 127, 128].

4.5 The Transmission Line Matrix Method (TLM)

An alternative modelling method is the Transmission Line Matrix (TLM) method introduced by Johns in 1974 [108]. TLM describes the modelled space using a regular grid of nodes connected by transmission line sections called link-lines. The propagation of electromagnetic waves through the system is described by the scattering and reflection of electrical impulses travelling through the transmission lines. The capacitance and inductance of link-lines affect how electric pulses travel through the mesh, mirroring the way permittivity and permeability of a medium affect electromagnetic wave propagation. Thus, voltage and current in the TLM mesh are used to represent electric and magnetic fields in space.

While their paradigms are quite different, TLM and FDTD are numerically very similar, and largely have the same benefits and disadvantages in terms of modelling capability and computational requirements. However, TLM has some advantage over FDTD. Firstly, electric and magnetic fields are calculated on exactly the same mesh, without the half voxel offset characteristic of FDTD. TLM is also unconditionally stable, the timestep being determined by the mesh resolution. But the main advantage of TLM is that it uses a conceptual framework that will already be familiar to any elec-

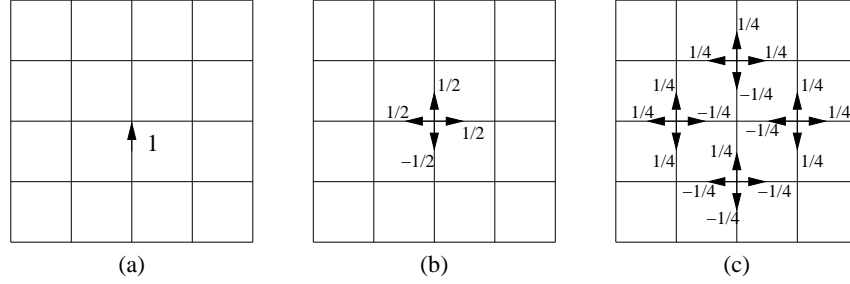


Figure 4.2: Scattering of an impulse on the TLM mesh

tronic engineer [129]. The TLM method was used for all electromagnetic simulation presented in this thesis, using a mesh of Symmetric Condensed Nodes (SCNs) [130].

TLM is a discrete time-domain model. At each timestep n , voltage pulses incident upon a node ${}_n\mathbf{V}^i$ from its link lines are considered. Taking account of the impedance of all link-lines meeting at a node, scattering of the incident impulses can be calculated and the reflected voltages ${}_n\mathbf{V}^r$ can be computed (fig. 4.2). The reflected voltage pulses travel back out through the link-lines, to become incident on adjacent nodes at the next timestep. This basic cycle of scatter and connect is used to propagate waves through the mesh. It can be written as

$${}_n\mathbf{V}^r = \mathbf{S} {}_n\mathbf{V}^i \quad (4.8)$$

$${}_{n+1}\mathbf{V}^i = \mathbf{C} {}_n\mathbf{V}^r \quad (4.9)$$

where \mathbf{S} is the scattering and \mathbf{C} the connection matrix.

A twelve port node, the basic unit of the SCN mesh, is shown in fig. 4.3. Voltage pulses can enter a node from any of six directions. Along each axis there are two possible wave polarisations, represented as a pair of non-coupling transmission lines, giving a total of twelve transmission lines meeting at a node. The scattering matrix is derived in the next section. The connect stage consists simply of transferring the voltage pulses reflected from a node to incident pulses entering the surrounding nodes. The scatter-connect cycle is then repeated until the system reaches a stable state.

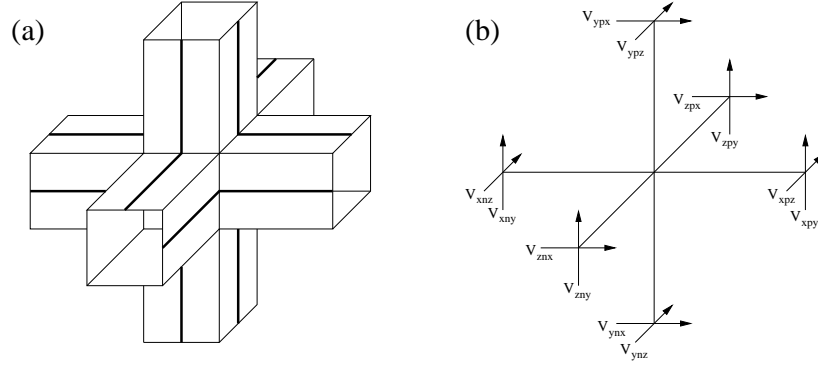


Figure 4.3: (a) 12-port symmetric condensed node and (b) notation used to identify voltage impulses

4.5.1 The Scattering Matrix

The scattering matrix for the SCN is now derived from first principles, following the method used by Herring [131]. The port labelling scheme (fig. 4.3(b)) also follows that of Herring. The first subscript gives the port axis, the second indicates the negative or positive side of the node and the third subscript gives the polarisation of the voltage pulse. Thus V_{xnz} would be a z -polarised pulse on the negative x branch of the node.

Four conditions are applied to derive the scattering matrix:

- conservation of electric charge
- conservation of magnetic flux
- continuity of electric field
- continuity of magnetic field

For charge conservation, charge leaving the node must equal charge entering it

$$\frac{1}{2}C (V_{ynx}^i + V_{ypx}^i + V_{znx}^i + V_{zpx}^i) = \frac{1}{2}C (V_{ynx}^r + V_{ypx}^r + V_{znx}^r + V_{zpx}^r) \quad (4.10)$$

where $\frac{1}{2}C$ is the capacitance of the half link-lines. Writing similar equations for the other axes, we obtain

$$V_{ynx}^i + V_{ypx}^i + V_{znx}^i + V_{zpx}^i = V_{ynx}^r + V_{ypx}^r + V_{znx}^r + V_{zpx}^r \quad (4.11a)$$

$$V_{zny}^i + V_{zpy}^i + V_{xny}^i + V_{xpy}^i = V_{zny}^r + V_{zpy}^r + V_{xny}^r + V_{xpy}^r \quad (4.11b)$$

$$V_{xnz}^i + V_{xpz}^i + V_{ynz}^i + V_{ypz}^i = V_{xnz}^r + V_{xpz}^r + V_{ynz}^r + V_{ypz}^r \quad (4.11c)$$

Similarly, for conservation of magnetic flux we can write

$$\frac{1}{2}L (I_{ynz}^i + I_{zpy}^i - I_{ypz}^i - I_{zny}^i) = \frac{1}{2}L (I_{ynz}^r + I_{zpy}^r - I_{ypz}^r - I_{zny}^r) \quad (4.12)$$

where $\frac{1}{2}L$ is the inductance of the half link-lines. Using Ohm's law the current is calculated as $I^i = V^i/Z_0$ and $I^r = -V^r/Z_0$. Writing similar equations for the other components we obtain

$$V_{ynz}^i + V_{zpy}^i - V_{ypz}^i - V_{zny}^i = -(V_{ynz}^r + V_{zpy}^r - V_{ypz}^r - V_{zny}^r) \quad (4.13a)$$

$$V_{znx}^i + V_{xpz}^i - V_{zpx}^i - V_{xnz}^i = -(V_{znx}^r + V_{xpz}^r - V_{zpx}^r - V_{xnz}^r) \quad (4.13b)$$

$$V_{xny}^i + V_{ypx}^i - V_{xpy}^i - V_{ynx}^i = -(V_{xny}^r + V_{ypx}^r - V_{xpy}^r - V_{ynx}^r) \quad (4.13c)$$

For continuity of the electric field, the field due to link-lines parallel to the y -axis must equal the field due to link lines parallel to the z -axis

$$V_{ynx} + V_{ypx} = V_{znx} + V_{zpx} \quad (4.14)$$

The total voltage on each port is the sum of the incident and reflected pulse $V = V^i + V^r$. The full equations along all three axes are then

$$(V_{ynx}^i + V_{ypx}^i) - (V_{znx}^i + V_{zpx}^i) = (V_{ynx}^r + V_{ypx}^r) - (V_{znx}^r + V_{zpx}^r) \quad (4.15a)$$

$$(V_{zny}^i + V_{zpy}^i) - (V_{xny}^i + V_{xpy}^i) = (V_{zny}^r + V_{zpy}^r) - (V_{xny}^r + V_{xpy}^r) \quad (4.15b)$$

$$(V_{xnz}^i + V_{xpz}^i) - (V_{ynz}^i + V_{ypz}^i) = (V_{xnz}^r + V_{xpz}^r) - (V_{ynz}^r + V_{ypz}^r) \quad (4.15c)$$

Applying the same continuity argument for the magnetic field we can write

$$I_{ynz} - I_{ypz} = I_{zpy} - I_{zny} \quad (4.16)$$

The total current on a port is given by $I = (V^i - V^r)/Z_0$. The full equations for all three axes are then

$$(V_{ynz}^i - V_{ypz}^i) - (V_{zpy}^i - V_{zny}^i) = (V_{ynz}^r - V_{ypz}^r) - (V_{zpy}^r - V_{zny}^r) \quad (4.17a)$$

$$(V_{znx}^i - V_{zpx}^i) - (V_{xpz}^i - V_{xnz}^i) = (V_{znx}^r - V_{zpx}^r) - (V_{xpz}^r - V_{xnz}^r) \quad (4.17b)$$

$$(V_{xny}^i - V_{xpy}^i) - (V_{ypx}^i - V_{ynx}^i) = (V_{xny}^r - V_{xpy}^r) - (V_{ypx}^r - V_{ynx}^r) \quad (4.17c)$$

Equations 4.11, 4.13, 4.15 and 4.17 form a set of linear equations that can be solved to give the scattering matrix. Matrix notation provides a compact description of the TLM process. However, the scattering matrix is sparse making it is more efficient to evaluate each reflected pulse directly. For efficiency and clarity, the method of Naylor and Ait-Sadi has been used [132]

$$\begin{aligned} V_{ynx}^r &= V_x - Z_0 I_z - V_{ypx}^i \\ V_{ypx}^r &= V_x + Z_0 I_z - V_{ynx}^i \\ V_{znx}^r &= V_x + Z_0 I_y - V_{zpx}^i \\ V_{zpx}^r &= V_x - Z_0 I_y - V_{znx}^i \\ V_{zny}^r &= V_y - Z_0 I_x - V_{zpy}^i \\ V_{zpy}^r &= V_y + Z_0 I_x - V_{zny}^i \\ V_{xny}^r &= V_y + Z_0 I_z - V_{xpy}^i \\ V_{xpy}^r &= V_y - Z_0 I_z - V_{xny}^i \\ V_{xnz}^r &= V_z - Z_0 I_y - V_{xpz}^i \\ V_{xpz}^r &= V_z + Z_0 I_y - V_{xnz}^i \\ V_{ynz}^r &= V_z + Z_0 I_x - V_{ypz}^i \\ V_{ypz}^r &= V_z - Z_0 I_x - V_{ynz}^i \end{aligned} \quad (4.18)$$

where V_k are the node voltages

$$V_x = \frac{1}{2} (V_{ypx}^i + V_{zpx}^i + V_{ynx}^i + V_{znx}^i) \quad (4.19a)$$

$$V_y = \frac{1}{2} (V_{zpy}^i + V_{xpy}^i + V_{zny}^i + V_{xny}^i) \quad (4.19b)$$

$$V_z = \frac{1}{2} (V_{xpz}^i + V_{ypz}^i + V_{xnz}^i + V_{ynz}^i) \quad (4.19c)$$

and I_k are the loop currents

$$I_x = \frac{1}{2Z_0} (V_{ypz}^i - V_{zpy}^i - V_{ynz}^i + V_{zny}^i) \quad (4.20a)$$

$$I_y = \frac{1}{2Z_0} (V_{zpx}^i - V_{xpz}^i - V_{znx}^i + V_{xnz}^i) \quad (4.20b)$$

$$I_z = \frac{1}{2Z_0} (V_{xpy}^i - V_{ypx}^i - V_{xny}^i + V_{ynx}^i) \quad (4.20c)$$

4.5.2 Heterogeneous Modelling and Stubs

The TLM mesh described so far can only model homogeneous media. Initially, extending the model to include heterogeneous media appears to be as simple as changing the capacitance and inductance of the link lines to account for local changes in permittivity ε or permeability μ . However, these changes will alter the wave propagation velocity u

$$u = \frac{1}{\sqrt{\varepsilon\mu}} \quad (4.21)$$

which will desynchronise the scatter-connect cycle, as voltage pulses will now arrive at a node at different times according to the local media.

A different approach is to model changes in permittivity or permeability by adding extra capacitance or inductance to a node in the form of stubs (short lengths of transmission line [94]). Capacitance is added by including an open-circuit stub (fig. 4.4a). Any signal entering the stub will, on reaching the open-circuit termination, be reflected back into the node. By setting the stub length to $\Delta\ell/2$, the round-trip time for a pulse to enter the stub and arrive back at the node is set to one timestep Δt . When a pulse enters a node, it will now be scattered into the link-lines and into the stub. On the next iteration the pulse from the stub will re-enter the node, thus adding a time delay to the node and reducing the wave velocity, without reducing the mesh velocity.

Similarly, inductance can be added to a node by including a short-circuit stub (fig. 4.4b), which will invert the reflected pulse. The stub length is again chosen such that the reflected pulse arrive back in the node exactly one iteration after entering it.

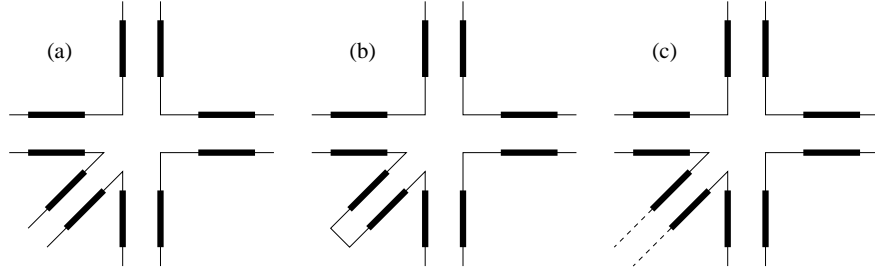


Figure 4.4: A 2D node showing (a) capacitive, (b) inductive and (c) lossy stubs

Finally, real materials dissipate some energy through Ohmic losses. This can be modelled by adding an infinitely long resistive transmission line to the node. As the transmission line is infinitely long, pulses entering it will never be reflected back into the mesh, and energy is absorbed out of the system.

The only drawback in introducing stubs is the increased size of the scattering matrix. As all three axes operate independently in the mesh, three of each type of stub have to be added to every node for full modelling, increasing the scattering matrix from 12×12 to 21×21 elements, increasing the storage and number of calculations required per scatter cycle. As the permeability of tissue varies very little from that of water [133], only dielectric and lossy stubs are modelled in this work giving an 18×18 scattering matrix.

4.5.3 Mesh Parameters

Having discussed the principles behind TLM modelling, it is now shown how to calculate the mesh parameters. Parameters are derived using an isotropic mesh ($\Delta x = \Delta y = \Delta z = \Delta \ell$). This is not a requirement of TLM, but simplifies the following derivation. The impedance and velocity of the underlying mesh are first discussed. Calculation of stub parameters is then demonstrated and the required modifications to the scattering matrix are shown.

The characteristic impedance of the transmission lines is

$$Z_{tl} = \sqrt{\frac{L_d}{C_d}} = \sqrt{\frac{L}{C}} \quad (4.22)$$

where L_d and C_d are the inductance and capacitance per unit length and L and C are the total link-line inductance and capacitance.

The velocity of a pulse travelling along the transmission line is

$$u_{tl} = \frac{\Delta \ell}{\Delta t} \quad (4.23)$$

where Δt is the time taken for a voltage pulse to travel from the one node to the next, which is the fundamental timestep of the TLM simulation. The propagation velocity can also be calculated using the electrical properties of the transmission line

$$u_{tl} = \frac{1}{\sqrt{L_d C_d}} = \frac{\Delta \ell}{\sqrt{LC}} \quad (4.24)$$

Combining eqn.s 4.23 and 4.24 the timestep is

$$\Delta t = \sqrt{LC} \quad (4.25)$$

The link-line capacitance and inductance can then be written

$$C = Y_{tl} \Delta t \quad (4.26)$$

$$L = Z_{tl} \Delta t \quad (4.27)$$

where Y_{tl} is the transmission line admittance (reciprocal of impedance) and the subscript tl indicates a parameter of the underlying transmission line rather than the modelled medium.

The x -directed node capacitance is defined as

$$C_x = \varepsilon \frac{\Delta y \Delta z}{\Delta x} = \varepsilon \Delta \ell \quad (4.28)$$

The link-lines V_{ynx} , V_{ypx} , V_{znx} and V_{zpx} contribute to the x -directed capacitance, each of length $\frac{1}{2}\Delta \ell$. Using eqn. 4.26, the capacitance can then be

written in terms of the link-line admittance

$$C_x = 4 \left(\frac{1}{2} Y_{tl} \right) \Delta t = 2 Y_{tl} \Delta t \quad (4.29)$$

Similarly, link-lines V_{ypz} , V_{zpy} , V_{ynx} and V_{zny} contribute to the x -directed inductance

$$L_x = \mu \frac{\Delta y \Delta z}{\Delta x} = \mu \Delta \ell \quad (4.30)$$

which can be written in terms of link-line impedance using eqn. 4.27

$$L_x = 4 \left(\frac{1}{2} Z_{tl} \right) \Delta t = 2 Z_{tl} \Delta t \quad (4.31)$$

The addition of stubs can only decrease the wave propagation speed, so the underlying transmission line properties are determined by the fastest wave velocity to be modelled. In most cases this is free space, requiring the mesh to model permittivity ε_0 and permeability μ_0 .

The velocity of a wave travelling through the modelled medium can be defined as

$$c_0 = \frac{1}{\sqrt{\varepsilon_0 \mu_0}} \quad (4.32)$$

Using eqn.s 4.28 and 4.30 we can substitute the node capacitance and inductance for ε_0 and μ_0

$$c_0 = \frac{\Delta \ell}{\sqrt{C_x L_x}} \quad (4.33)$$

If we then substitute eqn.s 4.26 and 4.27 the wave velocity can be written in terms of the simulation timestep and node size

$$c_0 = \frac{\Delta \ell}{\sqrt{2 Y_0 \Delta t \cdot 2 Z_0 \Delta t}} = \frac{\Delta \ell}{2 \Delta t} \quad (4.34)$$

This is a slightly surprising result. The wave propagation velocity c_0 is half the velocity of a voltage pulse travelling on the underlying transmission line u_{tl} , defined in eqn. 4.23. The practical effect of this result is that the simulator timestep should be set to

$$\Delta t = \frac{\Delta \ell}{2 c_0} \quad (4.35)$$

In the case of a non-isotropic mesh $\Delta \ell$ is the smallest of Δx , Δy and Δz .

The impedance of the underlying transmission lines can be calculated using modelled medium properties by substituting eqn.s 4.26 and 4.27 into eqn. 4.22.

$$Z_{tl} = \sqrt{\frac{\mu_0 \Delta \ell}{\varepsilon_0 \Delta \ell}} = Z_0 \quad (4.36)$$

Therefore the underlying transmission lines have the same impedance as the modelled medium.

The use of stubs to model heterogeneous media is now considered. The base permittivity of the mesh is modelled by link-lines as described above. Any increase in permittivity is modelled by a stub of capacitance

$$C_x^s = \varepsilon \Delta \ell - 4C \quad (4.37)$$

where $4C$ is the capacitance already modelled by the link-lines. Using eqn. 4.26 and the relation $\varepsilon_0 = Y_0/c_0$ this can be rewritten as

$$C_x^s = Y_0 \left(\frac{\varepsilon_r}{c_0} \Delta \ell - 2\Delta t \right) \quad (4.38)$$

To maintain mesh synchronism, a pulse entering the stub should reflect back at time $\Delta t/2$ to re-enter the node at the next time step. The required stub admittance (normalised to the mesh admittance) is then

$$\hat{Y}_x^s = \frac{2C_x^s}{Y_0 \Delta t} = 2 \left(\frac{\varepsilon_r}{c_0} \frac{\Delta \ell}{\Delta t} - 2 \right) \quad (4.39)$$

which can be simplified using eqn. 4.35 to

$$\hat{Y}_x^s = 4(\varepsilon_r - 1) \quad (4.40)$$

To guarantee mesh stability a stub must represent a positive capacitance, requiring that $\varepsilon_r \geq 1$ as expected.

Calculations involving the resistive stubs are much simpler. The transmission line conductances are calculated as

$$\hat{G}_x = \frac{\sigma_x \Delta \ell}{Y_0} \quad (4.41a)$$

$$\hat{G}_y = \frac{\sigma_y \Delta \ell}{Y_0} \quad (4.41b)$$

$$\hat{G}_z = \frac{\sigma_z \Delta \ell}{Y_0} \quad (4.41c)$$

where σ is the node conductivity and the values are again normalised to the mesh admittance.

The scattering procedure is modified to take account of the lossy and dielectric stubs. Firstly, three extra equations are added to eqn. 4.18 to account for voltage pulses scattered into the open circuit stubs

$$V_{esx}^r = V_x - V_{esx}^i \quad (4.42a)$$

$$V_{esy}^r = V_y - V_{esy}^i \quad (4.42b)$$

$$V_{esz}^r = V_z - V_{esz}^i \quad (4.42c)$$

Voltage pulses scattered into the resistive stubs are not explicitly calculated as the pulses never re-enter the mesh. They are accounted for in the modified calculation of the nodal electric fields, along with the dielectric stubs. Eqns. 4.19 are replaced by

$$V_x = \frac{2}{4 + \hat{Y}_x^s + \hat{G}_x^s} \left(V_{ypx}^i + V_{zpx}^i + V_{ynx}^i + V_{znx}^i + \hat{Y}_x^s V_{esx}^i \right) \quad (4.43a)$$

$$V_y = \frac{2}{4 + \hat{Y}_y^s + \hat{G}_y^s} \left(V_{zpy}^i + V_{xpy}^i + V_{zny}^i + V_{xny}^i + \hat{Y}_y^s V_{esy}^i \right) \quad (4.43b)$$

$$V_z = \frac{2}{4 + \hat{Y}_z^s + \hat{G}_z^s} \left(V_{xpz}^i + V_{ypz}^i + V_{xnz}^i + V_{ynz}^i + \hat{Y}_z^s V_{esz}^i \right) \quad (4.43c)$$

where \hat{Y}^s and \hat{G}^s are the normalised admittance and conductivity of the dielectric and lossy stubs. Scattered pulses are then calculated as before using eqn. 4.18.

4.5.4 Voxel Size, Timestep and Stability

Voxel size (the spacing between nodes) is determined by the highest frequency of interest, simulation speed, and the required field resolution. The frequency mesh size limit in TLM is recommended as [134]

$$\Delta\ell \leq \frac{\lambda}{10} \quad (4.44)$$

This limits dispersion errors due to mesh discretisation to less than 1% giving an upper cell size limit of $\Delta\ell \leq 100\text{mm}$ at 300MHz. In order to see the ‘shape’ of fields generated inside the human head we clearly require a resolution higher than 100mm, so mesh dispersion is not a limiting factor in this case.

The simulation timestep Δt is determined by transmission line velocity u and the node spacing $\Delta\ell$

$$\Delta t = \frac{\Delta\ell}{2u} \quad (4.45)$$

As the mesh resolution is increased the timestep Δt decreases, so that more iterations are required to simulate the same period of time. The voxel size used in this work in $3 \times 3 \times 3 \text{ mm}^3$, chosen as compromise between simulation run time and spatial resolution.

The transmission line velocity is chosen as the fastest wave velocity to be represented in the model, usually c_0 for models containing free space, giving a transmission line impedance of 377Ω . All stubs in the mesh then increase permittivity or permeability. This is important as it means the stubs represent passive components with real values, making the network unconditionally stable [134].

4.5.5 Extracting the Fields

The TLM simulation process produces information about the incident and scattered voltage pulses in the mesh. Determining the magnetic and electric fields in the model requires a further calculation. Both fields can be calcu-

lated either at nodes or on link lines [131]. In this implementation, all fields are calculated at nodes.

4.5.5.1 Rotating B_1 Field

The magnetic field is proportional to the current circulating around the node (fig. 4.5a). The three components of the magnetic field are given by

$$B_x = \frac{\mu_0 I_x}{\Delta x} = \frac{\mu_0}{2Z_0 \Delta x} (V_{ypz}^i - V_{zpy}^i - V_{ynz}^i + V_{zny}^i) \quad (4.46a)$$

$$B_y = \frac{\mu_0 I_y}{\Delta y} = \frac{\mu_0}{2Z_0 \Delta y} (V_{zpx}^i - V_{xpz}^i - V_{znx}^i + V_{xnz}^i) \quad (4.46b)$$

$$B_z = \frac{\mu_0 I_z}{\Delta z} = \frac{\mu_0}{2Z_0 \Delta z} (V_{xpy}^i - V_{ypx}^i - V_{xny}^i + V_{ynx}^i) \quad (4.46c)$$

The magnetic field calculated above is the instantaneous value. For RF probe design we require the rotating components of the transverse magnetisation. The transverse field may be written in complex form as

$$B(t) = B_x(t) + iB_y(t) \quad (4.47)$$

The rotating field components can be calculated by comparing the magnetic field at two points in time t and $t + \tau_{\pi/2}$, where $\tau_{\pi/2}$ is the duration of a quarter cycle. If B_1 is rotating at frequency ω , multiplying $B_1(t + \tau_{\pi/2})$ by $-i$ will rotate it back into phase with $B_1(t)$, and the two field components sum[49]. If B_1 is rotating at $-\omega$, multiplying $B_1(t + \tau_{\pi/2})$ by $-i$ will rotate it into antiphase with $B_1(t)$, and the two fields cancel out. Therefore

$$B_1^+ = \frac{1}{2} [B(t) - iB(t + \tau_{\pi/2})] \quad (4.48)$$

Similarly, the counter-rotating field can be calculated as

$$B_1^- = \frac{1}{2} [B(t) + iB(t + \tau_{\pi/2})] \quad (4.49)$$

The B_z field component is small compared to gradient fields applied during imaging, and may be ignored.

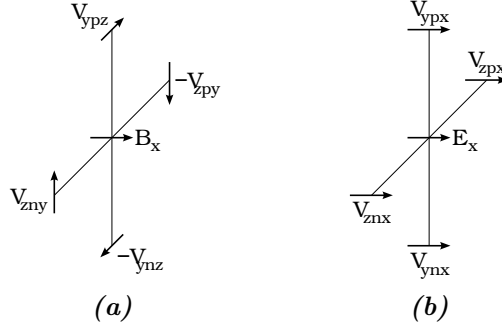


Figure 4.5: Calculating the (a) magnetic and (b) electric field at a node, from the incident voltage pulses.

4.5.5.2 Electric Field and SAR

The electric field is proportional to the voltage across the node (fig. 4.5b), calculated as

$$E_x = -\frac{V_x}{\Delta x} = -\frac{V_{ynx}^i + V_{ypx}^i + V_{znx}^i + V_{zpx}^i}{2\Delta x} \quad (4.50a)$$

$$E_y = -\frac{V_y}{\Delta y} = -\frac{V_{zny}^i + V_{zpy}^i + V_{xny}^i + V_{xpy}^i}{2\Delta y} \quad (4.50b)$$

$$E_z = -\frac{V_z}{\Delta z} = -\frac{V_{xnz}^i + V_{xpz}^i + V_{ynz}^i + V_{ypz}^i}{2\Delta z} \quad (4.50c)$$

If the local tissue density and conductivity are also known, the SAR at each voxel can be calculated using

$$SAR = \frac{\sigma (E_x^2 + E_y^2 + E_z^2)}{\rho} \quad (4.51)$$

Note that although NMR is only affected by the transverse component of the rotating magnetic field, all three electric field components contribute to SAR.

4.5.6 Excitation

To produce a field, the simulated model must first be excited. This can be done by applying an ideal voltage or current source across a node. A voltage

source is applied as an electric field across a node, while a current source is applied as a magnetic field. A voltage or current source has a position, amplitude, frequency, phase and direction.

For a voltage source, the field applied across a node is calculated by reversing eqn. 4.50 to give

$$V_{ynx} = V_{ypx} = V_{znx} = V_{zpx} = -\frac{1}{2}E_x \cos(2\pi fn\Delta t + \phi)\Delta x \quad (4.52a)$$

$$V_{zpy} = V_{zny} = V_{xpy} = V_{xny} = -\frac{1}{2}E_y \cos(2\pi fn\Delta t + \phi)\Delta y \quad (4.52b)$$

$$V_{xpz} = V_{xnz} = V_{ypz} = V_{ynz} = -\frac{1}{2}E_z \cos(2\pi fn\Delta t + \phi)\Delta z \quad (4.52c)$$

where n is the iteration number and E_k is the amplitude of the electric field along axis k (fig. 4.5b). A voltage source V is applied across opposite node faces. The electric field it produces across the node is then

$$E_k = \frac{V}{\Delta k} \quad (4.53)$$

where k is either the x , y or z axis.

Similarly, a current source is modelled as a magnetic field element (fig. 4.5a). By reversing eqn. 4.46, current can be applied to a node using

$$V_{ypz} = -V_{zpy} = -V_{ynz} = V_{zny} = \frac{1}{2Z_0}I_x \cos(2\pi fn\Delta t + \phi) \quad (4.54a)$$

$$V_{zpx} = -V_{xpz} = -V_{znx} = V_{xnz} = \frac{1}{2Z_0}I_y \cos(2\pi fn\Delta t + \phi) \quad (4.54b)$$

$$V_{xpy} = -V_{ypx} = -V_{xny} = V_{ynx} = \frac{1}{2Z_0}I_z \cos(2\pi fn\Delta t + \phi) \quad (4.54c)$$

4.5.7 Boundary Conditions

The space modelled by TLM is finite, and the behaviour at boundaries must be defined. The simplest boundary is an absorbing wall, where all link lines are terminated by a matched impedance. Any pulse scattering into the wall will be absorbed and its energy taken out of the TLM mesh. In practice a matched termination will only act as a perfect absorber for incident waves perpendicular to the wall. A better formulation is to use Berenger's Perfectly

Matched Layer (PML) [135] which is designed to absorb waves incident at all angles. A TLM implementation of Berenger's PML is described in [136], although this has not yet been implemented in the simulator used in this work.

Electric and magnetic walls can easily be modelled by leaving link lines at a boundary short or open circuited respectively. These can be used to exploit symmetry in the modelled system, and so reduce the size of the required mesh speeding up the simulation [134]. However, most of the simulations in this study use a coil driven in quadrature, breaking any potential symmetry about the sagittal plane. Simple absorbing boundaries have been used at all six faces of the simulation space.

Metals can be modelled either by reducing the electrical resistance of a lossy node, or by modelling the node as a special Perfect Electrical Conductor (PEC) in which each link line entering the node is short circuited with itself. While these two methods produce different scattering matrices, the practical differences are found to be small [131]. This implementation uses low resistance lossy nodes, as they require no extension of the code.

4.5.8 Frequency Response and Convergence

The frequency response of a system can be determined by recording its impulse response and Fourier transforming the result [65]. This method has previously been applied to both TLM [137] and FDTD [138] modelled probes. The probe is excited with an impulse and the field timecourse is monitored at some point in the probes field of view. Fourier transforming the timecourse will reveal the resonant modes as strong peaks in the frequency response. As the probe and sample are modelled as a single system, the frequency response automatically includes the effects of probe-sample coupling.

For B_1 field investigation, the coil is driven in CW mode. After a coil is first excited it takes some time for a stable field to establish due to the finite wave velocity. To monitor field formation, a single representative point can again

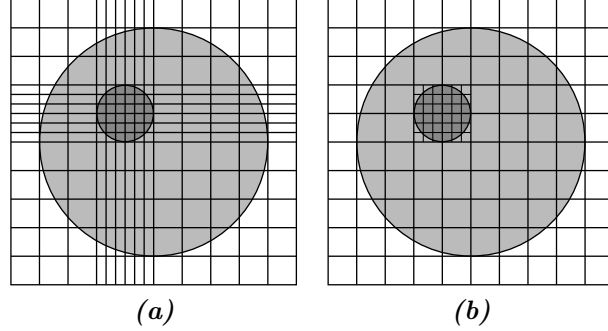


Figure 4.6: A variable mesh using (a) graded or (b) multigrid mesh.

be monitored. Examining the timecourse will show when the amplitude of a field component (B_x for example) has reached a steady state.

An alternative method is to monitor the whole field on successive cycles. Taking a field difference between $B_1(\phi)$ and $B_1(\phi + 2\pi)$ will show when the field has reached a steady state. However, this method is more computationally intensive, since it requires calculating many more field points.

4.5.9 Alternative Mesh Geometries

TLM has been formulated here using a regular Cartesian mesh, but other geometries are also possible, such as a cylindrical mesh [139] or even a generalised curvilinear mesh [140]. A difficulty when using these alternative meshes is that the voxel size varies throughout the model. In the case of a cylindrical mesh, for example, the centre of the mesh is covered in more detail than the perimeter. A related problem is that small voxels require a small timestep, slowing down the whole simulation.

Several methods also exist for modelling some parts of the system in more detail than others, allowing fine features to be modelled without increasing the size of the whole mesh. The simplest is to use a variable or graded mesh [131] shown in fig. 4.6a, in which the mesh spacing is varied along each axis. When using this method the velocity in each cell has to be adjusted to maintain synchronicity over the whole mesh.

A more flexible method is to use a multigrid mesh [141] shown in fig. 4.6*b*, in which some cells in the mesh are further subdivided into smaller cells, allowing much finer detail to be represented without affecting the whole mesh. Synchronicity is maintained by using a smaller timestep inside the fine mesh than in the main model, chosen such that the larger timestep is an integer multiple of the finer one. The finer mesh is then iterated several times for each single step on the main mesh.

The simulation work presented in this thesis was all performed on a regular Cartesian mesh. In the case of modelling an MR probe, almost the entire modelled volume contains fine detail that is of interest. We would like to model resonant probe elements in detail to accurately model their behaviour. At the same time, we would like to model the load (the human head) in equal detail to examine fields generated inside it. It was thus felt that mesh optimisation offered little practical benefit in this application.

As a final possibility, a TLM formulation using an arbitrary tetrahedral mesh has recently been published [142], analogous to that used for finite element modelling. This offers interesting possibilities for probe modelling in MRI, allowing fine detail such as skin around the head to be modelled. However, such extra capability comes at the cost of additional computational effort, increasing simulation run time.

4.5.10 Implementation Details

The TLM simulator is written in approximately 2000 lines of standard C++, making use of object oriented design and the standard library [143]. One of the advantages of C++ is its portability. The current version of the simulator has been successfully compiled and run on three different platforms (Linux x86 PC, Sun UltraSPARC, Compaq/DEC Alpha) without modification.

Some attention has been paid to optimising the code, although there are probably still further improvements to be made. Currently the simulator will run a 1.8 million node mesh for 6700 iterations using a 5ps timestep (10

cycles at 300MHz) in 4 hours on a 2.4GHz Intel P4 Linux system, requiring 210MB RAM to run.

The simulator can output a 3D map of electric or magnetic field vectors. Alternatively a small number of locations can be monitored at every iteration, producing a timecourse for both electric and magnetic field vectors. This facility is intended for use in tuning and convergence testing, where saving a complete field map at every iteration is unnecessary. The simulator can also save its complete state at any iteration, allowing the simulation to be later reloaded and continued if necessary.

4.6 Simulation Models

The TLM simulator describes the modelled space using a three dimensional Cartesian mesh of nodes, each node potentially having different electrical properties. However, a model will typically contain millions of nodes describing less than 60 different material types. To reduce the space required to store material information, the simulator stores the model description in two separate parts. The spatial description is stored as a three dimensional array of indices. Each index refers to an entry in the material properties list describing the conductivity σ , permittivity ϵ_r and density ρ of the material. This system also makes the models frequency independent. To use the model at a different frequency only the material properties list has to be changed.

A simulation makes no distinction between the probe and the sample, the whole system being described in a single model. All probe-probe and probe-sample coupling is automatically described by the model. Simulations presented in this thesis were run using a $(3\text{mm})^3$ mesh of 1,771,561 nodes $(121 \times 121 \times 121)$. The model resolution was chosen to achieve a reasonable simulation run time (several hours), while still including enough detail to model the main features of the human head. An investigation by Mason *et al* has shown that within the range of a few millimetres, voxel size has little impact on simulated peak or average SAR levels [144].

4.6.1 Probe Models

Probe models were constructed using custom written code, based on Bresenham's line and circle drawing algorithms [145]. Most probe designs are fairly homogeneous along the z -axis. Such a probe can be modelled by building a small number of cross sections which are then extruded to form the complete model.

Probe designs enclosed in an RF shield were modelled inside a cylindrical hole bored out from a solid block of conductor. This has the advantage that the boundary conditions are naturally described as part of the model. A second benefit is that solid conductors do not support internal fields, reducing the number of calculations to be performed and speeding up the simulation.

4.6.2 Human Models

The development of more detailed simulations of electromagnetic interaction with the human body has driven the development of more realistic human body models. Early studies used basic geometric elements such as a homogeneous cylinders with tissue like conductivity and permittivity [92, 93]. A slightly more detailed approach was to build a model from several geometric elements, such as the monkey head model built from six spherical shells developed by Shapiro *et al* [146]. Simple geometric models are attractive as they can be used with analytic as well as numerical techniques.

Numerical simulation methods naturally support the use of more complex heterogeneous body models. In 1981 Morgan developed a finite element head model built from a vertical stack of disk elements [147]. The use of FDTD simulations further pushed phantom development, producing multiple tissue [148] and fully voxelised whole body models [149, 150].

Current body models are produced from either CT or MRI data automatically segmented into different tissue types, although some manual correction of the final model is still performed. Several models are available, such as

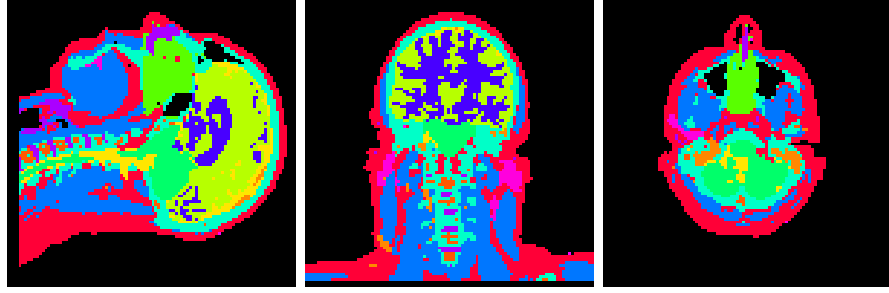


Figure 4.7: Three orthogonal sections through the HUGO head model.

NORMAN and NAOMI developed by the National Radiological Protection Board [151, 152] or the Asian male and female phantoms developed by Nagaoaka *et al* [153]. All of these models are built at $(2\text{mm})^3$ resolution.

The HUGO model (ViewTec Ltd, Switzerland) is used in this work. The model is derived from the Visible Human Project [154], classified into 30 different tissue types on a $(1\text{mm})^3$ mesh. The model was resampled onto a $(3\text{mm})^3$ mesh for this work, in which only the head and shoulders have been used (fig. 4.7).

4.6.3 Tissue Properties

Biological tissue is dispersive, meaning that its electrical properties are frequency dependent. Although the TLM method works in the time domain, the models being used are resonant at a particular frequency. This allows tissue to be modelled with fixed permittivity and conductivity, calculated at the resonant frequency of the probe. Tissue properties used for the work presented in this thesis are shown in table 4.1, calculated using data from Gabriel and Gabriel [155, 156].

Tissue density is also included in the material data to allow the calculation of SAR values. Materials listed with zero density are excluded from SAR calculations.

Material	64MHz		128MHz		300MHz		ρ (kg/m ³)
	σ (S/m)	ϵ_r	σ (S/m)	ϵ_r	σ (S/m)	ϵ_r	
air	0	1	0	1	0	1	0
marrow	0.02109	7.21	0.02363	6.233	0.02737	5.758	1810
fat	0.03528	6.506	0.03687	5.921	0.03957	5.634	920
bone (cancellous)	0.1608	30.87	0.1799	26.28	0.2156	23.16	1810
white matter	0.2915	67.84	0.3421	52.53	0.4133	43.78	1040
grey matter	0.5109	97.43	0.5867	73.52	0.6924	60.02	1040
skin	0.4357	92.17	0.5227	65.44	0.6414	49.82	1010
eye (vitreous)	1.503	69.13	1.505	69.06	1.518	69.02	1170
muscle	0.6882	72.23	0.7192	63.49	0.7705	58.2	1040
blood	1.207	86.44	1.249	73.16	1.316	65.65	1060
neuron (cerebellum)	0.719	116.3	0.8294	79.74	0.9732	59.72	1040
eye (lens)	0.5858	60.53	0.6089	53.07	0.6478	48.95	1100
csf	2.066	97.31	2.143	84.04	2.224	72.73	1010
cartilage	0.4521	62.91	0.4884	52.92	0.5525	46.77	1100
mucus-membrane	0.488	76.72	0.5442	61.59	0.6308	51.9	1040
ganglia	0.7783	73.95	0.8042	66.78	0.8512	62.45	1040
copper	5.8e7	1	5.8e7	1	5.8e7	1	0

Table 4.1: Electrical properties of tissue in the human head model.

Chapter 5

Radiofrequency Probe Modelling

5.1 Introduction

This chapter is divided into three sections. In the first section, a simple non-resonant model of a Birdcage probe is used to demonstrate the electromagnetic modelling of an RF probe using the TLM simulator and a detailed head model. Instantaneous magnetic fields produced by the simulator are shown, and the extraction of complex rotating fields demonstrated. The effect of increasing the operating frequency from 64MHz to 300MHz is investigated, on both the magnitude and phase of the B_1 field. The effect of sample conductivity on B_1 field homogeneity is shown using a simulated saline phantom of varying conductivity. Calculation of the relative signal-to-noise ratio (SNR) and specific absorption rate (SAR) is then demonstrated.

The microstrip is then introduced as an RF probe element. Microstrip theory and the use of microstrips as resonant RF probe elements is discussed. A resonant simulation model is introduced, and the numerical tuning of that model described. Magnetic and electric fields produced by the microstrip, operating at 300MHz, are then shown and the SNR and SAR distribution inside the head investigated. The effects of varying the microstrip width,

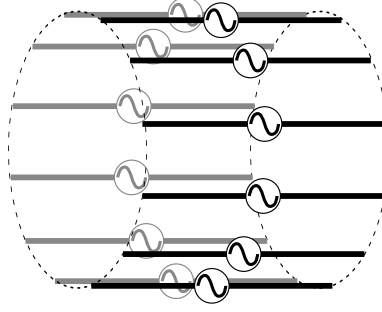


Figure 5.1: Simplified birdcage probe, modelling only the rungs. Each rung n is driven by an current source I_n at its centre, where $I_n = I_0 \cos(\omega t + 2\pi/n)$.

length and height are then investigated, to determine the optimum strip dimensions for imaging the human head.

An array probe, constructed from four microstrip elements, is then simulated. Each strip is individually tuned while the other strips are grounded. The coupling between strips is examined, and the B_1 fields generated by each strip with one strip and all strips tuned are investigated. The homogeneity of the combined field is examined during quadrature transmission and quadrature and parallel reception.

5.2 The Birdcage Probe

A Birdcage probe was investigated, operating at 64, 128 and 300MHz, using a simplified simulation model. Only the probe rungs were modelled, with the end rings omitted (fig. 5.1). Each rung was driven by an independent voltage source at its centre. This model approximates the ideal low frequency probe current distribution $I = I_0 \cos \theta \hat{z}$ (eqn. 3.40), allowing the generated B_1 field to be investigated without considering the frequency limits of the birdcage design itself.

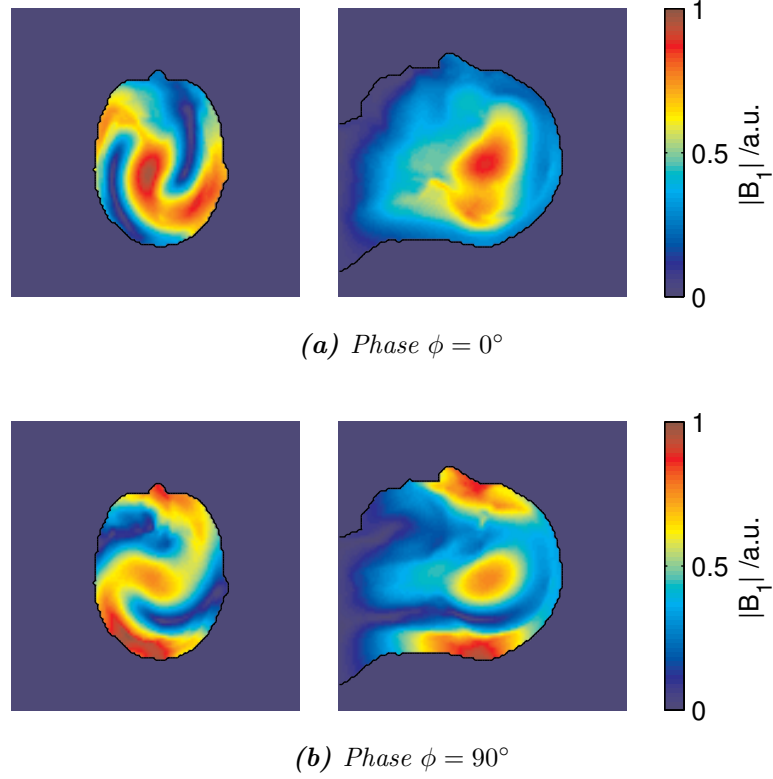


Figure 5.2: The instantaneous magnetic field generated inside the HUGO model by the Birdcage probe at 300MHz at (a) $\phi = 0^\circ$ and (b) $\phi = 90^\circ$.

5.2.1 Instantaneous and Rotating Fields

Instantaneous B_1 fields generated inside the HUGO model by the simplified Birdcage probe, driven in quadrature mode at 300MHz, are shown in fig. 5.2. At this frequency the wavelength in tissue is 13cm (assuming $\epsilon_r = 60$) which is approximately two-thirds of the width of the human head. In the time taken for the magnetic field to propagate into the centre of the head, the phase of the field at the surface changes significantly, giving rise to the distinctive swirling pattern in the transverse plane. The complex rotating magnetic field B_1^+ (fig. 5.3) is then calculated from the instantaneous fields as described in section 4.5.5.1. The field is highly inhomogeneous, showing the strong central ‘bright’ region that is characteristic of high field probes.

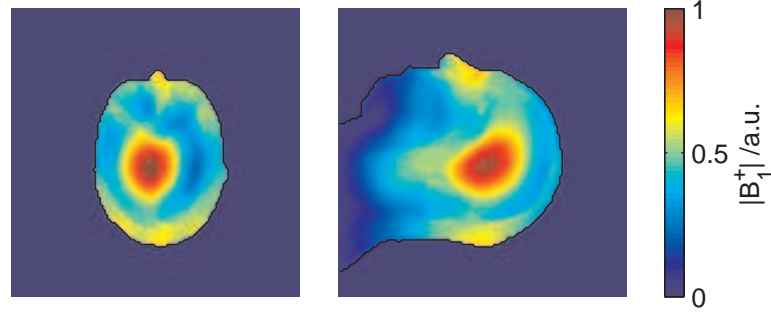


Figure 5.3: The positive rotating magnetic field B_1^+ generated inside the HUGO model by the Birdcage probe at 300MHz.

5.2.2 Field Homogeneity vs. Frequency

Fig. 5.4 shows the B_1^+ field generated inside the HUGO model at 64, 128 and 300MHz. At 64MHz the field is uniform in the centre of the head, decaying in magnitude towards either end of the probe. At 128MHz the relative field intensity has increased at the centre of the head. At 300MHz the central brightening is surrounded by a trough, forming the classic ‘bullseye’ pattern, indicating field cancellation. Fig. 5.5 shows transverse and axial cross sections through the B_1^+ field.

When driven in quadrature mode, a probe will also generate a small field component rotating in the opposite direction to the desired field. This counter-rotating field component does not contribute to the nutation of sample magnetisation. However, its associated electric field does contribute towards energy dissipated in the sample. Similarly, during reception the sample magnetisation only precesses in one direction, detected as a signal rotating in the B_1^- sense (opposite to the transmit direction). Any counter-rotating field (rotating in the B_1^+ direction) detected by the probe is due to noise, generated either in the sample or in the probe. It is therefore desirable to minimise the generation of B_1^- during transmission and sensitivity to B_1^+ during reception.

Fig. 5.6 shows the counter-rotating B_1^- field generated inside the HUGO model by the Birdcage probe driven in quadrature mode. At 64MHz, only a small proportion of the magnetic field rotates against the driven direction.

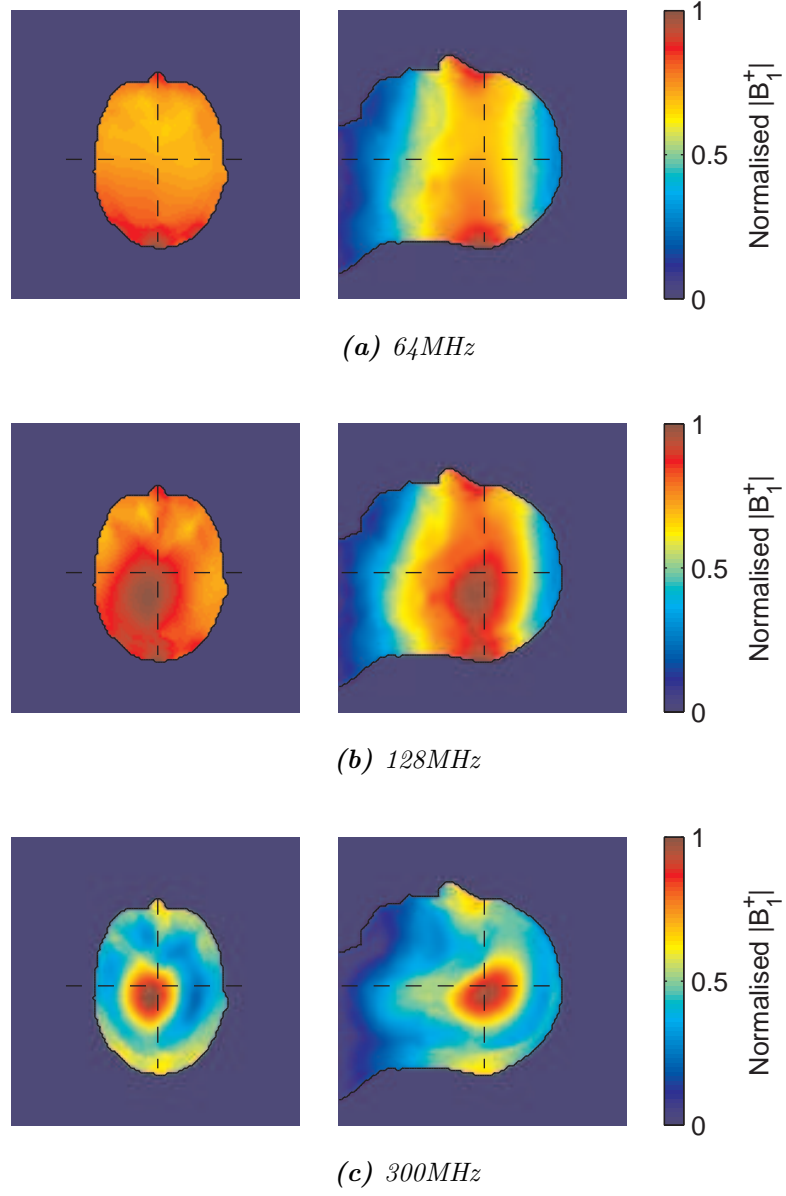


Figure 5.4: Magnitude of the positive rotating magnetic field $|B_1^+|$ inside the HUGO model in the Birdcage probe driven at (a) 64MHz, (b) 128MHz and (c) 300MHz in quadrature mode.

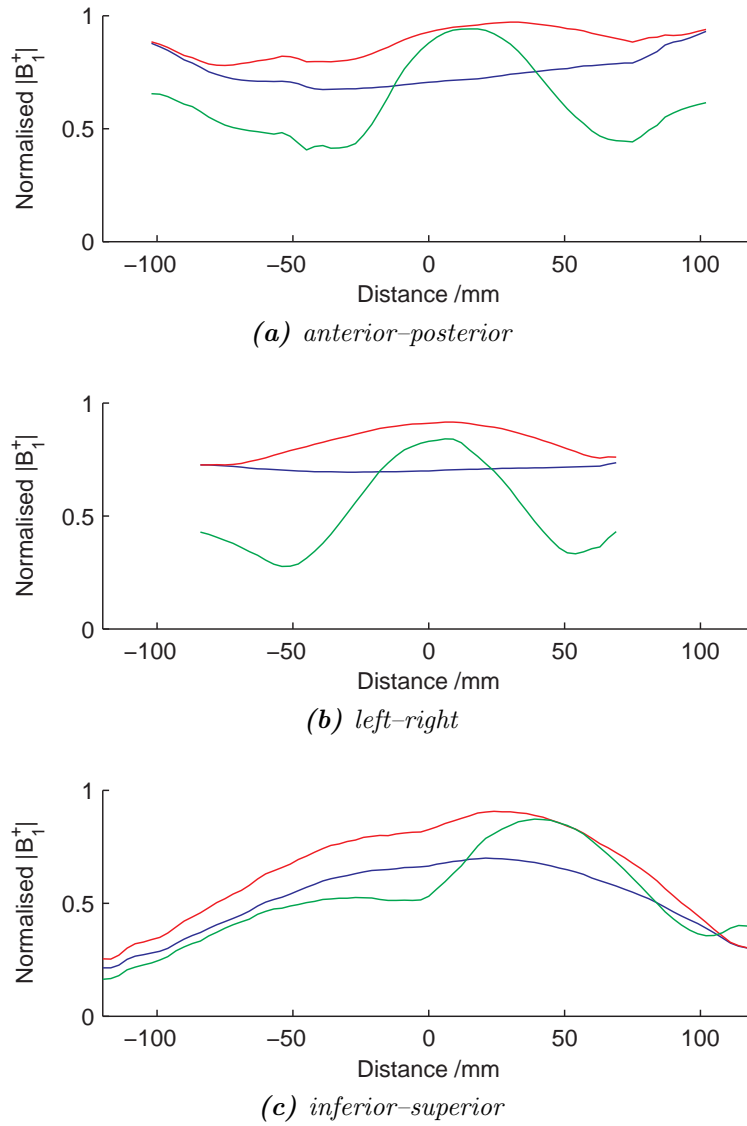


Figure 5.5: Cross sections through the $|B_1^+|$ field at 64 (blue), 128 (red) and 300 (green) MHz, taken along the dashed lines in fig. 5.4.

This proportion increases with increasing operating frequency. Comparing fig. 5.6c to fig. 5.4c, it can be seen that at 300MHz the central bright region of the positive rotating field is surrounded by a negative rotating region.

5.2.3 Phase Variation vs. Frequency

Figure 5.7 shows the phase of the transmit B_1^+ field produced by the Birdcage probe inside the HUGO model; cross sections through these fields are shown in fig. 5.8, taken along the dashed lines in fig. 5.7. At 64MHz the signal phase is almost uniform over the probe volume, having a standard deviation $\sigma = 5.9^\circ$ over the head. At 128MHz a phase shift towards the centre of the sample is seen ($\sigma = 14.2^\circ$), which becomes much stronger at 300MHz ($\sigma = 50.5^\circ$). This phase shift, caused by the finite propagation velocity of the magnetic field inside tissue, is an inherent problem in high field imaging.

5.2.4 Sample Conductivity

Figure 5.9 shows the B_1 field magnitude inside a spherical phantom of conductivity $\sigma=0.05, 0.5$, and 1.0 S/m, placed inside a Birdcage probe driven in quadrature at 300MHz. At low conductivity, a strong interference artifact is seen. As the sample conductivity is increased, the RF penetration depth decreases, counteracting the effect of the central brightening artifact. In this way, the conductivity of the human head helps to reduce the central brightening artifact observed. Graphs in fig. 5.10 plot the maximum and average field variation inside the phantom against the phantom conductivity. The maximum field variation is measured using

$$\delta_{max} = \frac{|B_1^{max} - B_1^{min}|}{B_1^{ave}} \quad (5.1)$$

where B_1^{max} and B_1^{min} are the maximum and minimum B_1 field values inside the phantom, and B_1^{ave} is the mean field magnitude inside the phantom. The

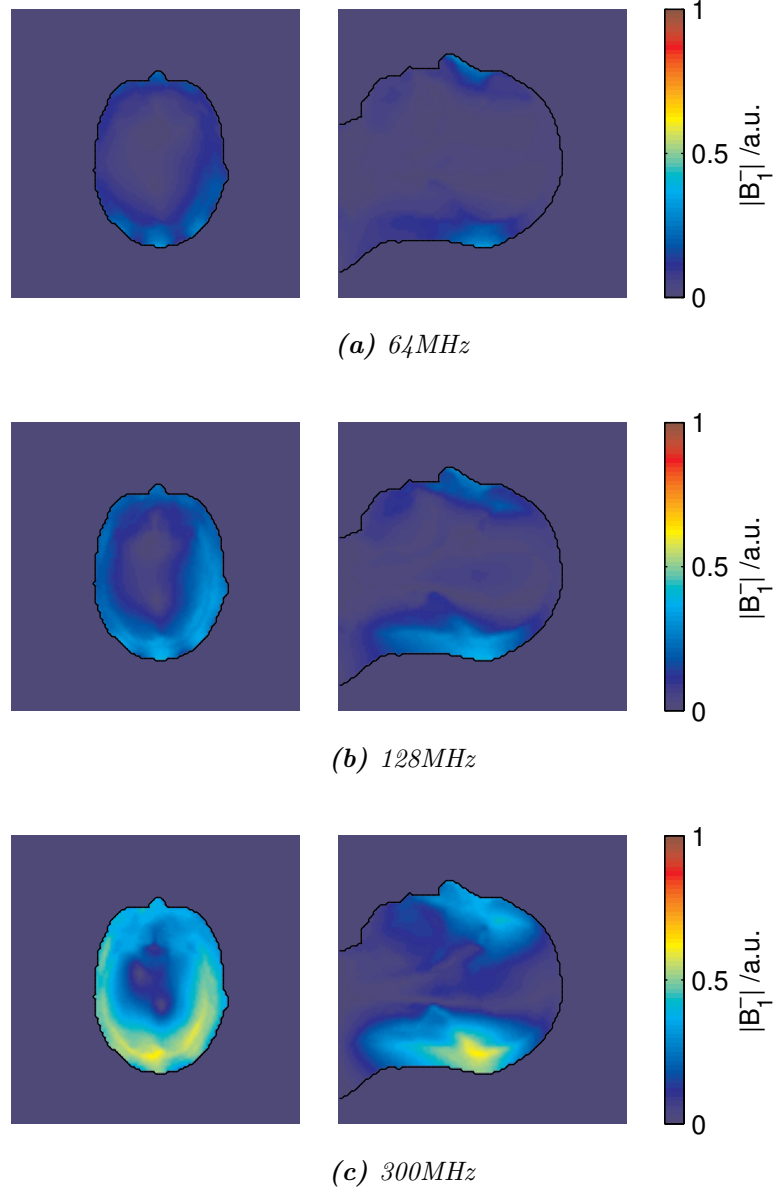


Figure 5.6: When the probe is driven in quadrature mode, the counter rotating magnetic field component $|B_1^-|$ increases as the driving frequency is increased.

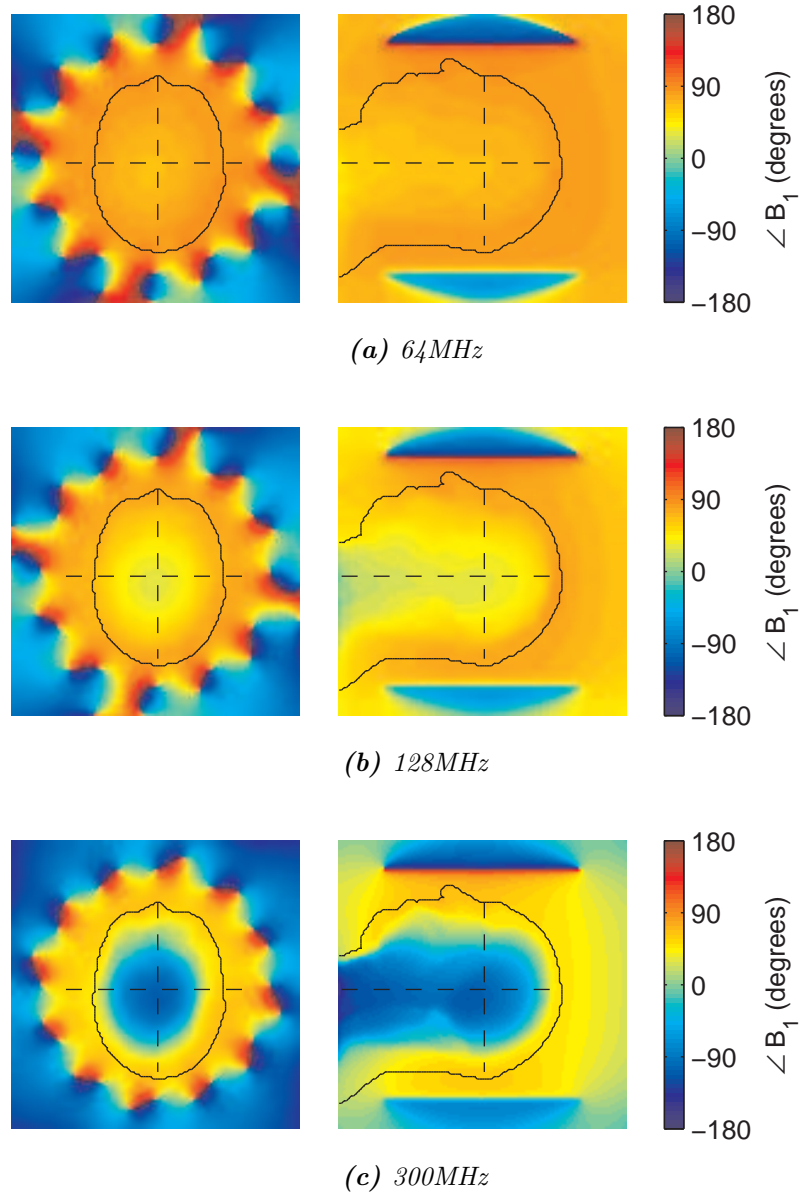


Figure 5.7: Phase of the B_1 transmit field inside the HUGO model in the Birdcage probe driven at (a) 64MHz, (b) 128MHz and (c) 300MHz in quadrature mode.

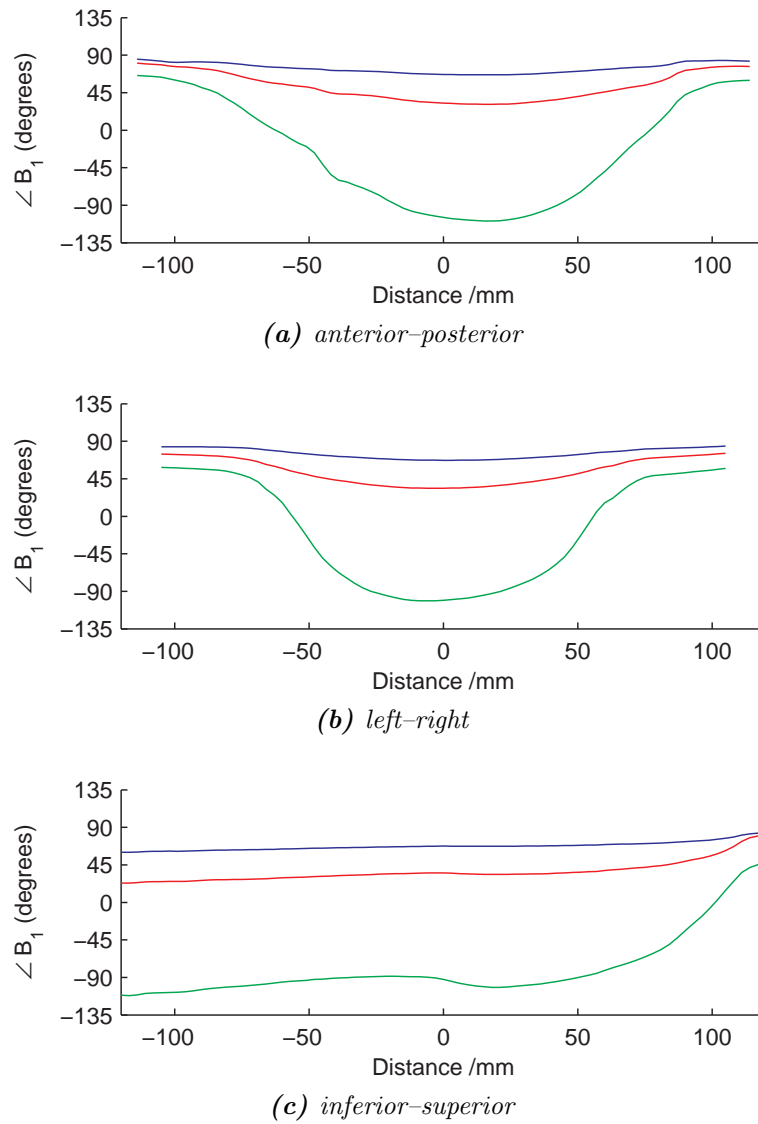


Figure 5.8: Cross sections through the B_1 phase maps at 64 (blue), 128 (red) and 300 (green) MHz, taken along the dashed lines in fig. 5.7.

average field variation is measured using

$$\delta_{ave} = \frac{1}{V} \int_V \frac{|B_1 - B_1^{ave}|}{B_1^{ave}} dV \quad (5.2)$$

where V is the phantom volume [40].

At 64MHz the maximum B_1 field variation δ_{max} is independent of conductivity, while the average variation δ_{ave} increases with increasing conductivity. This is due to a central darkening caused by the reduced RF penetration as shown in fig. 5.11a. At 128MHz a slight decrease in δ_{max} can be seen with increasing conductivity as the reduced RF penetration is counteracted by the formation of a central brightening. At 300MHz the effect is more pronounced, with a drop in δ_{max} and δ_{ave} as the conductivity increases. However, above 1.0 S/m, the effect of the reduced RF penetration outways the central brightening effect (fig. 5.11c), and B_1 field variation increases. This mechanism was previously discussed by Sled *et al.* [133].

It was found that the TLM simulator performs poorly when the model presents no loss (i.e. $\sigma = 0$). Fig. 5.12 shows the B_1 field generated in the spherical phantom with zero conductivity. The high frequency artifact introduced when the simulation begins does not decay away as it does in a lossy load, producing a noisy field map. However, this was not a problem in practice, as any realistic probe load presents a significant loss.

5.2.5 Signal-to-Noise Ratio (SNR)

In order to compare different probe arrangements, it is useful to compare the available signal-to-noise ratio (SNR), rather than the raw magnetic and electric fields. The signal available from a voxel is assumed to be proportional to the precession frequency, the sine of the nutation angle, and the local receive sensitivity of the probe, which is proportional to B_1^- [49, 157]. Sample noise is proportional to the precession frequency and the square root of the absorbed power P_{abs} [55].

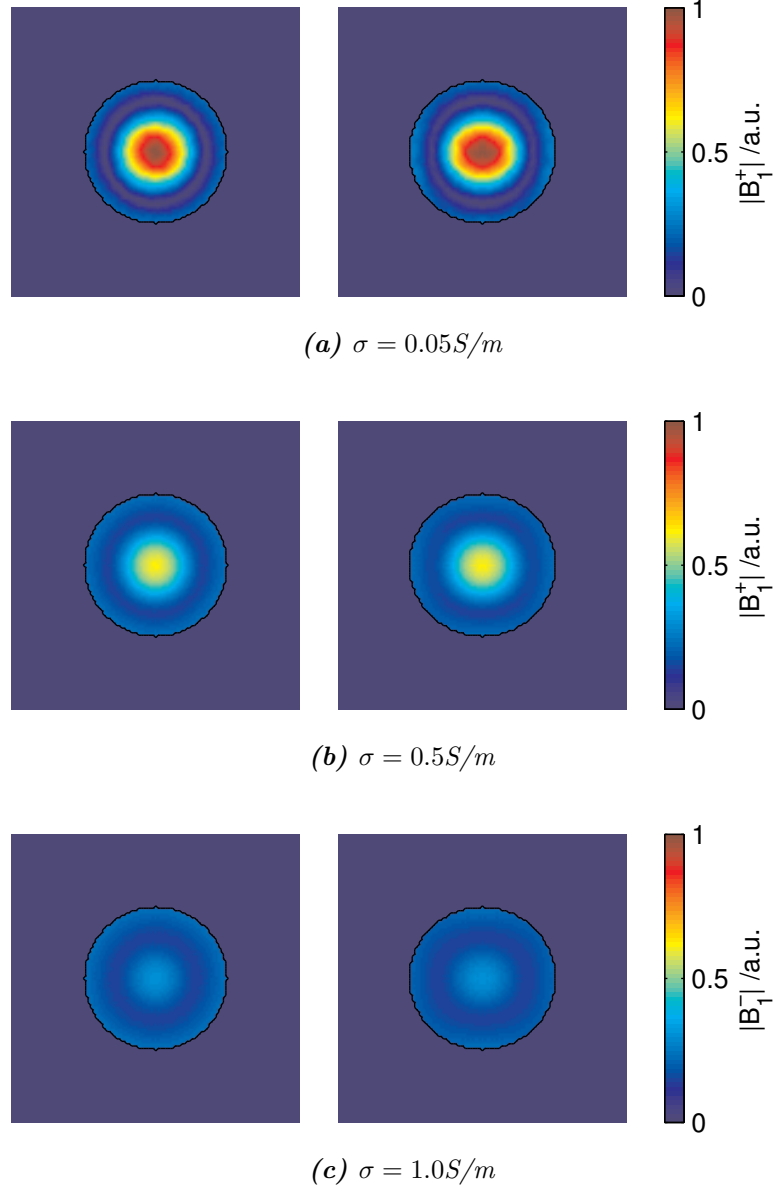


Figure 5.9: The B_1^+ field inside a spherical phantom with conductivity (a) $\sigma = 0.05S/m$, (b) $\sigma = 0.5S/m$, and (c) $\sigma = 1.0S/m$.

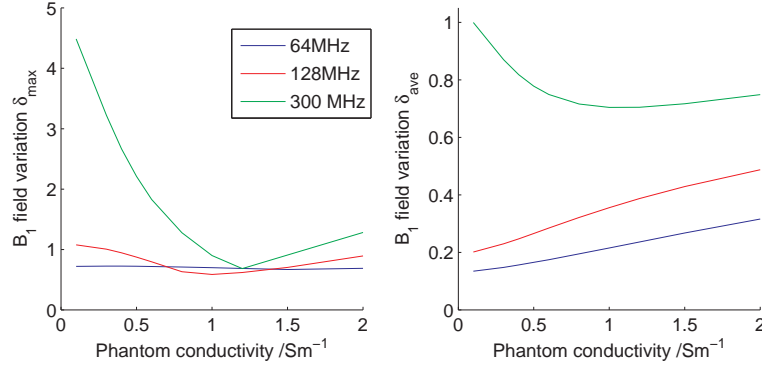


Figure 5.10: Maximum (left) and average (right) B_1 field variation as a function of phantom conductivity.

The nutation produced by the transmit field B_1^+ is

$$\alpha = \gamma \tau V |B_1^+| \quad (5.3)$$

where γ is the gyromagnetic ratio, τ is the RF pulse duration and V is a dimensionless scaling factor. Since B_1^+ is the field produced when a 1V signal is applied to the probe, V can be considered as the probe driving voltage, producing the field $V B_1^+$. The transmit field is normalised to produce a 90° nutation at the peak B_1^+ location inside the brain. If a 3ms rectangular RF pulse is used, the required field strength is $1.957\mu\text{T}$. Neglecting relaxation effects, the available SNR is then

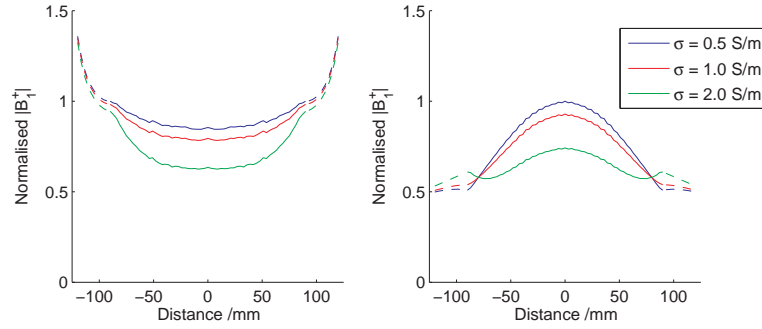
$$\text{SNR}(\mathbf{r}) \propto f \frac{|\sin(V B_1^+(\mathbf{r}) \gamma \tau) B_1^-(\mathbf{r})|}{\sqrt{P_{abs}}} \quad (5.4)$$

Note that while the transmit field is normalised using the factor V (equivalent to adjusting the transmit power), there is no normalising factor for the receive field. Increasing the preamplifier gain amplifies both signal and noise, maintaining the ratio $B_1^-/\sqrt{P_{abs}}$.

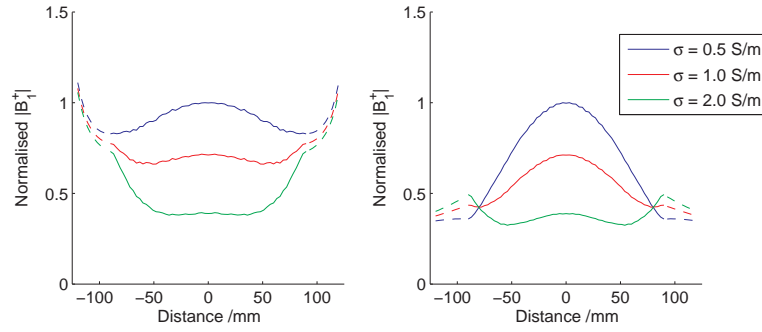
The absorbed power is calculated using

$$P_{abs} = \frac{1}{2} \sum_n (\sigma_n E_n^2) \Delta x \Delta y \Delta z \quad (5.5)$$

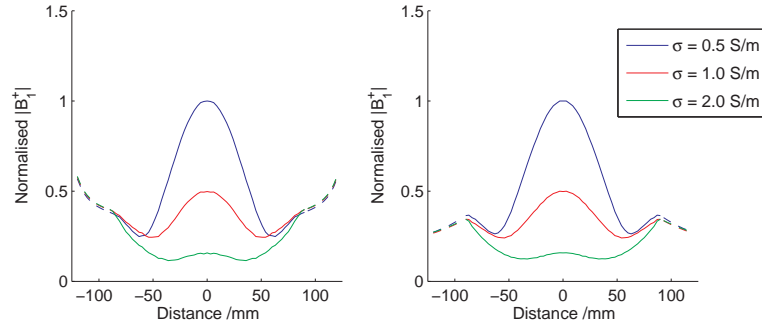
where E_n is the magnitude of the electric at voxel n , σ_n is the voxel conductivity and Δx , Δy and Δz are the voxel dimensions. The sum is taken



(a) 64MHz



(b) 128MHz



(c) 300MHz

Figure 5.11: Transverse (left) and axial (right) cross section across a spherical phantom at (a) 64, (b) 128 and (c) 300MHz. As the conductivity increases the penetration depth reduces. At low frequency this increases B_1 field variation inside the phantom. At higher frequency this counteracts the central brightening artifact. The dashed section shows the field outside the phantom.

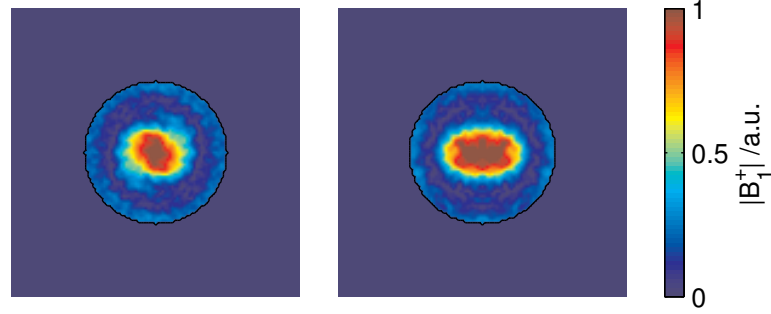


Figure 5.12: When the Birdcage model is loaded with a lossless phantom ($\sigma = 0$), the B_1 fields produced by TLM simulation are noisy.

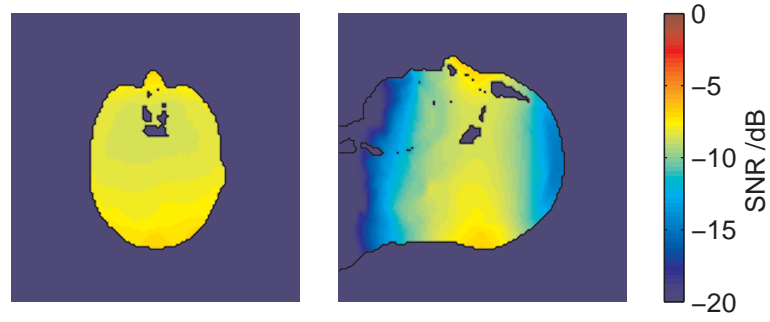
Frequency /MHz	Maximum /dB	Mean /dB	Std. dev. %
64	-7.19	-9.08	3.1
128	-3.86	-5.55	8.0
300	0	-4.82	18.1

Table 5.1: Relative SNR measured over the brain, using the Birdcage probe.

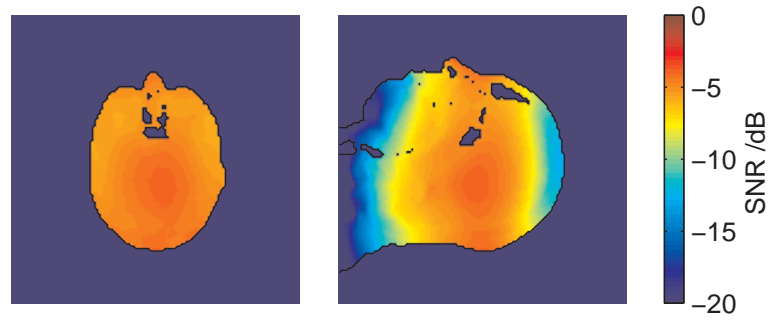
over the whole excited volume (in this case the head) as, unlike the NMR signal, noise is not localised.

Relative SNR maps for the Birdcage probe operated at 64, 128 and 300MHz are shown in fig. 5.13. This figure demonstrates both the reason for moving to a higher static field strength, and the challenges this presents. Table 5.1 shows the maximum, mean and standard deviation in relative SNR over the brain. At 64MHz the available SNR over the probe volume is uniform. Increasing the operating frequency to 128MHz approximately doubles the available SNR, but also increases its spatial variation by a factor of 2.58. Moving to 300MHz again increases the mean SNR, but by a much smaller factor (1.18), while the spatial variation in SNR increases significantly.

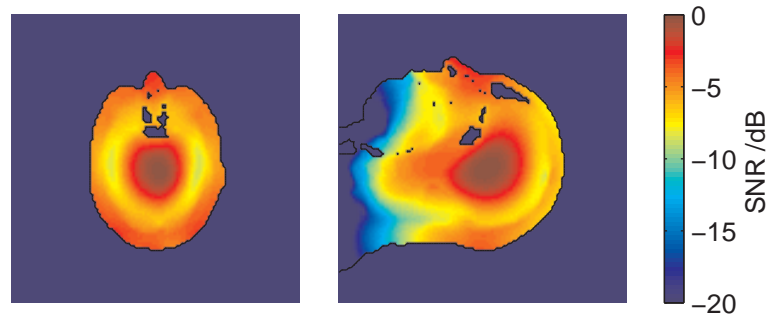
Clearly the available SNR increases with increasing frequency, but not at the linear rate that is potentially available (eqn. 3.32). This is due to field cancellation in both the transmit and receive B_1 fields as the wavelength of the excitation signal decreases. The challenge of high field probe design



(a) 64MHz



(b) 128MHz



(c) 300MHz

Figure 5.13: Relative SNR maps for the Birdcage probe driven in quadrature. The maps are all normalised to the same scale.

is to excite the sample and detect the resulting signal without interference, thus approaching the linear increase in available SNR offered by increasing the static field strength.

5.2.6 Specific Absorption Rate (SAR)

The simulated electric field may be used to calculate the SAR experienced by the subject during an RF pulse. The SAR is defined as

$$\text{SAR} = \frac{\sigma E^2}{2\rho} \quad (5.6)$$

where σ is the tissue conductivity, E is the electric field magnitude and ρ is the tissue density. The electric field produced by the simulator is the result of driving the modelled probe with a 1V signal. As explained in the previous section, this is multiplied by a scaling factor V to produce a 90° nutation at the maximum B_1^+ point inside the brain. The same scaling factor must be applied to the electric field, giving

$$\text{SAR}_{90^\circ} = \frac{\sigma V^2 E^2}{2\rho} \quad (5.7)$$

Local SAR levels are of particular concern at high field, as the electric field distribution is less uniform. The IEC local SAR limit is 10W/kg over a 10g sample of tissue [59]. The SAR limit is determined per mass, rather than per volume, making it rather difficult to calculate from simulated data. High SAR levels tend to occur in soft tissue, which have a high electrical conductivity [157]. Soft tissue also has a high water content, so its density is approximately 1g/cm^3 , allowing 10g of tissue to be approximated as a volume of 10cm^3 . Local SAR levels presented in this work were calculated at three different volumes: $1 \times 1 \times 1$, $3 \times 3 \times 3$ and $7 \times 7 \times 7$ voxels, approximately corresponding to 0.03g, 0.73g and 9.26g tissue samples. A $7 \times 7 \times 7$ voxel cube can be used to give an estimate of the 10g local SAR limit specified by the IEC [59]

$$\text{SAR}_{10g}(i, j, k) \approx \frac{1.08}{7^3} \sum_{i'=i-3}^{i+3} \sum_{j'=j-3}^{j+3} \sum_{k'=k-3}^{k+3} \text{SAR}(i', j', k') \quad (5.8)$$

Similarly, a 1g local SAR value may be calculated over a $3 \times 3 \times 3$ voxel cube using

$$\text{SAR}_{1g}(i, j, k) \approx \frac{1.37}{3^3} \sum_{i'=i-1}^{i+1} \sum_{j'=j-1}^{j+1} \sum_{k'=k-1}^{k+1} \text{SAR}(i', j', k') \quad (5.9)$$

In both cases, the slightly reduced volume over which the SAR is averaged make the limit more, rather than less, stringent.

Plots of the SAR generated inside the head model by a quadrature driven Birdcage probe at 64, 128 and 300MHz are shown in fig. 5.14. The SAR distribution changes as the operating frequency is increased. At 64MHz the locations of highest SAR are on the surface of the head, in the regions closest to the probe. The surface of the head is naturally cooled via convection. At 128MHz the high SAR region on the back of the head has shifted to the surface of the brain. At 300MHz this region has moved further into the brain, with the high SAR region around the nose also moving deeper into the head. This is significant as the cooling mechanisms deeper inside the head are less efficient, potentially giving a greater rise in temperature than would be seen for the same SAR level on the surface.

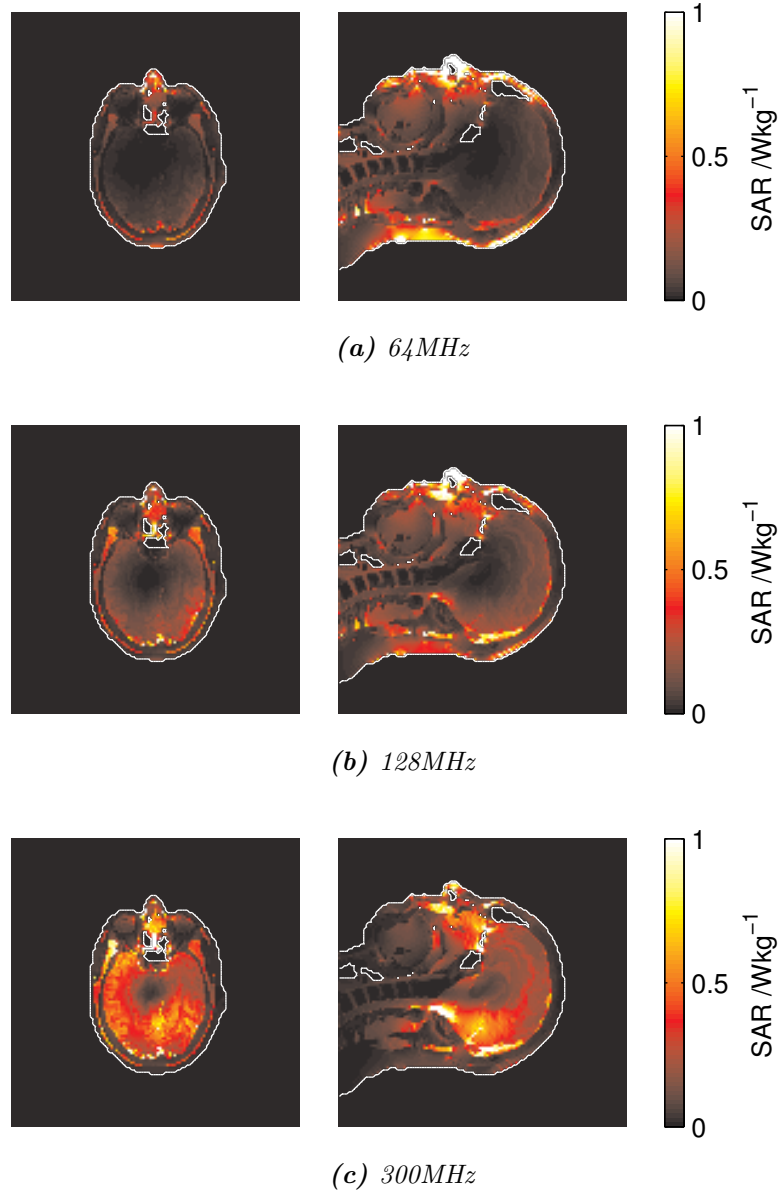


Figure 5.14: The Specific Absorption Rate (SAR) distribution changes as the driving frequency of the probe is increased. Maps here are shown at (a) 64, (b) 128 and (c) 300MHz for the Bird-cage probe driven in quadrature. The units are W/kg .

5.3 The Microstrip

In this section, the microstrip is introduced as an RF probe element. Microstrips are widely used circuit components, having two common applications. The first is as a transmission line element at microwave frequencies, where the microstrip is designed to transfer signals with the minimum of loss. The second application is as antennas, particularly in mobile devices, where the microstrip is designed to produce the maximum radiation. For use as an RF probe element, our requirements are somewhere in between these two uses. The microstrip must generate a magnetic field over a large enough volume to illuminate the sample, but we require the conservative near field rather than the far field generated by an antenna; radiation from a probe represents signal loss.

5.3.1 Microstrip Theory

A microstrip consists of a thin conducting strip separated from a ground plane by a dielectric slab (fig. 5.15). The important parameters of a microstrip are its width w , its height h above the ground plane and the permittivity of the dielectric slab ϵ_r . The thickness of the strip is assumed small compared to the width, and is neglected.

The propagation velocity of a TEM wave in a lossless transmission line embedded in a homogeneous dielectric is determined by the dielectric constant of the medium, and is independent of the transmission line geometry. The

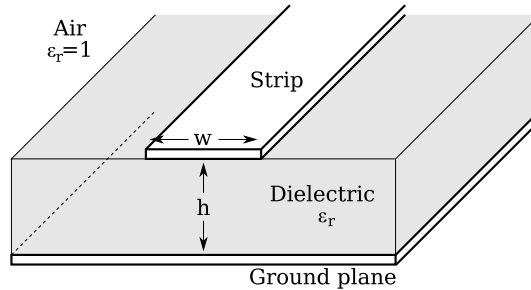


Figure 5.15: A microstrip line

propagation velocity is

$$v_p = \frac{1}{\sqrt{\mu\varepsilon}} = \frac{c}{\sqrt{\varepsilon_r}}, \quad (5.10)$$

assuming the relative permeability of the medium $\mu_r = 1$.

A wave travelling along a microstrip propagates through two different media (air and dielectric). Inside the dielectric it travels at v_p while above the strip it travels at the free space velocity c . Hence a microstrip cannot support pure TEM waves. However, in many practical applications the electromagnetic wave travelling along a microstrip can be approximated as a quasi-TEM wave. This is done by modelling the air and dielectric layers as a single homogeneous medium of effective relative permittivity ε_{eff} , giving the model the same capacitance per unit length as the actual microstrip. The effective relative permittivity is then given by the ratio

$$\varepsilon_{eff} = \frac{C}{C_{air}} \quad (5.11)$$

where C is the microstrip capacitance per unit length and C_{air} is the capacitance per unit length with the dielectric layer replaced with air. The propagation velocity of a quasi-TEM wave is then

$$v_p = \frac{c}{\sqrt{\varepsilon_{eff}}} \quad (5.12)$$

Analytically calculating the effective permittivity is difficult, so it is usually computed numerically [158]. It may be approximated, for $w/h \leq 1$, using the expression

$$\varepsilon_{eff} = \frac{\varepsilon_r + 1}{2} + \frac{\varepsilon_r - 1}{2} \left(\frac{1}{\sqrt{1 + 12h/w}} + \frac{(1 - w/h)^2}{25} \right) \quad (5.13)$$

and for $w/h > 1$,

$$\varepsilon_{eff} = \frac{\varepsilon_r + 1}{2} + \frac{\varepsilon_r - 1}{2} \frac{1}{\sqrt{1 + 12h/w}} \quad (5.14)$$

Note that the effective permittivity, and hence the propagation velocity, now depends upon the strip geometry.

The dielectric layer below the microstrip may be air filled, in which case the effective permittivity $\varepsilon_{eff} = 1$ and the propagation velocity is independent of the strip geometry. In this case the wavelength of the wave travelling along the strip is the free space wavelength.

The characteristic impedance of the microstrip may be approximated from the effective permittivity [158]. For $w/h \leq 1$,

$$Z_0 = \frac{60}{\sqrt{\varepsilon_{eff}}} \ln \left(\frac{8h}{w} + \frac{w}{4h} \right) \quad (5.15)$$

while for $w/h \geq 1$,

$$Z_0 = \frac{120\pi}{\sqrt{\varepsilon_{eff}} \left\{ \frac{w}{h} + 1.393 + 0.667 \ln \left(\frac{w}{h} + 1.444 \right) \right\}} \quad (5.16)$$

The wavelength of the quasi-TEM wave travelling along the microstrip is

$$\lambda = \frac{\lambda_0}{\sqrt{\varepsilon_{eff}}} \quad (5.17)$$

where λ_0 is the free-space wavelength. A microstrip is resonant when it is half a wavelength long (or an integer multiple thereof), with either open or short circuit terminations at both strip ends. When the ends are short-circuited, the strip current is at a maximum at the strip ends while the voltage is at a maximum in the strip centre (fig. 5.16*a*). When the strip ends are open-circuit terminated, the opposite is true, with a current maximum at the strip centre and a voltage maximum at the strip ends (fig. 5.16*b*). This arrangement is well suited to use as an MR probe element, as the strip current generates the magnetic field we would like to maximise, while the strip voltage generates an electric field that we wish to minimise to reduce the probe SAR.

At 300MHz the half-wavelength is 50cm in air, which is impractically long for a probe element. The strip can be electrically shortened by increasing the permittivity of the dielectric layer and increasing the ratio of the strip dimensions w/h . Alternatively, a portion of a strip end may be replaced by its lumped element equivalent. In the case of a strip with open-circuit ends, the equivalent lumped element is a capacitor (section 4.5.2). A capacitor-

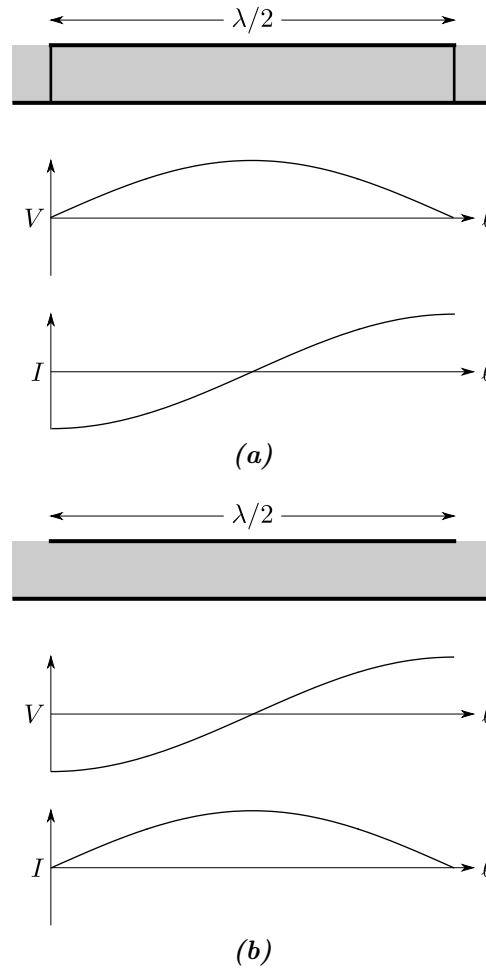


Figure 5.16: The voltage V and current I distribution along a half wave microstrip line with (a) short and (b) open circuited ends.

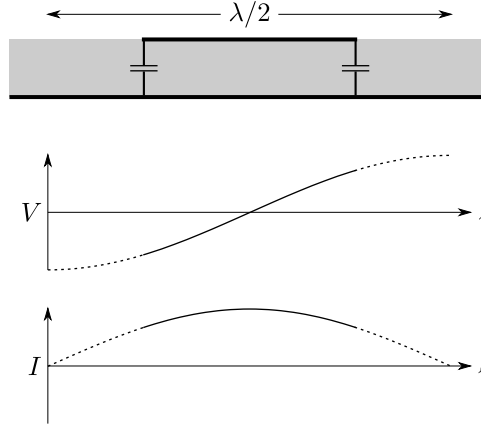


Figure 5.17: The half-wave microstrip can be electrically shortened by adding a capacitor to each end.

shortened strip is shown in fig. 5.17. The voltage and current distribution along the strip section are exactly the same as for full-length strip. The current and voltage that was previously seen across the end sections of the strip is now concentrated across the lumped capacitors. This has the advantage of concentrating the high electric field seen at the strip ends (fig. 5.16b) across the capacitors, reducing SAR in the sample. The location of the voltage node along the strip, and hence the location of the highest magnetic field, may be moved by adjusting the ratio of the two capacitors.

5.3.2 The Microstrip as a Probe Element

To be useful as a probe element, a microstrip should produce a strong transverse magnetic field, coupling well to the sample, while producing a small electric field to maintain a low SAR. A single microstrip is symmetric about its longitudinal axis, and so only operates in linear mode. An array of microstrips can, however, be driven in quadrature mode.

Figure 5.18 shows the simulation model used in this section, with the HUGO head phantom placed 12 mm above a 93 mm long \times 33 mm wide microstrip, 30 mm above the ground plane (green). The microstrip is tuned using a pair of capacitors, one in each leg. The model is built using a $(3 \text{ mm})^3$ mesh.

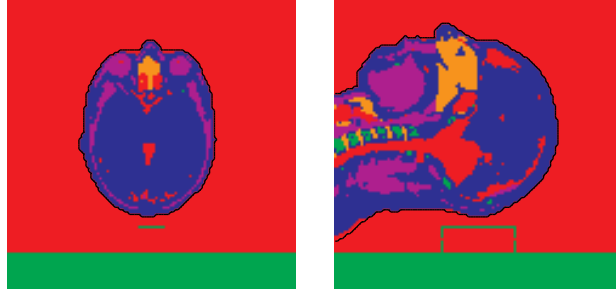


Figure 5.18: The simulation model showing HUGO placed above a microstrip.

5.3.3 Time and Frequency Response

The Birdcage probe model used earlier in this chapter was not resonant; capacitors were instead modelled using voltage sources, enforcing the ‘correct’ current distribution around the probe. The microstrip model is resonant, with capacitors modelled using voxels with a high permittivity along the capacitor axis. This gives a more accurate simulation of the probe behaviour, including the effects of sample loading and parasitic capacitance.

A resonant model must be tuned, in much the same manner as a real probe. The model is excited with an electrical impulse, and the magnetic or electric field monitored for a period of time at some point in the model (usually the centre). The Fourier transform of the impulse response gives the spectral characteristics of the probe, with resonant modes showing up as sharp peaks in the spectrum. In practice, a better response is given if the model is excited by a pulse with a Gaussian envelope rather than a true impulse, the width being chosen to cover the bandwidth of interest [131]. This reduces the excitation of spurious high frequency modes in the TLM mesh.

Figure 5.19 shows a typical microstrip impulse response. Initially, no signal is seen while the field generated by the microstrip propagates through the TLM mesh. The early signal reaching the observation point is noisy, containing a high frequency component as the TLM mesh initialises. This is a simulation artifact rather than a real signal. The main body of the impulse response is an exponentially decaying sinusoid, as would be expected of a high Q system.

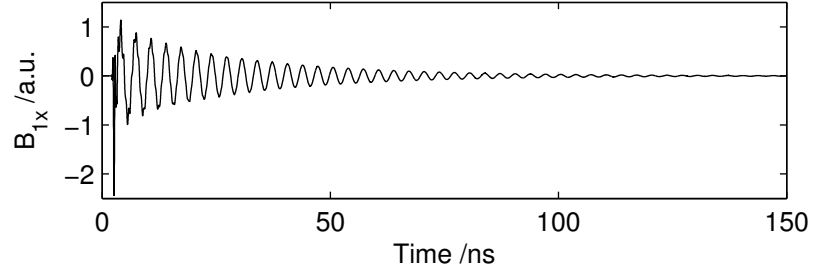


Figure 5.19: Magnetic field strength recorded in the centre of the head model, when the microstrip is excited with an impulse.

The Fourier Transform of the impulse response, sampled over 5, 10, 20 and 40 RF cycles, is shown in fig. 5.20. One 300MHz RF cycle takes 666.2 TLM iterations, when using a 3mm mesh. The resolution of the spectrum improves as the duration for which the impulse response is sampled increases. Running the simulation for 40 RF cycles produces a smooth spectrum, but takes approximately $5\frac{1}{2}$ hours runtime (using a 2.2MHz AMD Opteron processor, $(121)^3$ voxel mesh). In this work, the frequency response of a model was measured over 20 RF cycles, as a compromise between simulation runtime and accuracy of the resonant frequency estimate.

The spectrum may be improved by multiplying the timecourse by a windowing function (a Hamming window was used here), increasing the height of the resonance peak (fig. 5.21b). A further improvement is seen, particularly in the high frequency response, if data from the first RF cycle is discarded (fig. 5.21c). This cycle contains the high frequency noise previously noted as the TLM mesh initialises (fig. 5.21d).

Probe models are tuned iteratively. An initial estimate C_{est} of the required capacitance is provided to the simulator. Simulations are then run with slightly lower and slightly higher capacitance ($C_1 = C_{est} - \Delta C$, $C_2 = C_{est} + \Delta C$), and the respective resonant frequencies f_1 and f_2 measured. An estimate of the capacitance required to resonate at f_0 is then calculated using

$$C_{est} = \frac{1}{\frac{f_0 - f_1}{f_2 - f_1} \left(\frac{1}{C_2} - \frac{1}{C_1} \right) + \frac{1}{C_1}}, \quad (5.18)$$

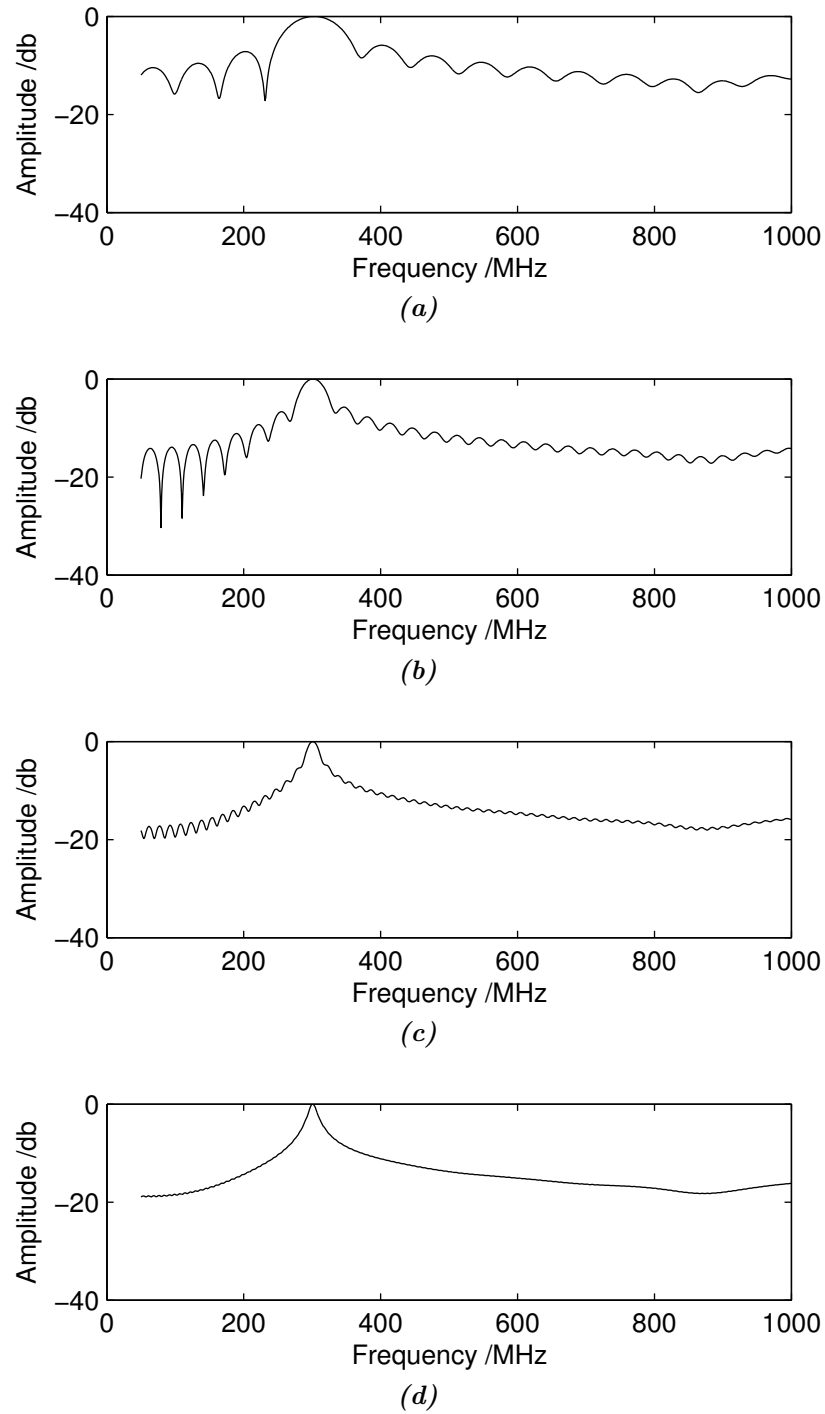


Figure 5.20: The Discrete Fourier Transform of the microstrip impulse response, recorded over (a) 5, (b) 10, (c) 20 and (d) 40 RF cycles.

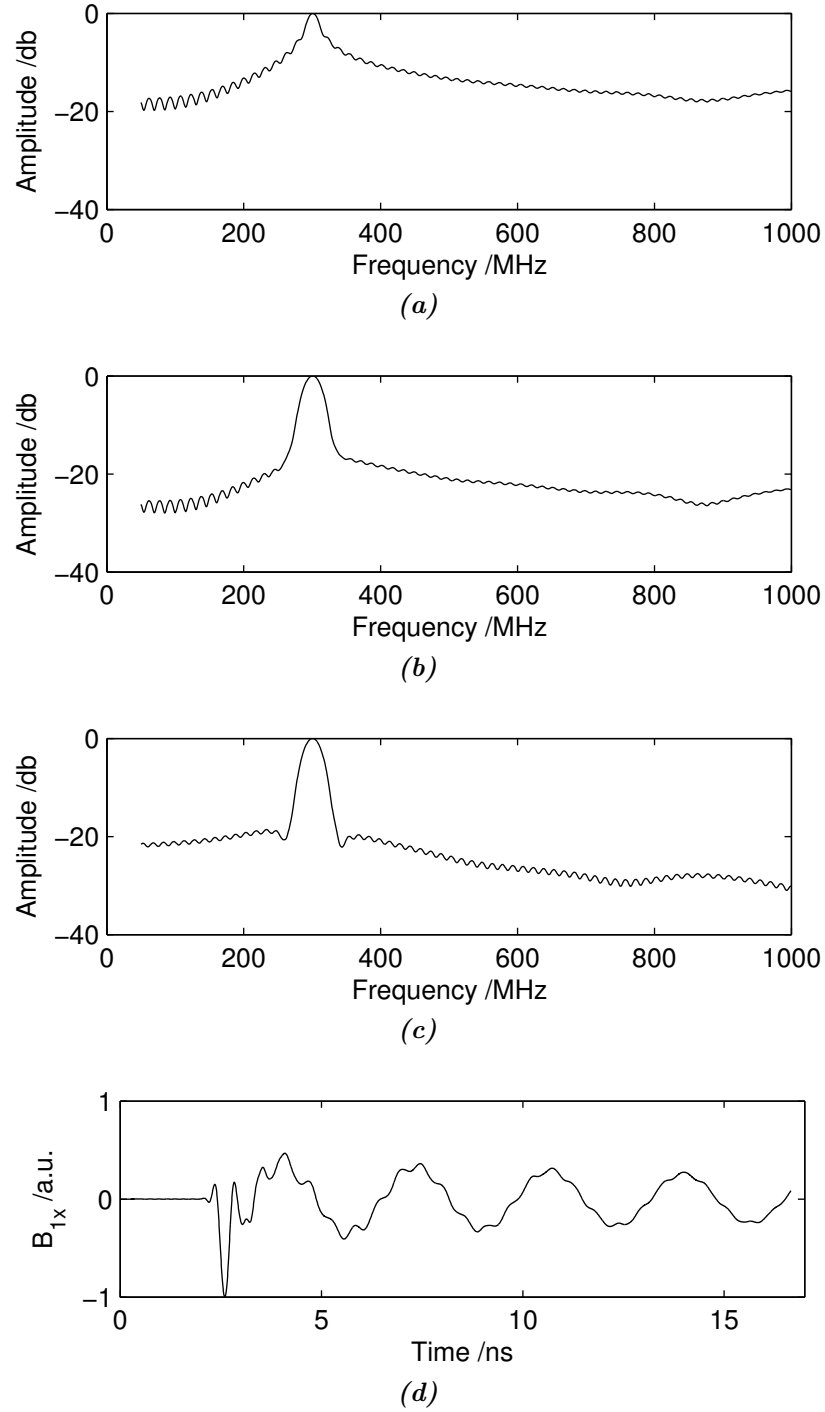


Figure 5.21: Improving the spectrum: (a) the raw Discrete Fourier Transform (shown for 20 RF cycles) may be improved by (b) applying a Hamming window; a further improvement is seen by (c) discarding the first RF cycle of data, as this contains (d) high frequency noise generated as the TLM mesh initialises.

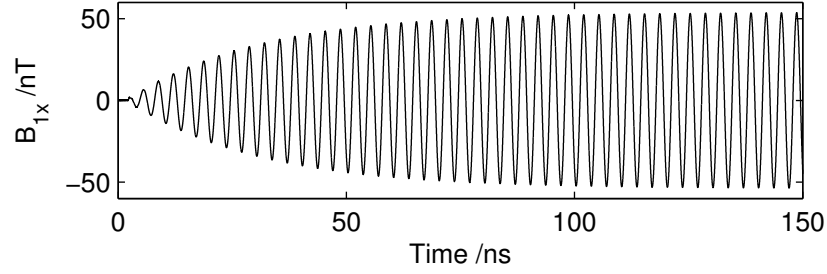


Figure 5.22: Magnetic field strength recorded in the centre of the head model, when the microstrip is excited with a sinusoidal voltage source.

and the simulation is rerun with the new value. If the resulting resonant frequency $f_{est} = f_0$, the simulation is terminated. Otherwise, C_{est} is used to replace either C_1 or C_2 in the above equation (whichever gives the larger error in f), C_{est} is recalculated, and the simulation is rerun. This cycle is repeated until the model is tuned to the desired frequency, usually requiring 3–5 iterations.

Once the model is tuned, a further simulation is run, driving the probe with a sinusoidal voltage source at the resonant frequency, to generate steady-state magnetic and electric fields inside the sample (e.g. figs. 5.24 and 5.26). Fig. 5.22 shows the build up of the magnetic field inside the head as the microstrip is excited. In this work, steady state fields were recorded after 20 RF cycles (13,324 iterations).

5.3.4 Microstrip Fields

The microstrip was tuned using the procedure described above, while loaded with the HUGO head model. The impulse response of the loaded and unloaded tuned microstrip was then compared (fig. 5.23). The unloaded and loaded microstrip Q -factors were measured to be 87.7 and 26.1. Both figures are rather low for a microstrip (an unloaded Q of several hundred might be expected), but a reduction in Q by a factor of 3.3 on loading indicates that the microstrip is coupling to the sample. There was no measurable shift in the resonant frequency of the strip when the sample was removed.

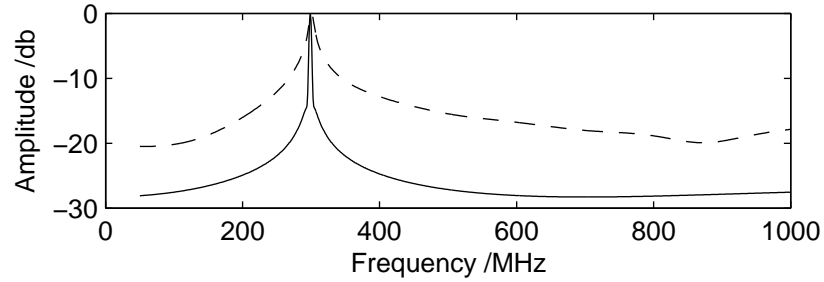


Figure 5.23: The impulse response of the loaded (dashed) and unloaded (solid) microstrip.

The transmit (B_1^+) and receive (B_1^-) magnetic fields generated by a microstrip are shown in fig. 5.24. The B_1 field is strongest at the centre of the strip, falling off rapidly with distance from it. The highest field intensity occurs between the strip and the ground plane. The strip is driven by a $1V_{peak}$ source, producing a maximum field inside the head of $1.08 \mu\text{T}$. The transmit and receive fields are clearly different, being approximately mirrored about the sagittal plane.

Figure 5.25 shows a relative SNR map for the probe when it is used as both transmitter and receiver, calculated using eqn. 5.4. The sensitivity of the probe is reasonably uniform close to the surface across the back of the head. Such a probe could be used to image the visual cortex, for example. Although the transmit and receive fields produced by the probe are asymmetric, the sensitivity resulting from their combination is symmetric.

Figure 5.26 shows the electric field generated by the microstrip. A null can be seen in the centre of the strip, with the highest electric field concentrated around the capacitors as expected. It is interesting to note the relatively high electric field at the tip of the nose, the point furthest from the microstrip.

Figure 5.27 shows the SAR levels induced by the microstrip with the transmit amplitude scaled to produce a 90° nutation at the location of the maximum $|B_1^+|$ field inside the brain. Peak SAR levels occur in the brain and brain stem, rather than skin and bone that is closer to the microstrip (c.f. fig. 5.26).

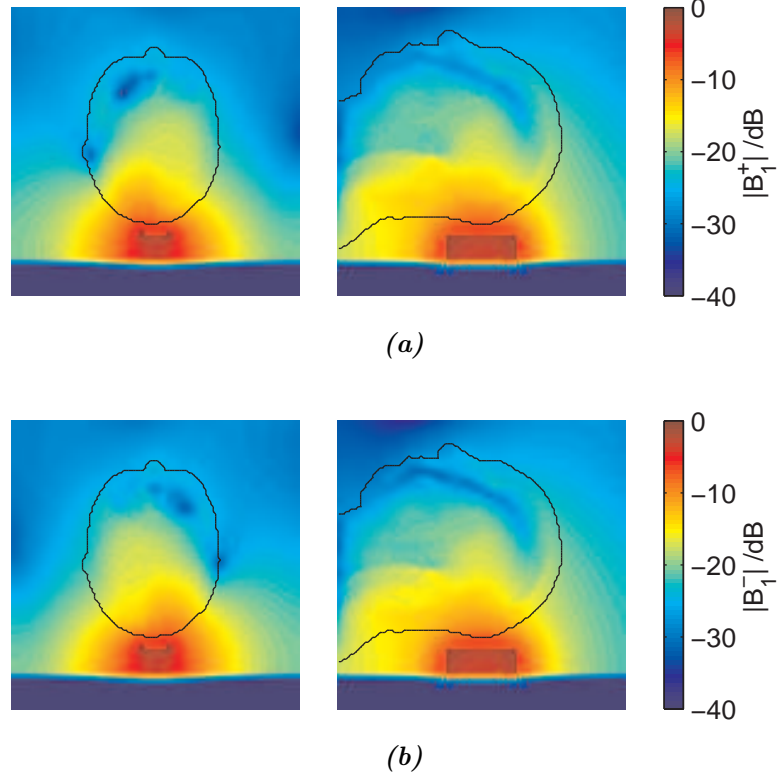


Figure 5.24: B_1 (a) transmit and (b) receive fields generated by a microstrip element placed at the back of the head. The contours show -3, -6 and -9 dB levels, relative to the maximum field inside the head.

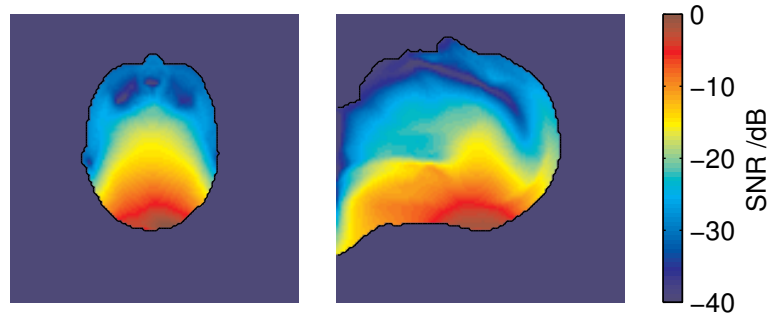


Figure 5.25: Relative SNR inside the head, using a single microstrip as both a transmit and receive element.

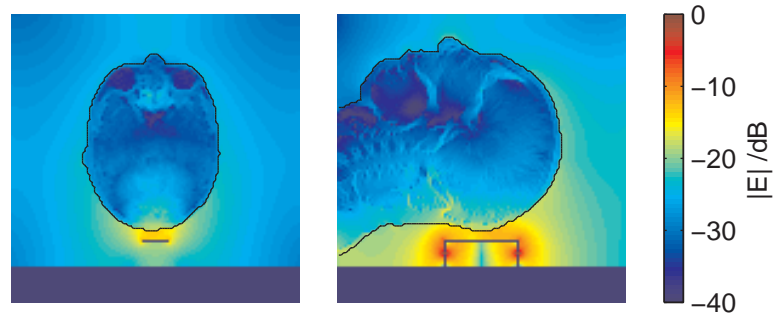


Figure 5.26: The electric field generated by the microstrip.

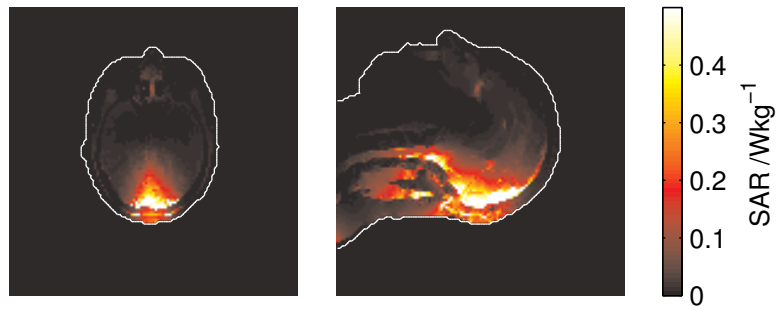


Figure 5.27: SAR (W/kg) per voxel inside the head due to a single microstrip.

5.3.5 Strip Geometry

In this section the effect of varying the microstrip width, length and height above the ground plane is investigated.

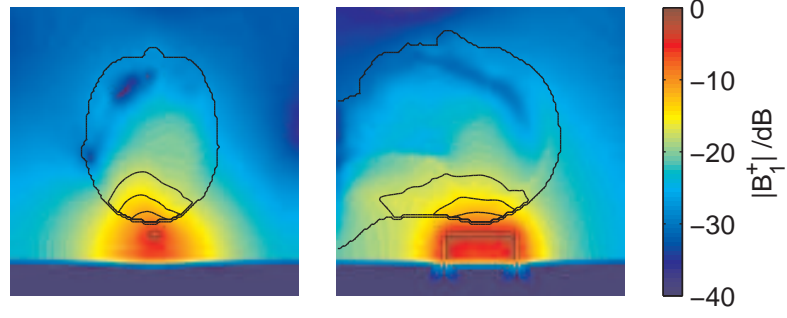
The transmit (B_1^+) and receive (B_1^-) fields produced by microstrips of three different widths ($w=9, 57$ and 111mm , $\ell=93\text{mm}$, $h=30\text{mm}$) are shown in figs. 5.28 and 5.29 respectively. The thin microstrip produces a very localised magnetic field which does not couple strongly to the head. As the strip is widened, it becomes less efficient at generating a magnetic field, but the field it produces is more uniform inside the head. Note that each transmit field in fig. 5.28 has been normalised to the peak value inside the head, equivalent to adjusting the transmit power to produce the same peak nutation, while the receive fields in fig. 5.29 are all shown on the same scale. The relative SNR of the three strips is plotted as a function of depth inside the head in fig. 5.31. The thin strip produces a higher SNR close to the head surface, but at depths greater than 30mm inside the head, wider strips give slightly higher SNR. The smaller field range produced by the 111mm strip is better suited for use as a transmit element, while the 9mm strip is better suited to reception due to its higher absolute sensitivity.

Electric fields produced by the three strips are shown in fig. 5.30. Like the magnetic field, the electric field inside the head also increases with increasing strip width, raising the SAR level (fig. 5.32). Fig. 5.33 shows the unloaded and loaded Q -factor of the microstrip as a function of strip width. The unloaded Q remains almost constant, while the loaded Q decreases as the strip width increases. This is consistent with sample-strip coupling increasing with strip width.

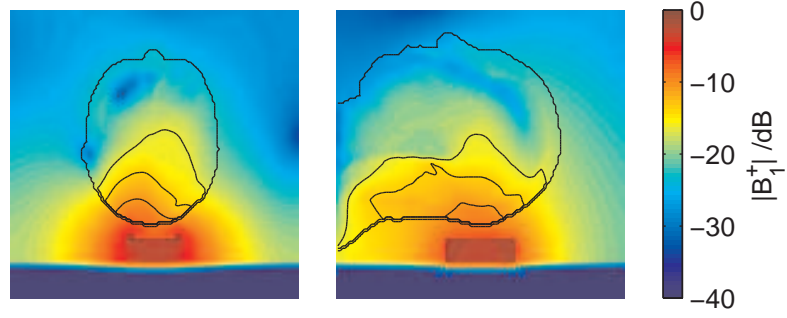
Transmit (B_1^+) and receive (B_1^-) fields produced by microstrips at three different lengths ($\ell=33, 117$ and 243mm , $w=33\text{mm}$, $h=10\text{mm}$) are shown in figs. 5.34 and 5.35, again scaling the transmit fields individually while showing all receive fields on the same scale. Increasing the strip length increases the penetration depth of the magnetic field, as well as the superior-inferior coverage (fig. 5.37). Increasing the strip length improves both the transmit and receive properties of the strip. The electric field inside the head

also increases, due to the larger region in close proximity to the longer strips, causing a slight increase in the peak SAR, but virtually no increase in the volume averaged SAR (fig. 5.38). The ratio of loaded to unloaded Q -factor increases with increasing strip length, again due to increased sample-strip coupling.

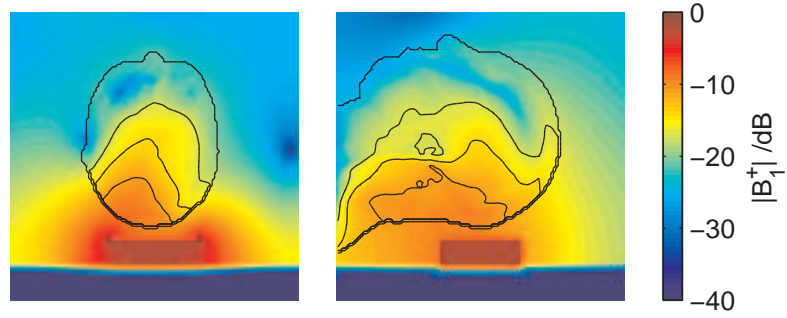
Transmit (B_1^+) and receive (B_1^-) fields produced by microstrips at three different heights ($h=6, 21$ and 54mm , $w=33\text{mm}$, $\ell=105\text{mm}$) are shown in figs. 5.40 and 5.41. The microstrip height was adjusted by lowering the ground plane, maintaining a constant distance between the strip and the head. Reducing the distance between the strip and the ground plane concentrates the magnetic field closer to the strip, reducing the field penetration into the head. Raising the strip further away from the ground plane gives stronger coupling to the head, but also requires more space for the probe. Increasing the gap between strip and ground plane again improves both the transmit and receive properties of the element. The change in SNR with different strip heights is small except at the surface of the head (fig. 5.43). Changing the strip height changes the electric field intensity below the strip, but has little effect on the electric field above it (fig. 5.42). The unloaded Q -factor of the probe is again constant, while the loaded Q decreases with increasing strip height.



(a) strip width = 9mm

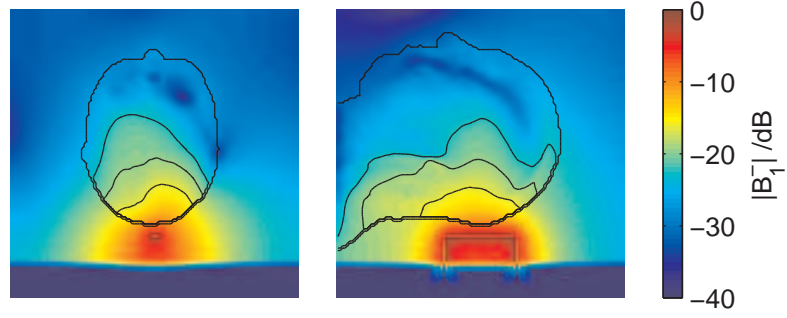


(b) strip width = 57mm

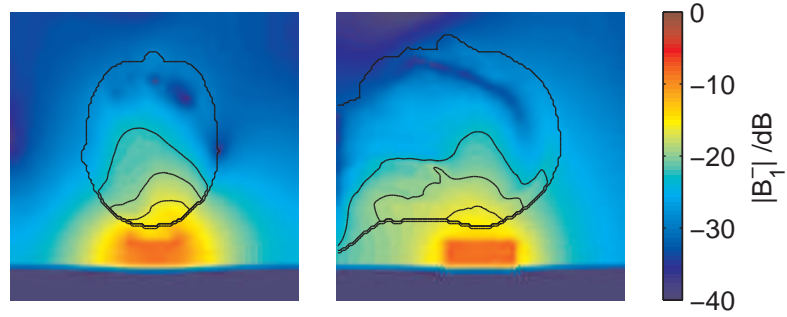


(c) strip width = 111mm

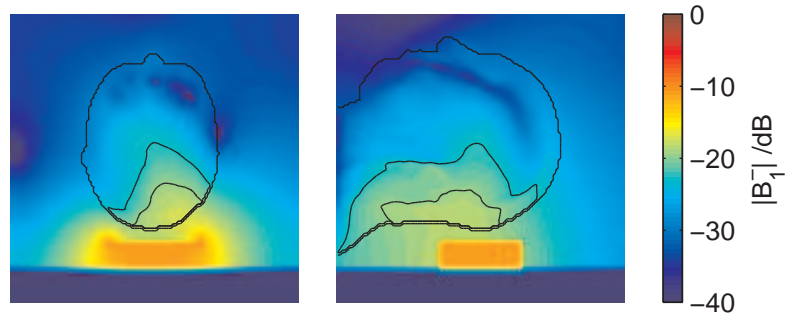
Figure 5.28: The transmit $|B_1^+|$ field produced by (a) 9 mm, (b) 57 mm and (c) 111 mm wide strips. Each strip field has been individually normalised to its peak value; contours show -3, -6 and -9dB levels relative to the peak field inside the head.



(a) strip width = 9mm

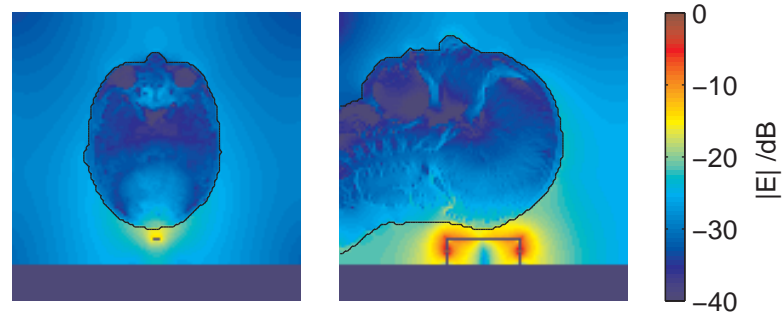


(b) strip width = 57mm

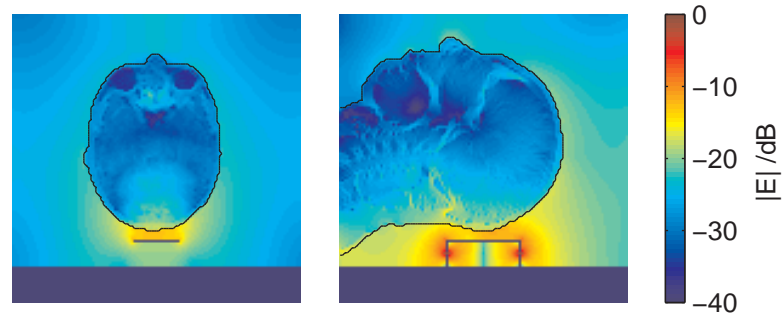


(c) strip width = 111mm

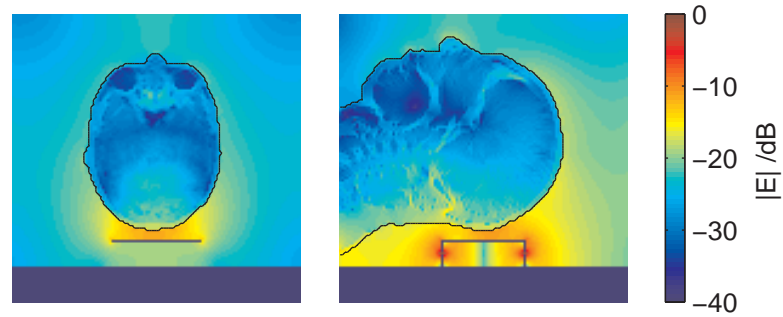
Figure 5.29: The receive $|B_1^-|$ field produced by (a) 9 mm, (b) 57 mm and (c) 111 mm wide strips. All fields are shown on the same scale, normalised to the peak $|B_1^-|$ value; contours show -3, -6 and -9dB levels relative to the peak field inside the head.



(a) strip width = 9mm



(b) strip width = 57mm



(c) strip width = 111mm

Figure 5.30: The electric field produced by (a) 9 mm, (b) 57 mm and (c) 111 mm wide strips.

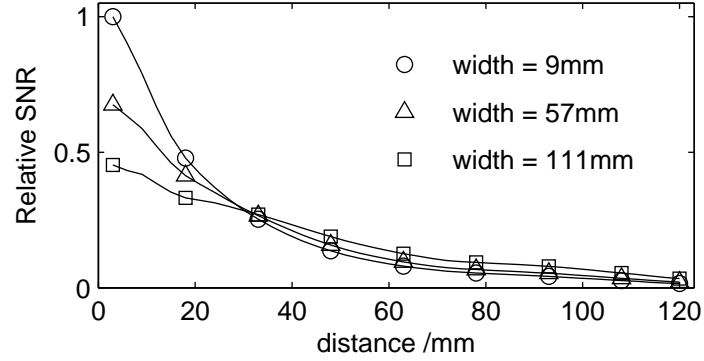


Figure 5.31: Relative SNR along an anterior-posterior line through the centre of the brain, as the width of the microstrip is varied.

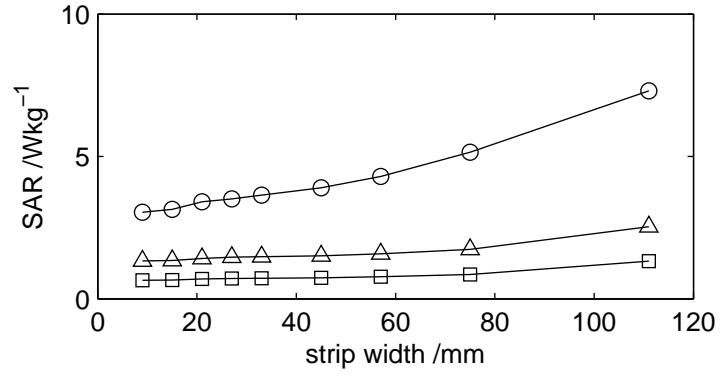


Figure 5.32: The peak SAR, averaged over 1 voxel (○), 3³ voxels (△) and 7³ voxels (□), as the microstrip width is varied.

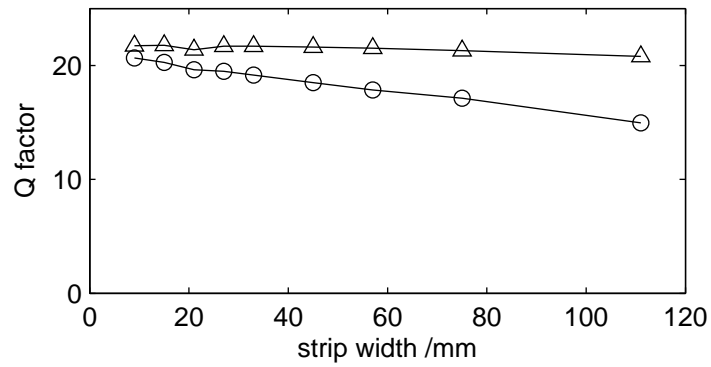
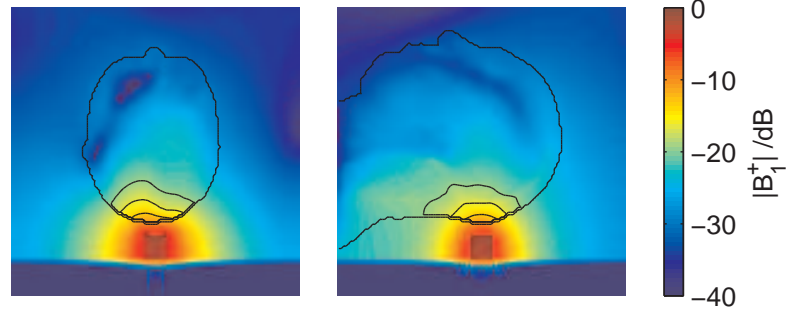
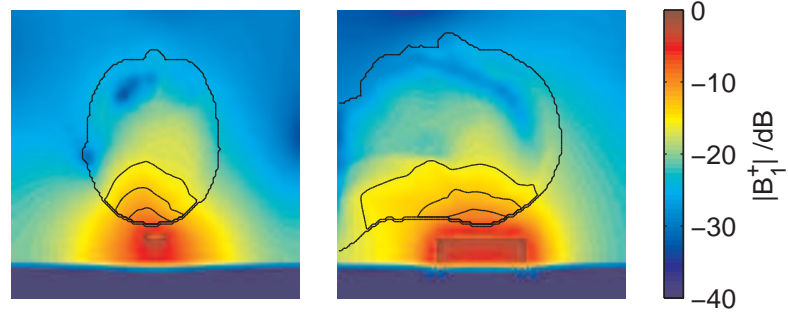


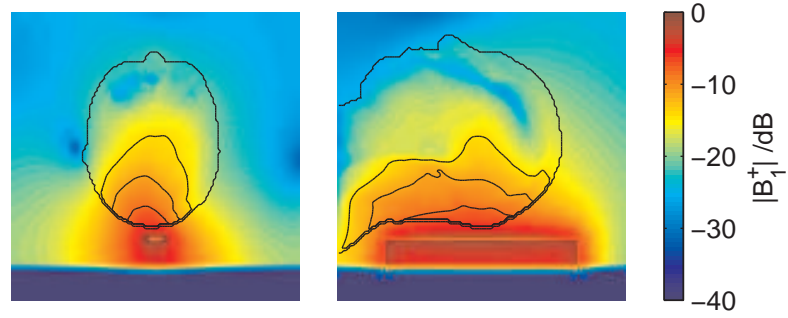
Figure 5.33: The unloaded (△) and loaded (○) Q factor as a function of strip width.



(a) strip length = 33mm

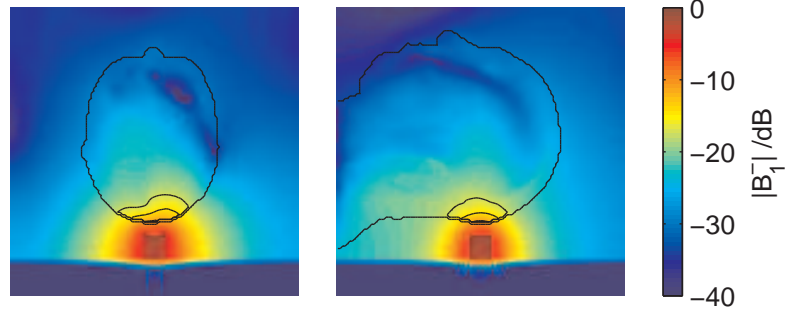


(b) strip length = 117mm

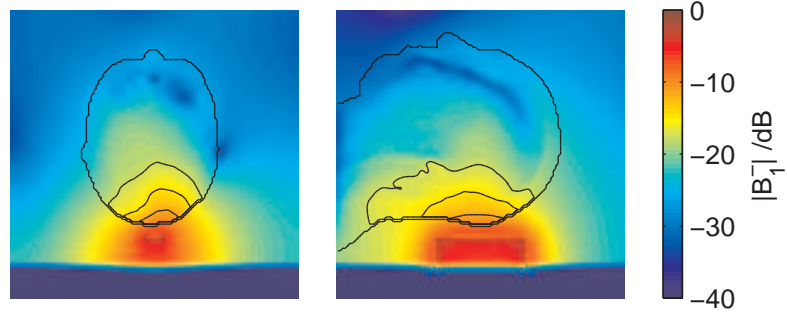


(c) strip length = 243mm

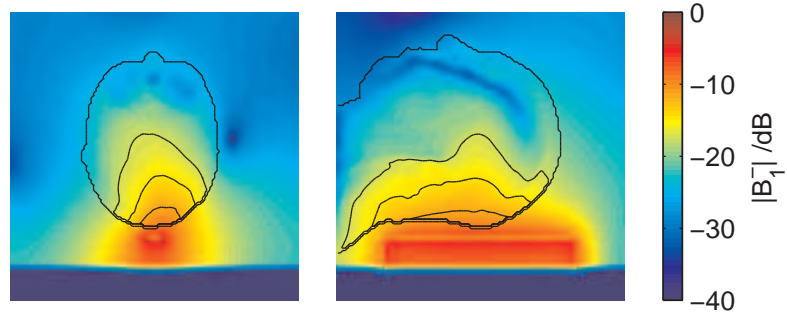
Figure 5.34: The transmit $|B_1^+|$ field produced by (a) 33 mm, (b) 117 mm and (c) 243 mm wide strips. Each strip field has been individually normalised to its peak value; contours show -3, -6 and -9dB levels relative to the peak field inside the head.



(a) strip length = 33mm

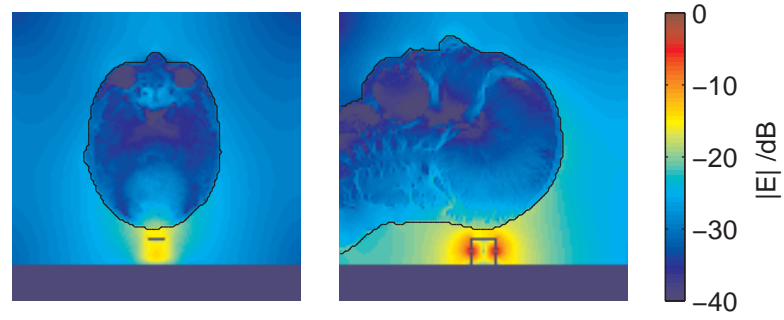


(b) strip length = 117mm

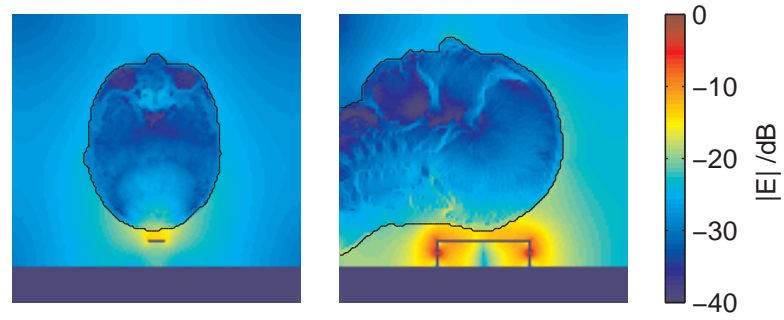


(c) strip length = 243mm

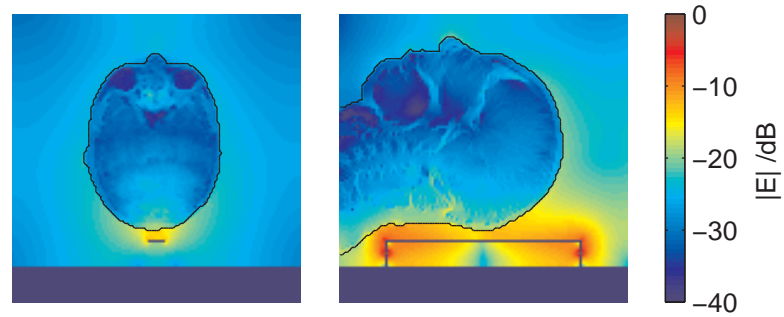
Figure 5.35: The receive $|B_1^-|$ field produced by (a) 33 mm, (b) 117 mm and (c) 243 mm wide strips. All fields are shown on the same scale, normalised to the peak B_1^- value; contours show -3, -6 and -9 dB levels relative to the peak field inside the head.



(a) strip length = 33mm



(b) strip length = 117mm



(c) strip length = 243mm

Figure 5.36: The electric field produced by (a) 33 mm, (b) 117 mm and (c) 243 mm wide strips.

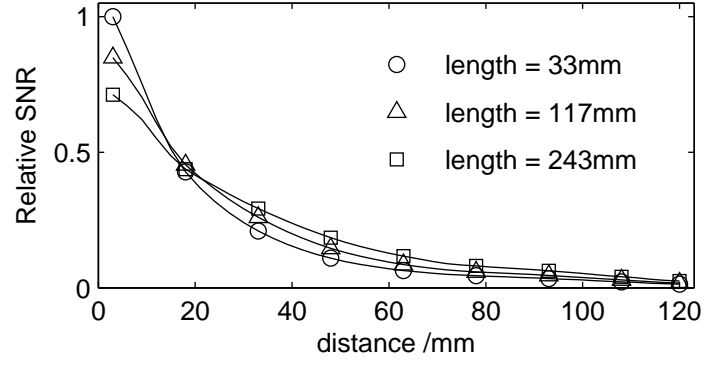


Figure 5.37: Relative SNR along a anterior-posterior line through the centre of the brain, as the length of the microstrip is varied.

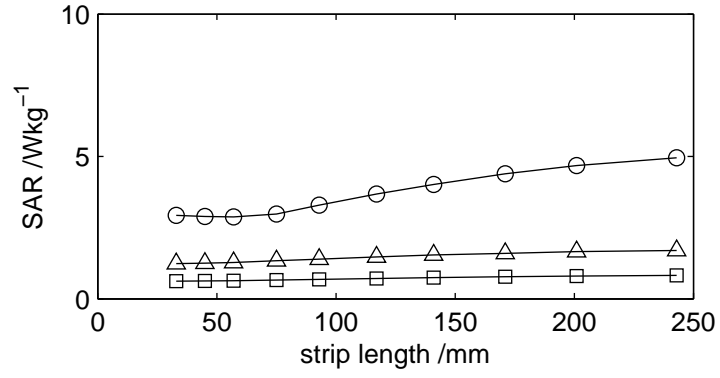


Figure 5.38: The peak SAR, averaged over 1 voxel (○), 3^3 voxels (△) and 7^3 voxels (□), as the microstrip length is varied.

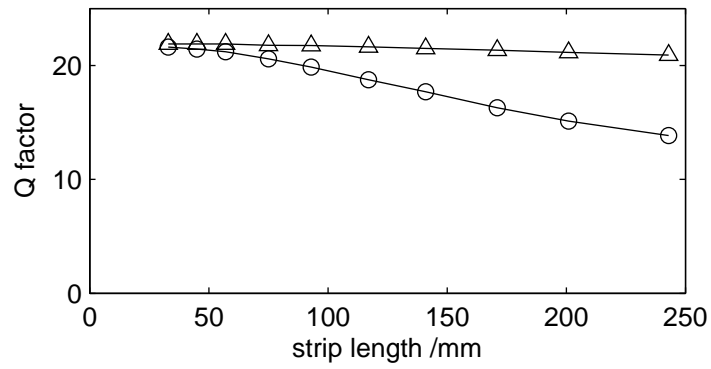
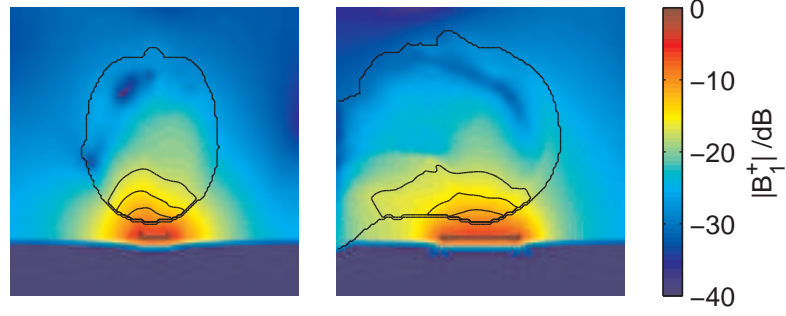
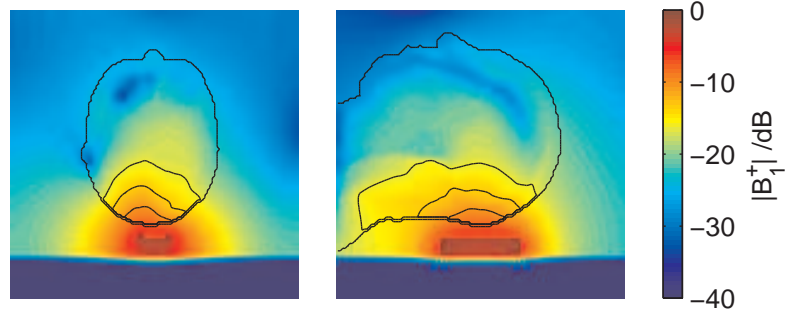


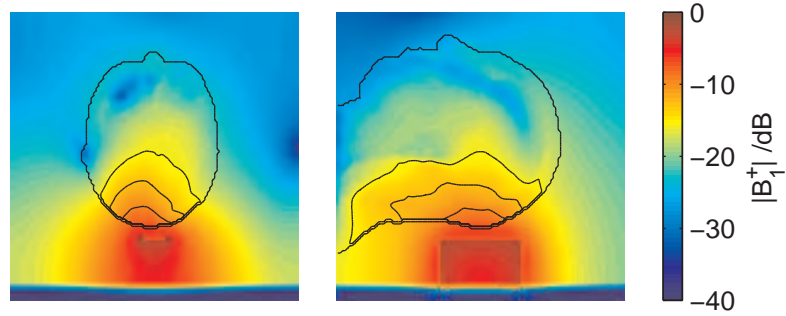
Figure 5.39: The unloaded(△) and loaded (○) Q factor as a function of strip length.



(a) strip height = 6mm

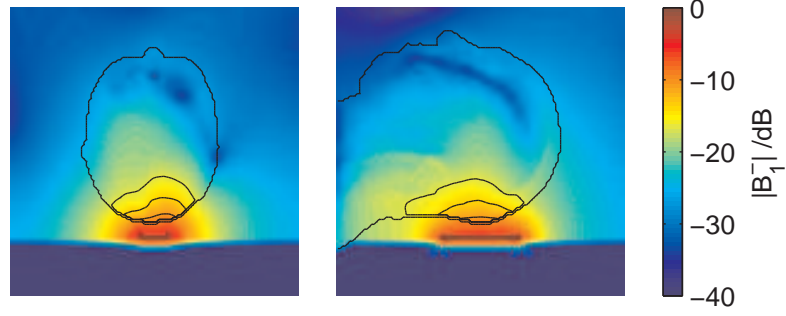


(b) strip height = 21mm

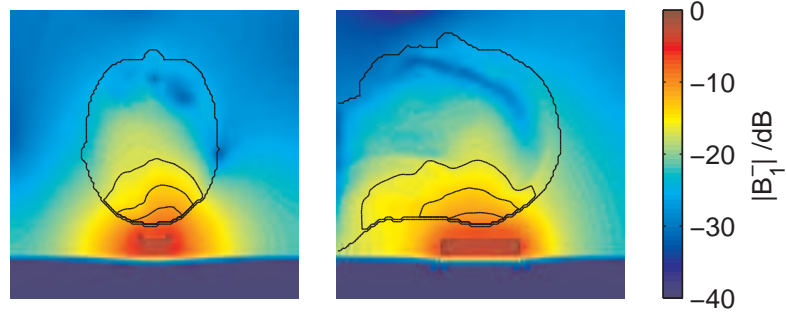


(c) strip height = 54mm

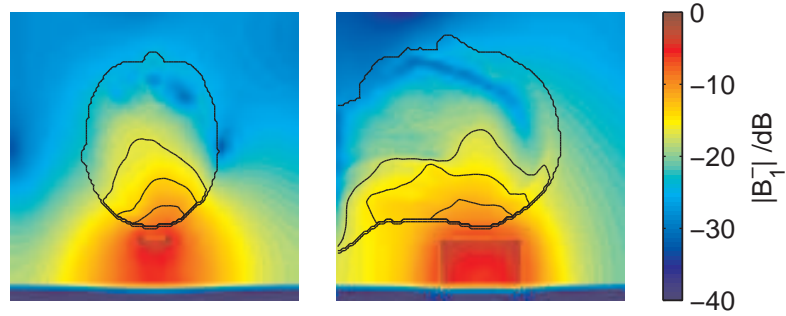
Figure 5.40: The transmit $|B_1^+|$ field produced by microstrips (a) 6 mm, (b) 21 mm and (c) 54 mm above the ground plane. Each strip field has been individually normalised to its peak value; contours show -3, -6 and -9dB levels relative to the peak field inside the head.



(a) strip height = 6mm

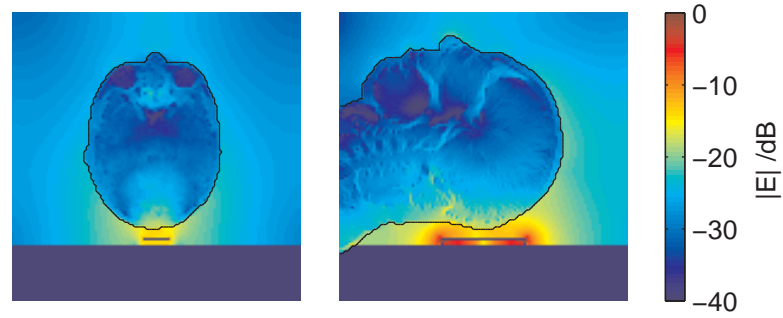


(b) strip height = 21mm

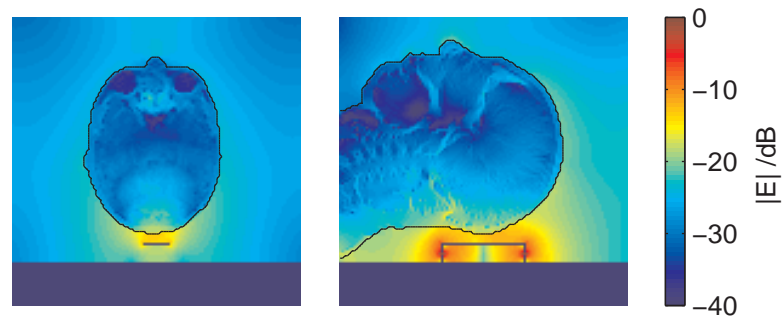


(c) strip height = 54mm

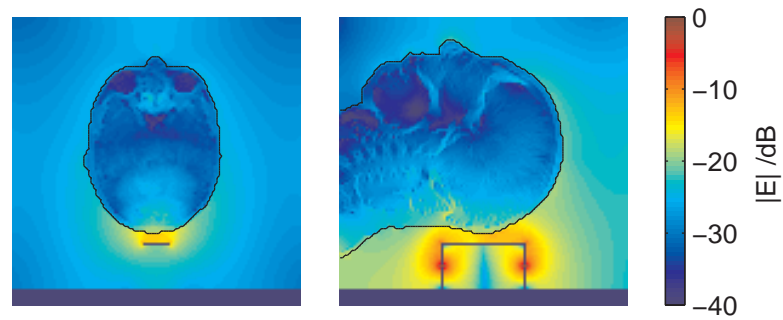
Figure 5.41: The receive $|B_1^-|$ field produced by microstrips (a) 6 mm, (b) 21 mm and (c) 54 mm above the ground plane. All fields are shown on the same scale, normalised to the peak B_1^- value; contours show -3, -6 and -9dB levels relative to the peak field inside the head.



(a) strip height = 6mm



(b) strip height = 21mm



(c) strip height = 54mm

Figure 5.42: The electric field produced by microstrips
 (a) 6 mm, (b) 21 mm and (c) 54 mm above the ground plane.

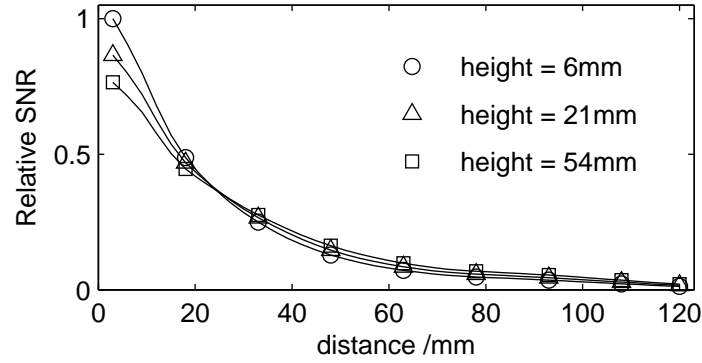


Figure 5.43: Relative SNR along a anterior-posterior line through the centre of the brain, as the height of the microstrip is varied.

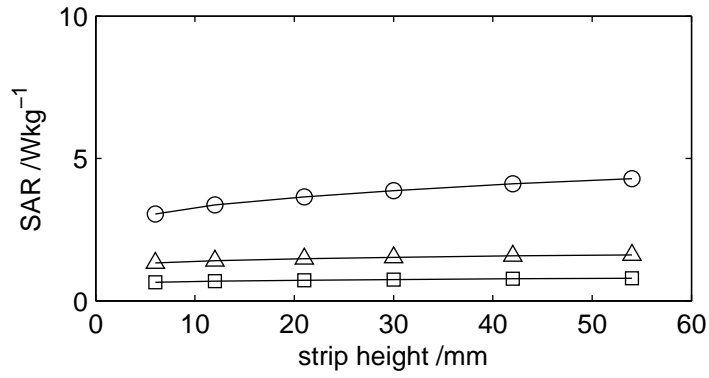


Figure 5.44: The peak SAR, averaged over 1 voxel (\circ), 3^3 voxels (\triangle) and 7^3 voxels (\square), as the microstrip height is varied.

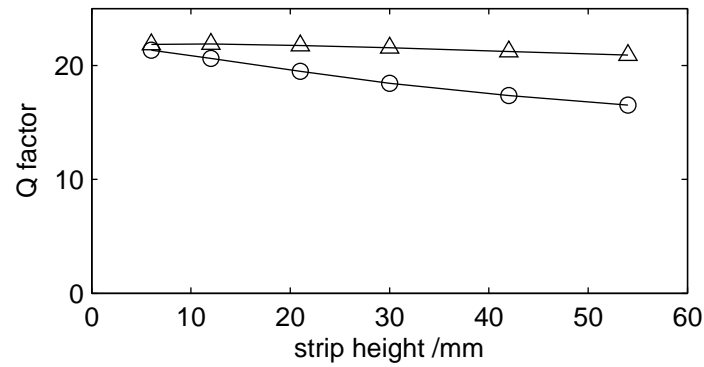


Figure 5.45: The unloaded(\triangle) and loaded (\circ) Q factor as a function of strip height.

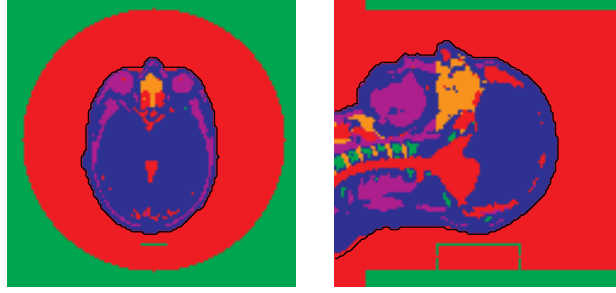


Figure 5.46: The shielded microstrip model.

Parameter	Symbol	Without shield	With shield	Units
Peak transmit B_1 field	$B_{1,max}^+$	0.208	0.228	μT
Peak receive B_1 field	$B_{1,max}^-$	0.192	0.213	μT
Peak electric field	E	9.32	11.6	V/m
Peak SAR over 1g of tissue	SAR_{1g}	0.62	0.64	W/kg
Peak SAR over 10g of tissue	SAR_{10g}	0.24	0.24	W/kg

Table 5.2: Changes in maximum field quantities when a shield is added around the microstrip. All fields have been masked to only show values inside the head.

5.3.6 Adding an RF Shield

Most RF probes are shielded to avoid coupling to structures inside the bore of the MR scanner, such as the gradient coils. Fig. 5.46 shows a model for a shielded microstrip. The shield is modelled as a solid block of copper, with a cylindrical cut-out for the probe cavity (324mm diameter). The relative position of the HUGO model to the microstrip, and the height of the microstrip above the ground plane, are identical to those in fig. 5.18.

Adding a shield lowers the resonant frequency of the microstrip from 300MHz to 289MHz. The probe was retuned to 300MHz, requiring a reduction in the capacitance at each end of the strip from 10.4pF to 9.47pF. A small change in both the magnetic and electric fields was observed, summarised in table 5.2.

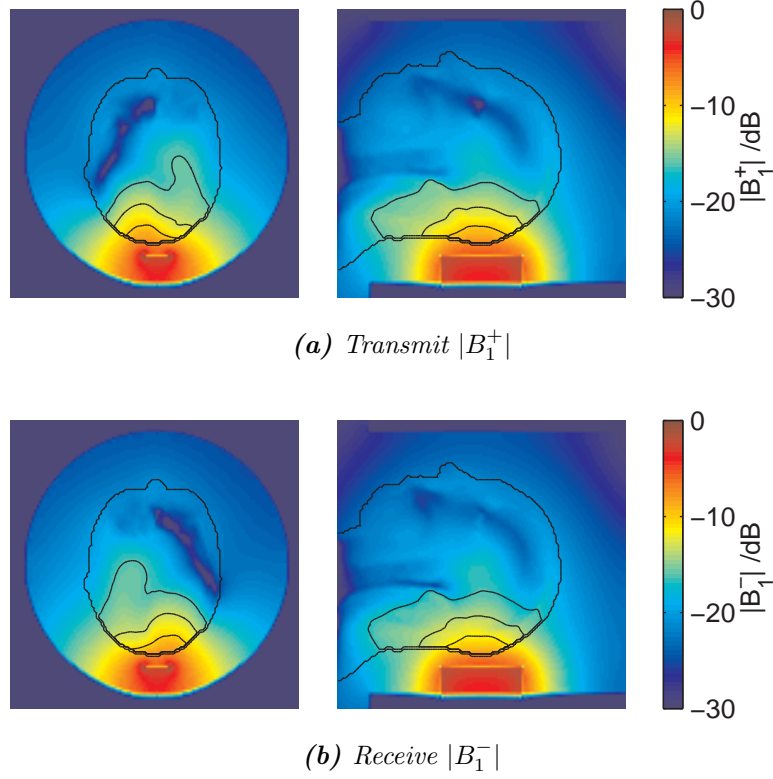


Figure 5.47: Rotating magnetic fields generated by a microstrip element placed at the back of the head, inside an RF shield. The contours show -3, -6 and -9dB levels relative to the peak field inside the head.

Figs. 5.47 and 5.49 show the magnetic and electric fields generated by the microstrip inside the RF shield, with the resulting SNR and SAR maps shown in figs. 5.48 and 5.50 respectively. By comparing figs. 5.47 to 5.24 it can be seen that, with the addition of the shield, the magnetic field penetrates slightly further into the head. There is also a small increase in the electric field around the face (furthest from the strip), but the effect is too small to show up on the SAR map. After retuning, changes introduced by the addition of an RF shield around the microstrip are small.

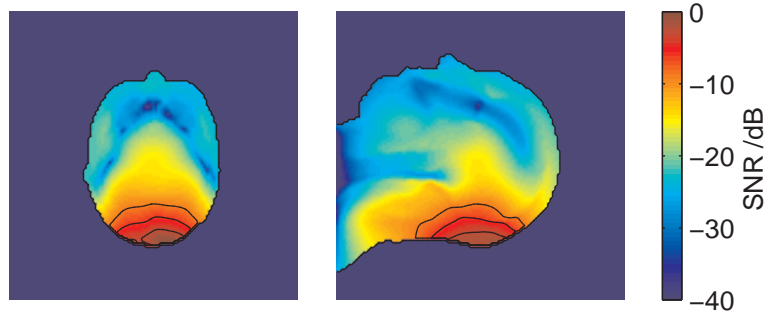


Figure 5.48: Relative SNR inside the head, using a single microstrip as both a transmit and receive element.

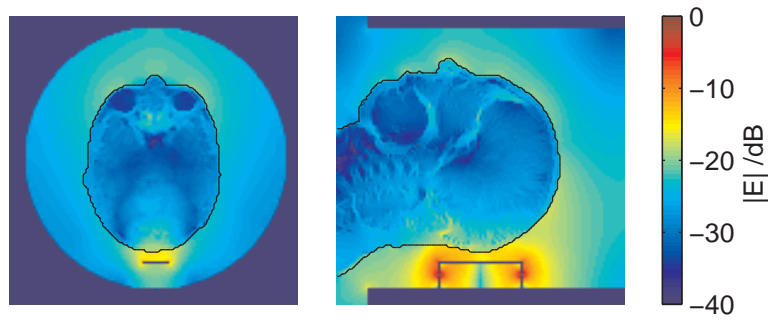


Figure 5.49: The electric field generated by a microstrip.

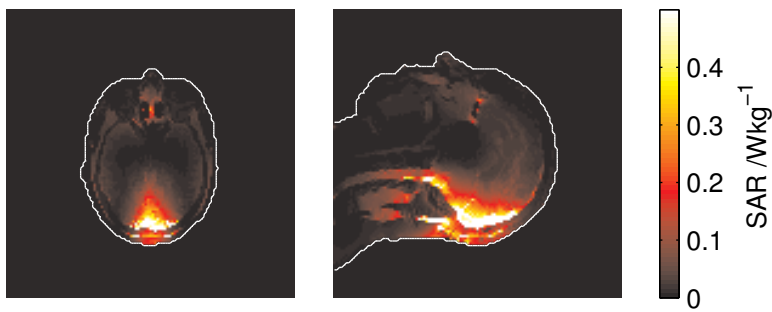


Figure 5.50: SAR per voxel inside the head due to a single microstrip inside an RF shield.

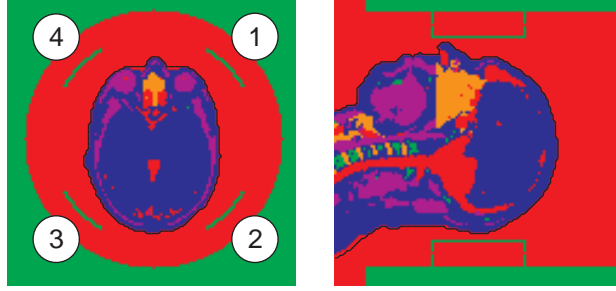


Figure 5.51: The four-microstrip array probe model. The numbers indicate strip labels.

5.4 A Microstrip Array Probe

In this section an array probe for use at 300MHz, constructed from four microstrips, is investigated. The probe model is shown in fig. 5.51. The microstrips are built on a 258mm diameter cylindrical surface surrounding the HUGO model. The ground plane forms a continuous RF shield around the probe. Coupling between the probe elements, and it's effect upon B_1 field distribution, is investigated. The performance of the array as a quadrature transmit probe, and a quadrature and parallel receive probe is then investigated.

5.4.1 Single Strip Response

The first step was to tune the probe. Each element was tuned to 300MHz using the method described in section 5.3.3. The capacitance required to tune each strip was determined while the remaining strips were detuned by replacing their capacitor voxels with copper (equivalent to short circuiting the capacitors). Simulations were then run with all strips tuned simultaneously, to investigate the effects of coupling between strips. Each strip was excited in turn with an impulse, and the response from all four strips recorded (fig. 5.52). A second resonant mode can be seen for each strip at approximately 650MHz, which becomes stronger when all strips are tuned. This is especially true for the fourth strip, whose 300MHz resonance almost completely disappears when all strips are tuned.

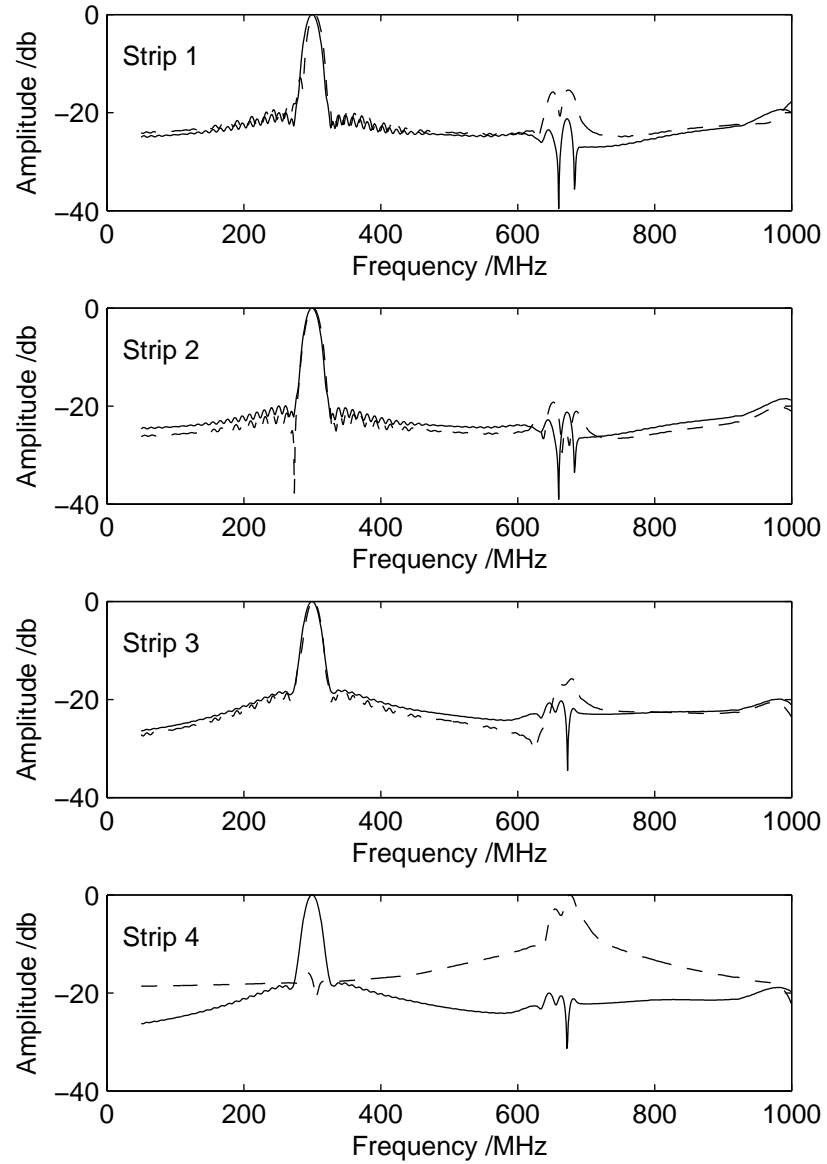


Figure 5.52: Impulse response of each strip with non-driven strips detuned (solid) and tuned (dashed).

		Receive			
		1	2	3	4
Transmit	1	0	-3.1	-5.4	-9.0
	2	-3.4	0	-6.4	-7.8
	3	-5.4	-6.0	0	-12.9
	4	-5.4	-6.2	-7.4	0

Table 5.3: Coupling between strips in the array probe (dB).

The coupling between strips was measured by exciting one strip with an impulse, and recording the voltage induced in all four strips (fig. 5.53), and calculating the height of the resonant peak in each strip. Note that despite the higher frequency mode found in strip 4 (fig. 5.52), the coupled response shows a strong peak at 300MHz. This procedure was repeated for each strip and the coupling calculated at a range of strip widths (table 5.3).

The coupling matrix is not symmetric, suggesting that the coupling calculation contains a high error. The poor resonant response of strip 4 can be seen, producing low coupling to all other strips. This is probably due to the poor resonance of strip 4, rather than lower coupling between this and other strips.

All the coupling figures are rather high. This may be an artifact of the spectral estimate, rather than a true result. It is hoped to improve upon the frequency domain modelling by using Prony's method [159, 160] in place of the Fourier transform, reducing the error in the resonant frequency and the height of the resonant response.

The B_1^+ fields produced when each strip is excited with a sinusoidal voltage source, while the other strips are detuned, are shown in fig. 5.54. Fig. 5.55 shows the fields obtained when one strip is driven while all strips are tuned, clearly showing the difference in magnetic field induced around the non-driven strips via coupling. The magnetic field inside the head, however, remains relatively unchanged.

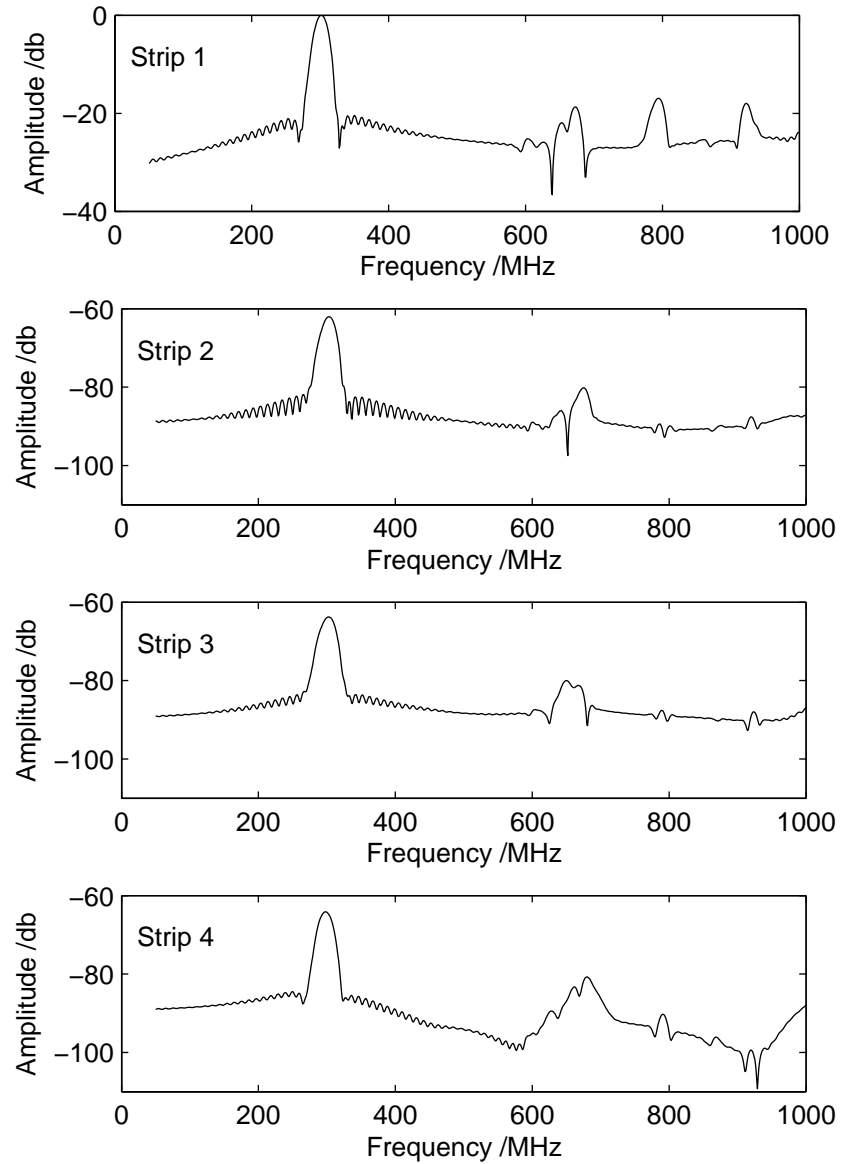


Figure 5.53: The impulse response recorded in strips 1–4, when strip 1 is given an impulse.

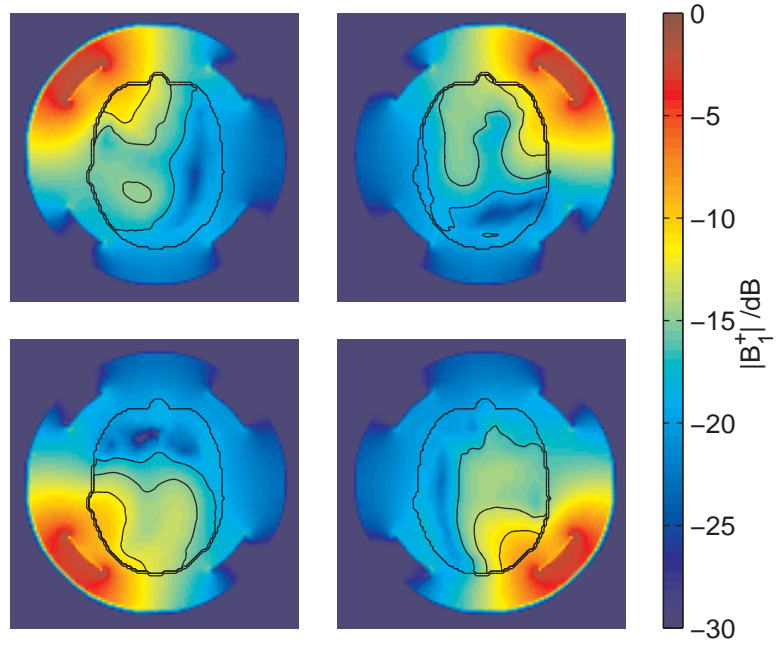


Figure 5.54: The $|B_1^+|$ field produced by each strip, with the other strips grounded.

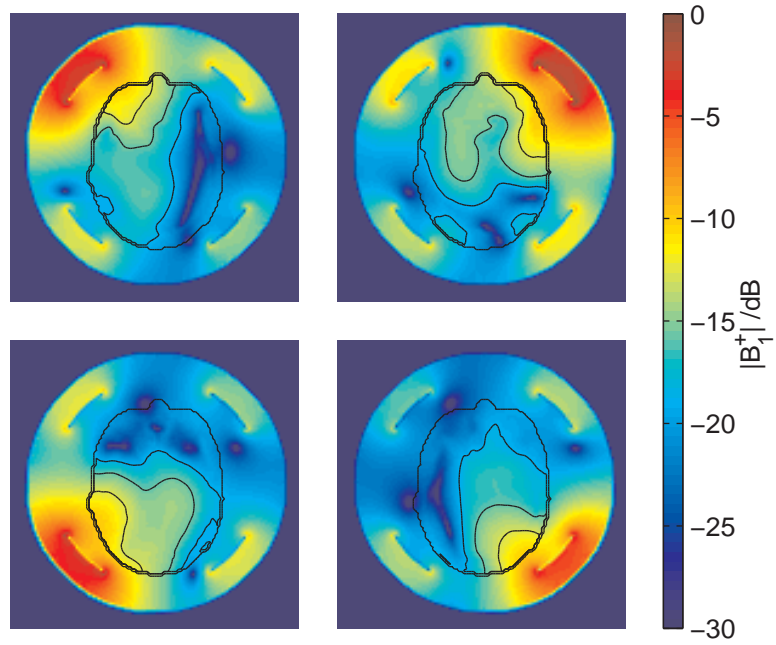


Figure 5.55: The $|B_1^+|$ field produced by each strip, with the other strips tuned.

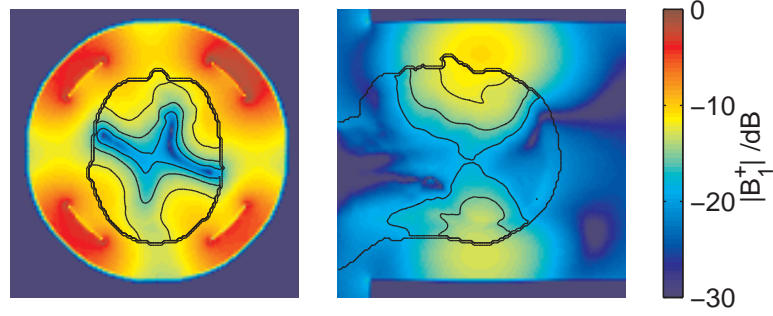


Figure 5.56: B_1^+ magnetic field produced by the array probe operated in quadrature mode. The contours show -3, -6 and -9 dB levels, relative to the maximum field inside the head.

5.4.2 Transmission

The transmit field generated when the array probe is driven in quadrature mode (i.e. strips are driven with sinusoidal voltage sources at phase $\phi = 0, \pi/2, \pi$ and $3\pi/2$) is shown in fig. 5.56. The field is far from uniform, containing a strong central null, which might not be expected from inspection of fig. 5.55. The null can be explained by examining the phase of the transmit signals generated by the strips (fig. 5.57). In the centre of the head, two strip fields have positive phase and two have negative phase, cancelling out to produce the null. One solution to this problem is RF shimming, where the phase (and amplitude) of the transmit channels are adjusted to produce the maximum field homogeneity [102].

5.4.3 Reception

The receptive field of the array probe is shown in fig. 5.59, operating in quadrature and parallel mode. In quadrature mode, signals from all four strips are phase shifted to account for their different positions around the probe and summed. This is equivalent to the operation of a standard volume probe such as the Birdcage. The field shows significant intensity variation over the volume of the head.

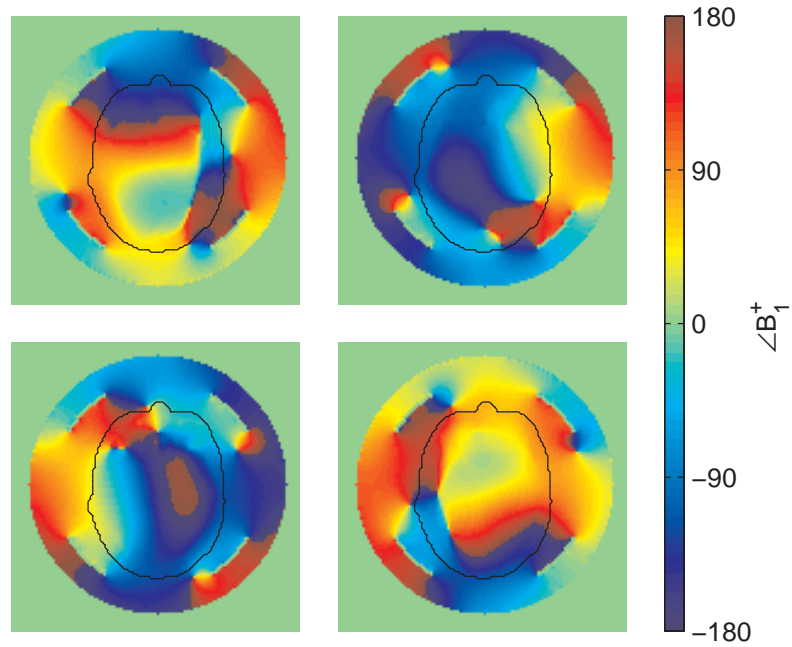


Figure 5.57: The phase of the transmit field produced by each strip. The phase has not been unwrapped, so sharp red-blue transitions are actually smooth phase wraps.

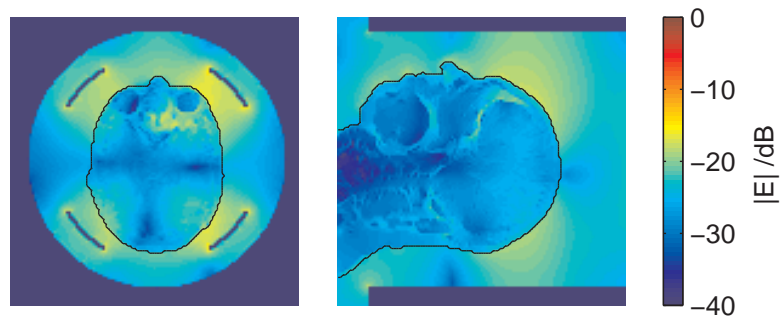


Figure 5.58: Electric field produced by the array probe operated in quadrature mode.

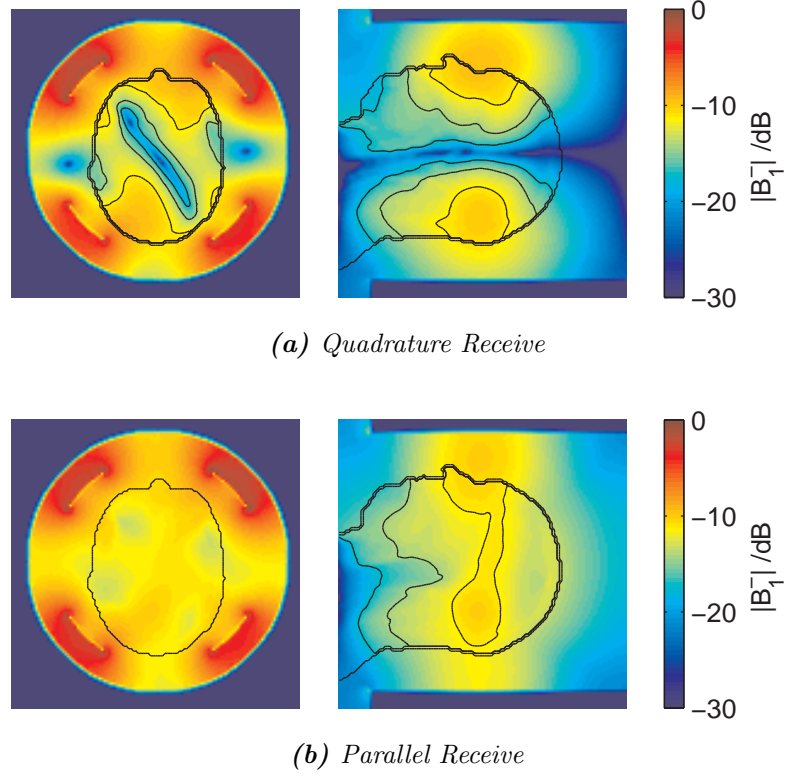


Figure 5.59: The receptive $|B_1^-|$ fields of the array probe operated in (a) quadrature and (b) parallel mode. Contours show -3, -6 and -9 dB levels, relative to the maximum field inside the head.

In parallel mode each strip is connected to an independent receive channel. Images detected by each channel are then be reconstructed separately, before being combined. The advantage of this method is that interference in the received signal is removed, clearly seen as higher field homogeneity in fig. 5.59b, where the entire coronal section is within -3dB of the peak value. This field map was constructed by summing the $|B_1^-|$ fields produced by driving each strip individually. All four strips were tuned during this experiment to fully model coupling between strips.

5.5 Discussion

This chapter introduced the full wave electromagnetic modelling of RF probes using the Transmission Line Matrix (TLM) method.

The Birdcage probe simulations demonstrate the transition from long to short wavelength, and the effect this has on B_1 field homogeneity. It is common to consider only the magnitude of B_1 fields produced by different probe elements. At 128MHz and below, the B_1 field has virtually the same phase at all locations across the sample, and the composite B_1 field is approximately the sum of the magnitudes of the separate fields. At higher frequency the B_1 field phase varies significantly across the sample, and the vector sum of fields from different probe elements must be considered, allowing the possibility of field cancellation through interference. Interference can occur between independent elements of an array probe, or between spatially separate parts of a volume probe.

A consequence of changes in the electric field produced by the probe, as the operating frequency increases, is shown to be a shift in location of peak SAR from the surface of the head to deeper regions such as the brain and brain stem. This is significant because natural cooling mechanisms function most efficiently at the surface. Therefore not only does SAR increase at higher frequency, but cooling efficiency decreases.

The simplified Birdcage probe model was deliberately used, as it demonstrates the general difficulty in designing volume probes for high frequency operation. The probe model was not resonant, so does not suffer from coupling effects, either between probe elements or between the probe and the sample. These effects will only serve to further degrade the probe performance. Inhomogeneity in the magnetic field generated by this probe model is caused by its spatial extent, rather than any specifics of its design.

A half wave microstrip line has been shown to be suitable for use as a high frequency RF probe element. Tuning of a simulated resonant microstrip, loaded with the human head, was shown and loaded and unload Q -factors found. Fields produced by microstrips in a range of sizes were investigated.

It was shown that wider and longer microstrips, further from the ground plane, couple more strongly to the head, and as a result the magnetic field they produce penetrates further into the head. This is accompanied by a rise in peak SAR levels. It was further shown that adding an RF shield around the microstrip and head does not significantly change the magnetic field produced by the strip.

An array probe, consisting of four independent half wave microstrip elements, was then investigated. Resonant circuits placed in close proximity will inevitably couple to one another. Coupling between strip elements was examined by comparing the impulse response of each strip with the other strips both tuned and detuned. A higher frequency resonant mode, at approximately 650MHz, is seen when all strips are tuned. One strip in particular (strip 4) showed a much higher response at this frequency than at 300MHz. Unfortunately there is not enough resolution in the spectra to see splitting of the resonant peaks. Coupling between strips was also examined by exciting one strip and measuring the signal induced in the other strips. The coupling matrix is rather asymmetric, which is thought to be related to the unexplained behaviour of strip 4.

Magnetic fields produced by the array probe with one strip tuned and the other strip detuned, and with all strips tuned, were investigated. Coupling between tuned elements is seen to slightly improve the magnetic field inside the head when a single strip is driven. When all strips are driven in quadrature, a large central null is seen in the magnetic field, which is explained by examining the phase of the individual strip fields. The null is clearly caused by magnetic field cancellation. The receptive field of the probe is also investigated. When the probe is used in quadrature receive mode, a central null is again observed. If the signal from each strip is collected independently, the signals can be combined without phase information preventing field cancellation. This is equivalent to combining the magnitudes of the individual strip fields, which removes the central null and significantly improves the homogeneity of the receive field. Parallel receive probes therefore offer a significant increase in available signal when used at high frequency.

Chapter 6

Simulated Imaging

6.1 Introduction

In the previous chapter, the B_1 field generated by different probe designs was investigated. In this chapter, the effect of the calculated B_1 field inhomogeneity on the acquired image is explored.

In order to test different imaging sequences using highly inhomogeneous B_1 fields, a Bloch simulator was developed. The simulator models the evolution of bulk magnetisation in a test sample under an applied magnetic field. It does this by solving numerically the Bloch equations, allowing the effects of arbitrary transmit and receive B_1 fields to be investigated. In particular, it allows imaging sequences to be tested using B_1 fields generated by specific probe designs using TLM simulation.

In this chapter the Bloch simulator is introduced. It is then validated using three standard imaging sequences (Spinwarp, EPI and Burst) using ideal homogeneous B_1 fields. Echo Planar Imaging is then further investigated using realistic receive fields. Improvements in image quality are shown using both phased array and SENSE parallel imaging methods. The effect of a highly inhomogeneous transmit field is then explored. A new imaging sequence is introduced using sequential excitations by different probe elements

to achieve a further improvement in image homogeneity. The ability of the new sequence to separate images due to different excitation pulses (different transmit fields) is shown using test fields, and then TLM generated B_1 fields for the four microstrip probe modelled in the previous chapter.

6.2 Transmit and Receive Field Dependency

The magnetisation M induced in a sample can be calculated using

$$M \propto \rho \sin(\gamma\tau |B_1^+| V) \quad (6.1)$$

where ρ is the spin density, γ is the gyromagnetic ratio, τ is the pulse duration and V is a dimensionless scaling factor due to driving voltage. $|B_1^+|$ is the magnitude of the positively rotating transmit field.

Image intensity can then be calculated from the local sample magnetisation and the complex conjugate of the probe receive sensitivity B_1^-

$$I \propto \rho \sin(\gamma\tau |B_1^+| V) (B_1^-)^* \quad (6.2)$$

Image intensity depends upon the sine of the transmit field magnitude and linearly upon the receive field magnitude for simple single pulse sequences such as gradient echo EPI.

Neglecting the effects of relaxation, eqn. 6.2 can be used to simulate simple imaging sequences. More complicated multipulse sequences, and relaxation effects, can be modelled by numerically integrating the Bloch equation.

6.3 Bloch Simulation

The behaviour of the bulk magnetisation of a sample under an applied magnetic field is described by the Bloch equation, usually presented in the dif-

ferential form

$$\frac{d\mathbf{M}}{dt} = \gamma \mathbf{M} \times \mathbf{B} - \frac{M_x \hat{\mathbf{x}} + M_y \hat{\mathbf{y}}}{T_2} - \frac{(M_z - M_0) \hat{\mathbf{z}}}{T_1} \quad (6.3)$$

Neglecting the relaxation terms, this can be rewritten as the integral

$$\mathbf{M}(t) = \gamma \int \mathbf{M} \times \mathbf{B} dt \quad (6.4)$$

The applied magnetic field B has three components

$$\mathbf{B}(\mathbf{r}, t) = \mathbf{B}_0 + (\mathbf{G}(\mathbf{r}, t) \cdot \mathbf{r}) \hat{\mathbf{z}} + \mathbf{B}_1(t) \quad (6.5)$$

where \mathbf{B}_0 is the static field, \mathbf{G} is the field gradient as a function of position \mathbf{r} and time t and \mathbf{B}_1 is the RF excitation field. By using a rotating frame of reference, the effective \mathbf{B}_0 component is reduced to zero. Eqn. 6.5 can now be written in discrete form

$$\mathbf{B}_{ij}^n = (G_x i + G_y j) \hat{\mathbf{z}} + \mathbf{B}_1^n \quad (6.6)$$

where n is the iteration number and i and j are the voxel co-ordinates. Eqn. 6.4 can be rewritten as a discrete recursive expression

$$\mathbf{M}_{ij}^{n+1} = \mathbf{M}_{ij}^n + \gamma \Delta t (\mathbf{M}_{ij}^n \times \mathbf{B}_{ij}^n) \quad (6.7)$$

where Δt is the timestep, and the magnetisation \mathbf{M} is now represented by a 2D array of vectors.

An imaging sequence is define by the gradient and RF time series. Given these series, the NMR signal can be simulated by iterating through equations 6.6 and 6.7.

6.3.1 Relaxation

We now return to the relaxation terms in eqn. 6.3. After evaluating eqn. 6.7, the following relaxation terms can be applied

$$M_x \leftarrow M_x \exp\left(-\frac{\Delta t}{T_2^*}\right) \quad (6.8a)$$

$$M_y \leftarrow M_y \exp\left(-\frac{\Delta t}{T_2^*}\right) \quad (6.8b)$$

$$M_z \leftarrow M_z \exp\left(-\frac{\Delta t}{T_1}\right) + M_0 \left[1 - \exp\left(-\frac{\Delta t}{T_1}\right)\right] \quad (6.8c)$$

where T_1 and T_2^* are known from the sample model.

In practice, tissue relaxation times are complicated, depending on many different factors [161]. For this reason, spin relaxation was not modelled in this study. Contrast in simulated images is entirely due to variation in proton density in the modelled materials.

6.3.2 Instantaneous Nutation

RF excitation typically occupies a small part of a complete imaging sequence. The structure of an RF pulse is on a much shorter timescale than the gradient waveforms. A complete pulse typically lasts 5–20ms, comparable to the duration of a short gradient blip. Accurately modelling an RF pulse requires a very short timestep Δt , increasing the number of iterations required to simulate the entire imaging sequence.

As we are not trying to model the detailed form of the RF pulse, a nutation may be modelled as an instantaneous rotation of the magnetisation vector by the flip angle. This allows a larger timestep Δt to be used, which reduces the number of simulation iterations required to complete an imaging sequence and so reduces the total simulation run time. The rotation is applied using a rotation matrix

$$\mathbf{M}_{ij} \leftarrow \mathbf{R}_{RF}(\alpha, \phi) \mathbf{M}_{ij} \quad (6.9)$$

where α is the flip angle, ϕ is the phase of the nutation and \mathbf{M} is the sample magnetisation (fig. 6.1). In order to calculate the matrix, the nutation can be separated into three rotations

$$\mathbf{R}_{RF}(\alpha, \phi) = \mathbf{R}_z(\phi) \mathbf{R}_y(\alpha) \mathbf{R}_z(-\phi) \quad (6.10)$$

First the magnetisation \mathbf{M} is rotated by $-\phi$ about the z -axis into the xz -plane. This simplifies the nutation, which is now a rotation by α about the y -axis. Finally, \mathbf{M} is rotated back about the z -axis to its original phase angle ϕ . Matrices for rotation about the z and y axes are given by

$$\mathbf{R}_z = \begin{pmatrix} \cos \phi & \sin \phi & 0 \\ -\sin \phi & \cos \phi & 0 \\ 0 & 0 & 1 \end{pmatrix} \quad (6.11)$$

$$\mathbf{R}_y = \begin{pmatrix} \cos \alpha & 0 & -\sin \alpha \\ 0 & 1 & 0 \\ \sin \alpha & 0 & \cos \alpha \end{pmatrix} \quad (6.12)$$

Multiplying out the three matrices in 6.10 gives a single rotation matrix

$$\mathbf{R}_{RF} = \begin{pmatrix} \cos^2 \phi + \sin^2 \phi \cos \alpha & \sin \phi \cos \phi (1 - \cos \alpha) & -\sin \phi \sin \alpha \\ \sin \phi \cos \phi (1 - \cos \alpha) & \sin^2 \phi + \cos^2 \phi \cos \alpha & \cos \phi \sin \alpha \\ \sin \phi \sin \alpha & -\cos \phi \sin \alpha & \cos \alpha \end{pmatrix} \quad (6.13)$$

Returning to eqn. 6.7, the applied field \mathbf{B} now has only one component, the field gradient \mathbf{G}

$$\mathbf{M}_{ij} \leftarrow \gamma(\mathbf{M}_{ij} \times \mathbf{G}) \quad (6.14)$$

As \mathbf{G} is always z -oriented, the precession will always be about the z -axis. The angle θ by which M will precess in time Δt is calculated as

$$\theta = \gamma \mathbf{r} \cdot \int_t^{t+\Delta t} \mathbf{G}(\mathbf{r}, \tau) d\tau \quad (6.15)$$

$$\theta_{ij} = 2\pi\gamma\Delta t(G_x i + G_y j) \quad (6.16)$$

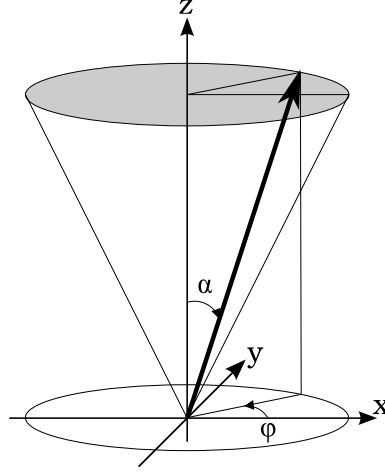


Figure 6.1: A nutation is described by two parameters: the flip angle α and the phase angle ϕ .

Finally, the rotation is applied to precess the sample magnetisation

$$\mathbf{M}_{ij} \leftarrow \mathbf{R}_z(\theta_{ij})\mathbf{M}_{ij} \quad (6.17)$$

6.3.3 Modelling RF Transmit Field Inhomogeneity

Up to this point, RF excitations have been considered only as a function of time and assumed perfectly spatially uniform. We wish to investigate what happens to an image when this is no longer the case, and the transmit field phase and magnitude vary significantly across the volume of interest.

For a pulse of duration τ the flip angle α is given by

$$\alpha(\mathbf{r}) = \int_0^\tau \gamma |B_1^+(\mathbf{r}, t)| \, dt \quad (6.18)$$

Note that α is now a function of position. Assuming a simple rectangular RF pulse

$$\alpha(\mathbf{r}) = \gamma |B_1^+(\mathbf{r})| \tau \quad (6.19)$$

An imaging sequence specifies an intended flip angle α_{ideal} . We now have to decide what that angle means. A reference point B_1^{ref} has to be selected

at which the desired flip angle will be achieved. At all other points in the image, the actual flip angle will be given by:

$$\alpha_{actual}(\mathbf{r}) = \frac{|B_1^+(\mathbf{r})|}{|B_1^{ref}|} \alpha_{desired} \quad (6.20)$$

where α_{actual} is the achieved flip angle, which varies with location. Similarly, the phase of the nutation ϕ will be altered by the phase of the transmit field:

$$\phi_{actual}(\mathbf{r}) = \phi_{ideal} + \angle B_1^+(\mathbf{r}) \quad (6.21)$$

where $\angle B_1^+ = \arctan(B_{1,y}^+/B_{1,x}^+)$. Different criteria for selecting B_1^{ref} are investigated in section 6.5.2.

6.3.4 Signal Reception and B_1^- Inhomogeneity

Modelling sample magnetisation is only part of the story. The reception process, by which a probe element detects sample magnetisation, should also be modelled, including the effect of inhomogeneity in the receive field. It was shown in chapter 3 that the signal induced in a receive coil is

$$V_c(t) = -\frac{\partial}{\partial t} \int_{\mathbf{r}} \mathbf{B}_1^{c-}(\mathbf{r}) \cdot \mathbf{M}(\mathbf{r}) d\mathbf{r} \quad (6.22)$$

which can be discretised to

$$V_c^n = \frac{1}{\Delta t} \sum_{i,j} \mathbf{B}_{1,ij}^{c-} \cdot \mathbf{M}_{ij}^n \quad (6.23)$$

where \mathbf{B}_1^{c-} is the receptive field of coil c . By recording the received signal over many iterations, a simulated NMR signal is constructed.

6.3.5 Echos and Intravoxel Dephasing

Modelling a single magnetisation vector per voxel allows gradient echo sequences to be simulated, but cannot represent a spin echo, as there is no mechanism to model intra-voxel dephasing.

To store this extra information, the array of magnetisation vectors is extended to store subvoxel magnetisation vectors. By modelling a linear distribution of magnetisation vectors spread across each voxel in the frequency encoded direction, spin echoes can be modelled. The gradient strength is now calculated at each of these locations, so each subvector will experience a slightly different precession rate. This was found to be particularly important for modelling the sequential transmit sequence described in section 6.6. Twelve subvoxels per voxel were modelled in this work.

6.3.6 Implementation Details

The Bloch simulator is written in almost 900 lines of C++, reusing some of the library routines written for the TLM simulator. A summary of the simulation process is shown in fig. 6.2. A typical 64×64 voxel EPI image is simulated in 4100 iteration. It takes approximately 90 seconds to run using an Intel P4 at 2.4GHz, requiring 3.6MB of RAM.

An imaging sequence is specified in a text file. Each line of text represents one iteration of the Bloch simulation. Each line contains the transmit channel number, RF pulse flip angle and phase, gradient amplitudes G_x , G_y and G_z , and the acquisition gate. The transmit channel number is used to determine which transmit field is used to modify a nutation, allowing the simulation of imaging sequences using multiple transmit elements. The acquisition gate is a binary flag, used to indicate which sections of the receive sequence are actually saved to file.

The user can specify a number of transmit and receive fields, which are in the same format used for the TLM simulator, making it easy to stack a Bloch simulation on results from TLM simulation. Where multiple receive fields are specified, each one represents a different receive coil. All receive channels operate in parallel with their data saved to separate files at the end of the simulation run, allowing parallel receive sequences such as SENSE to be simulated. The sample model is also specified using a sample model file as used for TLM simulations. For the Bloch simulator, this file provides T_1 ,

```

Load transmit and receive fields, imaging sequence, model
for  $n = 1$  to  $N$  do
  for all  $i, j$  do
    if RF pulse then
       $\alpha = \frac{|B_1^+|}{|B_1^{\text{ref}}|} \alpha_{\text{desired}}^n$ 
       $\phi = \phi_{\text{desired}}^n + \angle B_1^+$ 
       $M \leftarrow R_{RF}(\alpha, \phi)M$ 
    end if
     $M \leftarrow \text{Relax}(M)$ 
     $\theta = 2\pi\gamma\Delta t(G_x^n i + G_y^n j)$ 
     $M \leftarrow R_z(\theta)M$ 
  end for
  for each receive coil  $c$  do
     $V_c^n = 0$ 
    for all  $i, j$  do
       $V_c^n \leftarrow V_c^n + \frac{1}{\Delta t} B_{1c}^- \cdot M$ 
    end for
  end for
end for
for each receive coil  $c$  do
  Record  $V_c$  to file
end for

```

Figure 6.2: Pseudocode for the Bloch simulation process.

T_2^* and relative water content for all materials present, and the location of those materials.

For each receive channel a complex timecourse signal is recorded. If the receive coil is not operating in quadrature mode, the imaginary channel is simply be ignored. The data is saved to a binary file as pairs of signed 16 bit numbers. This is the same format used by the Nottingham 3T scanner, allowing real and simulated data to be processed using exactly the same software. Before saving to file, the whole timecourse is scaled to use the maximum available amplitude range. Images are then reconstructed using a set of custom scripts written in Matlab.

	Grey matter	White Matter
Conductivity (Sm^{-1})	0.692	0.413
Permittivity	60.0	43.9
Water content	82%	69%

Table 6.1: Electrical properties of the simulation phantom at 300MHz.

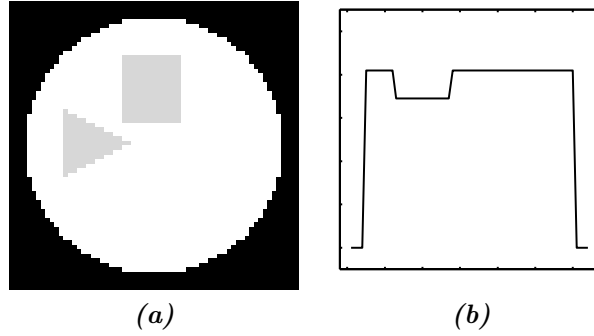


Figure 6.3: The simulated spherical phantom, constructed from grey matter with white matter inserts: (a) the central slice through the phantom, (b) water content of a horizontal section through (a).

6.4 Imaging Sequences

6.4.1 The Simulation Phantom

The phantom used in simulations throughout this chapter is shown in fig. 6.3. It consists of a 180mm diameter sphere of grey matter. Inserted into the sphere are a cube ($45 \times 45 \times 45 \text{ mm}^3$) and a prism ($45 \times 45 \text{ mm}$ base, 45 mm high) of white matter. The electrical properties of the two materials at 300MHz are given in table 6.1. The phantom is modelled on a Cartesian mesh using $3 \times 3 \times 3 \text{ mm}$ voxels. The central slice of the phantom (fig. 6.3a) was used in Bloch simulations to generate the 64×64 pixel images presented in this chapter. The full 3D phantom was used in TLM simulations to generate B_1 transmit and receive fields used in section 6.5.

6.4.2 Quantifying Image Error

In order to compare different imaging methods it is necessary to have a quantitative measure of the error between an intended and actual image. The images presented in this chapter are simulated so we have the luxury of knowing the reference image exactly, allowing absolute image error to be measured.

A useful measure of image error should be sensitive to differences between a test image and its reference, while being independent of image size and overall image intensity. Independence from image size is achieved by presenting the mean error per pixel, rather than the overall error sum. Independence from image intensity is obtained by dividing each image by its mean value. For a reference image P and test image Q , normalised images are calculated as

$$\bar{P} = \frac{P}{\frac{1}{IJ} \sum_{i,j} P_{ij}} \quad (6.24)$$

$$\bar{Q} = \frac{Q}{\frac{1}{IJ} \sum_{i,j} Q_{ij}} \quad (6.25)$$

where I and J are the image dimensions in measured in pixels. The RMS error is then calculated using the normalised images

$$E_{rms} = \sqrt{\frac{1}{IJ} \sum_{i,j} |\bar{P}_{ij} - \bar{Q}_{ij}|^2} \quad (6.26)$$

As normalised image intensities have been used, the resulting error measure is dimensionless, expressed as a percentage of the mean image intensity.

6.4.3 Simulated Two Dimensional Imaging

The Bloch simulator was first tested with three different imaging sequences simulated under ideal conditions using uniform transmit and receive B_1 fields. Spinwarp imaging is demonstrated in fig. 6.4. The k -space image

is shown in fig. 6.4*a*, displaying a strong central bright region, tapering off towards the edges. The Fourier transform of the k -space data is shown in fig. 6.4*b*, exhibiting a ringing artifact around the phantom edges (seen most clearly on the image cross section). This was removed by multiplying the k -space data by a Hamming window [162], demonstrated in fig. 6.4*c*. A Hamming window has been applied to all subsequent images in this chapter.

Spinwarp is the only multishot imaging sequence simulated. It differs from single shot imaging in that sample magnetisation has to relax back to its initial state between the acquisition of lines of k -space. In simulating single shot sequences, relaxation can be neglected and images are still produced. As previously discussed, relaxation times are difficult to specify, and so will be omitted for the remainder of this chapter.

Fig. 6.5*a* shows a simulated echo planar image, showing a strong Nyquist ghosting artifact. This was corrected by phase shifting alternate lines in k -space as described in section 2.3.9, and demonstrated in fig. 6.5*b*. A cross section through the phase corrected image is shown in figure 6.5*c*.

Finally, a simulated Burst image is shown in fig. 6.6. In this image, phase encoding is along the vertical axis, while the horizontal axis is encoded by a series of 64 RF pulses of 1.4° each.

6.5 Imaging with the Microstrip Probe

In the previous chapter a four element microstrip probe was developed for use at 300MHz. Using TLM, the transmit and receive fields generated by the probe were simulated. Those fields are now imported into the Bloch simulator to investigate their effect on image homogeneity.

Image reception is first investigated, using TLM generated receive fields and an ideal uniform transmit field. Destructive interference is demonstrated when the probe is used in quadrature receive mode. The benefit of using the probe in parallel receive mode is then shown using sum-of-squares reconstruction.

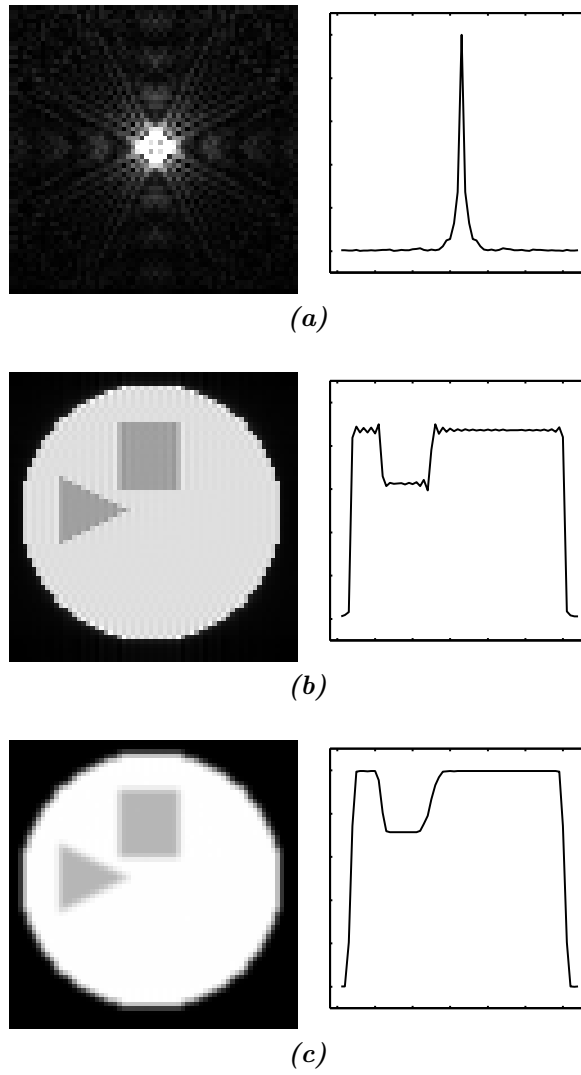


Figure 6.4: Simulated Spinwarp image: *a* k -space image, *b* real image without windowing, and *c* real image using the Hamming window.

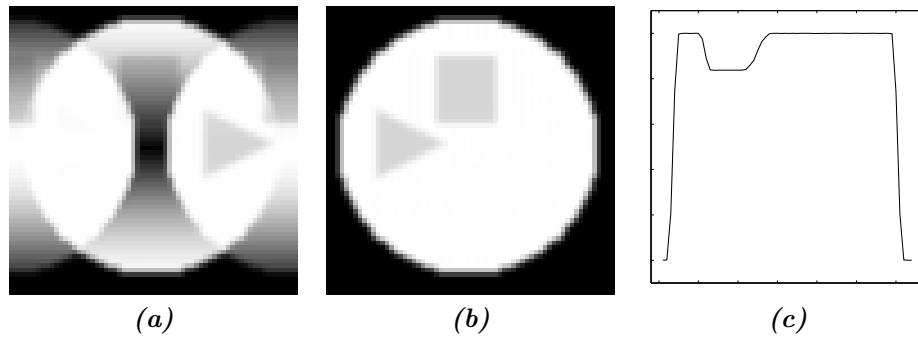


Figure 6.5: Echo planar imaging: (a) simulated Echo Planar image, with strong Nyquist ghost artifact, (b) the same image after phase correction, and (c) horizontal cross section through the centre of (b).

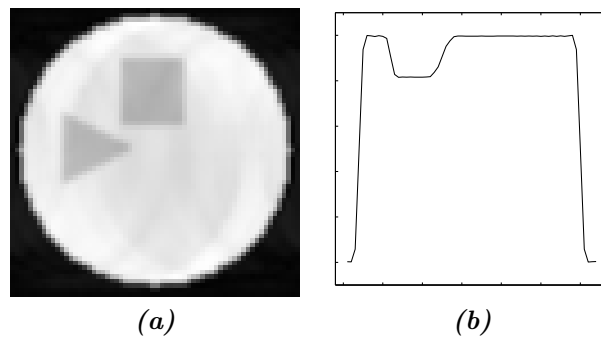


Figure 6.6: (a) A simulated Burst image and (b) a horizontal cross section through it.

TLM generated transmit fields are then introduced. Field cancellation is again shown to be a source of signal loss. An alternative imaging sequence is developed to avoid this interference. The method excites each probe element sequentially, rather than in parallel, and so avoids signal cancellation during transmission, producing an improvement in overall image homogeneity.

Finally, simulated imaging results using the SENSE reconstruction algorithm are shown. By taking the sensitivity profile of probe elements into account, SENSE can correct for image intensity variation caused by variation in probe sensitivity, and can be used to accelerate image reception.

6.5.1 Reception

TLM generated receive fields, inside the test phantom, for each element of the microstrip probe are shown in fig. 6.7. To mimic the behaviour of a standard volume probe, the microstrip probe can be connected in quadrature receive mode (fig. 6.8). Each strip detects a different image due to its individual receptive field (fig. 6.9). The images are phase shifted in 90° increments to account for the locations of the strip elements around the sample, summed in hardware and recorded using a single receive channel.

Fig. 6.10a show the resulting image and a horizontal cross section through its centre. The image suffers badly from signal dropout, giving a 42.3% error when compared to the reference image. The raw images (fig. 6.9) show that probe elements are sensitive to the central region, but the composite image is dark in the centre. The problem is that different elements detect the central region at different phase shifts. When the signals from the different elements are combined they interfere, cancelling out in the central region to produce the dark patch in fig. 6.10a.

Image homogeneity can be improved by using the probe in parallel receive mode (fig. 6.11). This requires four independent receive channels, but allows the full signal from each channel to be recorded without interference. The image is then reconstructed offline, allowing much more flexibility in how this is done. Taking the sum-of-squares of the separate channels (i.e. removing

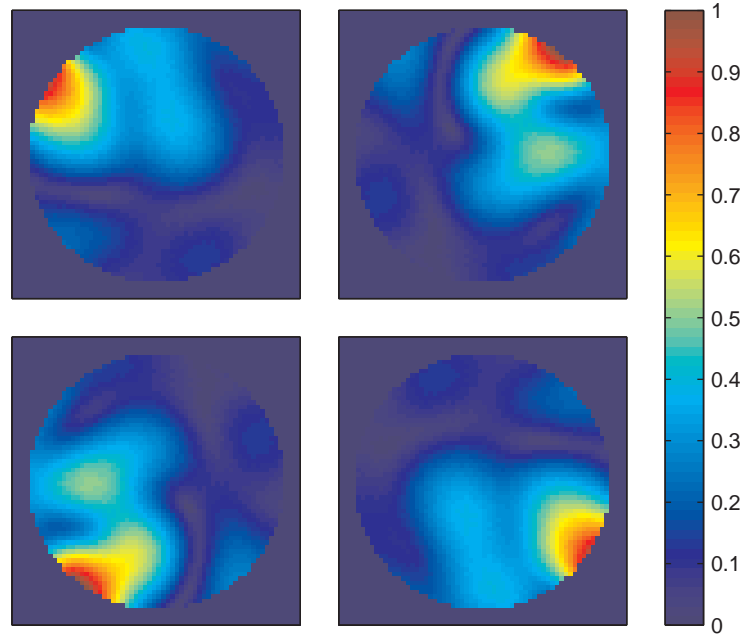


Figure 6.7: B_1^- receive field magnitude maps generated for the microstrip probe at 300MHz, using TLM simulation, masked to show only the field inside the phantom.

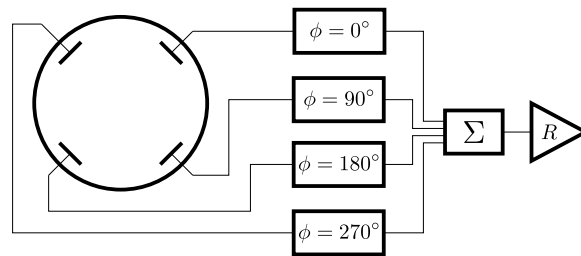


Figure 6.8: The microstrip probe connected in quadrature receive mode.

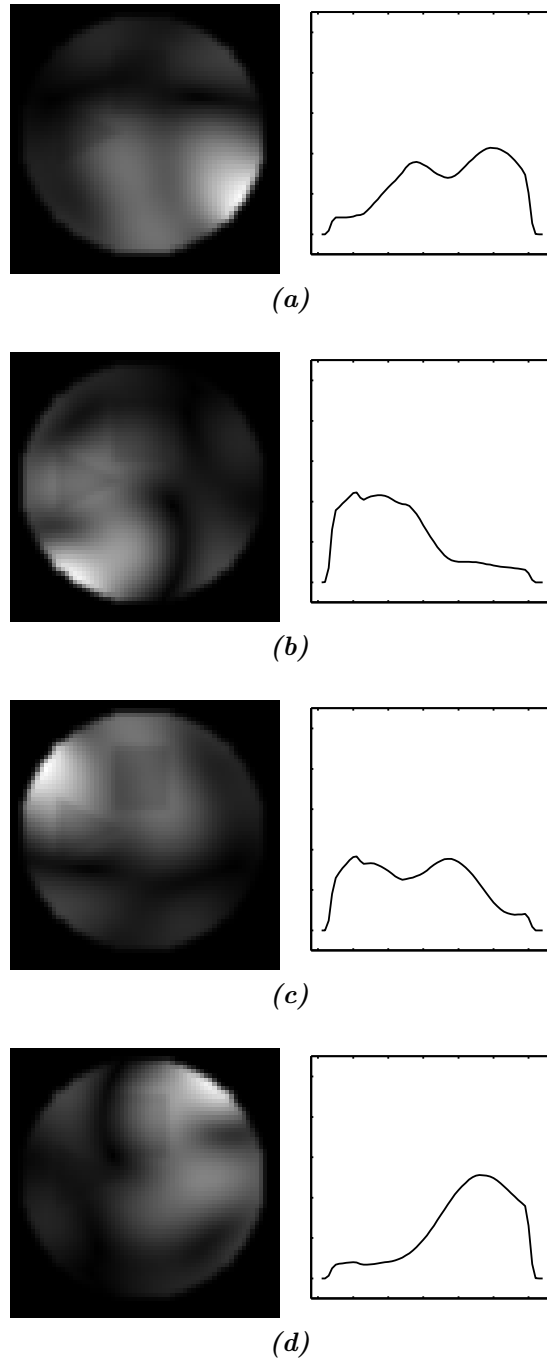


Figure 6.9: Simulated EPI using a uniform transmit field and TLM simulated receive fields. Images detected by each receive channel are shown on the left, with horizontal cross sections through those images shown on the right.

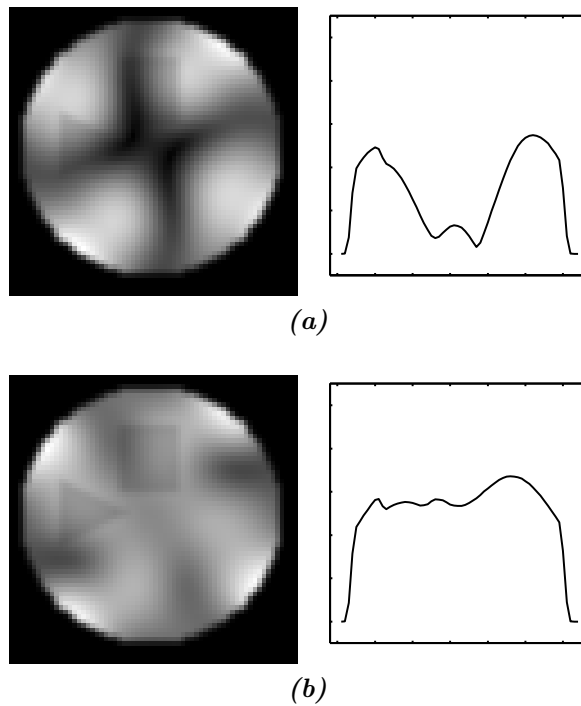


Figure 6.10: Image reconstruction, using raw images from fig. 6.9. Quadrature mode (a) suffers signal loss due to interference between channels. This can be avoided by using the probe in parallel receive mode, combining the raw images using sum-of-squares (b) reconstruction.

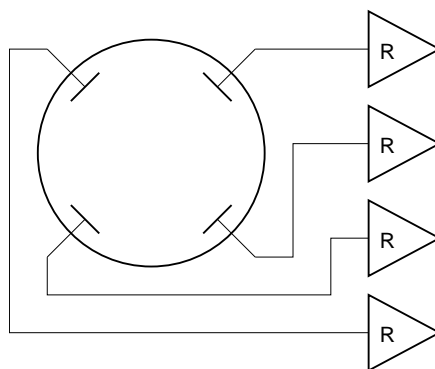


Figure 6.11: The microstrip probe connected in parallel receive mode, using four separate receive channels.

phase information) reduces the image error to 25.1%, producing the image shown in fig. 6.10*b*.

6.5.2 Transmission

Interference is also a problem when exciting a sample at high frequency. As the phase of the excitation fields vary significantly across the sample, constructive and destructive interference produce a highly inhomogeneous net excitation field, leading to contrast variation across the image. At lower frequency ($\leq 128\text{MHz}$) field variation is smooth, and can be removed in post-processing. As the excitation frequency is increased, variation in the B_1 field becomes more sample dependent and on a similar scale to anatomical features, making its effect harder to separate from real image contrast.

While image intensity can, at least in principle, be corrected if the B_1 field map is known, loss in SNR is not recoverable. In some regions in the sample, destructive interference almost completely cancels out the transmit field. The nutation in these regions will be very small, giving a weak signal and low SNR. Intensity correcting signal from these regions will amplify the noise to an unacceptable level.

If the B_1 transmit field is inhomogeneous, it is not possible to achieve the intended flip angle at all points across the sample (using a simple pulse envelope), so a compromise must be chosen. For a 90° nutation, flipping

too far has the same effect as not flipping far enough and the NMR signal amplitude is reduced (and phase shifted 180°). This is demonstrated in fig. 6.12, using a transmit field with a Gaussian profile. In this case the flip angle varies by a factor of 3.6 across the sample. Normalising the transmit field to produce a 90° nutation at the peak B_1^+ value maximises SNR at the centre of the image, sacrificing signal at the edges where the field is weaker (fig. 6.12*b*). If the transmit field is normalised to give a 90° nutation at the mean B_1^+ value (fig. 6.12*c*), image intensity is much stronger at the edges but vanishes in the centre, where the actual flip angle is 157° .

A further point to consider is that image intensity depends upon the sine of the flip angle, making the error in a 90° pulse less significant than the error in a 45° pulse. Consider an excitation field with a $\pm 10\%$ variation in magnitude across the sample. For a 90° nutation, this will lead to a 1.2% intensity variation in the acquired image. For a 45° nutation, the image intensity variation will be 16%.

Returning to the microstrip probe, TLM generated transmit fields for the four elements are shown in fig. 6.13. Imaging was simulated using TLM generated transmit and receive fields with the probe driven in quadrature mode (fig. 6.14) and receiving in parallel mode (fig. 6.11). Four raw images from a simulated EPI sequence are shown in fig. 6.15, each image detected by a different probe element. The impact of the non-uniform transmit field upon image quality is clear when fig. 6.15 is compared to fig. 6.9. The raw images were then combined using the root sum-of-squares and two different normalisation factors. Normalising the transmit field to its peak value (fig. 6.16*a*) gave flip angles ranging from 14° to 90° and leads to an image error of 35.1%. Normalising the transmit field to its mean value (fig. 6.16*b*) gave flip angles in the range 50° to 315° and an image error of 36.5%. Both images exhibit significant signal dropout.

The cause of the poor image homogeneity can be understood by examining the composite B_1^+ transmit field. In section 6.2 it was shown that image signal intensity is proportional to the sine of the transmit field magnitude. When multiple probe elements are operated simultaneously, the sample experiences the vector sum of the different transmit fields, the magnitude of

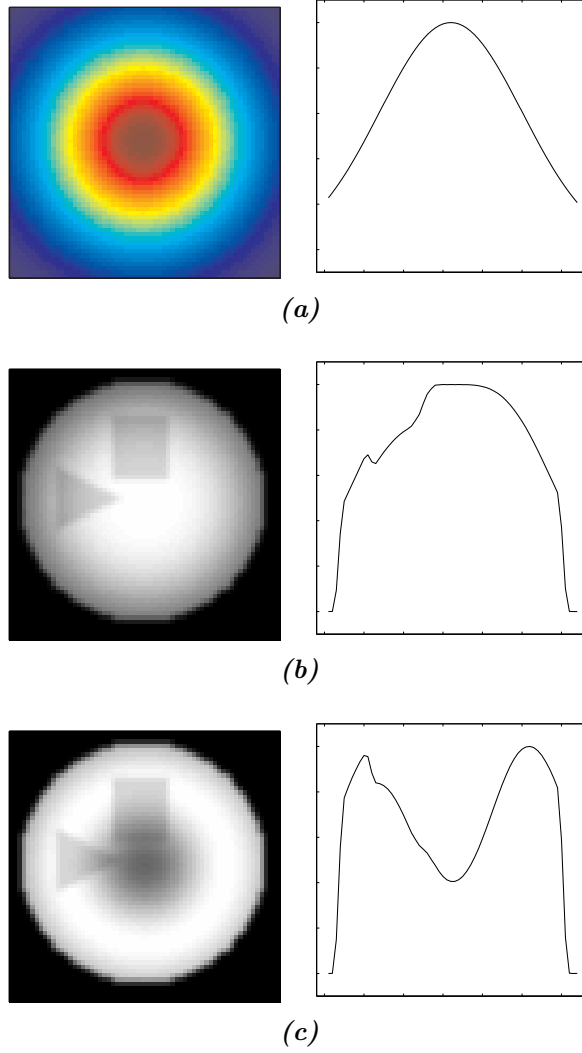


Figure 6.12: An inhomogeneous transmit field B_1^+ causes the flip angle to vary across the image. A transmit field with a Gaussian profile (a) is used here to demonstrate the effect. The flip angle in (b) has been normalised to the peak value, leading to a darkening of the image at its edge. In (c) the flip angle has been normalised to the mean, leading to a nutation greater than 90° at the image centre, causing the central darkening.

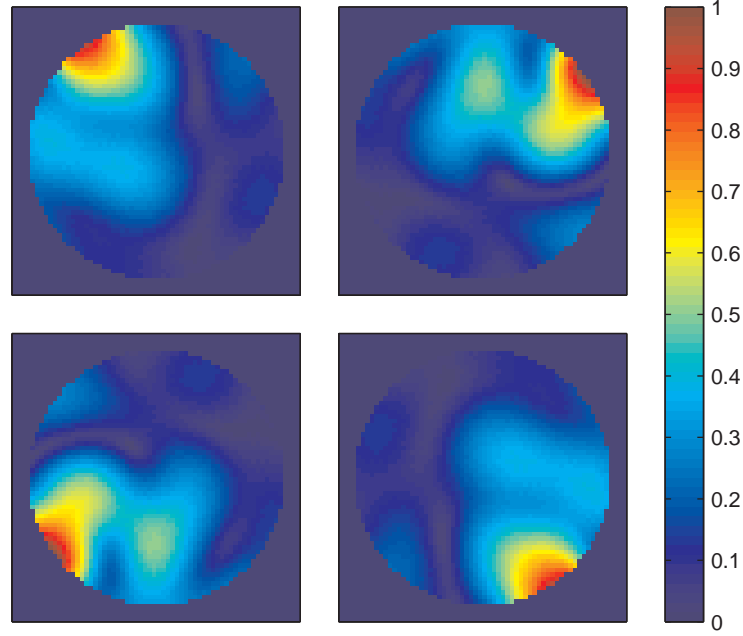


Figure 6.13: B_1^+ transmit field magnitude maps generated for the microstrip probe at 300MHz, using TLM simulation, masked to show only the field inside the phantom.

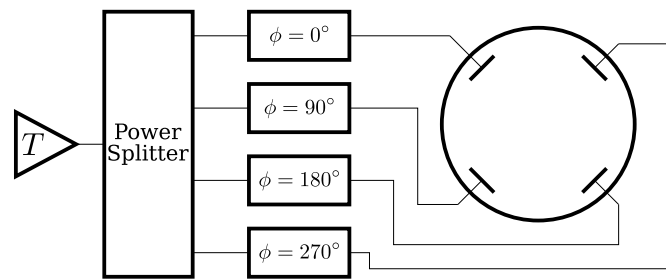
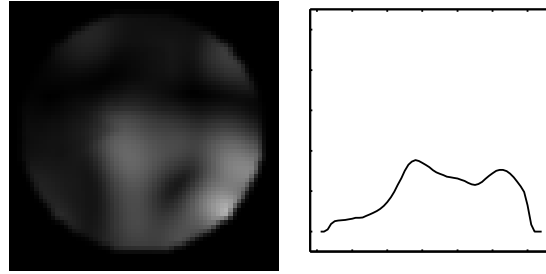
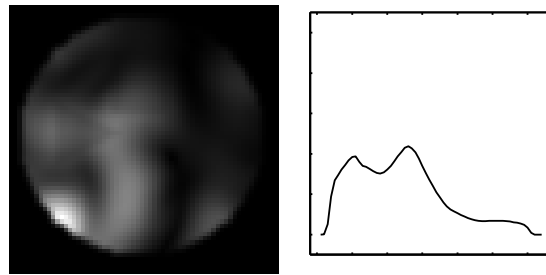


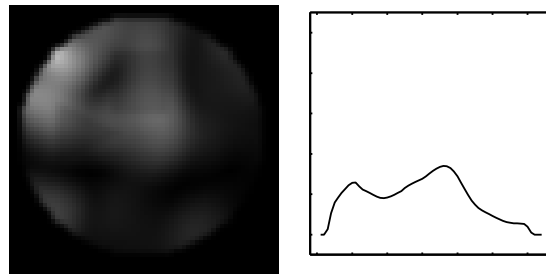
Figure 6.14: The microstrip probe connected for quadrature drive.



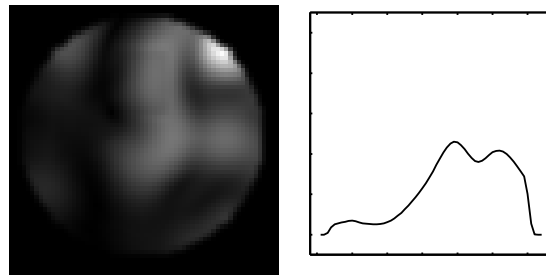
(a)



(b)



(c)



(d)

Figure 6.15: Simulated EPI using TLM generated transmit and receive fields for the microstrip probe. Each image is detected by a different strip. The probe was driven in quadrature mode (fig. 6.14), receiving in parallel mode (fig. 6.11).

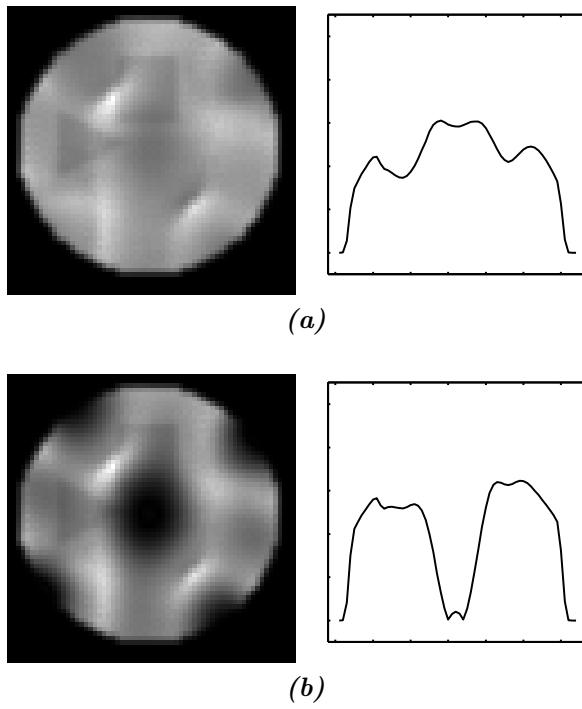


Figure 6.16: Simulated EPI using TLM generated transmit and receive fields, combined using the sum-of-squares, with the flip angle normalised to (a) the peak and (b) the mean angle.

which is

$$\left| B_{1,\text{net}}^+ \right| = \left| \sum_e B_{1,e}^+ \right| \quad (6.27)$$

where e counts the probe elements. The net transmit field generated by the microstrip probe driven in quadrature mode is shown in figure 6.17(a). The field shows a strong central peak, corresponding to the central brightening commonly reported in UHF images [75]. Transmit fields can interfere because they are vector quantities, i.e. they contain magnitude and phase information. It was demonstrated in the receive case that combining the magnitudes of images received by different probe elements (removing phase information) produces a more uniform net image. If the transmit fields are combined without phase information

$$\left| B_{1,\text{net}}^+ \right| = \sum_e \left| B_{1,e}^+ \right| \quad (6.28)$$

the resulting excitation field is stronger and more uniform (fig. 6.17(b)). Unfortunately there is no transmit equivalent to parallel reception. In parallel reception, several different probe elements are used to simultaneously detect signal from a single source (the sample). If the signals are directly summed they interfere. By acquiring each channel independently and combining image magnitudes, interference is avoided. When multiple probe elements transmit simultaneously, the vector field summation (and hence interference) takes place inside the sample. The only way to prevent this summation, and thus maintain separability of the transmit fields, is to excite each probe element at a different time.

6.6 Sequential Transmit Imaging

Transmitting an RF pulse from each probe element in sequence, rather than simultaneously, provides a way to excite the sample without interference between the different transmit fields [118]. However, sample magnetisation is also a vector quantity. When an RF pulse is applied, sample magnetisation is tipped by an angle determined by the transmit field amplitude, at the same phase as the transmit field in the transverse plane. Using complex notation,

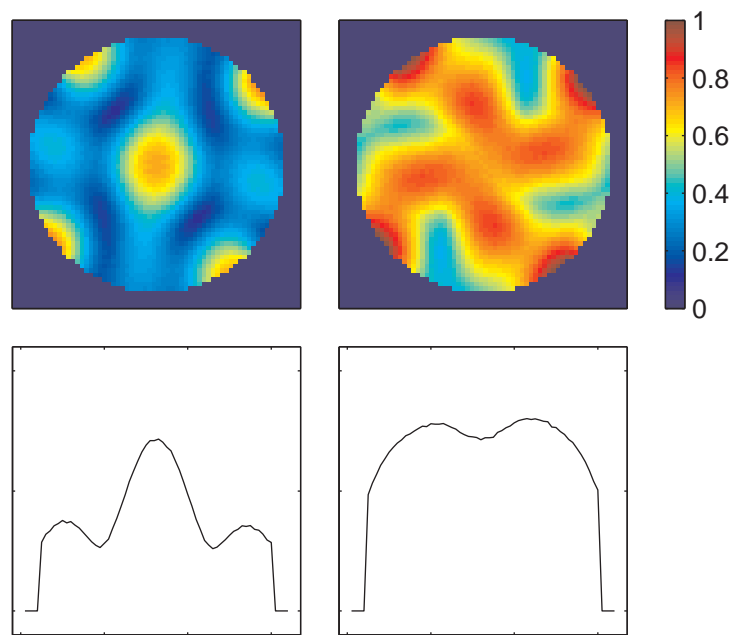


Figure 6.17: Combining transmit fields with and without interference: summing the vector fields (left) causes interference, reducing both homogeneity and field intensity; summing field magnitudes (i.e. removing phase information) gives a more uniform field (right).

the transverse magnetisation is given by

$$M(\mathbf{r}) \propto \sin(\gamma\tau |B_1^+(\mathbf{r})| V) \cdot e^{i\angle B_1^+(\mathbf{r})} \quad (6.29)$$

The phase of the sample magnetisation $\angle M(\mathbf{r})$ stores the phase of the transmit field. If a second RF pulse is then applied, it will interfere with the sample magnetisation in just the same way that two simultaneous RF pulses would interfere, albeit with a phase shift due to magnetisation precession in the time between the two RF pulses. As sample magnetisation stores phase information, phase cancellation will still occur [101].

We require a method to store information due to an RF pulse in a manner that will not interfere with subsequent pulses. Burst imaging uses a train of RF pulses in the presence of a constant gradient field to encode a spatial dimension [27]. During image readout each RF pulse is refocused at a different point in time, allowing the magnetisation of different strips through the sample to be recorded. Fig. 6.18 shows a variation of the Burst encoding scheme, modified to encode different excitation fields rather than different locations. A slice selective RF pulse is applied by each transmit element in sequence. The slice gradient is inverted between each RF pulse to maintain phase coherence across the depth of the excited slice. Between each RF pulse a dephasing blip is applied to the readout gradient. The first RF pulse will tip the sample magnetisation in the normal manner (fig. 6.19(a)). Applying a short gradient pulse then dephases sample magnetisation around B_0 , forming a cone of magnetisation vectors (fig. 6.19(b)). An echo may be formed at any point by applying the reverse gradient to refocus the magnetisation. Applying a further RF pulse will then tip the whole cone of spins (fig. 6.19(c)), which is again dephased with a gradient pulse. There are now two different echoes stored in the sample magnetisation, which can be individually refocused by applying a suitable gradient. The principle can be extended to store several excitations simultaneously.

A more detailed description of the imaging sequence can be developed using an extended phase graph, a method invented to describe sequences involving multiple RF pulses [28]. An extended phase graph of the new imaging sequence is shown in fig. 6.20. Four excitation pulses are applied as previously described, each pulse produces a branching in phase coherence. The

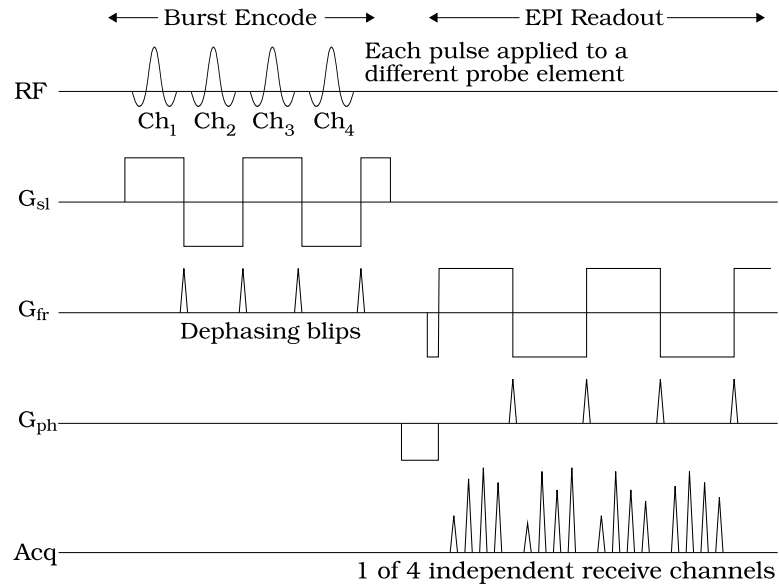


Figure 6.18: A Burst-like encoding sequence allows a separate image to be acquired for each excitation pulse.

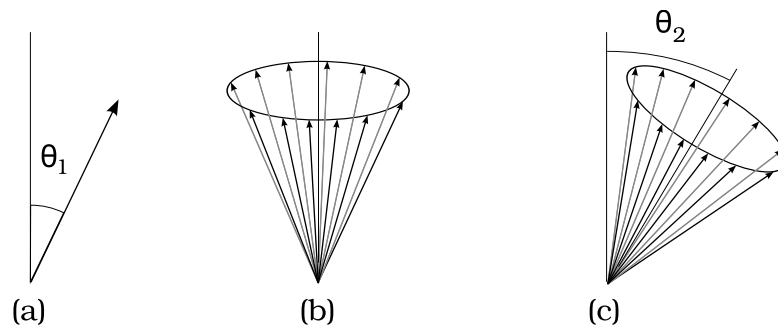


Figure 6.19: The effect of the new imaging sequence on sample magnetisation: (a) the first RF pulse tips sample magnetisation in the normal way, (b) a gradient blip dephases the magnetisation vectors about B_0 and (c) the next RF pulse tips the whole cone of magnetisation vectors.

dephasing gradient blips then produce a rapid advance in the signal phase, appearing as vertical steps in phase coherence.

Applying a readout gradient then reverses the direction of phase evolution, refocusing n_e primary echoes (where n_e is the number of excitation pulses). A primary echo is generated by a single RF pulse, and contains spatial information due to that pulse only. In common with Burst, the new sequence also generates $(n_e - 1)$ higher order echoes, which are generated by the interaction of two or more RF pulses, and are not refocused or recorded. Reversing the readout gradient sweeps back across k -space in the opposite direction, refocusing the same n_e echoes in reverse order. A short pulse is applied to the phase encoding gradient between readout gradient reversals, as for a standard EPI sequence. The k -space trajectory of the new imaging sequence is shown in fig. 6.21. Four image spaces are now traversed in a single sweep across k -space, corresponding to the four excitation pulses. The acquired data is first re-ordered to account for the traversal of k -space in alternating directions, as would be done for standard EPI data. It is then divided into n_e blocks, each of which is Fourier transformed to produce an image in the normal way.

An inherent advantage of sequential transmit imaging is that only one RF transmit channel is required, which is switched between probe elements using a multiplexer (shown schematically in fig. 6.22). The multiplexer is discussed in more detail in chapter 7.

6.6.1 Testing the New Sequence

The Bloch simulator is now used to test the feasibility of the new imaging scheme, in particular to demonstrate that images due to different excitation pulses are separable. The new sequence was first tested with four simple, artificial ramped transmit fields (fig. 6.23*a-d*). A single receive channel with a uniform field was simulated, so that variation in image intensity depends only upon the phantom and the transmit fields. Four 22.5° RF pulses, one for each transmit field, were applied to the sample.

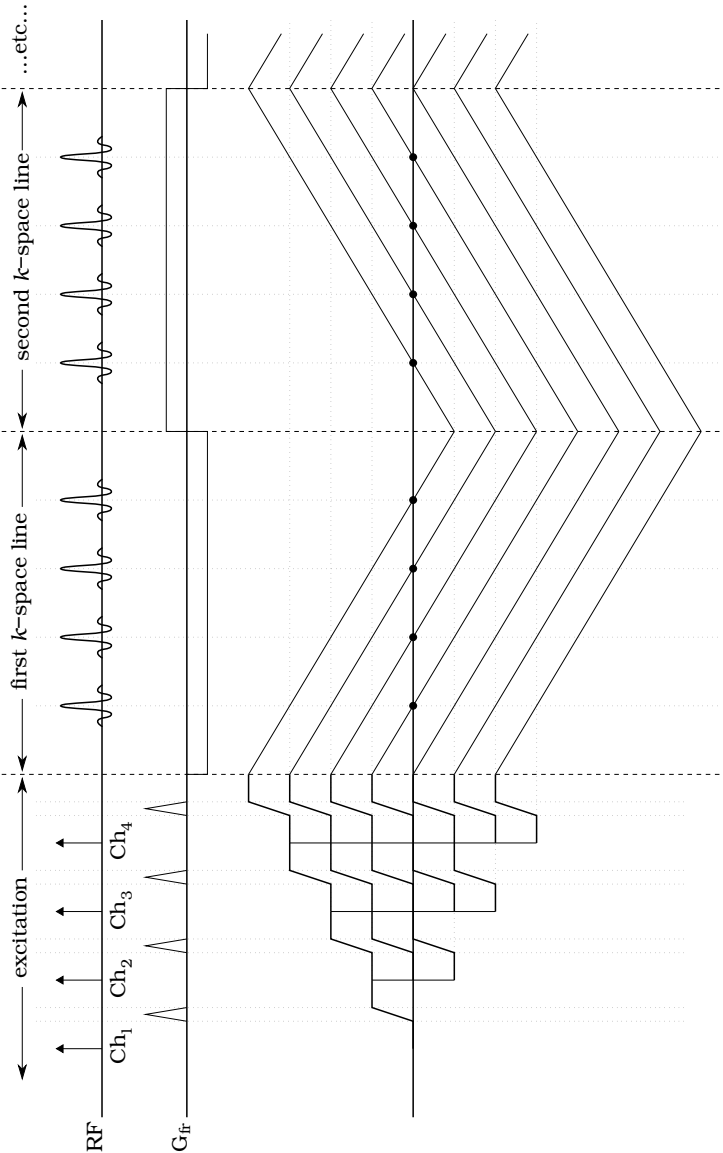


Figure 6.20: Extended phase graph for the new sequence, showing four echoes refocused on each traversal of k-space.

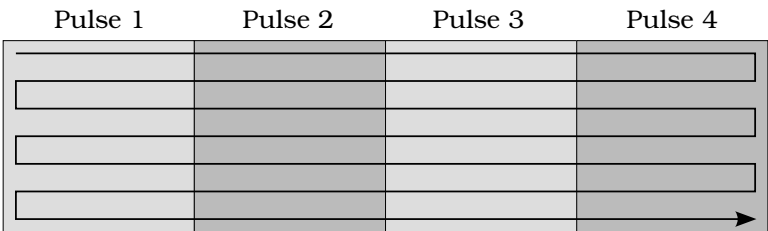


Figure 6.21: The trajectory of the new imaging sequence in k -space, traversing four independent imaging planes in each phase encode step.

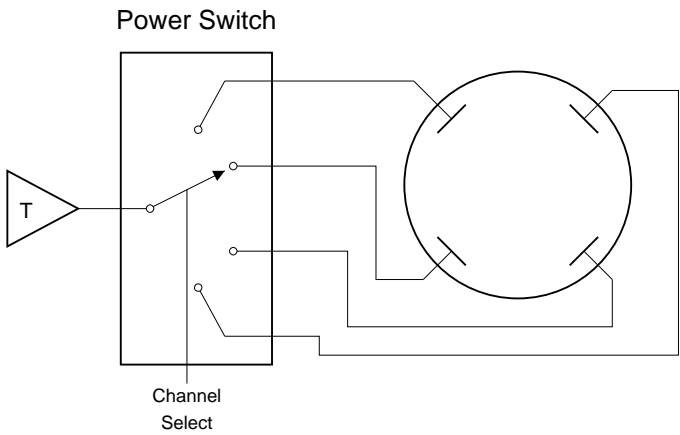


Figure 6.22: The microstrip probe connected for the new imaging sequence, using a power switch to sequentially excite different probe strips.

The resulting simulated k -space data clearly shows four echoes refocused at different locations (fig. 6.23*e*). Separating the data into four blocks and Fourier transforming each block produces four different images, each clearly depending upon a single transmit field (fig. 6.23*f-i*). Cross sections through these images are shown in fig. 6.24, showing the close correspondence between transmit fields and received images.

The new imaging sequence was also simulated using TLM generated transmit (fig. 6.13) and receive (fig. 6.7) fields for the four element microstrip probe. All four probe elements were used for transmission and reception, generating 16 raw images (fig. 6.25). Each transmit channel generates a different excitation profile. Each receive channel detects sample magnetisation according to its receptive field. The leading diagonal (figs. 6.25*a, f, k* and *p*) show images due to transmission and reception on the same element.

Combining the images using the sum-of-squares produces the composite image shown in fig. 6.26. The image error (32.5%) is not much better than quadrature transmit imaging (35.1%). However, while fig 6.26 shows intensity variation there is no complete signal dropout (in comparison to fig. 6.16), and the image may be corrected by adjusting for sensitivity if B_1 field maps are known.

It is interesting to examine the orientation of sample magnetisation following each dephasing blip in the new imaging sequence. Variation in the flip angle at this point is entirely due to B_1^+ inhomogeneity. For maximum signal, and hence maximum SNR, the sample magnetisation should be nutated through 90° . The histograms in fig. 6.27 show simulated results after applying four RF pulses, each of 22.5° (peak), using TLM simulated fields for the microstrip probe. Fig. 6.27*a* shows that while a small proportion of the sample is nutated by more than 20° , 67% is nutated by less than 10° . After subsequent RF pulses the sample nutation does not increase significantly. Following the last dephasing blip, only 10% of the sample is nutated by more than 22.5° , the peak nutation being 31.5° . Increasing the amplitude of each RF pulse to produce an 80° peak nutation makes better use of the available nutation range (fig. 6.28), and leads to only 1.25% of the sample being nutated by more than 90° . The sum-of-squares composite image now

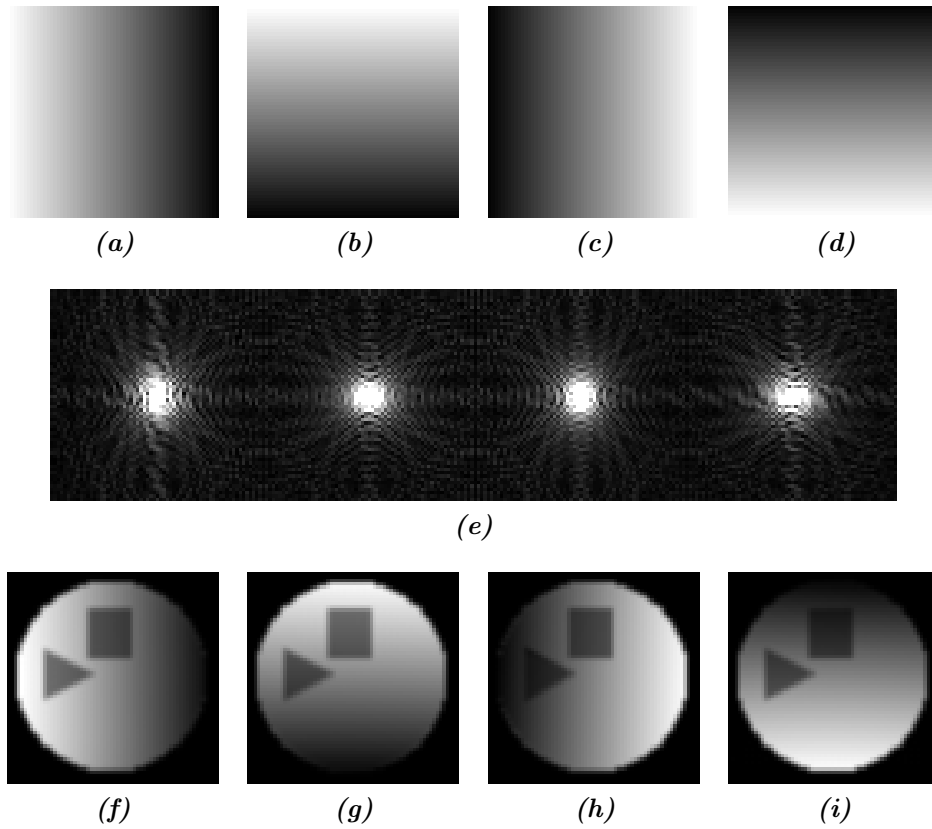


Figure 6.23: A simulation of the new imaging sequence, using four linearly ramping transmit fields (a)-(d) and a single uniform receive field; (e) shows four refocusing points in k -space, each due to a different excitation pulse; (f)-(i) are the resulting images, demonstrating that images due to different transmit fields are separable.

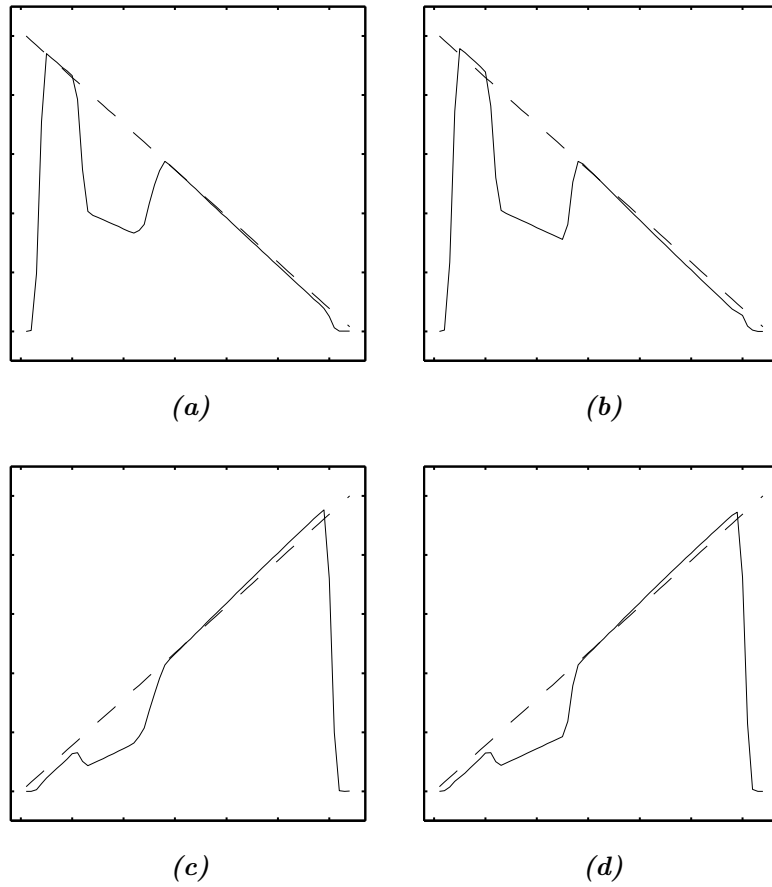


Figure 6.24: Cross sections through the ramped transmit fields (dashed line) and received images (solid line) from fig. 6.23.

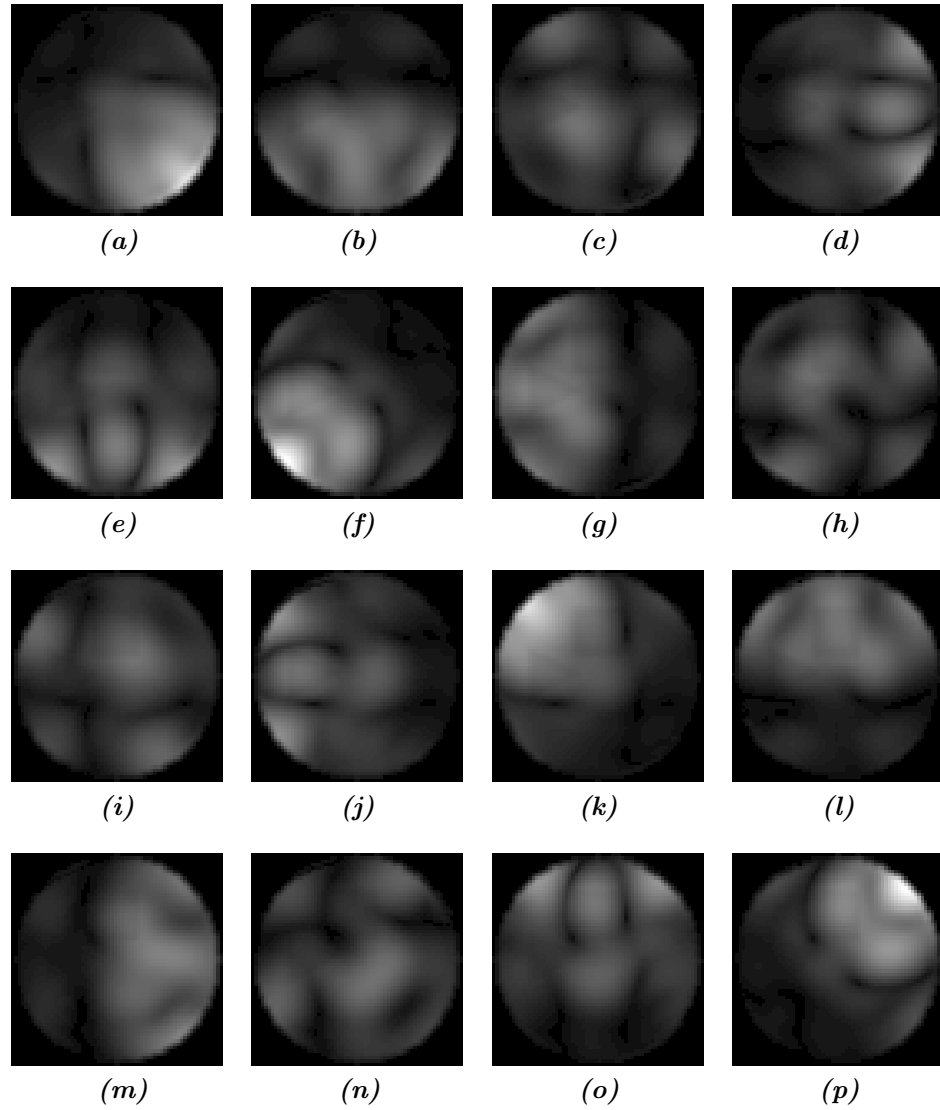


Figure 6.25: Bloch simulation of the new imaging sequence using B_1 transmit and receive fields for the microstrip probe generated using TLM simulation.

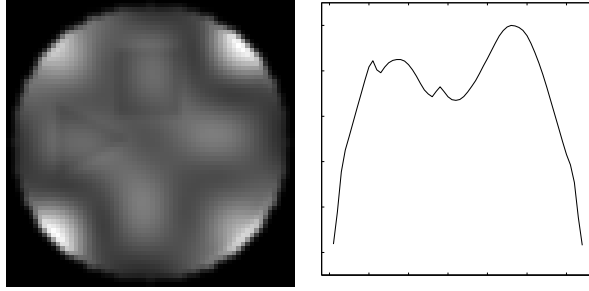


Figure 6.26: The 16 images from fig. 6.25 reconstructed into a single image using sum-of-squares reconstruction.

shows more dependence on spin density in the sample and less dependence on B_1 field inhomogeneity, reducing the image error to 24.7% (fig. 6.29).

6.6.2 SENSE Reconstruction

The new imaging sequence requires more time to acquire a complete image than a standard sequence. The time required to apply extra excitation pulses is minimal, but reading out a subimage due to each excitation slows down acquisition by a factor of n_e , where n_e is the number of applied pulses. In this section partially parallel imaging is investigated as a means to recover image acquisition time, using SENSE [38].

The k -space trajectory of a standard image acquisition is shown in fig. 6.30a (in this case EPI, but the method could equally be applied to any gradient echo sequence). The new imaging sequence reads out a separate subimage due to each excitation pulse; applying n_e excitations extends the k -space trajectory by a factor of n_e in the frequency encoded direction (fig. 6.30b). SENSE undersamples the image in the phase encoded direction, reducing the number of data points acquired. Combining SENSE with the new imaging sequence can reduce the number of acquired data points back to the number acquired for the original image, although the k -space coverage is different (fig. 6.30c).

SENSE is usually applied to reconstruct an image received in parallel by several different probe elements, following excitation by a single volume

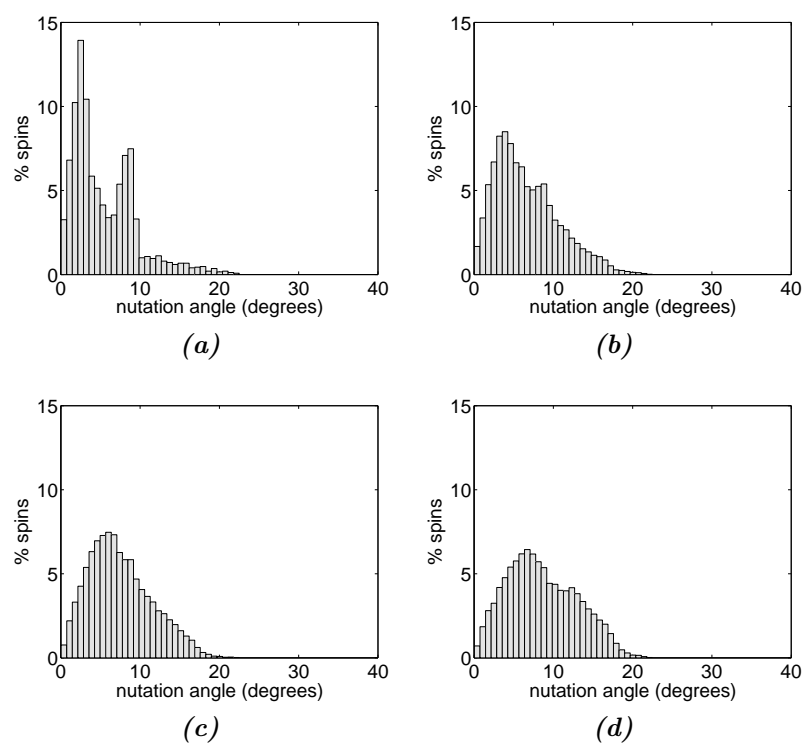


Figure 6.27: Distribution of nutation angles immediately following the (a) first, (b) second, (c) third and (d) fourth dephasing blips using the new imaging sequence. Each RF pulse was 22.5° , normalised to the peak value.

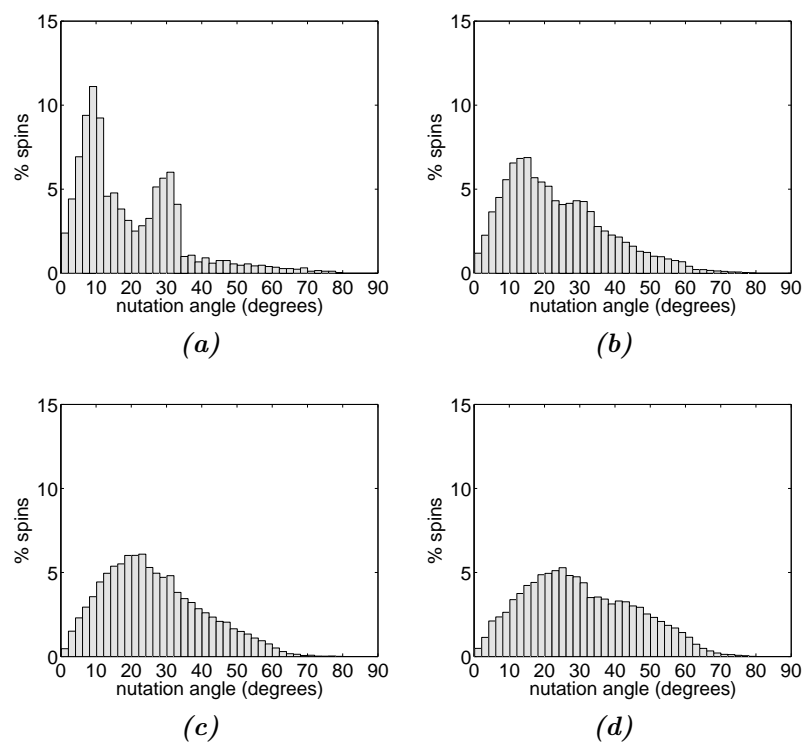


Figure 6.28: Distribution of nutation angles immediately following the (a) first, (b) second, (c) third and (d) fourth dephasing blips using the new imaging sequence with 80° RF pulses.

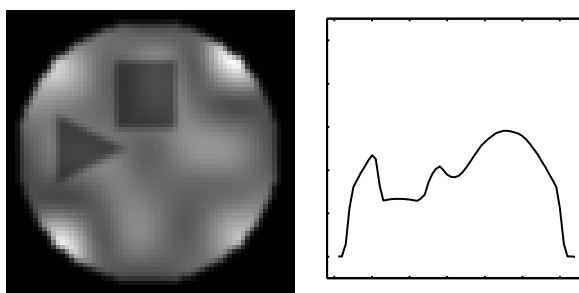


Figure 6.29: Sum-of-squares reconstruction using the new imaging sequence with 80° pulses.

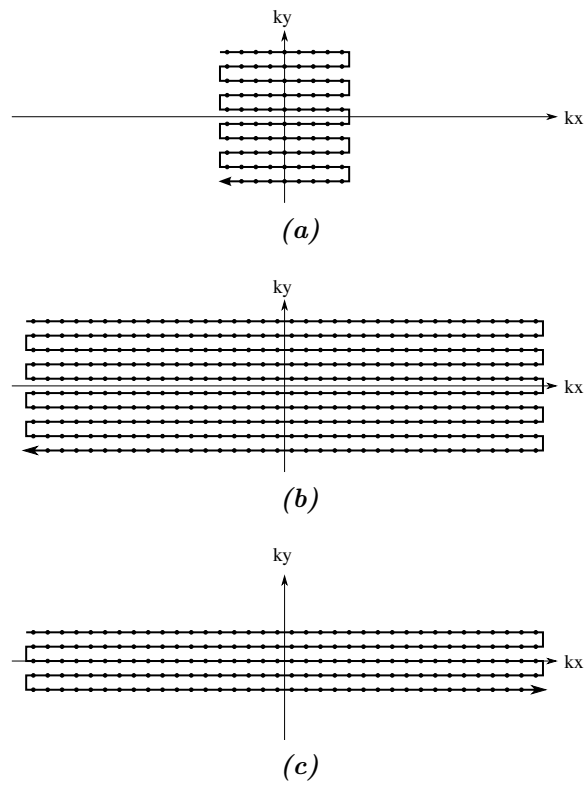


Figure 6.30: Trajectories in k -space: (a) standard EPI trajectory, (b) extended along the frequency encoded axis for the new imaging sequence and (c) reduced along the phase encoded axis by SENSE.

probe. The new imaging sequence generates subimages that differ in both the transmit and receive element used. The sensitivity map for each subimage is calculated as a combination of both the transmit B_1^+ and receive B_1^- fields

$$S_{ij,\rho} = B_{1i}^+(\mathbf{r}_\rho) \cdot B_{1j}^-(\mathbf{r}_\rho) \quad (6.30)$$

where i and j index the transmit and receive elements, ρ counts the superimposed pixels and \mathbf{r}_ρ denotes the position of pixel ρ .

If all images are detected simultaneously, thermal noise from the sample is correlated between those images. Using the new sequence, each receive channel sequentially detects n_e images. Thermal noise will be correlated across receive channels (simultaneously detected) but not between images detected by a single channel (sequentially detected). Assuming all elements are used in both transmit and receive mode, the noise correlation matrix Ψ is $n_e^2 \times n_e^2$, and block diagonal to reflect correlation between simultaneously received, but not sequentially excited, images

$$\Psi = \begin{pmatrix} \Psi' & 0 & 0 & 0 \\ 0 & \Psi' & 0 & 0 \\ 0 & 0 & \Psi' & 0 \\ 0 & 0 & 0 & \Psi' \end{pmatrix} \quad (6.31)$$

where Ψ' is the standard noise correlation matrix

$$\Psi' = \begin{pmatrix} 1 & \psi_{12} & \psi_{13} & \psi_{14} \\ \psi_{21} & 1 & \psi_{23} & \psi_{24} \\ \psi_{31} & \psi_{32} & 1 & \psi_{34} \\ \psi_{41} & \psi_{42} & \psi_{43} & 1 \end{pmatrix} \quad (6.32)$$

and ψ_{ij} is the noise correlation between receive channels i and j [31].

Noise has not yet been modelled in this work, so the receiver noise matrix Ψ has been replaced with the identity matrix, equivalent to assuming zero noise coupling between receive channels. If the data were noisy, this would result in an SNR reduction in the unwrapped image, but would not otherwise effect the reconstruction [38]. This simplifies the calculation of the unfolding

matrix \mathbf{U} to

$$\mathbf{U} = (\mathbf{S}^H \mathbf{S})^{-1} \mathbf{S}^H \quad (6.33)$$

The unfolded composite image is then

$$\mathbf{v} = \mathbf{U} \mathbf{a} \quad (6.34)$$

where \mathbf{a} is an $n_p \times n_e^2$ matrix containing aliased image data, and n_p is the number of image points. The resulting vector \mathbf{v} , of length n_p , contains the unfolded image.

Simulated images acquired using the new imaging sequence and reconstructed with SENSE at acceleration factors $R=1,2,3$ and 4 are shown in figure 6.31. With no acceleration (fig. 6.31a) the image intensity correction inherent in SENSE produces a much more homogeneous image than sum-of-squares reconstruction, reducing the image error to 13.7% (fig. 6.26).

Undersampling the acquisition by a factor of $R = 2$ produces an almost identical image to the unaccelerated case, showing a 13.8% error (fig. 6.31b). As the acceleration factor is increased further, folding artifacts become apparent in the reconstructed images (fig. 6.31c, d).

An important consideration in probe design for parallel acquisition is the geometry factor. Geometry factor maps for the four element probe at $R=2, 3$ and 4 are shown in fig. 6.32, with peak and mean g -factors and noise levels given in table 6.2. At $R=1$ no aliasing occurs, making the g -factor map unity at all points.

The maximum g -factor remains low, even at higher acceleration where folding artifacts are clearly present in the reconstructed image. The basic SNR map for the four microstrip probe is shown in fig. 6.33. It shows considerable variation, due to the highly inhomogeneous B_1 fields found at short wavelength. Variation in the underlying SNR map is much greater than variation in the g -factor maps. Poor image reconstruction occurs when the aliased images superimpose two regions having low SNR on all channels.

An obvious difficulty when using SENSE at high field strength is the acquisition of probe sensitivity maps, in the absence of a volume transmit or

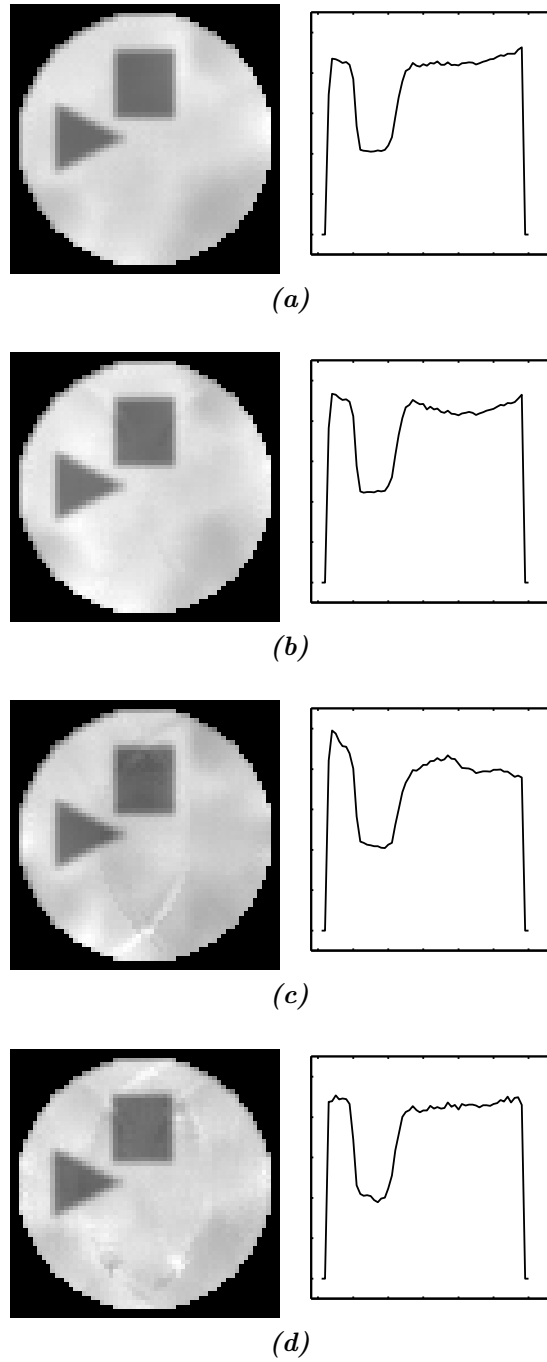


Figure 6.31: Simulated images using the new imaging sequence and SENSE reconstruction at a reduction factor of (a) $R=1$, (b) $R=2$, (c) $R=3$ and (d) $R=4$.

Reduction factor	g_{mean}	g_{peak}	N_{mean}	N_{peak}
1	1.00	1.00	0.23	1.00
2	1.01	1.07	0.24	1.01
3	1.08	1.51	0.30	1.49
4	1.19	1.59	0.46	2.29

Table 6.2: Mean and peak g -factors and noise levels at different reduction factors. Noise levels have been normalised to N_{peak} at $R = 1$.

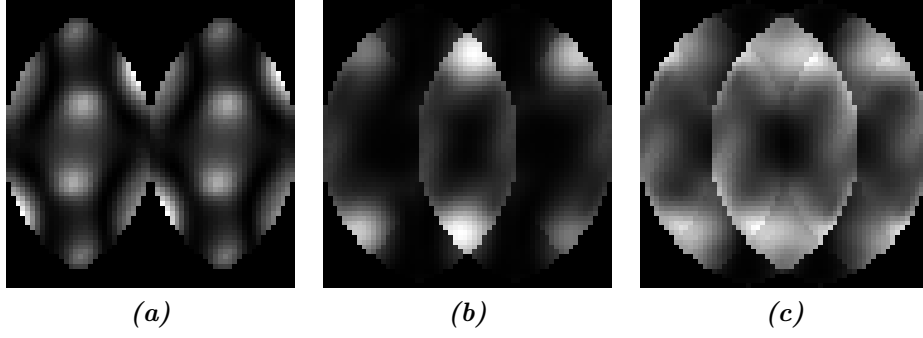


Figure 6.32: Geometry factor maps at reduction factor of (a) $R=2$, (b) $R=3$ and (c) $R=4$, with $g_{\text{max}}=1.07$, 1.51 and 1.59 respectively.

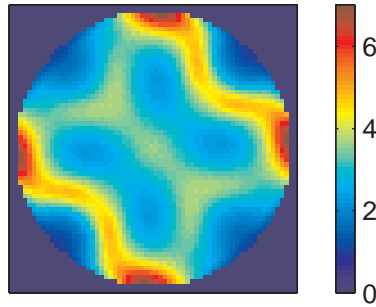


Figure 6.33: Image noise map for the four microstrip probe. Noise levels are higher in regions where probe sensitivity is low.

receive probe, although some methods have already been developed to acquire sensitivity maps without a volume image [163, 164]. Another potential solution is to use an autocalibrating method such as UNFOLD SENSE [165] or GRAPPA [166].

6.6.3 Limitations of the New Sequence

The main limitation of the new imaging sequence is that it cannot be used to generate an inversion pulse (180°), so it cannot be used with spin echo sequences. However, B_1 inhomogeneity at high field makes it difficult to achieve a 180° nutation across a sample slice, limiting the practical usefulness of spin echo imaging.

A further constraint is that the new sequence requires more time to read out images, when compared to acquisition using a standard volume probe, as a separate subimage must be acquired for each probe transmit element to build a single composite image. The time available to acquire image data is limited by T_2^* decay, which unfortunately accelerates as B_0 field strength increases [167]. However, as demonstrated in section 6.6.2, the new sequence is an ideal candidate for acceleration using parallel acquisition techniques, allowing a reduction in the total acquisition time.

Finally, noise acquired during imaging is increased, as a larger image space is acquired. However, despite these limitations, the new imaging sequence provides a promising method to combat the effects of B_1 inhomogeneity and realise the potential of high field imaging.

6.7 Discussion

In this chapter, a Bloch simulator was developed and used to evaluate the effect on image quality of inhomogeneity in transmit and receive B_1 fields. Images generated by a microstrip array probe were then investigated by importing TLM simulated B_1 fields into the Bloch simulator.

The effect of field cancellation on image quality during quadrature transmission and reception is demonstrated. It is shown that parallel reception offers a significant improvement in image quality, because the received signals do not suffer from interference.

There is no direct transmit equivalent to parallel reception. During reception the sample emits a signal, which is detected by spatially separate parts of a probe with different phase shifts. A volume probe sums these signals, causing interference. An array probe individually records the signal detected by each element without interference. During transmission, several probe elements transmit a signal into the sample. When multiple transmit elements are simultaneously active, their fields superimpose and their individual effects cannot be separated.

To avoid the effects of interference, a new imaging sequence was developed which excites probe elements sequentially rather than simultaneously. A Burst-like encoding scheme is used to store sample magnetisation produced by each excitation, in such a way that each excitation can be separately recalled at a later time. This allows multiple RF pulses to be applied to a sample in rapid succession, without waiting for the sample magnetisation to return to equilibrium between pulses. Magnetisation from all excitations is recalled in a single readout.

The method is not a complete imaging sequence, but a modification that can be applied to any gradient echo sequence. The method is limited to nutations of 90° or less, so cannot be applied to spin echo sequences.

A distinct advantage of the sequential imaging method is that it requires only a small hardware modification to the scanner. The TR switch is replaced with an RF multiplexer and an RF probe with multiple transmit elements is required. The sequence uses only one RF power amplifier, which the multiplexer switches between probe elements during the transmit sequence.

The multi-element probe can also be used as a volume probe, for transmission and reception, by driving or combining channels with an appropriate phase shift. By modifying the RF multiplexer, the probe could be switched

between array and volume mode during an imaging sequence if, for example, a 180° pulse is required.

Emerging potential solutions to the high field imaging problem often involve a combination of RF probe design and manipulation of sample magnetisation, as shown in this work and elsewhere [20, 101, 118]. The combination of Bloch simulation built on top of full wave electromagnetic simulation provides a powerful tool for investigating such methods.

Chapter 7

Hardware Implementation

7.1 Introduction

In the previous chapter a new imaging technique was developed, and demonstrated using Bloch simulation based on TLM simulated B_1 transmit and receive fields. In this chapter, the results are verified by constructing a multi-element probe and implementing the new imaging sequence.

The installation of the Philips 7T system was incomplete when this work was carried out, so the probe was built to operate at 128MHz for use in the Nottingham 3T system. Wavelength effects are not a serious problem at 128MHz, so the new imaging method does not offer a significant increase in image homogeneity at this frequency. However, the acquired images demonstrate that the new sequence allows images from sequentially applied RF pulses to be acquired separately, offering significant benefits when used at a higher static field strength.

To implement the new imaging sequence, an RF multiplexer was also designed and built. The multiplexer, which replaces the conventional TR switch, is used to switch the RF transmit channel between different probe elements.

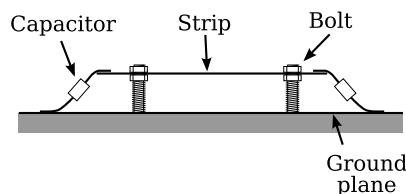


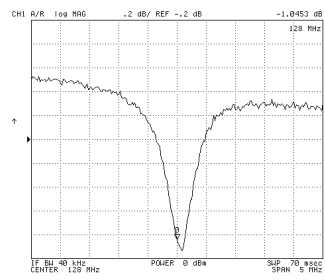
Figure 7.1: Microstrip construction, showing capacitors attached at either end of the strip and the mounting bolts used to tune the strip.

The Nottingham 3T system has only a single receive channel. The results presented in this chapter were obtained by repeating each experiment to acquire multiple receive channels. While this procedure will not demonstrate all potential problems with the imaging sequence (e.g. noise correlation), it does allow the acquisition of different images due to different excitation pulses.

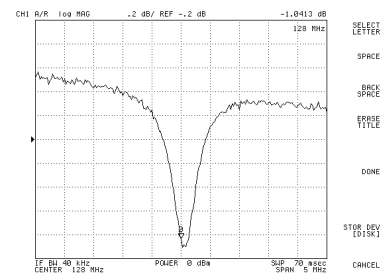
7.2 The Probe

A four element microstrip probe was constructed from double sided copper clad printed circuit board. Each microstrip was made from a $150\text{mm} \times 30\text{mm}$ strip of printed circuit board, mounted approximately 20mm above the $100\text{mm} \times 285\text{mm}$ ground plane using a pair of nylon bolts (fig. 7.1). The strip was connected to the ground plane at either end via 47pF power capacitors. The strip was tuned by adjusting its height above the ground plane. The strip was driven via a coaxial cable directly attached to one side of the strip at a point approximately a quarter of the way along its length. The exact position, chosen to match the strip to 50Ω , was found by sliding the feed cable along the strip and observing the impedance using a network analyser (model HP 4396B, HP, Bracknell, UK). Once the 50Ω point was located, the cable was soldered in place. The cable screen was soldered to the ground plane directly below the feed point. Strip impedances and Q -factors are given in table 7.1; resonance curves are shown in fig. 7.2.

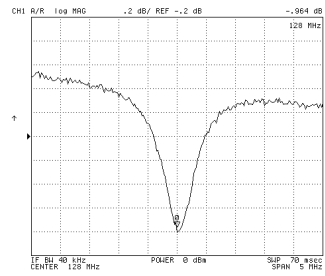
Four microstrip plates and four blank plates were then assembled to form an octagonal cavity (fig. 7.3a). The edges of the plates were coated with



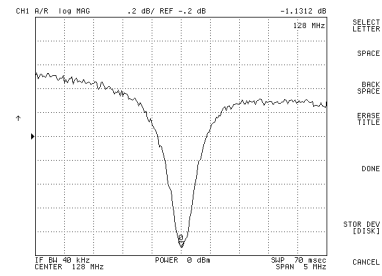
(a) strip 1



(b) strip 2



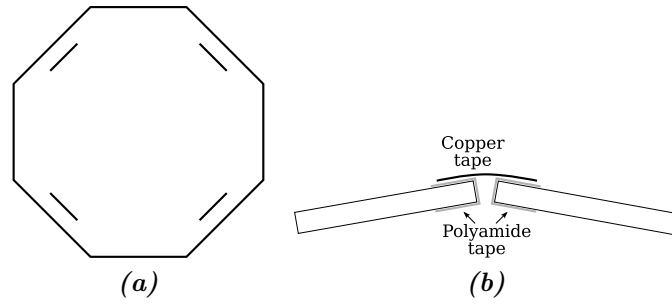
(c) strip 3



(d) strip 4

Figure 7.2: Strip resonance curves.

Strip No.	Impedance / Ω	Q -factor (unloaded)
1	$51.4 + 5.6i$	75
2	$55.2 - 9.4i$	82
3	$56.0 - 2.4i$	75
4	$51.2 + 0.0i$	79

Table 7.1: Probe impedance and Q factor.**Figure 7.3:** Probe construction details: (a) the strip arrangement inside the shield, and (b) detail of the connection between ground plates.

polyamide tape, and then joined together with copper tape (fig. 7.3b). This forms a small capacitance between adjacent plates, making a continuous shield at radiofrequencies, while displaying a high impedance at audio-frequencies to reduce eddy currents induced in the shield by the gradient coils. Once the probe was assembled, the strips were retuned and rematched. The complete probe is shown in fig. 7.4.

7.3 The Multiplexer

To implement the new imaging sequence on the Nottingham 3T scanner, a four channel multiplexer was designed and built to replace the TR switch. The multiplexer performs two tasks: it selects which probe element is connected to the power amplifier during transmission, and connects all probe elements to their respective preamplifiers during reception (fig. 7.5).

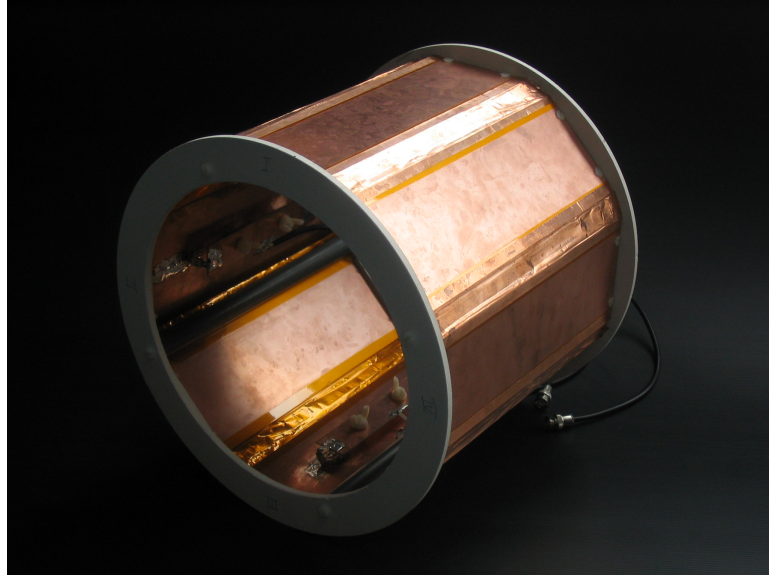


Figure 7.4: The four-microstrip probe.

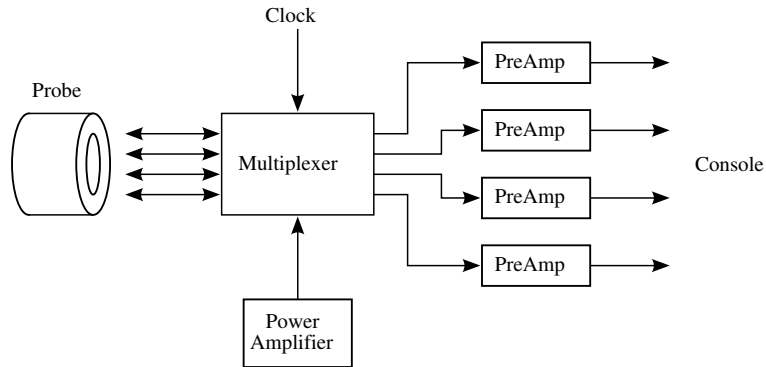


Figure 7.5: The multiplexer sits between the probe and the console, replacing the TR switches.

The circuit is separated into two parts: the RF board which performs the RF switching, and the interface board which contains control logic and drivers for the PIN diodes.

7.3.1 RF Switching

The switching circuit (fig. 7.6) uses PIN diodes to control four RF channels. The circuit has one input from the power amplifier (RF_{in}), four outputs to

the preamplifiers ($PreAmp_{1-4}$), and four connections to the probe elements ($Coil_{1-4}$). Any single probe element can be connected to the RF power amplifier, or all four elements simultaneously connected to their respective preamplifiers. The PIN diode switches are operated by five control lines (SW_{1-4} and $\overline{SW_{rx}}$).

Each channel consists of three sections. A series switch between the RF input and the probe element ($D_1 - D_4$) is designed to provide maximum isolation in the *off* state. A shunt switch between the probe element and preamplifier ($D_5 - D_8$) gives minimum insertion loss in the *on* state. To increase preamplifier isolation in the *off* state a quarter wave section is placed before the shunt switch. When the shunt switch is closed (i.e. short circuit to ground), the quarter wave line transforms the short circuit to appear as an infinite impedance at the opposite end, blocking signal from the probe or power amplifier.

The circuit was constructed on PCB. The RF transmit signal passes through capacitor C_1 , which must have a high enough breakdown voltage to withstand the high power signal. Capacitors $C_2 - C_9$, which carry only the low power received signals, are ordinary surface mount capacitors. The quarter wave sections were made from 160mm lengths of RG316 coaxial cable. Inductors $L_1 - L_9$ must be able to carry the 500mA signal used to bias the PIN diodes.

7.3.2 Control Logic

To simplify the interface to the console, the multiplexer was designed to include a counter, controlled by the RF gate signal (fig. 7.7). The counter selects which probe element is connected to the RF power amplifier. During transmission the console uses the gate signal to enable the RF power amplifier output. The multiplexer uses the falling edge of the gate signal to increment the channel counter, automatically incrementing the RF transmit channel at the end of each RF pulse (fig. 7.8).

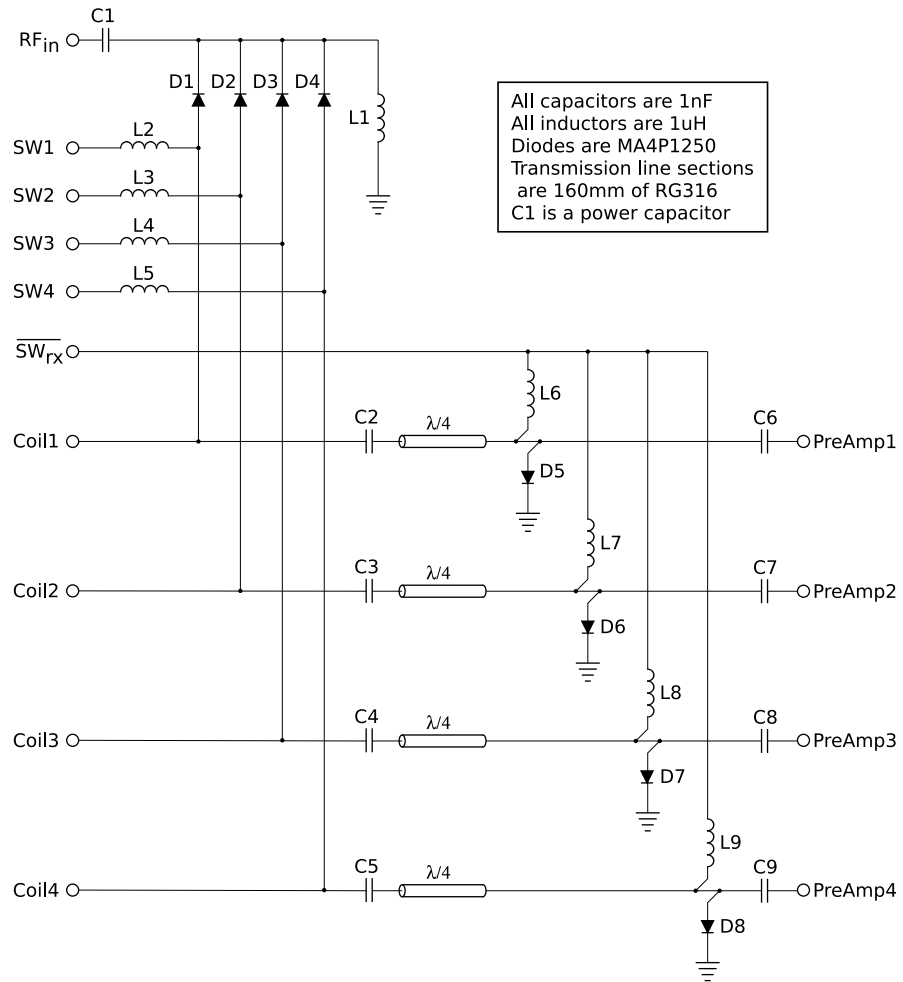


Figure 7.6: The multiplexer RF circuit.

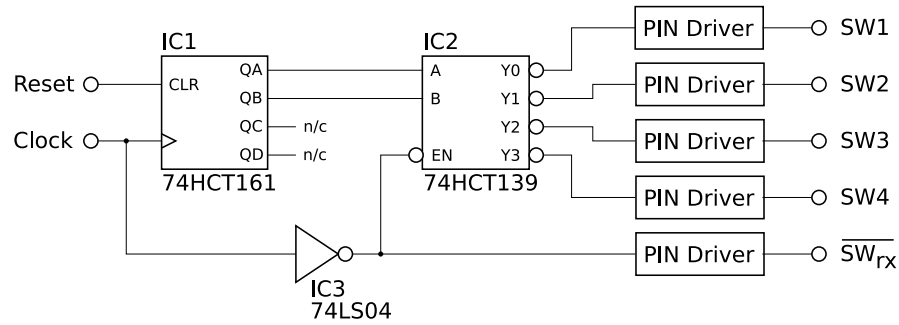


Figure 7.7: Counter circuit.

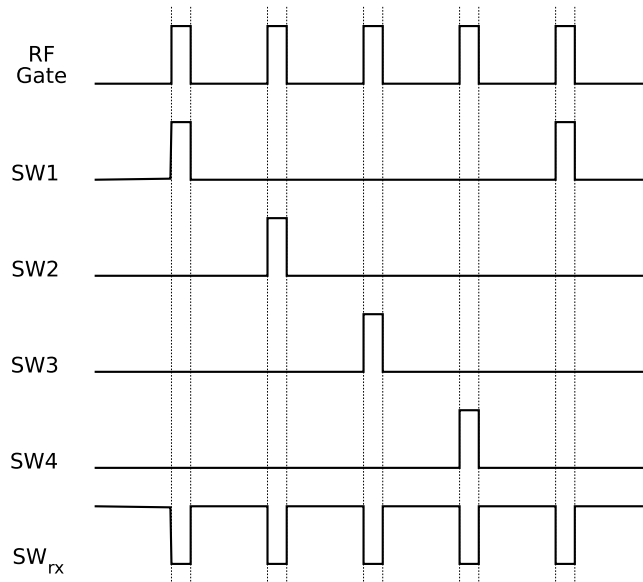


Figure 7.8: Output from the counter circuit.

The counter circuit can be replaced by an address decoder to allow the console to select an excitation element using two or more digital control lines. Element selection can then be incorporated into the imaging pulse sequence.

A driver circuit is used to boost the TTL output from the counter to bias the PIN diode switches (fig. 7.9). In the *off* state, the PIN diodes are reverse biased to -30V . This is sufficiently negative that the superimposed RF signal will not bring the diodes into conduction. Because the diodes are not conducting in this state, the negative power supply only needs to provide enough current to drive the switching circuit ($<20\text{mA}$). In the *on*

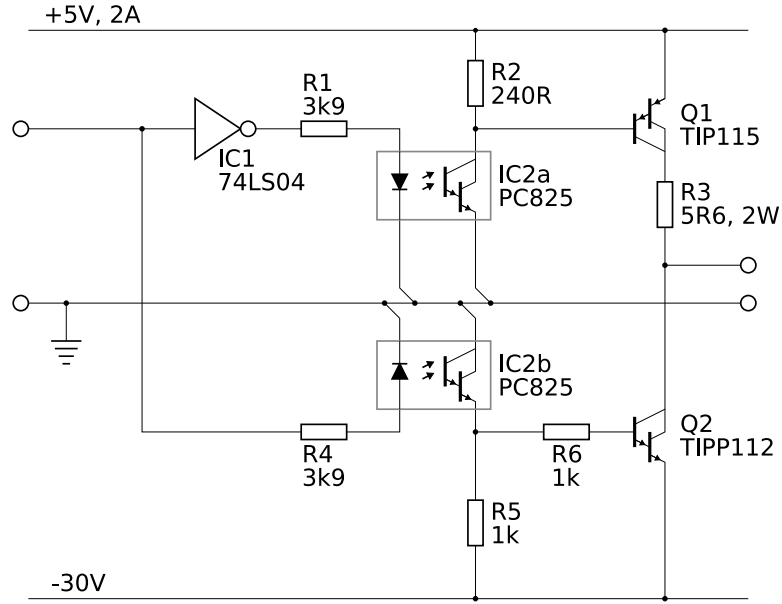


Figure 7.9: PIN diode drive circuit.

state the PIN diodes are forward biased at 500mA, giving a series resistance of 0.15Ω [168]. The driver circuit includes opto-couplers to isolate the high power RF signal from the low power logic circuit.

7.3.3 Performance

The insertion loss and isolation of the multiplexer, measured using a network analyser (model HP 4396B, HP, Bracknell, UK), are shown in table 7.2. Note that there are no DC blocking capacitors between the probe connectors and the switch control lines, so probe elements will carry a DC bias. Blocking capacitors would decrease the SNR of the received signal, as they add an extra component in the receive path. A 2.2nF capacitor was inserted between the network analyser and the $Coil_n$ terminals to isolate the network analyser from the DC bias signal used to enable the transmit channels. The capacitor was included in the cable calibration of the network analyser so that it does not affect the measurements.

The insertion loss of the receive pathways is low enough that the multiplexer is usable, but it could be improved upon with careful circuit layout. The

Input Port	Output Port	Insertion Loss /dB	Isolation /dB
RF_{in}	$Coil_{1-4}$	15.0	48.0
$Coil_1$	$PreAmp_1$	0.32	16.0
$Coil_2$	$PreAmp_2$	0.37	16.6
$Coil_3$	$PreAmp_3$	0.36	15.5
$Coil_4$	$PreAmp_4$	0.38	16.3

Table 7.2: Insertion loss and isolation of the multiplexer.

insertion loss of the transmit pathway is higher, which is expected as the transmit signal passes through a diode (D1–4, fig. 7.6). Loss in the transmit channel is more acceptable than the receive channel, as the transmit signal power may be increased to compensate. The isolation between the RF_{in} port and the preamplifier ports is high enough to protect the preamplifiers during transmission.

7.4 Imaging at 3T

The waveform controller was programmed to run the new imaging sequence by Dr. B. Wilton.

The first step in acquiring images with the new sequence was to shim for the sample. It was found that each probe strip required different shim settings. An iterative manual shimming process was used to achieve a compromise, producing the same linewidth on all four channels.

The imaging sequence was then run, but with only one of the four RF pulses enabled, allowing gradient amplitudes and pre-sampling delay to be set up in the normal manner. All four RF pulses were then enabled, and the inter-pulse delay adjusted to produce four non-overlapping echoes in k -space.

The Nottingham 3T scanner has only a single proton receive channel. Parallel image acquisition was approximated by running the imaging sequence

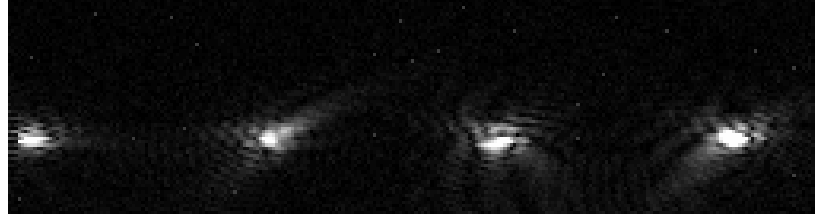


Figure 7.10: *A single k -space channel.*

four times, collecting data on a different channel each time. Unused receive channels were terminated with 50Ω loads.

Fig. 7.10 shows a k -space image (256×64 pixels) of data acquired from a single receive channel, following four RF pulses, each applied to a different probe element. The data has been re-ordered to account for the echo-planar trajectory. Four different refocussing centres are clearly visible. This data is then divided into four blocks (64×64 pixels) and reconstructed as a normal image. This procedure is repeated for all four receive channels, producing a separate image for each transmit/receive element combination (fig. 7.11). The significance of these images is that a single readout contains a series of independent images, each excited by a different RF pulse. The ability to separate different excitation profiles allows images to be acquired from a sequence of strip excitations without interference, which is the difference between figs. 5.59*a* and 5.59*b*.

The separate images were combined using sum-of-squares to produce the single composite image shown in fig. 7.12. The phantom image shows reasonable uniformity, despite the highly non-uniform images it is composed from. The imaging sequence was run at low RF power (well below a 90° pulse) as the coupling between probe strips was quite strong, accounting for the poor SNR of the images.

7.5 Discussion

The sequential excitation imaging method does not offer significant benefit at 3T, as wavelength effects are not a serious problem at 128MHz. The

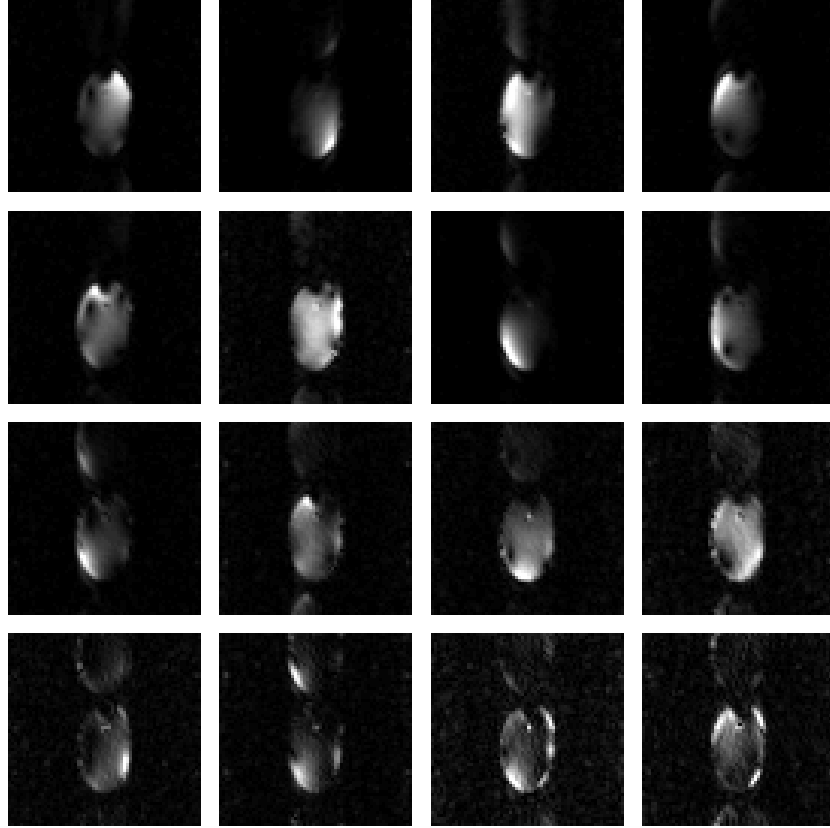


Figure 7.11: Images acquired at 3T using the new probe. Each row was excited by a different transmit channel, each column was acquired with a different receive channel.

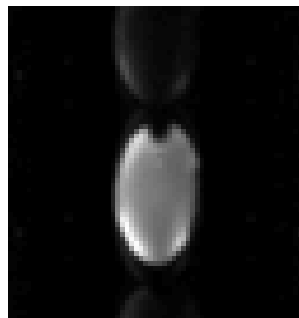


Figure 7.12: The sum-of-squares of the acquired images.

reason for implementing the method was to demonstrate that different excitation profiles, produced by different transmit elements, can be stored in the sample magnetisation and independently recalled using a single read-out. Each of the sixteen images in fig. 7.11 is different, being produced by a different combination of transmit and receive elements. This demonstrates that four different excitation profiles can be simultaneously stored in the sample magnetisation, and later recalled and separated.

The new imaging sequence was implemented on a scanner with a single transmit channel, demonstrating how simple the required hardware modifications are. The only hardware components to be changed were the RF probe itself, and the multiplexer which is used in place of the TR switch. The probe and multiplexer can be fitted, or the scanner returned to its normal operating mode, in minutes.

Chapter 8

Discussion

8.1 Summary

Work presented in this thesis investigates the design of RF probes for imaging at high field. The initial focus of this research was purely on the electromagnetic problem of designing a structure to produce a uniform B_1 field inside the human head. It was quickly realised that at short wavelength, such a structure does not exist, and a broader view of the problem is required. We are actually trying to produce uniform images of the sample; a uniform B_1 field is merely a way to attain that goal.

Magnetic resonance imaging can be considered as being composed of two different processes, happening on very different time scales. The first process is the propagation of magnetic fields through the sample, which happens on a scale of picoseconds. It is the finite time it takes for these fields to propagate through the head which leads to interference in the B_1 field at short wavelength. This is the timescale modelled by the TLM simulator.

The second part of the problem space is that of the NMR processes used to localise signal to generate images of a sample. Field gradients are typically switched in the audio-frequency range (milliseconds), while NMR relaxation processes in tissue take place on a scale of milliseconds to seconds. Spin

precession happens on a picosecond timescale but, working in the rotating frame of reference, we are interested only in changes in precession which again happen on a millisecond timescale. This is the timescale modelled by the Bloch simulator.

By considering the combination of the above processes, a new imaging sequence was developed to avoid interference in the B_1 field by sequentially exciting the sample and storing information from each excitation using the sample magnetisation. The information is then read back using field gradients to refocus sample magnetisation, as is done for a normal imaging sequence.

Using a combination of full wave electromagnetic simulation, using the Transmission Line Matrix method, and Bloch simulation, the advantage offered by the new imaging sequence has been demonstrated. The sequence has been tested at 3T (128MHz), demonstrating that it works as proposed, allowing magnetisation due to a sequence of RF excitations to be stored in the sample, recalled in a single image readout, and separated into independent images produced by each excitation pulse.

8.2 Future Work

The immediate task arising from this work is to implement the sequential excitation method at 7T. All the parts have been demonstrated: electromagnetic simulation has shown the suitability of the probe design, Bloch simulation has shown the potential of sequential imaging for removing wavelength artifacts, and the 3T implementation has shown that different excitation profiles are indeed separable. A 7T implementation will demonstrate all of these parts together, and is expected to show a significant improvement in image homogeneity and SNR.

Transmission Line Matrix modelling has been demonstrated as a valuable technique for evaluating a particular probe design, but the method is currently too slow to be used as part of an optimisation cycle. Tuning a probe model currently takes approximately 6–8 hours of computer runtime, and

generating steady-state fields requires another hour. Using improved spectral estimation methods, described below, it is expected that the time taken to tune simulation models can be reduced by a factor of ten. By implementing a parallel version of the TLM simulator, using the MPI libraries [169], a further reduction in simulation time can be achieved. If the simulation time for a single probe model can be reduced from hours to minutes, the simulation can be used to optimise probe designs. A high performance computing facility has recently become available at Nottingham University (a 1000 node AMD Opteron cluster), making large scale simulation a possibility.

Extracting parameters such as mutual coupling or Q -factors from simulated timecourse data has been found to be rather difficult. The exact figures depend strongly on factors such as the apodization window and the number of data points available. The peak splitting that is normally observed when probe elements couple has not been observed in simulated data. Frequency domain parameters have been estimated by taking the Discrete Fourier Transform (DFT) of simulated timecourses. The Fourier Transform is a general method, making no assumptions about the form of the spectrum. For a high Q system such as an RF probe, the form of the response is already known. By restricting our model of the impulse response to the expected form, it is possible to extract more information about the system using fewer data points. One technique for doing this is Prony's method, which directly approximates the impulse response as a series of exponentially damped sinusoids [159]. Prony's method has previously been used with TLM to great effect, producing an order of magnitude reduction in the required number of TLM iterations for the same spectral accuracy, when compared to the DFT [170].

The work presented in this thesis exclusively used a uniform Cartesian mesh. This was simple to implement and is fast to run, but sometimes compromises the accuracy of the simulation model. Using a uniform mesh restricts the detail with which fine features may be represented, which is important for modelling the thin copper strips typically used in probe construction. The mesh size may also be important for the accuracy of the human phantom. When using a $(3\text{mm})^3$ mesh, it is difficult to accurately model the skin, which is electromagnetically significant. One solution is to use a multi-grid

mesh (section 4.5.9), modelling different regions of the model at different resolution. Another interesting possibility is to use the tetrahedral TLM mesh currently being developed by Sewell *et al.* [142]. Both of these solutions will result in slower simulations, but would be useful for verifying the accuracy of simulations using a uniform mesh.

As the operating frequency of the RF probe increases, the SAR distribution inside the head becomes more localised. The regions of maximum SAR also move from the surface of the head where cooling mechanisms function most efficiently to deeper regions such as the brain (fig. 5.14). Tissue damage is caused by a rise in temperature, rather than the absorbed power (SAR). It is assumed that the temperature rise correlates closely with absorbed power, but this takes no account of the bodies natural cooling mechanisms. The author intends to develop a simulation model for heat dissipation within the body, using Penne's bioheat equation [171, 172] combined with TLM generated electric fields, to investigate how closely the temperature rise actually follows the local SAR.

Coupling between probe elements is a significant problem, especially at high frequency. The sequential excitation scheme uses only one transmit element at a time, allowing detuning of unused elements to prevent coupling during transmission. However, coupling between elements is still problematic during reception. Capacitive decoupling methods are currently under investigation as a potential solution to this problem [82]. Improvement methods for extracting the spectral response of probe elements from simulated data, described above, are intended to help the study of coupling between probe elements.

The work presented in this thesis addresses imaging the human head. However, ultra high field imaging is not limited to the head; the Nottingham 7T system, for example, is equipped with a full body magnet. The larger volume of the human torso will make wavelength effects in the transmit and receive B_1 field more apparent. The sequential excitation scheme developed in this work is equally applicable to imaging the torso and structures therein. Because the method removes interference during transmission, it is

expected to continue to function well as both imaging volume and excitation frequency are increased.

8.3 Conclusions

Full wave electromagnetic simulation using the Transmission Line Matrix (TLM) method has been demonstrated as a valuable tool for investigating potential probe designs, and for understanding the fields generated by probes at short wavelength. The combination of electromagnetic and Bloch simulation is particularly useful for investigating high field imaging methods, where proposed solutions often use a combination of probe design and NMR manipulation to achieve uniform images.

Ultra high frequency magnetic resonance imaging offers a significant improvement in available SNR, but realising that improvement, despite inhomogeneity in the B_1 field, is a significant technical challenge. As probe design moves away from the near-field regime, the advantage in using array probes for both reception and transmission becomes clear. It is unlikely that volume probes will continue to be used for high field imaging. Parallel receive MRI systems are already common. In the authors opinion, parallel transmit systems will become the standard for UHF MRI, either using a sequential method such as the one presented in this work, or using a simultaneous excitation method such as transmit SENSE [20].

References

- [1] E. M. Purcell, H. C. Torrey, and R. V. Pound. Resonance absorption by nuclear magnetic moments in a solid. *Physical Review*, 69:37–38, 1946.
- [2] F. Bloch. Nuclear induction. *Physical Review*, 70:460–474, 1946.
- [3] P. C. Lauterbur. Image formation by induced local interactions: Examples employing nuclear magnetic resonance. *Nature*, 242:190–191, 1973.
- [4] P. Mansfield and P. K. Grannell. NMR ‘diffraction’ in solids? *Journal of Physics C: Solid State Physics*, 6:L422–426, 1973.
- [5] S. Ogawa, T.-M. Lee, A. S. Nayak, and P. Glynn. Oxygenation-sensitive contrast in magnetic resonance image of rodent brain at high magnetic fields. *Magnetic Resonance in Medicine*, 14:68–78, 1990.
- [6] J. Belliveau, B. Rosen, H. Kantor, R. Rzedzian, D. Kennedy, R. McKinstry, J. Vevea, M. Cohen, I. Pykett, and T. Brady. Functional cerebral imaging by susceptibility-contrast NMR. *Magnetic Resonance in Medicine*, 14:538–546, 1990.
- [7] F. Bloch, W. W. Hansen, and M. Packard. The nuclear induction experiment. *Physical Review*, 70:474–485, 1946.
- [8] F. Mandl. *Quantum Mechanics*. Wiley & Sons, 1992.
- [9] P. Callaghan. *Principles of Nuclear Magnetic Resonance Microscopy*. Oxford University Press, 1991.
- [10] Z.-P. Liang and P. C. Lauterbur. *Principles of Magnetic Resonance Imaging*. IEEE Press, 2000.
- [11] S. Webb, editor. *The Physics of Medical Imaging*. Institute of Physics, 1988.

- [12] A. N. Garroway, P. K. Grannell, and P. Mansfield. Image formation in NMR by a selective irradiative process. *Journal of Physics C: Solid State Physics*, 7:L457–462, 1974.
- [13] A. Kumar, D. Welte, and R. R. Ernst. NMR fourier zeugmatography. *Journal of Magnetic Resonance*, 18:69–83, 1975.
- [14] P. Mansfield. Multi-planar image formation using NMR spin echoes. *Journal of Physics C: Solid State Physics*, 10:L55–58, 1977.
- [15] W. A. Edelstein, J. M. S. Hutchison, G. Johnson, and T. Redpath. Spin warp NMR imaging and applications to human whole-body imaging. *Physics in Medicine and Biology*, 25:751–756, 1980.
- [16] C.-N. Chen and D. I. Hoult. *Biomedical Magnetic Resonance Technology*. IOP Publishing, 1989.
- [17] D. I. Hoult. Zeugmatography: a criticism of the concept of a selective pulse in the presence of a field gradient. *Journal of Magnetic Resonance*, 26:165–167, 1977.
- [18] C. J. Hardy and H. E. Cline. Spatial localization in two dimensions using NMR designer pulses. *Journal of Magnetic Resonance Imaging*, 82:647–654, 1989.
- [19] J. M. Pauly, B. S. Hu, S. J. Wang, D. G. Nishimura, and A. Macovski. A three dimensional spin-echo or inversion pulse. *Magnetic Resonance in Medicine*, 28:2–6, 1993.
- [20] U. Katscher, P. Bornert, C. Leussler, and J. S. van den Brink. Transmit SENSE. *Magnetic Resonance in Medicine*, 49:144–150, 2003.
- [21] J. R. Hook and H. E. Hall. *Solid State Physics*. John Wiley & Sons, 1991.
- [22] S. Ljunggren. A simple graphical representation of fourier-based imaging methods. *Journal of Magnetic Resonance*, 54:338–343, 1983.
- [23] S. Clare. Ghost artefact in fMRI: comparison of techniques for reducing the N/2 ghost. In *Proceedings of the 12th ISMRM*, 1998.
- [24] J. Hennig. Multi-echo imaging sequences with low refocusing flip-angles. *Journal of Magnetic Resonance*, 78:397–407, 1988.
- [25] I. J. Lowe and R. E. Wysong. DANTE ultrafast imaging sequence (DUFIS). *Journal of Magnetic Resonance, Series B*, 101:106–109, 1993.

- [26] L. Zha and I. J. Lowe. Optimized ultra-fast imaging sequence (OUFIS). *Magnetic Resonance in Medicine*, 33:377–395, 1995.
- [27] J. Hennig and M. Hodapp. Burst imaging. *MAGMA*, 1:39–48, 1993.
- [28] J. Hennig. Echoes – how to generate, recognise, use or avoid them in MR imaging, part I. *Concepts in Magnetic Resonance*, 3:125–143, 1991.
- [29] J. Hennig. Echoes – how to generate, recognise, use or avoid them in MR imaging, part II. *Concepts in Magnetic Resonance*, 3:179–192, 1991.
- [30] J. S. Hyde, J. W. Froncisz, J. B. Kneeland, T. M. Grist, and N. F. Campagna. Parallel image acquisition from non-interacting local coils. *Journal of Magnetic Resonance*, 70:512–517, 1986.
- [31] P. B. Roemer, W. A. Edelstein, C. E. Hayes, S. P. Souza, and O. M. Mueller. The NMR phased array. *Magnetic Resonance in Medicine*, 16:192–225, 1990.
- [32] M. Hutchinson and U. Raff. Fast MRI data acquisition using multiple detectors. *Magnetic Resonance in Medicine*, 6:87–91, 1988.
- [33] M. Preston McDougall and S. M. Wright. 64-channel array coil for single echo acquisition magnetic resonance imaging. *Magnetic Resonance in Medicine*, 54:386–392, 2005.
- [34] J. W. Carlson. An algorithm for NMR imaging reconstruction based on multiple RF receive coils. *Journal of Magnetic Resonance*, 74:376–380, 1987.
- [35] S. Wright. Surface coils, arrays and the benefits of array imaging. In *First Würzburg Workshop on Parallel Imaging Basics and Clinical Applications*, 2001.
- [36] D. K. Sodickson and W. J. Manning. Simultaneous acquisition of spatial harmonics (SMASH): ultra-fast imaging with radiofrequency coil arrays. *Magnetic Resonance in Medicine*, 38:591–603, 1997.
- [37] M. Bydder, D. J. Larkman, and J. V. Hajnal. Generalized SMASH imaging. *Magnetic Resonance in Medicine*, 47:160–170, 2002.
- [38] K. P. Pruessmann, M. Weiger, M. B. Scheidegger, and P. Boesiger. SENSE: sensitivity encoding for fast MRI. *Magnetic Resonance in Medicine*, 42:952–962, 1999.
- [39] G. W. Stewart. *Introduction to Matrix Computations*. Academic Press, 1973.

- [40] J. Jin. *Electromagnetic Analysis and Design in Magnetic Resonance Imaging*. CRC Press, 1999.
- [41] R. Bowtell. Overview of an MRI system. In *Proceedings of the 12th ISMRM, (Educational Course)*, 2004.
- [42] I. Brown, J. Bird, I. McDougall, and D. Black. Magnet assembly for use in NMR apparatus. United States Patent 4,578,504, 1986.
- [43] J. Wilson and P. Jezzard. Fast, fully automated global and local shimming of the human brain. In *Proceedings of the 9th ISMRM*, 2001.
- [44] E. B. Boskamp. RF subsystem. In *Proceedings of the 12th ISMRM, (Educational Course)*, 2004.
- [45] A. Hasse, F. Odoj, M. von Kienlin, J. Warnking, F. Fidler, A. Weisser, M. Nittka, E. Rommel, T. Lanz, B. Kalusche, and M. Griswold. NMR probeheads for in vivo applications. *Concepts in Magnetic Resonance*, 12:361–388, 2000.
- [46] G. Adriany. Transmit and receive arrays for ultra high field parallel imaging. In *Second International Workshop on Parallel MRI*, 2004.
- [47] I. Graesslin, P. Vernickel, J. Schmidt, C. Findekle, P. P. Röschmann, C. Leussler, P. Haaker, H. Laudan, K. M. Luedeke, J. Scholz, S. Buller, J. Keupp, P. P. Börnert, H. Dingemans, G. Mens, G. Vissers, N. Blom, K. Swennen, J. vd Heijden, L. Mollevanger, P. P. Harvey, and U. Katscher. Whole body 3T MRI system with eight parallel RF transmission channels. In *Proceedings of the 14th ISMRM*, 2006.
- [48] L. DelaBarre, C. J. Snyder, K. Ugurbil, and J. T. Vaughan. A parallel transceiver for human imaging at 9.4T. In *Proceedings of the 14th ISMRM*, 2006.
- [49] D. I. Hoult. The principle of reciprocity in signal strength calculations – a mathematical guide. *Concepts in Magnetic Resonance*, 12(4):173–187, 2000.
- [50] C. M. Collins, W. Liu, W. Schreiber, Q. X. Yang, and M. B. Smith. Central brightening due to constructive interference with, without, and despite dielectric resonance. *Magnetic Resonance in Medicine*, 21(2):192–196, 2005.
- [51] A. Abragam. *Principles of Nuclear Magnetism*. Oxford University Press, 1961.

- [52] C. E. Hayes, W. A. Edelstein, J. F. Schenck, O. M. Mueller, and M. Eash. An efficient, highly homogeneous radiofrequency coil for whole-body NMR imaging at 1.5T. *Journal of Magnetic Resonance*, 63:622–628, 1985.
- [53] J. T. Vaughan, H. P. Hetherington, J. O. Otu, J. W. Pan, and G. M. Pohost. high frequency volume coils for clinical NMR imaging and spectroscopy. *Magnetic Resonance in Medicine*, 32:206–218, 1994.
- [54] J.T. Vaughan, G. Adriany, M. Garwood, E. Yacoub, T. Duong, L. de la Barre, P. Andersen, and K. Ugurbil. Detunable transverse electromagnetic (TEM) volume coil for high-field NMR. *Magnetic Resonance in Medicine*, 47:990–1000, 2002.
- [55] W. A. Edelstein, G. H. Glover, C. J. Hardy, and R. W. Redington. The intrinsic signal-to-noise ratio in NMR imaging. *Magnetic Resonance in Medicine*, 3:604–618, 1986.
- [56] P. Röschmann. Radiofrequency penetration and absorption in the human body: limitations to high-field whole body nuclear magnetic resonance imaging. *Medical Physics*, 14:922–931, 1987.
- [57] L. V. Blake. *Antennas*. Wiley & Sons, 1966.
- [58] J. T. Vaughan, G. Adriany, C. J. Snyder, J. Tian, T. Thiel, L. Bolinger, H. Liu, L. de la Barre, and K. Ugurbil. Efficient high-frequency body coil for high-field MRI. *Magnetic Resonance in Medicine*, 52:851–859, 2004.
- [59] Medical electrical equipment part 2-33: Particular requirements for the safety of magnetic resonance equipment for medical diagnosis. Technical Report IEC 60601-2-33:2002, International Electrotechnical Commission, 2002.
- [60] D. I. Hoult and R. E. Richards. The signal-to-noise ratio of the nuclear magnetic resonance experiment. *Journal of Magnetic Resonance*, 24:71–85, 1976.
- [61] J. B. Johnson. Thermal agitation of electricity in conductors. *Physical Review*, 32:97, 1928.
- [62] H. Nyquist. Thermal agitation of electric charge in conductors. *Physical Review*, 32:110–113, 1928.
- [63] D. I. Hoult and P. C. Lauterbur. Sensitivity of the zeugmatographic experiment involving human samples. *Journal of Magnetic Resonance*, 34:425–433, 1979.

- [64] H. D. Hill and R. E. Richards. Limits of measurement in magnetic resonance. *Journal of Physics E*, 1:977–983, 1968.
- [65] E. R. Davies. *Electronics, Noise and Signal Recovery*. Academic Press, London, 1993.
- [66] P. Horowitz and W. Winfield Hill. *The Art of Electronics*. Cambridge University Press, 3rd edition, 1989.
- [67] A. Reykowski, S. M. Wright, and J. R. Porter. Design of matching networks for low noise preamplifiers. *Magnetic Resonance in Medicine*, 33:848–852, 1995.
- [68] H. L. Krauss, C. W. Bostian, and F. H. Raab. *Solid State Radio Engineering*. Wiley & Sons, 1980.
- [69] American technical ceramics, product selection guide, 2006.
- [70] anon. The PIN diode circuit designers handbook. Technical report, Microsemi Corporation, 1998.
- [71] D. M. Ginsberg and M. J. Melchner. Optimum geometry of saddle shaped coils for generating a uniform magnetic field. *Review of Scientific Instruments*, 41:122–123, 1970.
- [72] H. J. Schneider and P. Dullenkopf. Slotted tube resonator: A new NMR probe head at high observing frequencies. *Review of Scientific Instruments*, 48:68–73, 1977.
- [73] D. W. Alderman and D. M. Grant. An efficient decoupler coil design which reduces heating in conductive samples in superconducting spectrometers. *Journal of Magnetic Resonance*, 36:447–451, 1979.
- [74] P. K. H. Röschmann. High frequency coil system for a magnetic resonance imaging apparatus. United States Patent 4,746,866, 1988.
- [75] J. T. Vaughan, M. Garwood, C. M. Collins, W. Liu, L. DelaBarre, G. Adriany, P. Anderson, H. Merkle, R. Goebel, M. B. Smith, and K. Ugurbil. 7T vs. 4T: RF power, homogeneity, and signal-to-noise comparison in head images. *Magnetic Resonance in Medicine*, 46:24–30, 2001.
- [76] J. Tian and T. Vaughan. Frequency limits and radiation resistance for volume coils. In *Proceedings of the 11th ISMRM*, 2003.
- [77] G. D. de Meester, Z. Zhai, M. A. Morich, C. Leussler, and C. Findelee. Numerical comparison between TEM head coil and birdcage head coil at 7T. In *Proceedings of the 12th ISMRM*, 2004.

- [78] R. D. Watkins and K. W. Rohling. 300MHz quadrature shielded bird-cage head coil for 7 Tesla. In *Proceedings of the 11th ISMRM*, 2003.
- [79] J. J. H. Ackerman, T. H. Grove, G. G. Wong, D. G. Gadian, and G. K. Radda. Mapping of metabolites in whole animals by ^{31}P NMR using surface coils. *Nature*, 283:167–170, 1980.
- [80] S. M. Wright and L. L. Wald. Theory and application of array coils in MR spectroscopy. *NMR in Biomedicine*, 10:394–410, 1997.
- [81] C. E. Hayes and P. B. Roemer. Noise correlations in data simultaneously acquired from multiple surface coil arrays. *Magnetic Resonance in Medicine*, 16:181–191, 1990.
- [82] A. Jones, P. Glover, and A. W. Magill. Decoupling method for high frequency strip-line probes gives truly independent elements. In *Proceedings of the 14th ISMRM*, 2006.
- [83] T. R. Fox. Capacitive network to cancel coupling between channels in MRI quadrature antenna. In *Proceedings of the 6th SMRM*, 1987.
- [84] J. Jevtic. Ladder networks for capacitive decoupling in phased-array coils. In *Proceedings of the 9th ISMRM*, 2001.
- [85] X. Zhang and A. Webb. Design of a capacitively decoupled transmit/receive NMR phased array for high field microscopy at 14.1T. *Journal of Magnetic Resonance*, 170:149–155, 2004.
- [86] R. F. Lee, R. O. Giaquinto, and C. J. Hardy. Coupling and decoupling theory and its application to the MRI phased array. *Magnetic Resonance in Medicine*, 48:203–213, 2002.
- [87] M. Weiger, K. P. Pruessmann, Leussler C., P. Roschmann, and P. Boesiger. Specific coil design for SENSE: a six-element cardiac array. *Magnetic Resonance in Medicine*, 45:495–504, 2001.
- [88] R. F. Lee, C. J. Hardy, D. K. Sodickson, and P. A. Bottomley. Lumped-element planar strip array (LPSA) for parallel mri. *Magnetic Resonance in Medicine*, 51:172–183, 2004.
- [89] M. A. Ohlinger, P. Ledden, C. A. McKenzie, and D. K. Sodickson. Effects of inductive coupling on parallel MR image reconstructions. *Magnetic Resonance in Medicine*, 52(3):628–639, 2004.
- [90] P. J. Wright, A. Peters, M. Brookes, R. Coxon, P. Morris, S. Francis, R. Bowtell, and P. Gowland. T_1 measurements for cortical grey matter, white matter and sub-cortical grey matter at 7T. In *Proceedings of the 14th ISMRM*, 2006.

- [91] A. M. Peters, M. J. Brookes, Hoogenraad F. G., P. A. Gowland, S. T. Francis, P. G. Morris, and R. W. Bowtell. Comparison of T2* measurements in human brain at 1.5, 3 and 7 T. In *Proceedings of the 14th ISMRM*, 2006.
- [92] P. A. Bottomley and E. R. Andrew. RF magnetic field penetration, phase shift and power dissipation in biological tissue: implications for NMR imaging. *Physics in Medicine and Biology*, 23(4):630–643, 1978.
- [93] P. Mansfield and P. G. Morris. *NMR imaging in biomedicine*. Academic Press, 1982.
- [94] J. D. Kraus and D. A. Fleisch. *Electromagnetics with applications*. McGraw-Hill, London UK, fifth edition, 1999.
- [95] PM. L. Robitaille, A. Kangarlu, and A. M. Abduljalil. RF penetration in ultra high field MRI. *Journal of Computer Assisted Tomography*, 23:845–849, 1999.
- [96] P. Röschmann and D. Jensen. Imaging of dielectric resonance mode patterns with a 4 Tesla whole body MR system. In *Proceedings of the 7th SMRM*, page 267, 1988.
- [97] T. S. Ibrahim, R. Lee, A. M. Abduljalil, B. A. Baertlein, and PM. L. Robitaille. Dielectric resonances and B_1 field inhomogeneity in UHFMRI: computational analysis and experimental findings. *Magnetic Resonance Imaging*, 19:219–226, 2001.
- [98] J. Tropp. Image brightening in samples of high dielectric constant. *Journal of Magnetic Resonance*, 167:12–24, 2004.
- [99] D. I. Hoult. Sensitivity and power deposition in a high-field imaging experiment. *Journal of Magnetic Resonance Imaging*, 12:46–67, 2000.
- [100] P. F. Van de Moortele, C. Akgun, G. Adriany, S. Moeller, J. Ritter, C. M. Collins, M. B. Smith, J. T. Vaughan, and K. Ugurbil. B_1 destructive interferences and spatial phase patterns at 7T with a head transceiver array coil. *Magnetic Resonance in Medicine*, 54:1503–1518, 2005.
- [101] C. M. Collins, B. L. Beck, J. R. Fitzsimmons, S. J. Blackband, and M. B. Smith. Strengths and limitations of pulsing coils in an array sequentially to avoid RF interference in high field MRI. In *Proceedings of the 13th ISMRM*, 2005.
- [102] T.S. Ibrahim, R. Lee, B.A. Baertlein, A.M. Abduljalil, H. Zhu, and P.L. Robataille. Effect of RF coil excitation on field inhomogeneity at ultra high fields: a field optimized TEM resonator. *Magnetic Resonance Imaging*, 19:1339–1347, 2001.

- [103] J. Tropp. The theory of the birdcage resonator. *Journal of Magnetic Resonance*, 82:51–62, 1989.
- [104] K. S. Yee. Numerical solution of initial boundary value problems involving Maxwell's equations in isotropic media. *IEEE Transactions on Antennas and Propagation*, pages 302–307, 14 1966.
- [105] R.F. Harrington. Matrix methods for field problems. *Proceedings of the IEEE*, 55:136–149, 1967.
- [106] M. J. Turner, R. W. Clough, H. C. Martin, and L. J. Topp. Stiffness and deflection analysis of complex structures. *Journal of Aeronautical Science*, 23:805–823, 1956.
- [107] J. H. Coggon. Electromagnetic and electrical modelling by finite element method. *Geophysics*, 36:132, 1971.
- [108] P. B. Johns. The solution of inhomogeneous waveguide problems using a transmission line matrix. *IEEE Transactions on Microwave Theory and Techniques*, MTT-22(3):209–215, March 1974.
- [109] O.P. Gandhi and I. Chatterjee. Radio-frequency hazards in the VLF to MF band. *Proceeding of the IEEE*, 70:1462–1464, 1982.
- [110] D. R. Lynch, K. D. Paulsen, and J. W. Strohbehn. Finite element solution of maxwell's equations for hyperthermia treatment planning. *Journal of Computational Physics*, 58:246–269, 1985.
- [111] O. P. Gandhi and J. Y. Chen. Numerical dosimetry at power-line frequencies using anatomically based models. *Bioelectromagnetics*, Suppl. 1:43–60, 1992.
- [112] O.P. Gandhi, G. Lazzi, and C.M. Furse. Electromagnetic absorption in the human head and neck for mobile telephones at 835 and 1900 mhz. *IEEE Transactions on Microwave Theory and Techniques*, 44:1884–1897, 1996.
- [113] G. M. J. Van Leeuwen, J. J. W. Lagendijk, B. J. A. M. Van Leersum, A. P. M. Zwamborn, S. N. Hornsleth, and A. N. T. J. Kotte. Calculation of change in brain temperatures due to exposure to a mobile phone. *Physics in Medicine and Biology*, 44:2367–2379, 1999.
- [114] L. S. Petropoulos, E. M. Haacke, R. W. Brown, and E. Boerner. Predicting RF field penetration in heterogeneous bodies using a 3D finite element approach: preliminary results. *Magnetic Resonance in Medicine*, 30:366–372, 1993.

- [115] D. Simunic, P. Wach, W. Renhart, and R. Stollberger. Spatial distribution of high-frequency electromagnetic energy in human head during MRI: Numerical results and measurements. *IEEE Transactions on Biomedical Engineering*, 43:88–94, 1996.
- [116] C. Guclu, G. Kashmar, A. Hacinliyan, and O. Nalcioglu. An FEM approach for the characterisation of the RF field homogeneity at high field. *Magnetic Resonance in Medicine*, 37:76–83, 1997.
- [117] W. T. Vetterling and B. P. Flannery. *Numerical Recipes in C++: The Art of Scientific Computing*. Cambridge University Press, 2nd edition, 2002.
- [118] P. J. Ledden and Y. Cheng. Improved excitation homogeneity at high frequencies with RF pulses of time varying spatial characteristics. In *Proceedings of the 12th ISMRM*, 2004.
- [119] C. M. Collins. Calculated B_1 homogeneity, SNR and SAR vs. frequency for the head in an idealized quadrature birdcage coil. In *Proceedings of the 7th ISMRM*. ISMRM, 1999.
- [120] T. S. Ibrahim, R. Lee, B. A. Baertlein, A. Kangarlu, and P. L. Robitaille. Application of finite difference time domain method for the design of birdcage RF head coils using multi-port excitation. *Magnetic Resonance Imaging*, 18:733–742, 2000.
- [121] H. Zhao, S. Crozier, and F. Liu. Finite difference time domain (FDTD) method for modeling the effect of switched gradients on the human body in MRI. *Magnetic Resonance in Medicine*, 48:1037–1042, 2002.
- [122] F. Liu, B. L. Beck, B. Xu, J. R. Fitzsimmons, S. J. Blackband, and S. Crozier. Numerical modeling of 11.1T MRI of a human head using a MoM/FDTD method. *Concepts in Magnetic Resonance Part B (Magnetic Resonance Engineering)*, 24B(1):28–38, 2005.
- [123] A. Taflove. *Computational Electrodynamics: The Finite Difference Time Domain Method*. Artech House, Boston MA, 1995.
- [124] F. Wei, Q. and Liu, L. Xia, and S. Crozier. An object-oriented designed finite-difference time-domain simulator for electromagnetic analysis and design in mri: applications to high field analyses. *Journal of Magnetic Resonance*, 172:222–230, 2005.
- [125] J. D. Jackson. *Classical Electrodynamics*. John Wiley & Sons, 3rd edition, 1999.
- [126] J. Jin and J. Chen. On the SAR and field inhomogeneity of birdcage coils loaded with the human head. *Magnetic Resonance in Medicine*, 38:953–963, 1997.

- [127] J. Chen, Z. Feng, and J.-M. Jin. Numerical simulation of SAR and B_1 -field inhomogeneity of shielded RF coils loaded with the human head. *IEEE Transactions on Biomedical Engineering*, 45(5):650–659, May 1998.
- [128] B. K. Li, F. Liu, and S. Crozier. Focused, eight-element transceive phased array coil for parallel magnetic resonance imaging of the chest – theoretical considerations. *Magnetic Resonance in Medicine*, 53:1251–1257, 2005.
- [129] P. B. Johns. On the relationship between TLM and finite-difference methods for maxwells equations. *IEEE Transactions on Microwave Theory and Techniques*, MTT-35(1):60–61, January 1987.
- [130] P. B. Johns. Symmetrical condensed node for the TLM method. *IEEE Transactions on Microwave Theory and Techniques*, MTT-35(4):370–377, April 1987.
- [131] J.L. Herring. *Developments in the transmission-line modelling method for electromagnetic compatability studies*. PhD thesis, Electrical and Electronic Engineering, University of Nottingham, UK, 1993.
- [132] P. Naylor and R. Ait-Sadi. Simple method for determining 3-d tlm nodal scattering in nonscalar problems. *Electronics Letters*, 28:2353–2354, 1992.
- [133] John G. Sled and G. Bruce Pike. standing-wave and RF penetration artifacts caused by elliptic geometry: an electrodynamic analysis of MRI. *IEEE Transactions on Medical Imaging*, 17(4):653–662, August 1998.
- [134] Christos Christopoulos. *The Transmission-Line Modeling Method TLM*. IEEE/OUP Series on Electromagnetic Wave Theory. IEEE Press/Oxford University Press, Oxford, UK, 1995.
- [135] J.-P. Berenger. A perfectly matched layer for the absorption of electromagnetic waves. *Journal of Computational Physics*, 114:185–200, 1994.
- [136] J.-L. Dubard and D. Pompei. Optimization of the PML efficiency in 3-D TLM method. *IEEE Transactions on Microwave Theory and technique*, 48(7):1081–1088, 2000.
- [137] P. J. Cassidy, S. Grieve, K. Clarke, and D. J Edwards. Electromagnetic characterisation of MR RF coils using the transmission-line modelling method. *Magnetic Resonance Materials in Physics, Biology and Medicine*, 14:20–29, 2002.

- [138] T. S. Ibrahim, R. Lee, B. A. Baertlein, Y. Yu, and P.L. Robitaille. Computational analysis of the high pass birdcage resonator: finite difference time domain simulations for high-field MRI. *Magnetic Resonance Imaging*, 18:835–843, 2000.
- [139] R. Cacoveanu, P. Saguet, and F. Ndagijimana. TLM method – a new approach for the central node in polar meshes. *Electronics Letters*, 31:297–298, 1995.
- [140] H. Meliani, D. De Cogan, and P. B. Johns. The use of orthogonal curvilinear meshes in TLM models. *International Journal of Numerical Modelling*, 1:221–238, 1988.
- [141] R. A. Desai, A. J. Lowery, C. Christopoulos, P. Naylor, J. V. M. Blanshard, and K. Gregson. Computer modelling of microwave cooking using the transmission-line model. *IEE Proceedings A: Science, Measurement and Technology*, 139(1):30–38, 1992.
- [142] P. Sewell, T. M. Benson, C. Christopoulos, D. W. P. Thomas, A. Vukovic, and J. G. Wykes. Transmission-line modeling (TLM) based upon unstructured tetrahedral meshes. *IEEE Transactions on Microwave Theory and Techniques*, 53:1919–1928, 2005.
- [143] Bjarne Stroustrup. *The C++ programming language*. Addison-Wesley, Harlow, UK, 2000.
- [144] P.A. Mason, W.D. Hurt, T.J. Walters, Dapos, J.A. Andrea, P. Gajsek, K.L. Ryan, D.A. Nelson, K.I. Smith, and J.M. Ziriak. Effects of frequency, permittivity, and voxel size on predicted specific absorption rate values in biological tissue during electromagnetic-field exposure. *IEEE Transactions on Microwave Theory and Techniques*, 48:2050–2058, 2000.
- [145] D. F. Rogers. *Procedural Elements for Computer Graphics*. McGraw-Hill, 1985.
- [146] A. R. Shapiro, R. F. Lutomirski, and H. T. Yura. Induced fields and heating within a cranial structure irradiated by an electromagnetic plane wave. *IEEE Transactions on Microwave Theory and Techniques*, 19:187–196, 1971.
- [147] M. A. Morgan. Finite element calculation of microwave absorption by the cranial structure. *IEEE Transactions on Biomedical Engineering*, 28:687–695, 1981.
- [148] D. M. Sullivan, D. T. Borup, and O. P. Gandhi. Use of the finite-difference time-domain method in calculating EM absorption in human

- tissues. *IEEE Transactions on Biomedical Engineering*, 34:148–157, 1987.
- [149] D. M. Sullivan, O. P. Gandhi, and A. Taflov. Use of the finite-difference time-domain method for calculating EM absorption in man made models. *IEEE Transactions on Biomedical Engineering*, 35:179–185, 1988.
- [150] P. Dimbylow and O. P. Gandhi. Finite-difference time-domain calculations of SAR in a realistic heterogeneous model of the head for plane-wave exposure from 600 MHz to 3 GHz. *Physics in Medicine and Biology*, 36:1075–1089, 1991.
- [151] P. Dimbylow. FDTD calculations of the whole-body averaged SAR in an anatomically realistic voxel model of the human body from 1 MHz to 1 GHz. *Physics in Medicine and Biology*, 42:479–490, 1997.
- [152] P. Dimbylow. Resonance behaviour of whole-body averaged specific energy absorption rate (sar) in the female voxel model, NAOMI. *Physics in Medicine and Biology*, 50:4053–4063, 2005.
- [153] T. Nagaoka, S. Watanabe, K. Sakurai, E. Kunieda, S. Watanabe, M. Taki, and Y. Yamanaka. Development of realistic high-resolution whole-body voxel models of Japanese adult males and females of average height and weight, and application of models to radio-frequency electromagnetic-field dosimetry. *Physics in medicine and Biology*, 49:1–15, 2004.
- [154] The visible human project. http://www.nlm.nih.gov/research/visible/visible_human.html.
- [155] C. Gabriel and S. Gabriel. Compilation of the dielectric properties of body tissues at RF and microwave frequencies. Technical Report AL/OE-TR-1996-0037, United States Air Force, 1996. Available at <http://www.brooks.af.mil/AFRL/HED/hedr/reports/dielectric/>.
- [156] Federal Communications Commission. Tissue dielectric properties. <http://www.fcc.gov/fcc-bin/dielec.sh>.
- [157] C. M. Collins and M. B. Smith. Calculations of B_1 distribution, SNR, and SAR for a surface coil adjacent to an anatomically-accurate human body model. *Magnetic Resonance in Medicine*, 45:692–699, 2001.
- [158] I. J. Bahl and D. K. Trivedi. A designer's guide to microstrip line. *Microwaves*, 16:174–182, 1977.
- [159] J. A. Lim and A. V. Oppenheim, editors. *Advanced Topics in Signal Processing*. Prentice Hall, 1988.

- [160] W. L. Ko and R. Mittra. A combination of FDTD and Prony's method for analyzing microwave integrated circuits. *IEEE Transactions on Microwave Theory and Techniques*, 39:2176–2181, 1991.
- [161] H.W. Fischer, P.A. Rinck, Y. Van Haverbeke, and R.N. Muller. Nuclear relaxation of human brain gray and white matter – analysis of field dependence and implications for MRI. *Magnetic Resonance in Medicine*, 16(2):317–334, 1990.
- [162] J. F. James. *A Student's Guide to Fourier Transforms*. Cambridge University Press, 1995.
- [163] J. A. de Zwart, P. van Gelderen, P. Kellman, and J. H. Duyn. Application of sensitivity-encoded echo-planar imaging for blood oxygen level-dependent functional brain imaging. *Magnetic Resonance in Medicine*, 48:1011–1020, 2002.
- [164] D. O. Walsh, A. F. Gmitro, and M. W. Marcellin. Adaptive reconstruction of phased array MR imagery. *Magnetic Resonance in Medicine*, 43:682–690, 2000.
- [165] B. Madore. UNFOLD-SENSE: A parallel mri method with self-calibration and artifact suppression. *Magnetic Resonance in Medicine*, 52:310–320, 2004.
- [166] M. A. Griswold, P. M. Jakob, R. M. Heidemann, M. Nittka, V. Jellus, J. Wang, B. Kiefer, and A. Haase. Generalized autocalibrating partially parallel acquisitions (GRAPPA). *Magnetic Resonance in Medicine*, 47:1202–1210, 2002.
- [167] D. G. Norris. High field human imaging. *Journal of Magnetic Resonance Imaging*, 18:519–529, 2003.
- [168] M/A-Com. MA4P1250 datasheet v3.00.
- [169] W. Gropp, E. Lusk, and A. Skjellum. *Using MPI*. MIT Press, 2nd edition, 1999.
- [170] J. D. Wills. Spectral estimation for the transmission line matrix method. *IEEE Transactions on Microwave Theory and Techniques*, 38:448–451, 1990.
- [171] H. H. Pennes. Analysis of tissue and arterial blood temperatures in the resting human forearm. *Journal of Applied Physiology*, 1:93–122, 1948.
- [172] C. M. Collins, W. Liu, J. Wang, R. Gruetter, J. T. Vaughan, K. Ugurbil, and M. B. Smith. Temperature and SAR calculations for a human

head within volume and surface coils at 64 and 300 MHz. *Journal of Magnetic Resonance Imaging*, 19:650–656, 2004.